PLASMONIC NANOLITHOGRAPHY MACHINE (PLM)

by

Mohamed E. Saad

A dissertation submitted to the faculty of
The University of North Carolina at Charlotte
in partial fulfillment of the requirements
for the degree of Doctor of Philosophy in
Mechanical Engineering

Charlotte

2013

Approved by:

_____
Dr. Robert J. Hocken

_____
Dr. Edward P. Morse

_____
Dr. Stuart T. Smith

_____
Dr. M. Taghi Mostafavi

_____
Dr. Faramarz Farahi

ABSTRACT

MOHAMED E. SAAD. Plasmonic nanolithography machine (PLM)
(Under the direction of Dr. ROBERT J. HOCKEN)

The Plasmonic Nanolithography Machine (PLM) is a prototype that adopts near field maskless plasmonic nanolithography to achieve 45 nm line widths at 45 nm half pitch. A plasmonic lens floating on a hydrodynamic air bearing rides on a disc with about a 35-mm radius writable substrate surface. A UV laser is used to excite surface plasmons in the lens, which, in turn, expose resist on the disk. The disc spins at nominally 1000 RPM and the lens traverses it in the radial direction. The machine linearly moves the lens across the disk. The traverse length is 42.4 mm, the alignment time is less than one minute, and the average traverse speed is 5 μm/s. The PLM's traverses the lens with a resolution of less than 5 nm and an angular error of less than 1 μrad.

The PLM is composed of a base and carriage. Two Halbach linear array motors move the carriage in the radial direction. The advantage of using the Halbach linear array is that it provides smooth contactless linear motion that is directly proportional to the current applied without generating much heat.

Vacuum preloaded air bearings are used to carry the carriage at a 5-micron flying height on diamond-turned surfaces located on the base. The air bearings have high angular stiffness, which makes them a good choice to reduce pitch and yaw errors.

Eddy current dampers are used on the PLM to provide the necessary damping during the carriage motion. The main advantage of these dampers is that they provide a smooth linear damping that is directly proportional to the carriage speed. At 5 μm/s carriage speed, the dampers provide about 4.28 mN damping force.

The PLM has many piezoelectric actuators that align and adjust the distance between the plasmonic lens and a pre-focusing lens that focuses the UV laser on the plasmonic lens. Also, capacitance gauges are used on the tailor-made pre-focusing flexure to determine the pre-focusing position.

The PLM has built-in interferometers. Their functions are to monitor the vibration of the plasmonic lens during the writing process so its position may be controlled. The carriage motion is constrained by two Hall-effect limit switches that provide a contactless means to stop the writing process when necessary. Also, there are pressure limit switches to monitor the pressure of the air bearings' air supply, and when triggered they stop the process and give an alarm to the user.

ACKNOWLEDGMENTS

No word can explain my deepest gratitude and appreciation to my advisor Dr. Robert J. Hocken for his guidance and continued support during my graduate studies. Special thanks to Dr. Jimmie Miller for his great support, valuable advice, and remarkable ideas. Great thanks to Mr. Greg Caskey for his great efforts in the PLM assembly and valuable advice during the design stage. I would like to thank Mr. John Brien for assembling the Halbach motors' stators and all his valuable efforts connecting all the PLM electronic system. I am very thankful to Dr. Stuart Smith for his valuable ideas and comments and his help to improve the prefocusing flexure. I deeply appreciate the help of Dr. Liang Pan for his brilliant ideas and suggestion. I would like to thank SINAM and therefore NSF for funding this project. Many thanks to Dr. Wen Wang for designing the original prefocusing flexure. I am very thankful to my colleagues Deepak Kohli, Christopher Hughes, Kang Ni, and Mark Rubeo for being a part of this project. I would also like to thank all of the members of IRG1, Dr. T-C Tsao, Dr. Adrienne Lavine, Dr. Yong Chen, Dr. José Fabra, Yen Chi Chang, Kevin Chou, Shaomin Xiong, and Jeongmin Kim. I also want to thank Roland Hege, Joel Pritchard, and Brian Dutterer for their valuable time in the machine shop during the fabrication of PLM. I really appreciate Tracee Jackson for her great help and efforts. Finally, I would like to thank my Ph.D. committee members very much for their time and effort.

DEDICATION

To

My loving parents
My brother Tarek and my sister Mona
My Brother Ibrahim who passed away before seeing my dream comes true
My Loving wife and my daughters Rania and Dalia
My Friends Tarek Elgayar and Ahmed Elraay

TABLE OF CONTENTS

LIST OF TABLES

LIST OF FIGURES

LIST OF ABBREVIATIONS

CPM	Center for precision metrology
EUV	Extreme ultraviolet
EBL	Electron beam lithography
IC	Integrated circuit
IRG	Internal research group
MAPS	Multi-scale alignment and positioning system
NIL	Nanoimprint lithography
PIL	Plasmonic imaging lithography
PZT	Piezoelectric transducer
SINAM	Center for scalable and integrated nano manufacturing
SPL	Scanning probe lithography
T-NIL	Thermal nanoimprint lithography
UV-NIL	Ultraviolet nanoimprint lithography
XRL	X-Ray lithography

CHAPTER 1: INTRODUCTION AND BACKGROUND

1.1. Introduction

The goal of this research project is to design, manufacture, assemble and calibrate a state-of-the-art plasmonic nanolithography machine. This project is a result of cooperation between the Center for Precision Metrology (CPM), located at the University of North Carolina at Charlotte, and the Center for Scalable and Integrated NanoManufacturing (SINAM), based at the University of California at Berkeley.

The Center for Precision Metrology has developed many instruments that satisfy the continued need for producing nano-structures with high throughput [Lemmons, 2012]. For instance, the development of the Multi-Alignment Positioning System (MAPS) is one example that was motivated by this need [Ozturk, 2007; Fesperman, 2006; Stuart, 2009; Ruben, 2002].Since the first integrated circuit was conceptualized and built [Taniguchi, 1974; Hocken, et al., 2007; Dummer,1952; Noyce, 1961; Kilby, 1964] there has been a continuous development in the lithography technology.

1.2. Background

Lithography can be carried out using many techniques, such as photolithography (optical, UV, EUV) [LLNL Review, 1997; Gwyn, et al., 1998; Stulen, 1999], E-beam/ion-beam lithography [Broers, et al., 1987; Fischer, 1993], x-ray lithography [Silverman,1997; Simon, et al., 1997; Spears, 1972; Early, et al.,1990], and interference

lithography and nanoimprint [Chou, et al., 1995, 1997; SINAM, 2001; Austin, et al., 2005; Hand, 2007; Braun, 2008]. Imprint lithography and optical lithography are highly attractive due to the high throughput for mass fabrication. Also, photolithography has been a major fabrication method in the integrated circuit (IC) and semiconductor industries over the past several decades. Nanoimprint lithography has demonstrated great capabilities, however, the leveling of the imprint template and the substrate during the printing process is a challenge.

Deep UV photolithography can offer a resolution of sub-100 nm, but the spacing between patterns and the minimum feature size are determined by the diffraction limit of light [Srituravanich, et al., 2004]. In order to overcome the diffraction limit some technologies were developed, such as near field interference lithography and phase shifting mask lithography [Srituravanich, et al., 2004].

Many researchers proposed methods with a resolution below the diffraction limit, such as Pieter G. Kik, et. al., who used broad beam illumination and standard photoresist [Kik. et al.. 2002]. Kik was able to generate feature sizes below λ/10. J.B. Pendry [Pendry, 2000] concluded that to overcome the wavelength effect associated with a conventional lens, a slab of negative refractive index material, such as silver, can be used to focus all Fourier components of a 2D image. Luo and Ishihara proposed the use of surface-plasmon polariton resonance of a metallic mask in the optical near field to produce sub-wavelength scale patterns [Luo, 2004]. On the other hand, dealing with the sub-wavelength structures may be challenge when it comes to defect inspection. Edward T. F. Rogers, et al. [Rogers, et al., 2012] argued that super-oscillation-based imaging has unbeatable advantages as it allows the object to be a large distance from the lens and can

operate at wavelengths from X-rays to microwaves. Also, Rogers, et. al., proved that plasmonic metamaterial under certain conditions can focus transmitted light into sub-wavelength hot spots located beyond the near field [Rogers, et al., 2012]. Sungrnin Huha, et. al., discussed a defect inspection technique up to 16 nm half pitch lithography [Huha, et al., 2009].

There are some critical concerns when generating sub-wavelength features from apertures smaller than the exposing wavelength, such as low transmission through the apertures, poor contrast, and limitation of the exposing distance [Srituravanich, et al., 2004]. One of the promising techniques to overcome these concerns is to use plasmonic lithography which introduces nano-structures (plasmonic lenses) that can enhance the intensity 100 times at the focal point compared to that of the incident light [Srituravanich, et al., 2008]. The basics of plasmonic lithography are discussed in the following pages.

1.2.1. Plasmonic Imaging Lithography (PIL)

Plasmonic Imaging Lithography (PIL) has many advantages, such as high resolution, maskless, lower cost, and high speed. Also, the PIL is highly flexible, user friendly, and has the potential to achieve throughputs that are two to five orders of magnitude higher than other maskless techniques.

A plasmon can be defined as the quantum of the plasma oscillation of the conduction electron gas in a metal [Zhiming, 2010; Srituravanich, et al., 2004; Liu , et al., 2005; Luo,2004]. A surface plasmon is a special plasma oscillation mode which happens at the interface of a metal of negative dielectric constant and a material of positive dielectric constant [Raether, 1988]. Figure 1 illustrates the principle of surface plasmons.

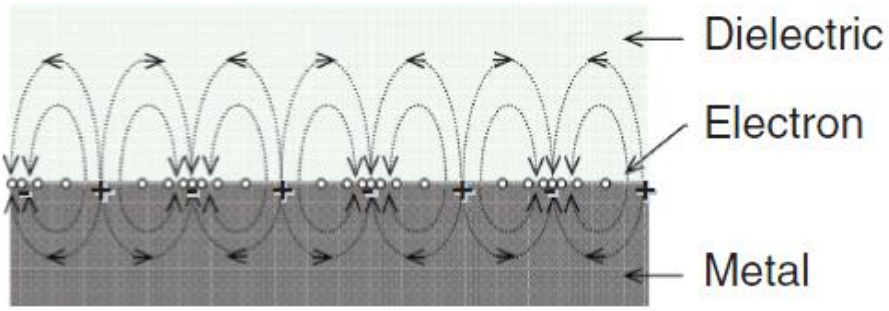

Figure 1: Illustration of the surface plasmon principle. [Wang, 2010]

Furthermore, surface plasmons can be defined as fluctuations in the electron density at the material boundaries and can couple with photons [Pitarke, et al., 2007]. Based on that, some metal structures have been introduced that can focus light into a nano-spot about 20 nm away from the lens surface. These structures are known as plasmonic lenses (PL) [Srituravanich, et al., 2008]. Figure 2 shows examples of common shapes of plasmonic lenses.

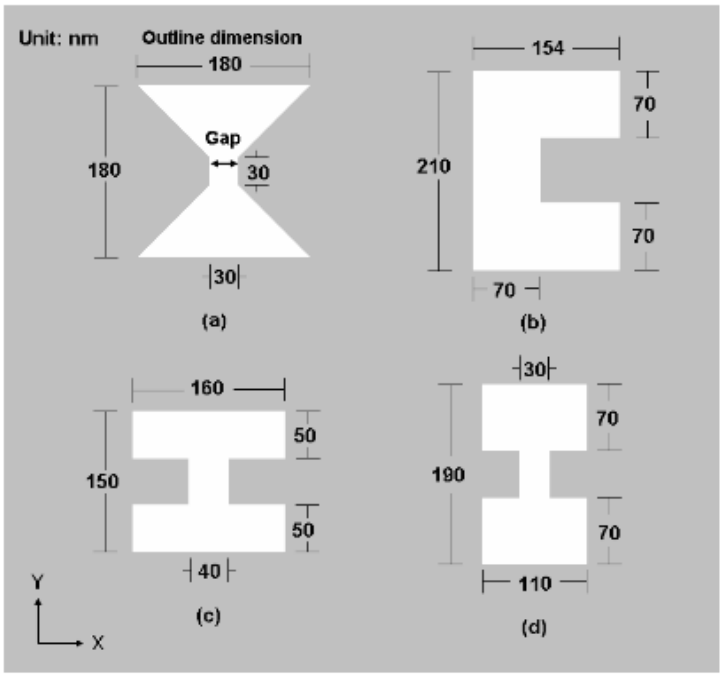

Figure 2: Schematic structure of common plasmonic lenses [Rao, et al., 2007].

One of the main challenges of this technology is that the nano-scale spots are formed on about 20 nm of the plasmonic lens surface, which makes it hard to scan a surface spinning at high speed. Liang Pan, Cheng Sun and others [Srituravanich, et al., 2008] were able to design a self-spacing air bearing that can fly the plasmonic lens array about 20 nm above a disk that is spinning at speeds of between 1000 and 3000 RPM, and they were able to make patterns of 80 nm linewidth. The following Figure 3 illustrates the air bearing surface developed by Liang, et. al. [Srituravanich, et al., 2008], and a simulation of the air bearing wedge that carries the air bearing during the process.

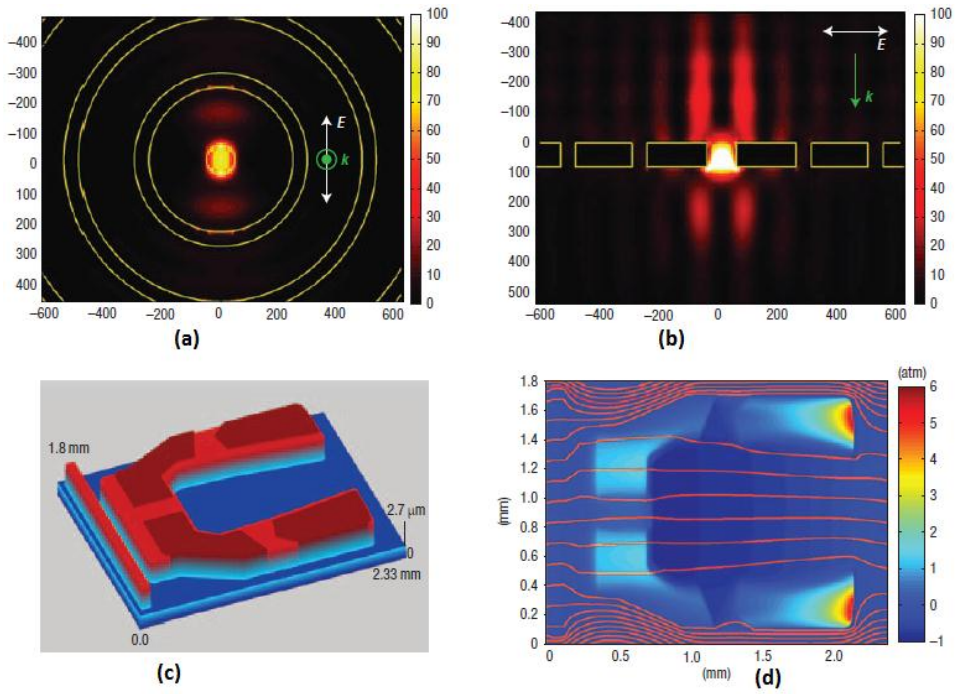

Figure 3: Illustration of plasmonic lens array and airbearing surface developed by Liang Pan, et al. [Srituravanich, et al., 2008]. (a) Plasmonic lens (PL), (b) Cross-sectional view of PL, (c) CAD model of the air bearing, (d) Aerodynamic simulation of the air bearing.

During this process, an ultraviolet (UV) laser is used to illuminate a plasmonic lens that floats on an air bearing on a spinning disk (like that used in magnetic disk drives). The laser exposes a thermally-activated resist as the disk spins, allowing high-speed writing on the disk surface. Once exposed, normal semiconductor processing will be used on the exposed disk. Figure 4 illustrates the process setup.

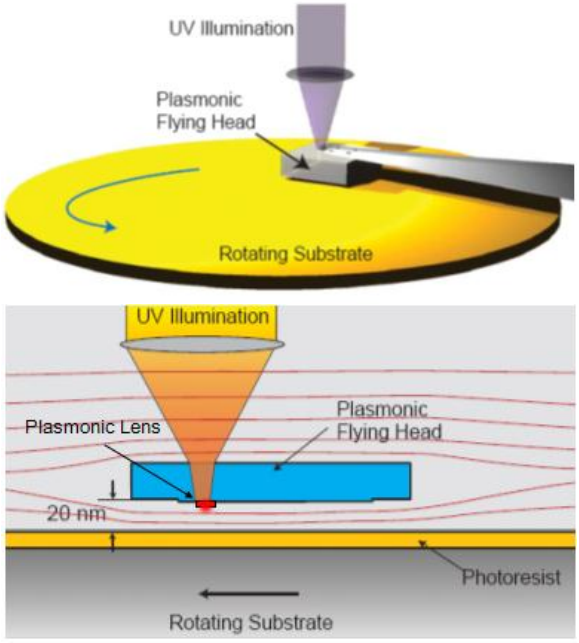

Figure 4: Illustration of plasmonic lithography [Srituravanich, et al., 2008]

In order to achieve an acceptable uncertainty using plasmonic lithography, it is important to have a robust mechanical design that allows the plasmonic flying head to move precisely above the rotating substrate. This motion must be controllable, accurate and repeatable in order to achieve an acceptable patterning quality. This challenge is the motivation behind starting the current research project. It was required to build a prototype that can perform plasmonic nanolithography. The goal is set to produce patterns of 45-nm linewidth with a resolution less than 5 nm. This goal led to the development of the Plasmonic Nano-Lithography Machine (PLM).

CHAPTER 2: PLM CAPABILITIES AND SPECIFICATIONS

2.1. PLM Capabilities

The PLM is designed to generate 45-nm linewidths at 45 nm half pitch using surface plasmons. Figure 5 illustrates the machine coordinate system.

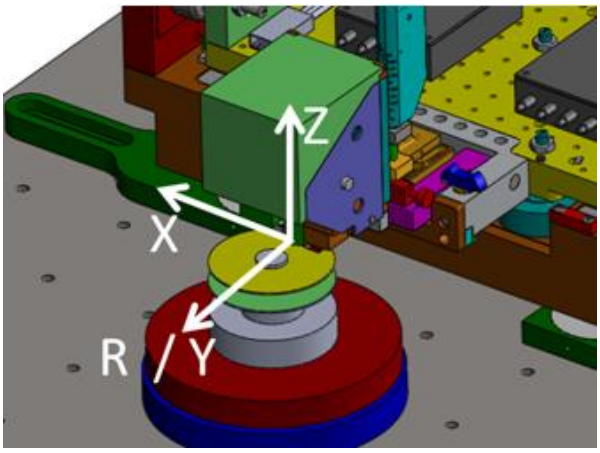

Figure 5: Coordinate system on the PLM

The PLM maximum travel length is 39 mm in the R direction. A tabulated list of the PLM performance specifications is shown in Table 1, below.

Table 1: PLM Performance Specifications.

Radial Length	39 mm
Radial Position Error	5 nm
Radial Resolution	< 5 nm
Radial Minimum Speed	100 nm/s

Radial Average Speed	5 μm/s
Pixel Size	45 nm
Uncertainty	5 nm
Prefocusing Stage Range	X and Y :50 μm Z :100 μm
Disk Spinning Speed Limits	1000-1500 RPM
Average Writing Time (full disk)	5 hrs
PL Lifetime (pre-alignment)	2 min
PL Lifetime (post-alignment)	20 min
Carriage Angular Stiffness	75 N/μ-rad
Carriage Linear (lateral) stiffness	26 N/μm
Carriage Linear (vertical) stiffness	39 N/μm
θ_x Leveling Error	1 μ-rad
Z-axis Fine Motion Travel	100 μm
Z-axis Coarse Travel (Vertical motor)	50.8 mm

2.2. PLM Features

(1) Halbach linear array motors

A Halbach magnet array motor (shown in Figure 6) provides contactless motion that can be controlled to an acceptable uncertainty level using a proper software interface. The frictionless motor is recommended for precision machines and has proven reliable performance in other machines such as MAPS [Fesperman, et al., 2012].

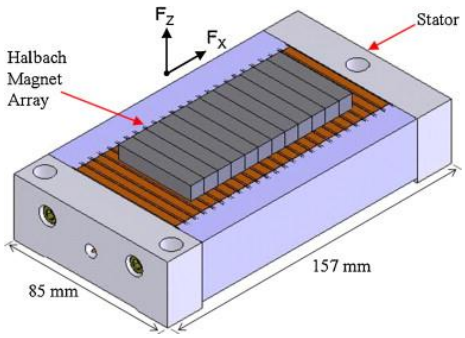

Figure 6: Layout of Halbach linear array motor [Fesperman, et al., 2012].

(2) Vacuum preloaded air bearings

The carriage moves on vacuum preloaded air bearings (NewWay™) which provide a stable, smooth linear motion. Also, the NewWay™ vacuum preloaded air bearing provides 15-20% damping ratio on background vibration modes up to 700 Hz [NewWay, 2013]. Figure 7 shows the air bearing location on the PLM.

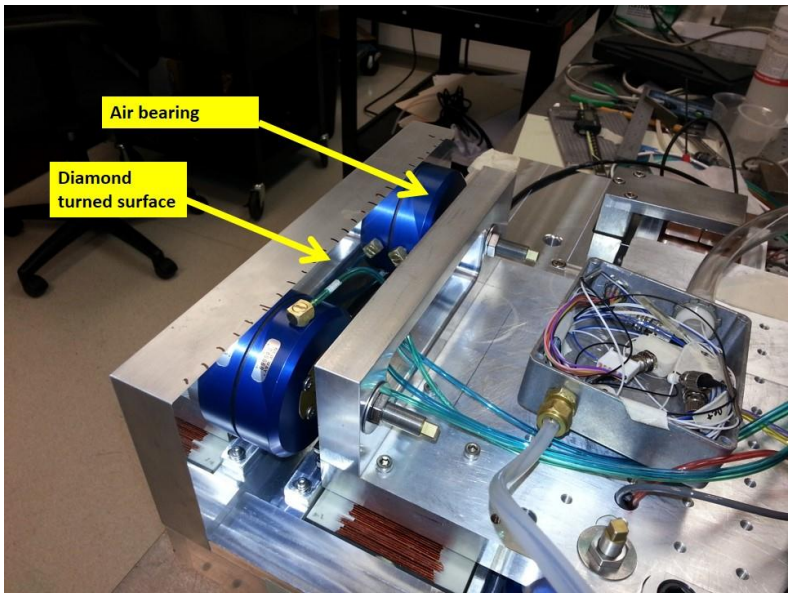

Figure 7: Side vacuum preloaded air bearings on the PLM.

The bearing base surface is graphite which is known to be self-lubricated. Also, the bearing process is based on averaging the projected area. This principal reduces the effects of any scratches that may occur on the diamond-turned surface.

(3) 5-nm resolution scales

The carriage linear displacement is measured using 5-nm resolution linear scales (Renishaw™) at both sides of the carriage, which are also used to determine yaw error that may occur during the motion. Figure 8 shows the location of one of the scales on the PLM.

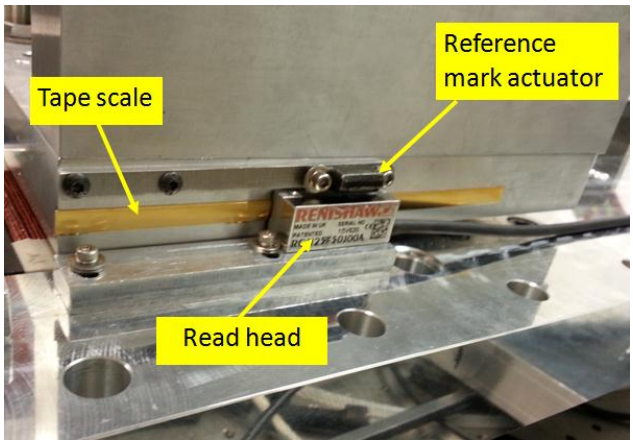

Figure 8: Location of one of the 5-nm resolution scales on the carriage side.

(4) Eddy current dampers

The eddy current dampers provide smooth linear damping of the carriage motion. The main advantages of this damper are being contactless and linearly proportional to the speed. The PLM has two eddy current dampers (see Figure 9), each providing 0.4 mN at 5 μm/s speed.

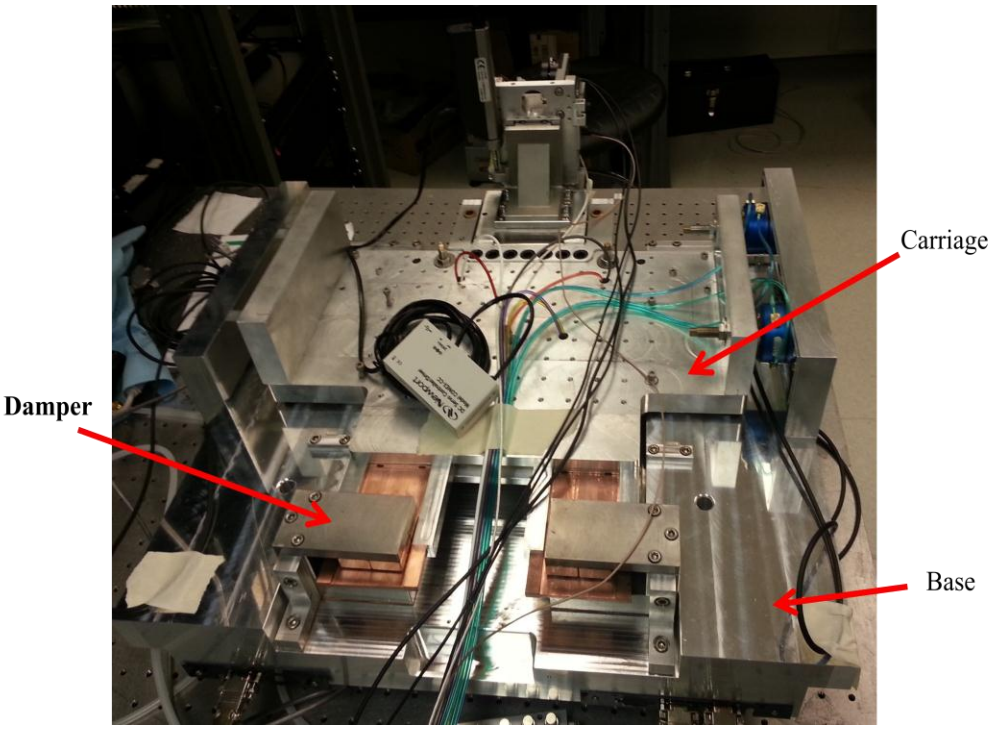

Figure 9: Location of the eddy current dampers on the PLM.

(5) Diode laser interferometer

The interferometer, designed by Mr. Christopher Hughes [Hughes, 2012], is used to measure the slider vibration during the writing process. The interferometer signal is used through a closed feedback system to reduce/eliminate the vibration using a two-dimensional shear actuator. Figure 10 shows the location of the interferometer on the PLM.

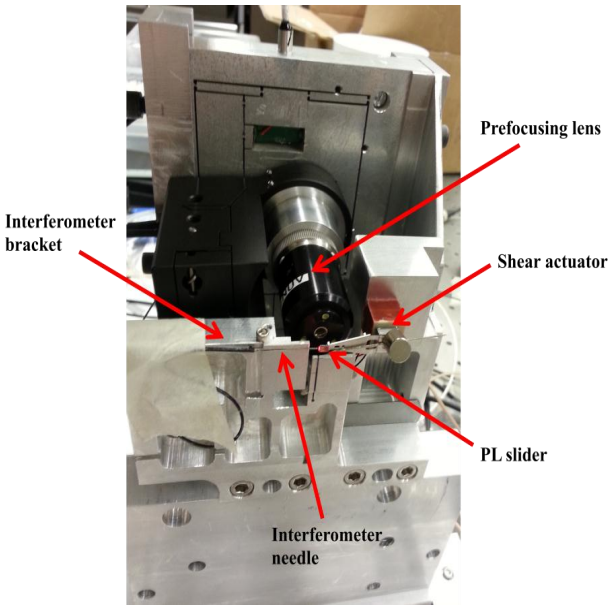

Figure 10: Location of the interferometer on the PLM's writing head.

(6) Prefocusing flexure

In order to provide a fine adjustment of the prefocusing lens a flexure was designed by Dr. Wen Wang and improved by Mark Rubeo. The flexure is equipped with capacitance gages and piezoelectric actuators to provide three-dimensional prefocusing capabilities. Figure 11 shows the location of the prefocusing flexure on the PLM's writing head.

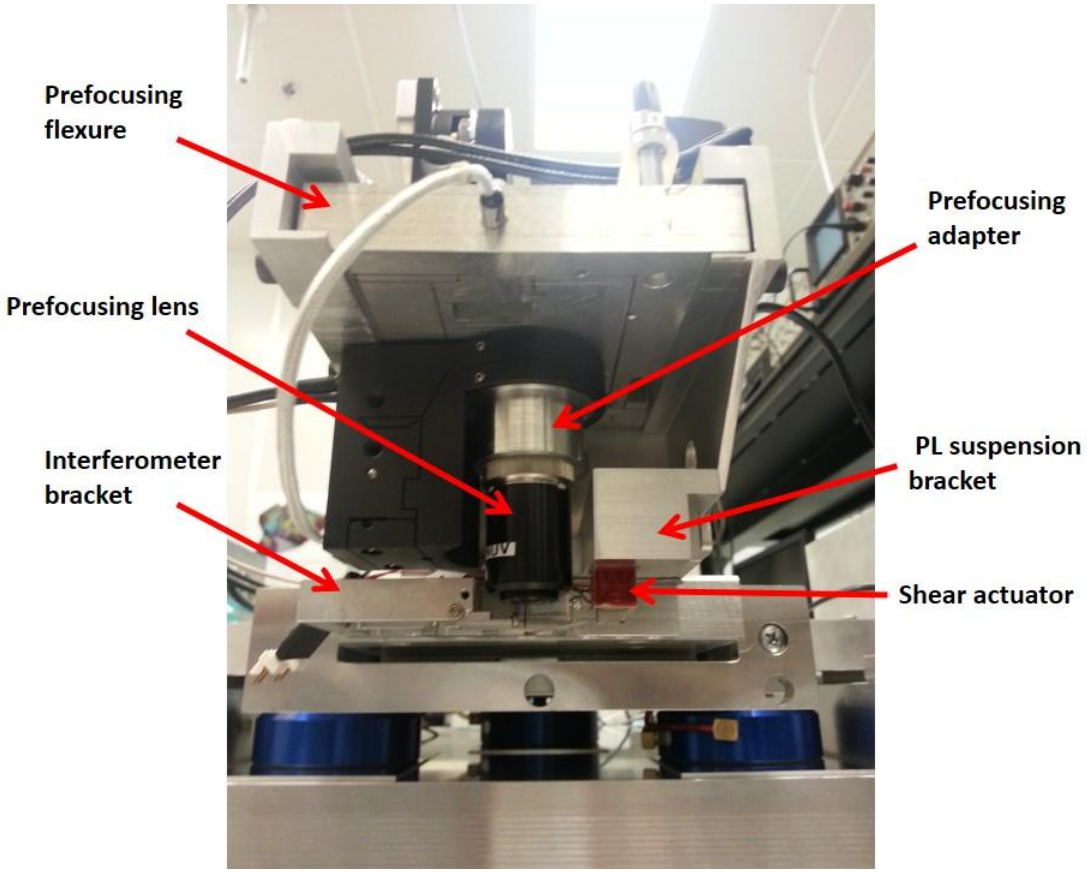

Figure 11: Location of the prefocusing flexure on the PLM's writing head.

(7) Coarse and fine adjustment devices:

The PLM has many coarse and fine adjustment devices to provide the necessary positioning of various elements with respect to each other during the writing and plasmonic lens changing phases. These devices, along with the design details of all the PLM's components, will be discussed in Chapter 3.

CHAPTER 3: PLM MECHANICAL DESIGN

3.1 Design Concept

By the end of fall 2009, Dr. José Yague-Fabra – as a member of the project team - developed an initial design concept for the Plasmonic Nanolithography Machine (PLM) as shown in Figure 12. The machine design proposed by Dr. Yague-Fabra consisted of a base and carriage and suggested Halbach linear motors to generate the required relative motion. Also, vacuum preloaded air bearings were suggested to carry the carriage and to provide high stiffness in the pitch and yaw directions. The basic concept of this design was to provide frictionless motion by the application of contactless motors and air bearings.

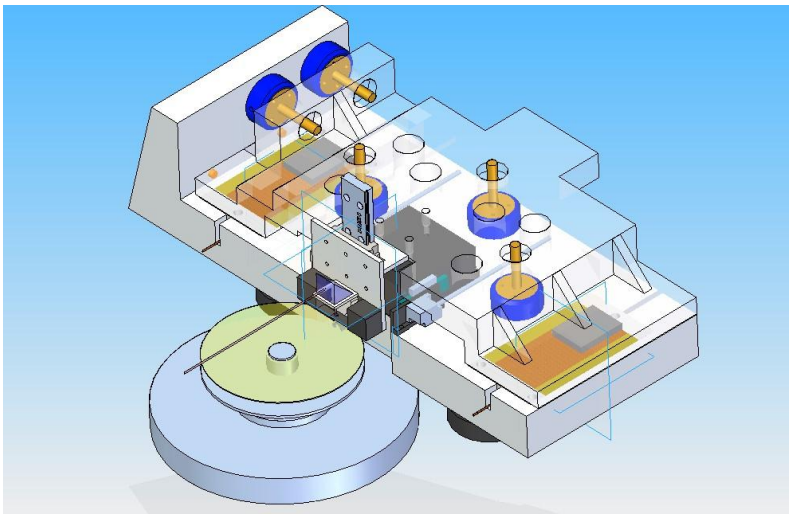

Figure 12: Preliminary concept design proposed by Dr. José Yague-Fabra [SINAM 2009].

This preliminary design was the basis to start a series of in-depth discussions of the design requirements specified by the project partners at the University of California at Berkeley. The brainstorming sessions were carried on weekly by the project team to develop a design that satisfies most of the requirements. For example, it is necessary to provide a means to hold the prefocusing and the plasmonic lenses. Also, the carriage and the base needed to be balanced. At the same time, the system needed many coarse and fine adjustment mechanisms. Figure 13 shows one of the initial proposed designs that satisfied most of these needs.

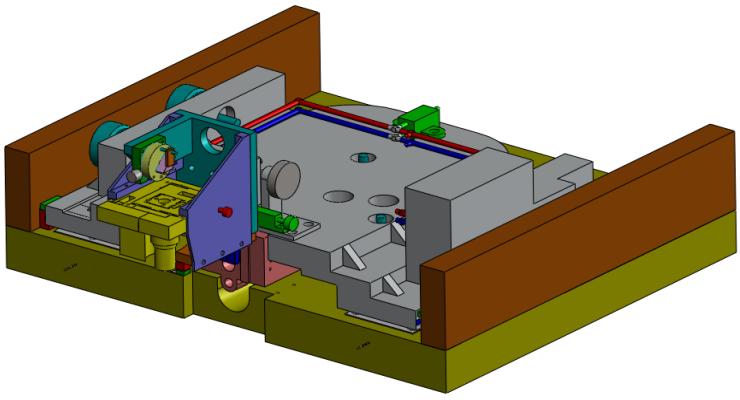

Figure 13: One of the initial machine designs.

The design was modified many times in order to achieve the requirements at minimum cost. One of these modifications was adding 5-nm scales on both sides of the carriage and adding eddy current dampers to the system. Also, the carriage design was modified in order to reduce the needed motor's power and consequently the heat generated. There was a need to add hard stops and limit switches and a system to monitor the slider position while flying on the disc.

Further design improvements took place after analyzing all machine components for static strains and vibration modes. After considering the final design requirements and considering all components, cables, fasteners, hoses and connectors, the PLM design is shown in Figure 14.

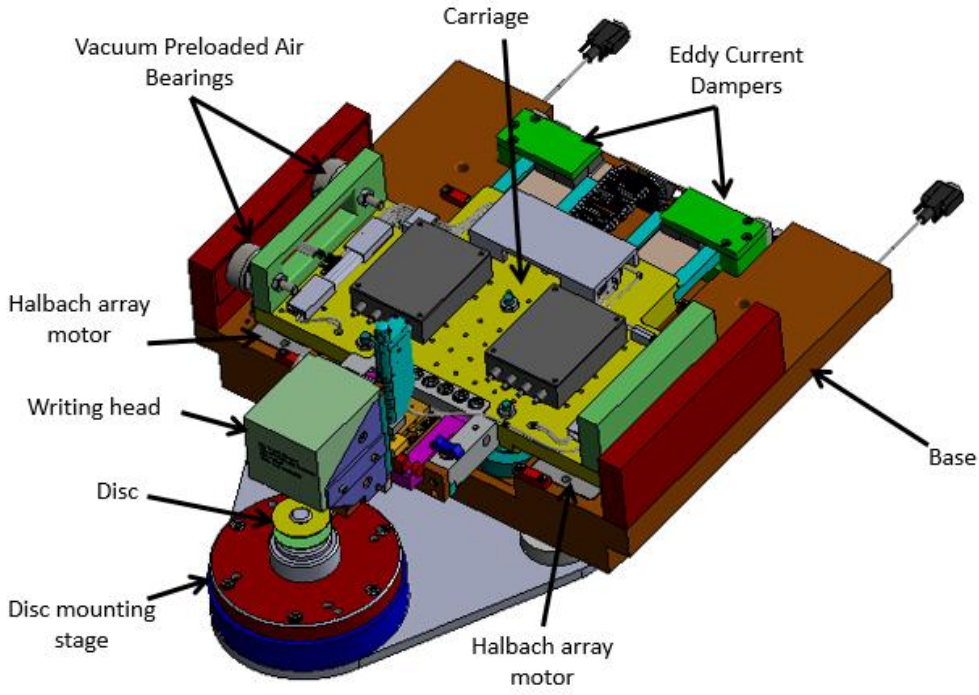

Figure 14: The PLM final design.

The PLM consists mainly of a base, carriage, and writing head. Most of the machine components are made of aluminum alloy 6061 (density 2698.8 kg/m^3) [Military Handbook, 2003] which caused the machine to be relatively light compared with ferrous metals (the machine total weight is about 68 kg). Also, Al 6061 is non-ferrous which is desirable to avoid any interaction with the magnetic fields generated by other machine components, such as the Halback linear motors and the eddy current dampers. The coefficient of thermal expansion of Al 6061 is about 23 ppm/˚K in the 20°-100°C range

[Military Handbook 2003]. In addition, Al 6061 has high thermal conductivity (1.67 joules/cm.s. °K [Military Handbook, 2003]), which makes the machine base act as a heat sink for the heat generated by the Halbach linear motors which have been proven to be the major source of heat in similar systems [Kim, et al., 2004;, Ruben, 2008]. Lastly, Al 6061 is highly resistive to corrosion and easy to manufacture, compared with ferrous metals, which reduced the machining costs.

The design software package Solidworks™ was used to design the machine and to analyze each component statically and dynamically. This package provides user-friendly tools to build individual parts as well as performing detailed finite element analysis (FEA). Also, the package allows assembly which was helpful to virtually build the PLM before manufacturing and examine the relative position between different parts. The PLM model is shown in Figure 14. The precision design rules are described at [Smith, 2003; Schellekens, et al., 1998; Hale, 1999].

3.2 Base

The base is made of Al alloy 6061 and was manufactured at University of North Carolina at Charlotte (UNCC). The base dimensions are 571.5 mm x 459.7 mm x 81.3 mm with a total weight of about 38.6 kg. The base also has two pockets to contain the stators of the Halbach motors and diamond fly cut surfaces. These latter surfaces provide the bearing surfaces to be used with three vacuum preloaded air bearings that carry the carriage. Figure 15 shows the base model and Figure 16 shows the manufactured base.

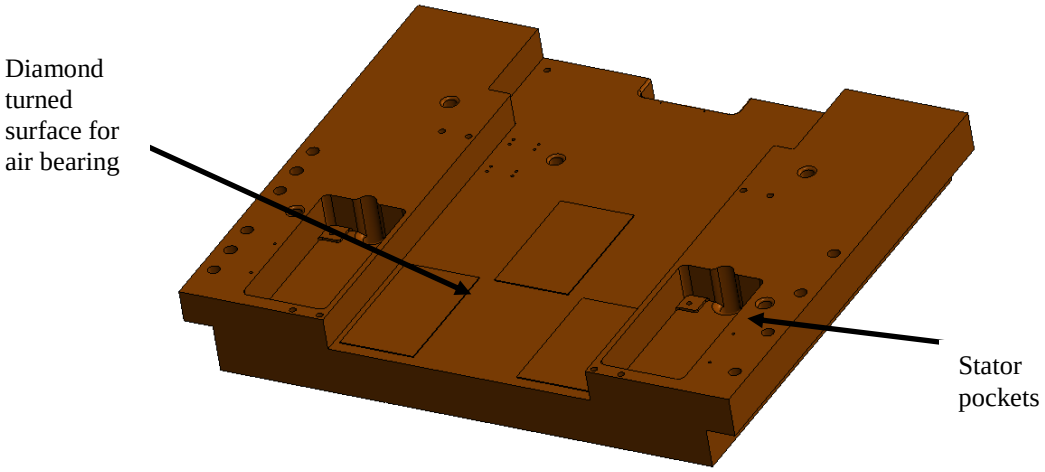

Figure 15: PLM's base model.

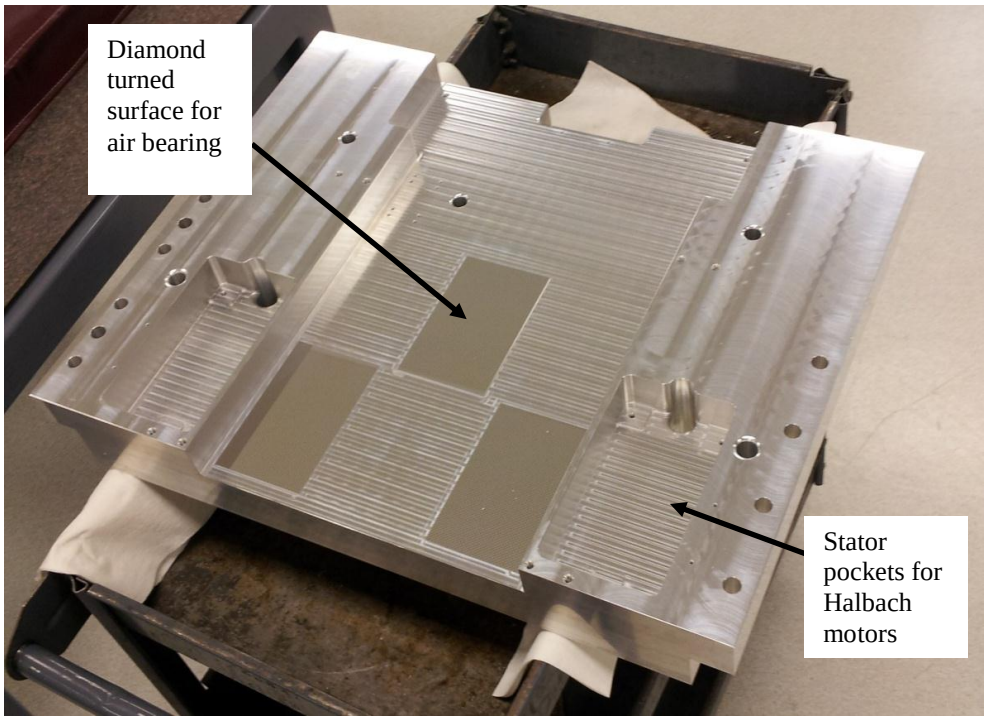

Figure 16: PLM base after manufacturing.

The base also has tapped holes to fasten the Hall effect limit switches, the linear scales' read heads, the eddy current dampers' yokes and the machine shoulders. The

machine is supported by three leveling feet. These feet are used to adjust the height and level of the whole machine. The PLM sets on a vibration isolation table (resonant frequency less than 3 Hz [Newport, 2013] to decouple the system from ground vibrations. Figure 17 shows the support positions on the base CAD model

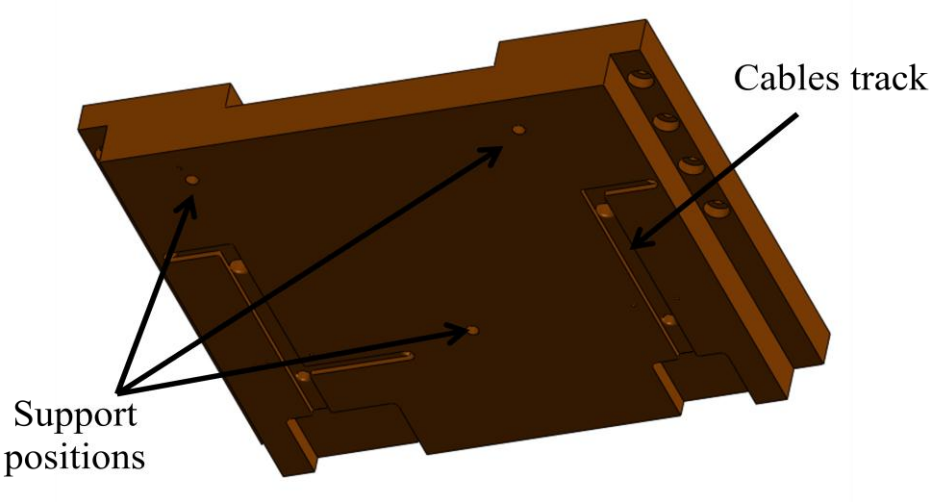

Figure 17: Base CAD model.

The base model was analyzed using Cosmos™ to determine the natural frequency and the first four harmonics. The base can be simplified as a mass set on three supports (leveling feet) and carrying another mass (the carriage assembly). This analogy is shown in Figure 18.

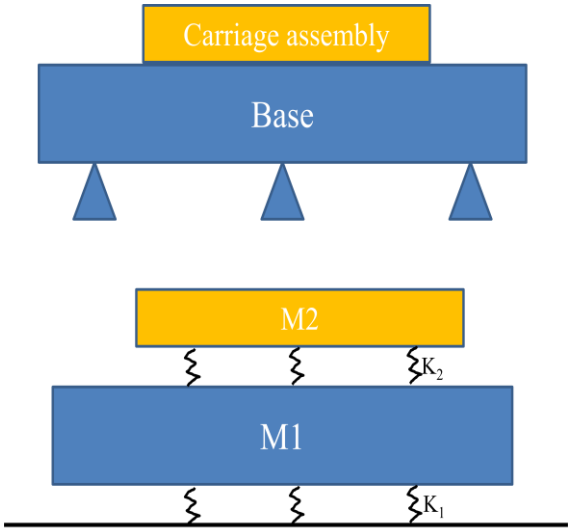

Figure 18: Analogy of the base for vibration analysis purpose.

Table 2 and Figure 19 show the first five vibration modes obtained using Cosmos™.

Table 2. Modal Analysis Results of the Base.

Mode No.	Frequency(Rad/sec)	Frequency(Hertz)	Period(Seconds)
1	2770.4	468.13	0.0022679
2	7299	602.29	0.00086082
3	9259.6	1382.8	0.00067856
4	14385	1472.1	0.00043679
5	17735	1715.3	0.00035428

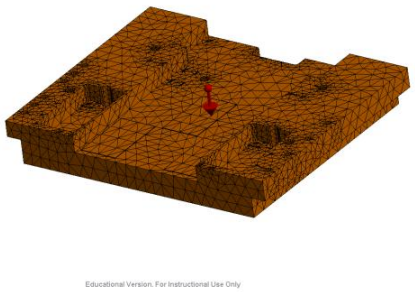

Base meshing

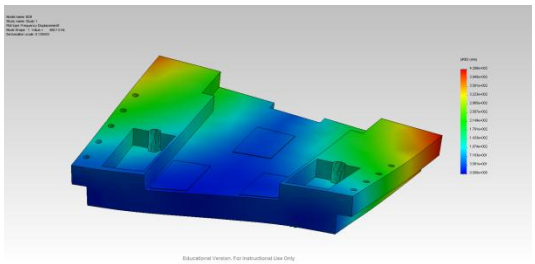

f_1 = 468.13 Hz

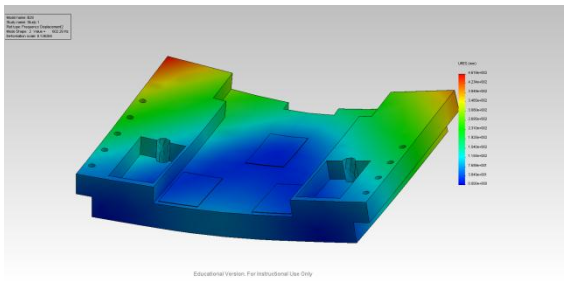

f_2= 602.29 Hz

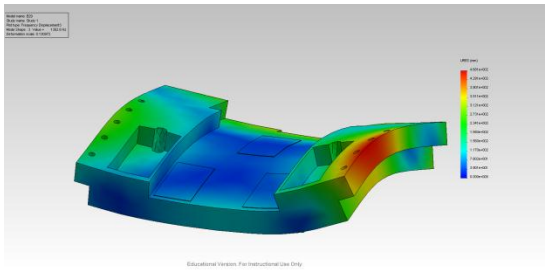

f_3= 1382.8 Hz

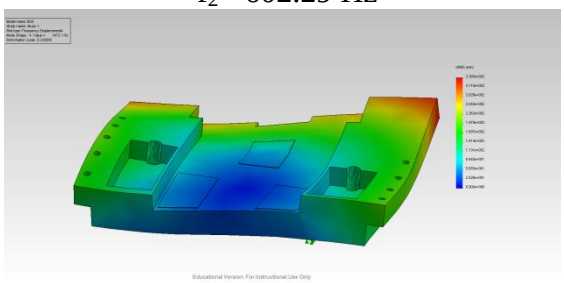

f_4 = 1472.1 Hz

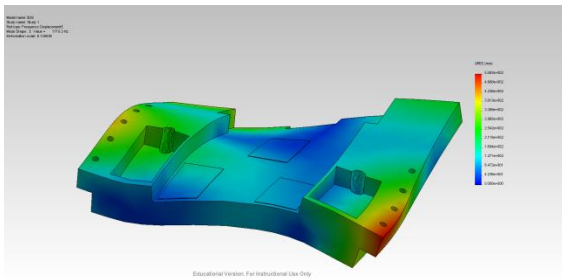

f_5 = 1715.3 Hz

Figure 19: Modal analysis of PLM's base.

3.3 Carriage

The carriage is designed to move 39 mm while carrying the writing head in the front and the copper plates of the eddy current dampers at the back. Also two shoulders were attached in addition to two magnet arrays that are a part of the Halbach linear

motors. In order to save power needed to move the carriage it was decided to make the carriage as light as possible which made aluminum a good choice based on its density. The carriage dimensions are 459.9 mm x 277.4 mm x 35.1 mm and its weight is 5.57 kg.

The top side of the carriage has an array of #10-32 tapped holes passing through the carriage thickness. These tapped holes will be used to attach any necessary components to the carriage top surface. Unless otherwise indicated all threaded fasteners in the PLM were English. Figure 20 shows the carriage model top side.

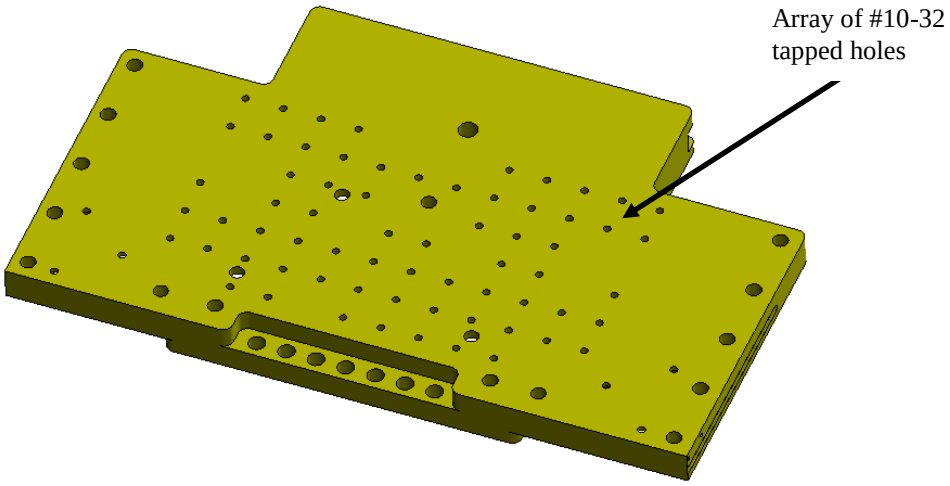

Figure 20: Model of the carriage top side.

On the bottom surface of the carriage there are many pockets to reduce the carriage weight. Also, there are two pockets – one on each side - to host the magnet arrays used for the Halbach motors. Figure 21 is an illustration of the carriage model top side. Figures 22 and 23 show the manufactured carriage top and bottom surfaces respectively.

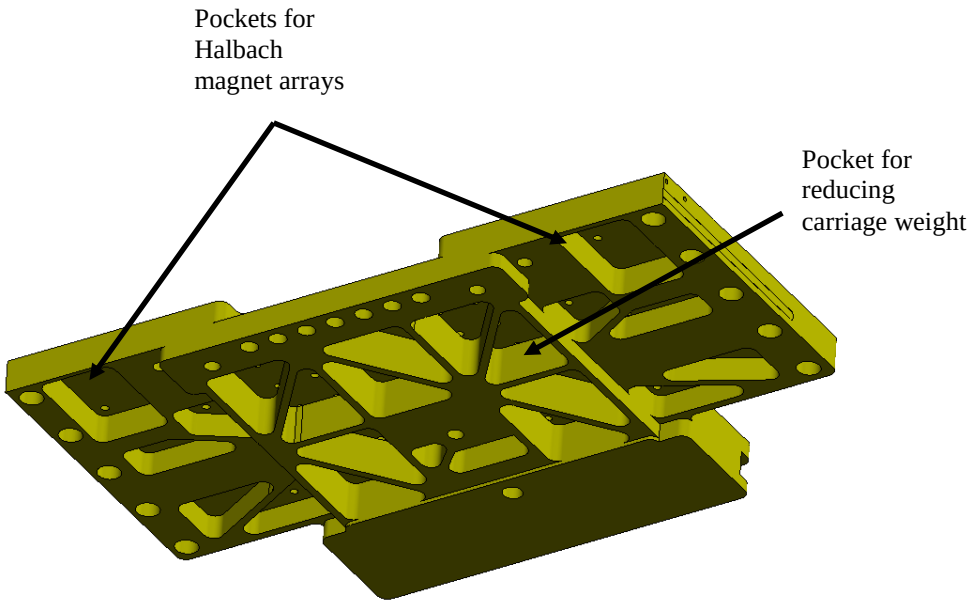

Figure 21: Model of the carriage bottom side

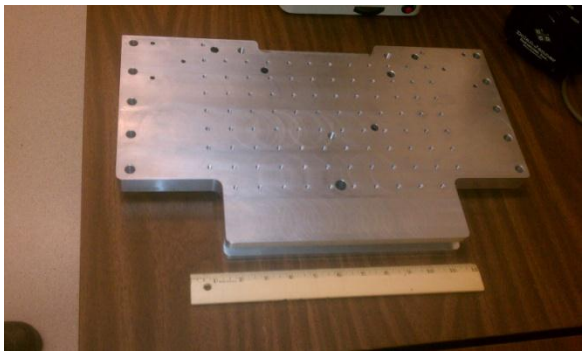

Figure 22: The carriage top surface

Figure 23: The carriage bottom surface

The carriage model was analyzed to determine the natural frequency and the first four harmonics. Table 3 and Figure 24 show the first five vibration modes.

Table 3. Modal Analysis Results of the Carriage.

Mode No.	Frequency (Rad/sec)	Frequency (Hertz)	Period (Seconds)
1	2770.4	440.93	0.0022679
2	7299	1161.7	0.00086082
3	9259.6	1473.7	0.00067856

4	14385	2289.4	0.00043679
5	17735	2822.6	0.00035428

Carriage meshing

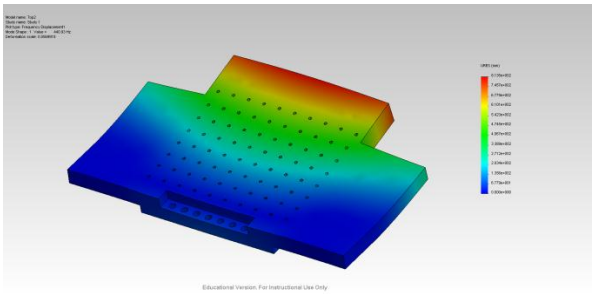

f_1 = 440.93 Hz

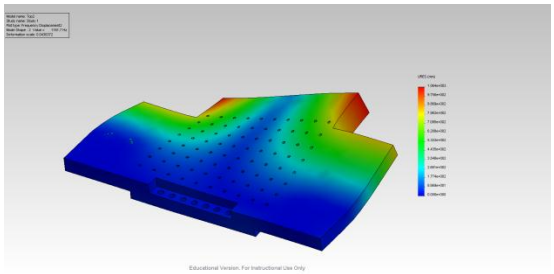

f_2 = 1161.7 Hz

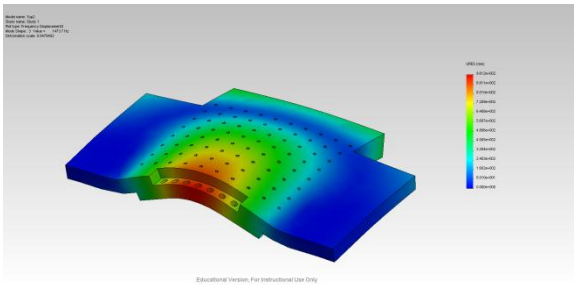

f_3 = 1473.7 Hz

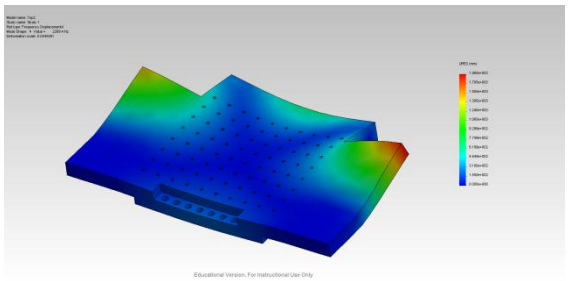

f_4 = 2289.4 Hz

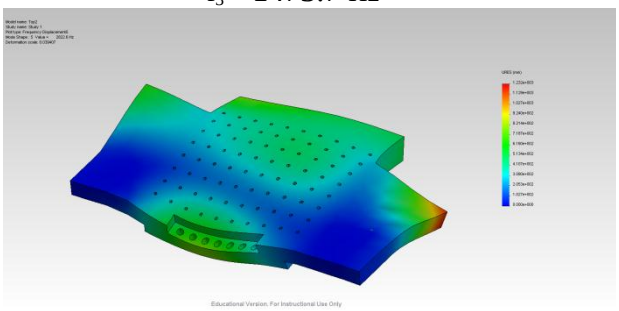

f_5 = 2822.6 Hz

Figure 24: PLM's carriage modal analysis.

3.4 Carriage Shoulders

In order to provide a straight linear contactless motion two air bearings were attached to the carriage side via a side shoulder. In order to keep the carriage balanced, another shoulder was added to the other side of the carriage. Both shoulders were made of Al

Alloy 6061. Figures 25 and 26 show the air bearing and the balancing shoulders on the carriage model.

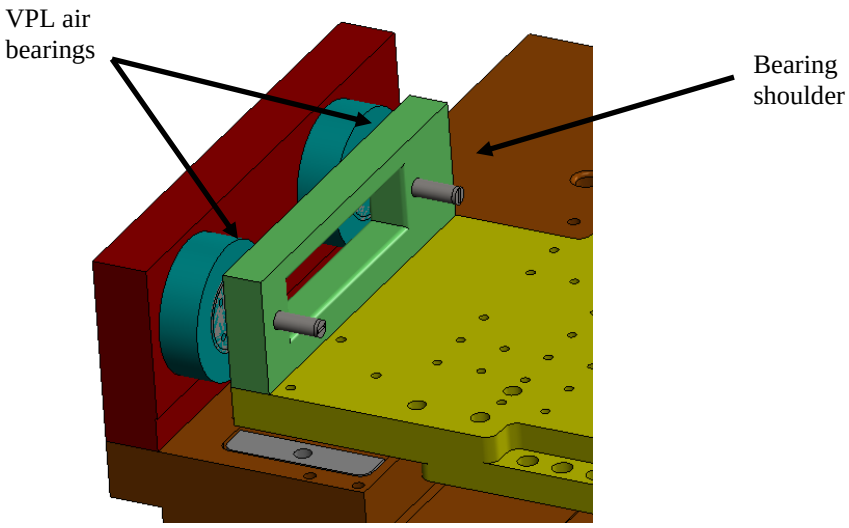

Figure 25: Illustration of the bearing shoulder on the carriage model.

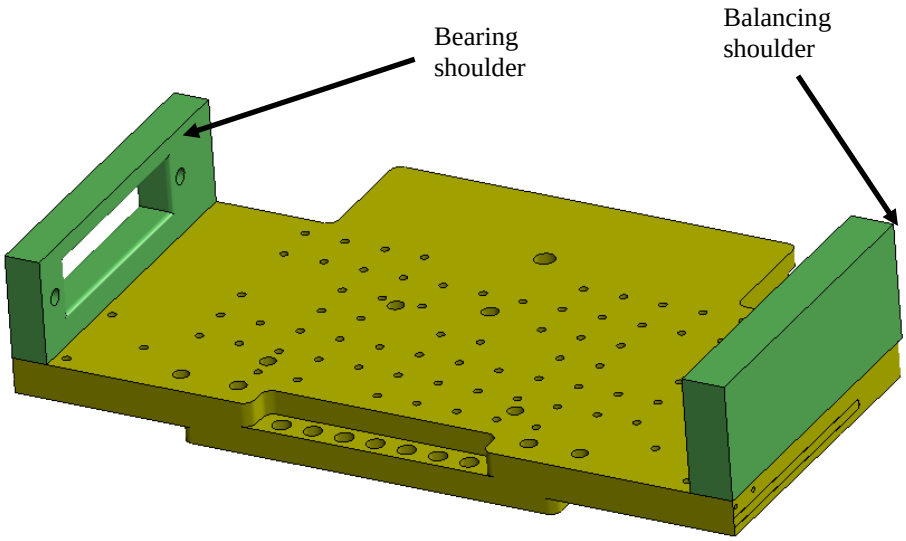

Figure 26: Illustration of the bearing and balancing shoulders on the carriage model.

3.5 Rotation Arm

The plasmonic lens should fly on a height of about 20 nm from the disc surface which makes it extremely hard to change the lens without causing damage such as

scratching the disc surface and it may cause an injury considering that the disk is spinning at 1000 RPM. In order to avoid this risk, the writing head is rotated 90˚ to change the plasmonic lens. Figures 27 and 28 show the writing head in the writing and plasmonic lens change positions.

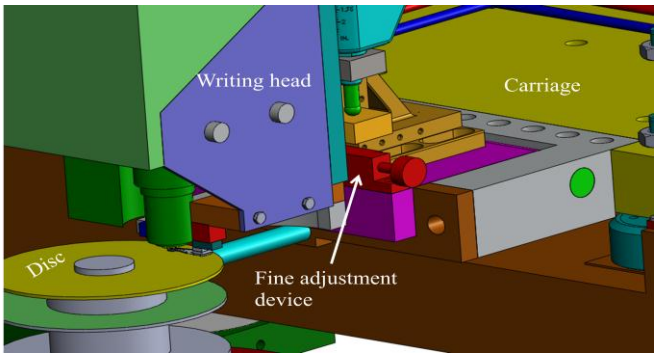

Figure 27: Illustration of writing head during the writing process.

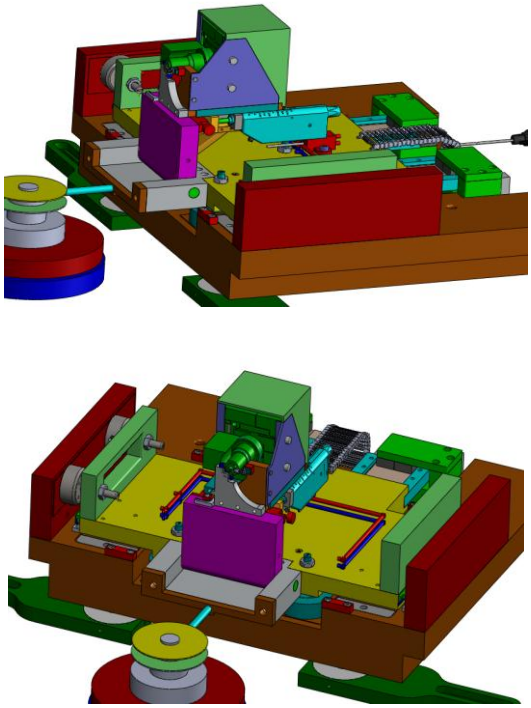

Figure 28: Illustration of the writing head in the lens changing position

In order to provide this 90˚ rotation to the system a rotation bracket was introduced. Figures 29 and 30 illustrate the rotation arm model and the manufactured arm respectively.

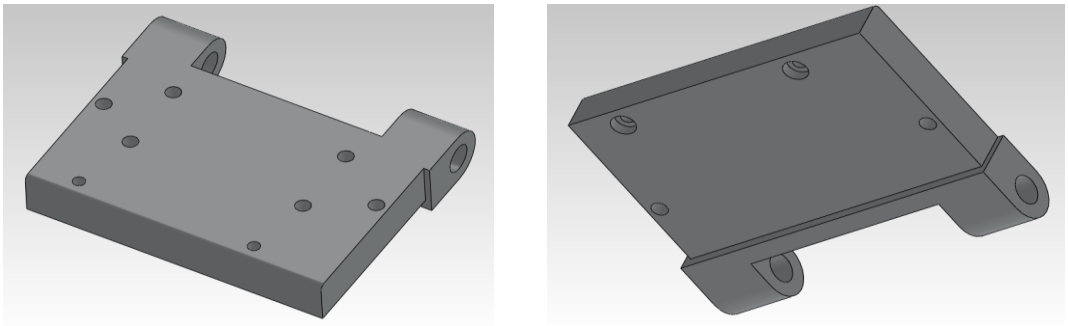

Top view Bottom view

Figure 29: The rotation arm model.

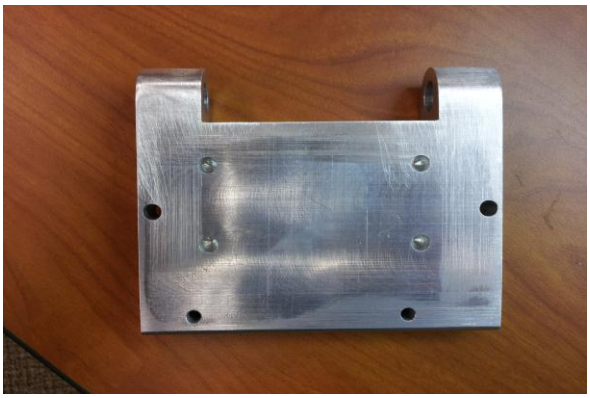

Figure 30: The rotation arm.

3.6 Monitoring System

A white light fringes monitoring system is used on the PLM in order to monitor the flying height of the plasmonic lens slider on the spinning disc during the writing process. This system consists of a monitoring bracket, monitoring arm, indexing bracket, image direction bracket, rotation base and 45˚ plane mirror. Figure 31 shows the location

of the monitoring system on the PLM CAD model. A photograph of the white light fringes is shown in Hughes' thesis [Hughes,2012].

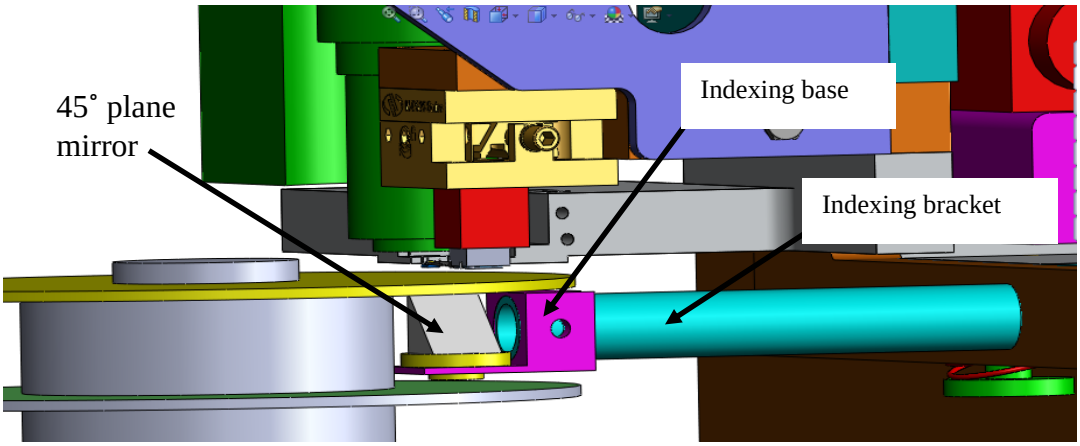

Figure 31: Location of the monitoring system on the PLM.

Figure 32 shows CAD models of the monitoring system assembly (a) and the monitoring arm assembly with the image direction bracket (b).

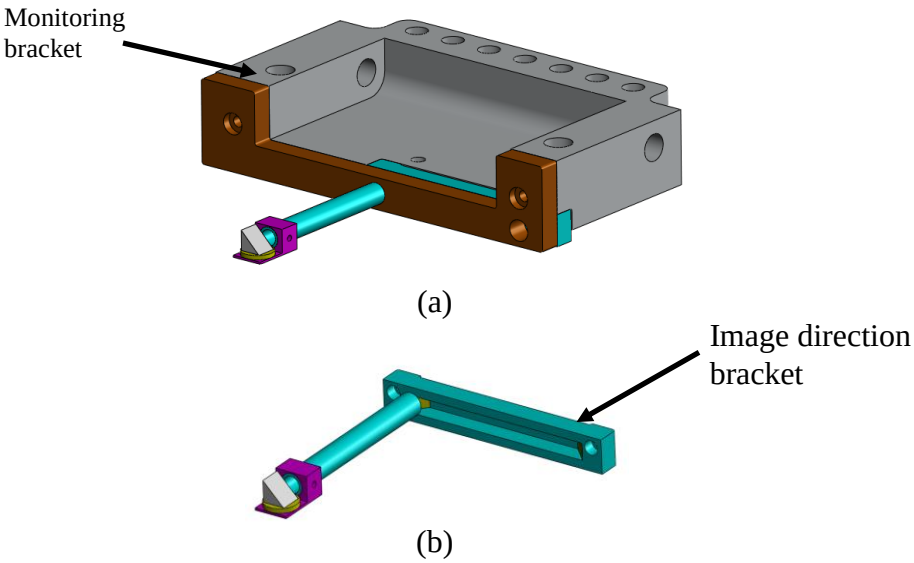

Figure 32 : CAD models of the slider monitoring system; (a) monitoring system, (b) the monitoring arm assembly with the image direction bracket.

3.7 Writing Head

The writing head is attached to the front side of the carriage and is composed of a main slider, shoulders, prefocusing lens, prefocusing lens flexure, flexure bracket, fiber optic interferometer bracket , plasmonic lens suspension, and a piezoelectric shear actuator. The challenge encountered when designing the writing head was to make a light ergonomic robust structure that could be accurately used to perform the writing process. One of the main requirements is to provide both coarse and fine motion which introduced mechanical and electromechanical subsystems to provide adjustments at the macro, micro, and nanoscale levels. Figure 33 illustrates a model of the writing head assembly.

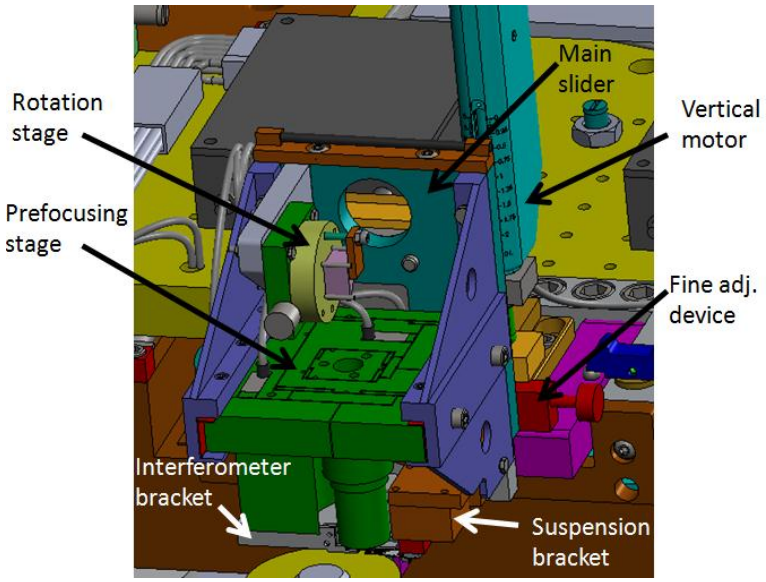

Figure 33: Illustration of the writing head components.

The main slider is equipped with a motor driven linear stage (range 50 mm) that provides vertical motion of the writing head during the plasmonic lens changing

procedure. The slider rests on a fine adjustment device which is attached to a rotation arm that provides the 90˚ rotation needed during the plasmonic lens changing procedure.

Through the following pages all items included in the writing head will be discussed in more detail.

3.7.1. Main Slider

This part is the main carrier of all writing head components. The main slider is made of Al 6061 due to its low density and machinability. Figures 34 and 35 show the main slider model.

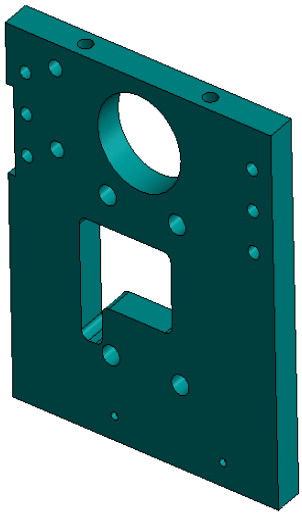

Figure 34: Main slider CAD model.

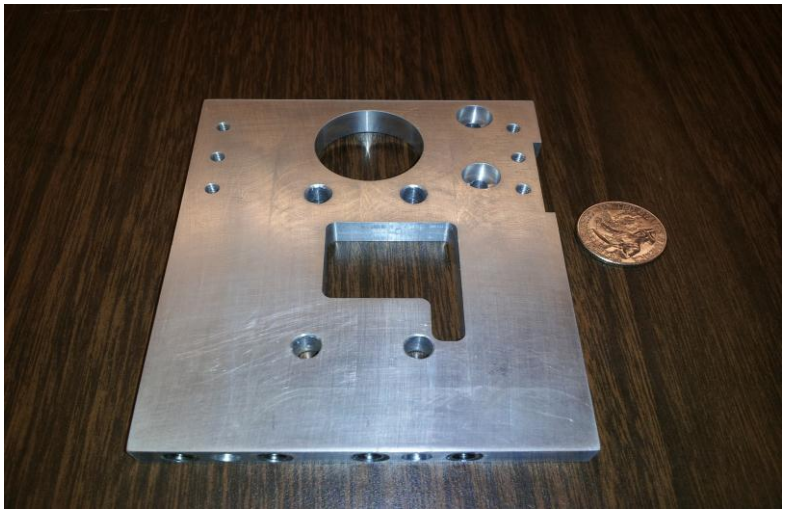

Figure 35: Main slider.

3.7.2. Fine Adjustment Device

The plasmonic lens slider is attached to the suspension system manually under the microscope which causes dimensional variation from one plasmonic lens assembly to another. This fact raised the need for a fine adjustment device which can be used to put the plasmonic lens in the right height with respect to the spinning disc. Figures 36 and 37 show models of the plasmonic lens suspension system.

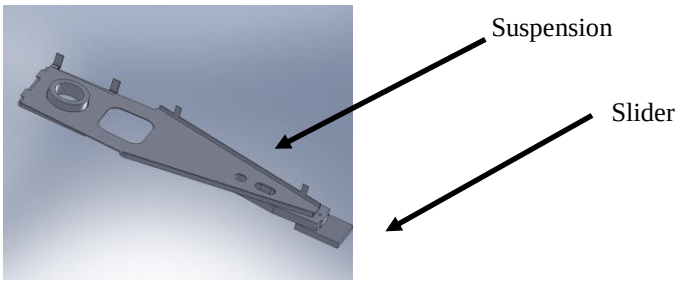

Figure 36: CAD model of the plasmonic lens suspension system.

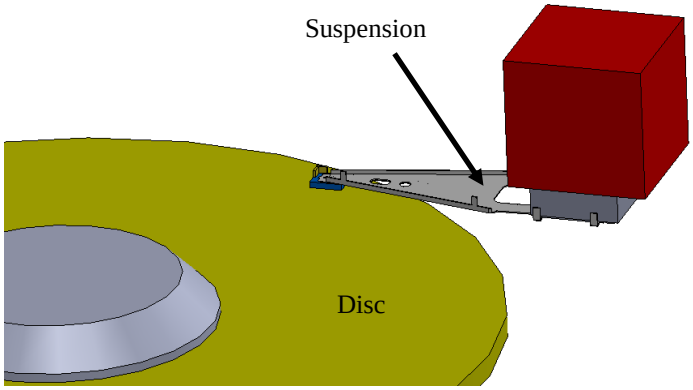

Figure 37: CAD model of the disc and plasmonic lens suspension system.

The fine adjustment device is located under the main slider as shown in Figure 38.

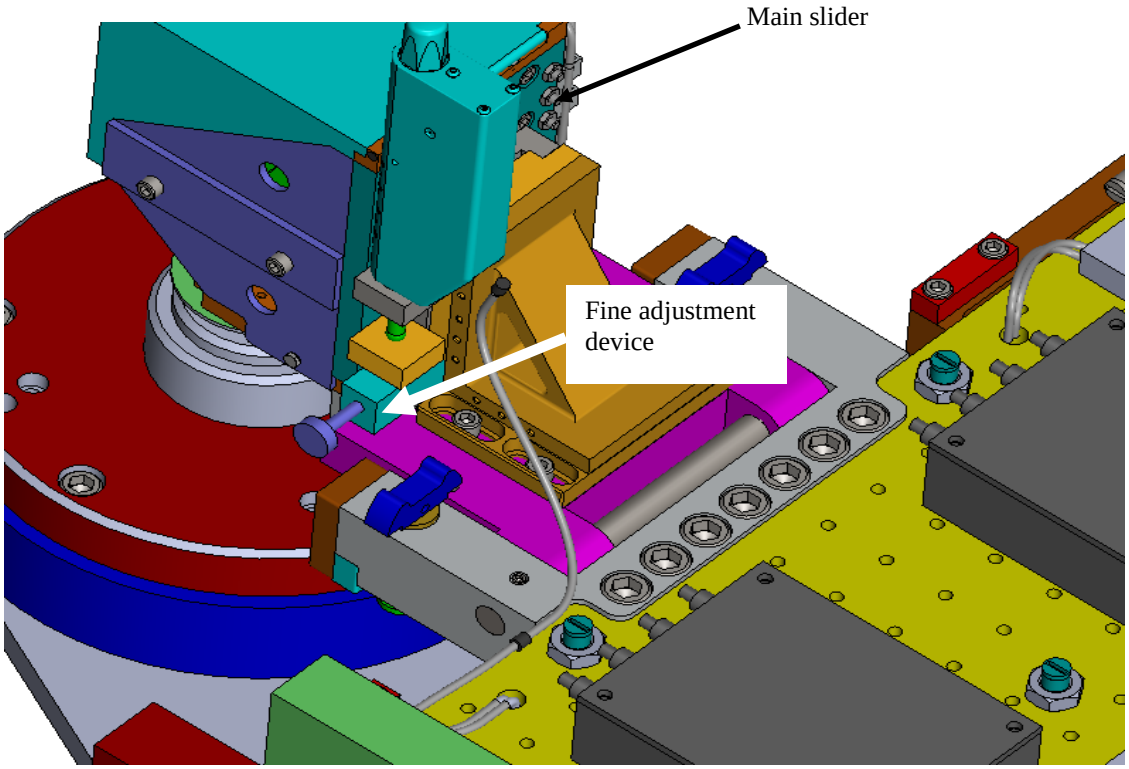

Figure 38: Location of fine adjustment device on PLM CAD model.

Also, it is attached to the rotation arm, as shown in Figure 39.

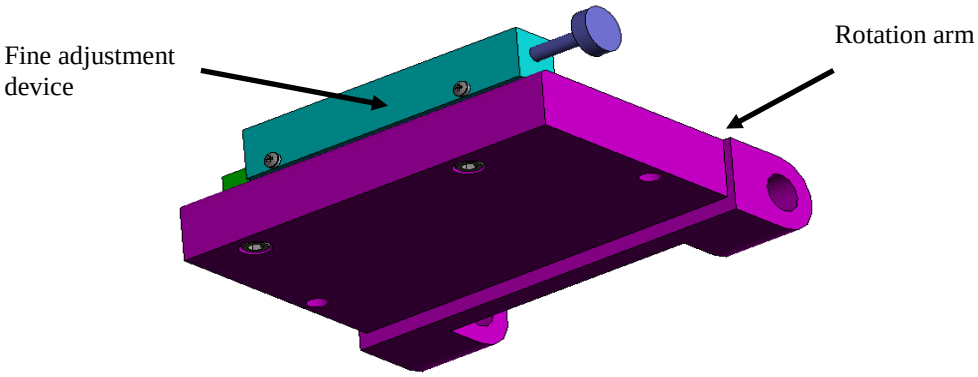

Figure 39: Location of fine adjustment device on the rotation arm CAD model.

The fine adjustment device design concept is based on using a sliding wedge and a screw drive to position the wedge as shown in Figure 40.

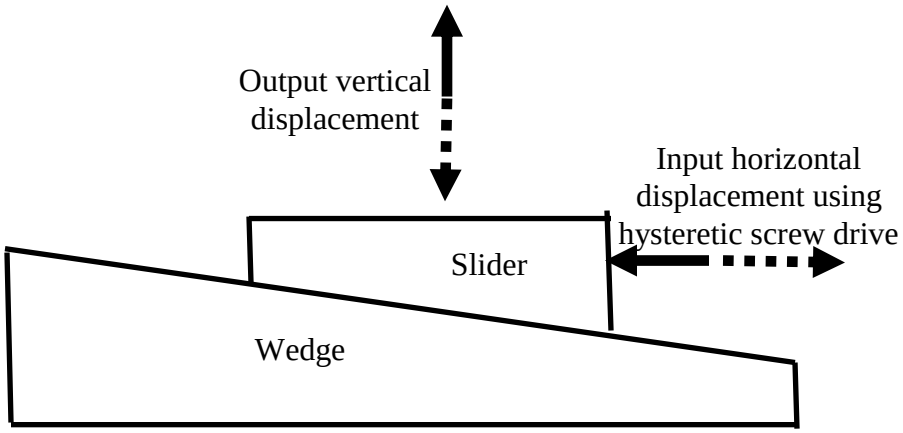

Figure 40 : Design concept of the fine adjustment device.

The fine adjustment device is composed of an aluminum base and cover, a bronze slider, a stainless steel slide way, and an adjustment knob. Figure 41 shows a CAD model of the fine adjustment device assembly and Figure 42 shows models of the device components.

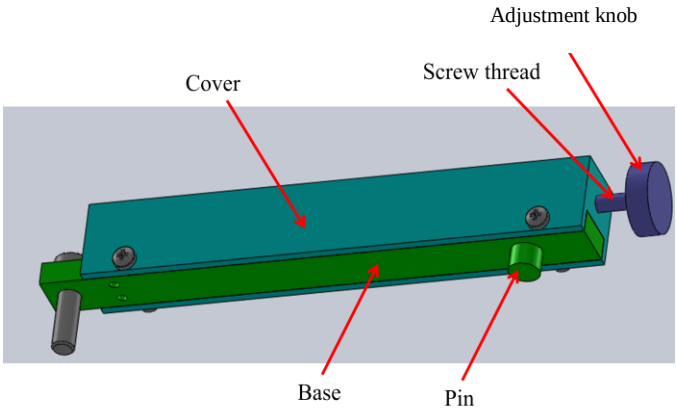

Figure 41: CAD model of the fine adjustment device assembly.

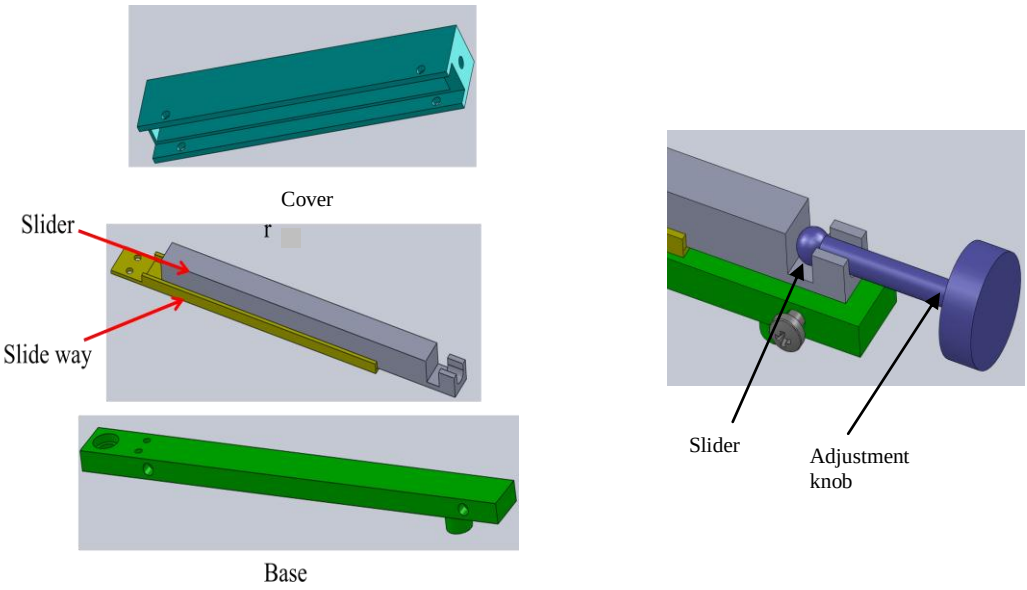

Figure 42 : Models of fine adjustment device.

3.7.3. Angle Bracket

In order to attach the writing head to the rotation arm, a 90˚ angle bracket is used. Figure 43 shows the bracket on the assembly.

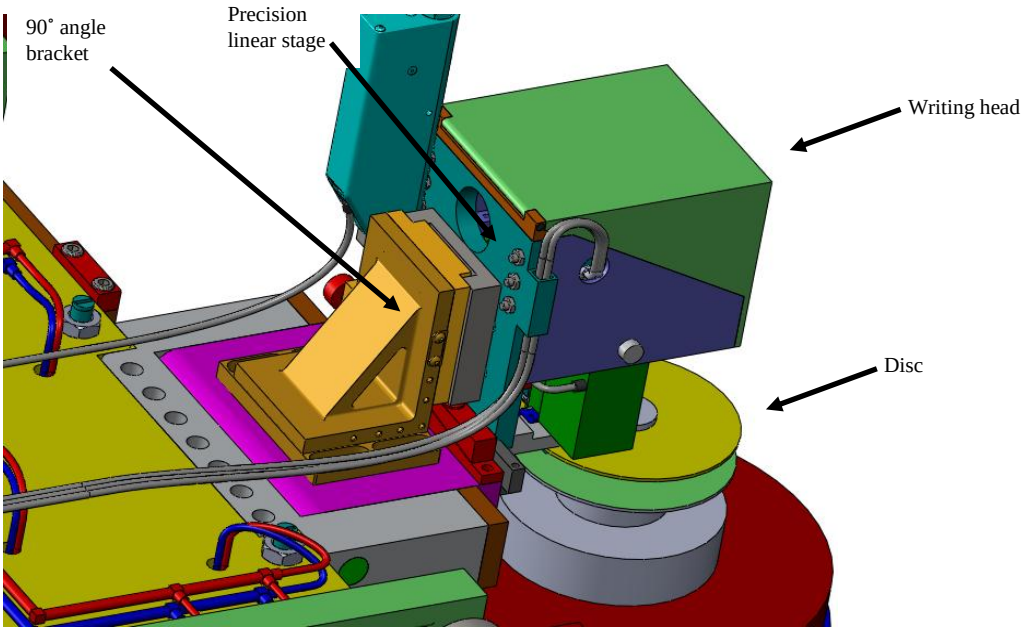

Figure 43: Illustration of the 90˚ angle bracket location on the PLM model.

A Newport™ linear crossed roller-bearing stage is used to attach the main slider to the 90˚ angle bracket, as indicated in Figure 46 [Newport™, 2009].

Figure 44: Crossed roller-bearing linear stage [Newport™, 2009].

3.7.4. Prefocusing Lens

In order to focus the UV laser on the plasmonic lens, an achromatic microspot focusing objective lens was chosen. The lens is made by Thorlabs™ (model number LMU-39X-NUV) and has a working distance of 2 mm and a numerical aperture (NA) of 0.5. Figure 45 shows the lens dimensions.

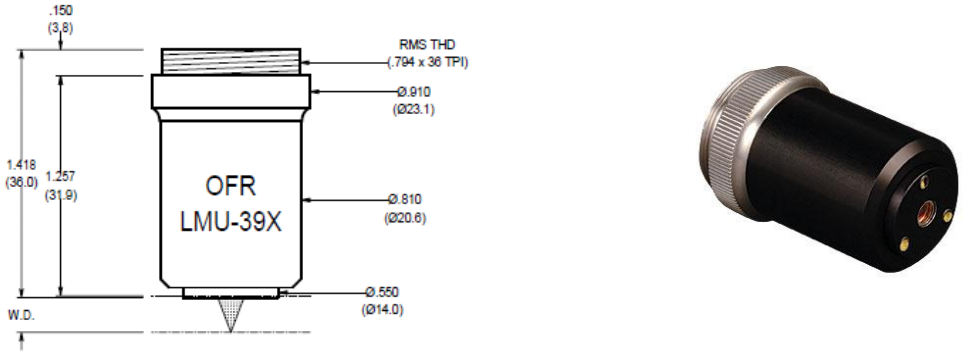

Figure 45: LMU-39X-NUV – MicroSpot Focusing Objective, 39X, 325 – 500 nm, NA=0.50 [Thorlabs, 2013]

3.7.5. Prefocusing Lens Flexure

In order to adjust the prefocusing lens to the write position a flexure two axis stage was designed by Dr. Wen Wang and improved by Mark Rubeo at the Center for Precision Metrology at UNC Charlotte. Figure 46 shows the location of the prefocusing flexure on PLM model.

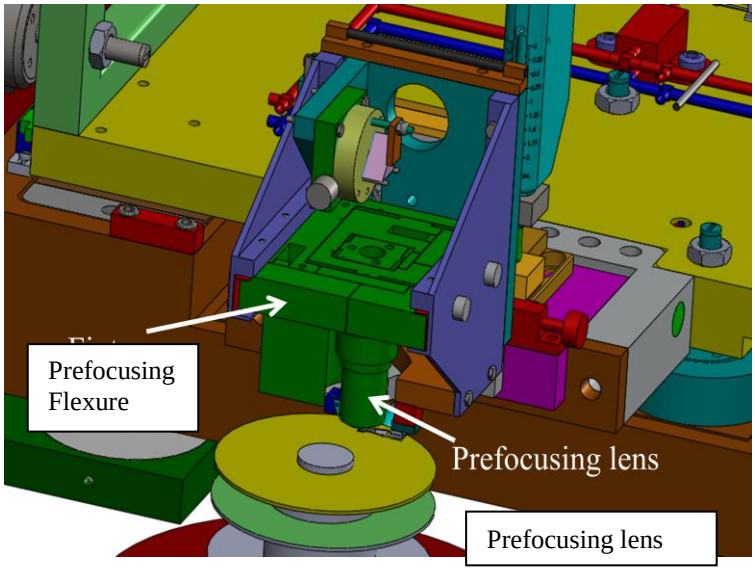

Figure 46: Illustration of the prefocusing lens and flexure

The flexure provides a 100-micron adjustment of the prefocusing lens in the down-track (R) and off-track (X) directions using orthogonal piezoelectric actuators. Figure 47 shows the prefocusing flexure assembled with piezoelectric actuators and cap gages.

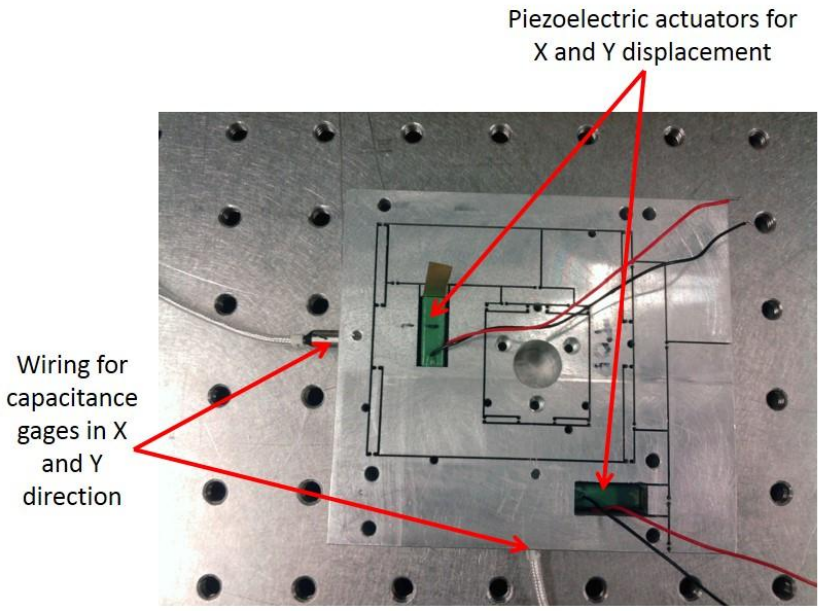

Figure 47: The prefocusing flexure designed by Dr. Wen Wang. On the PLM the Y direction is also called the R direction.

The piezoelectric actuators used on the X and R fine adjustment are made by Thorlabs™ (model AE0505D18F). These actuators can generate a maximum displacement of 15 μm if given a maximum voltage of 100 V. Figure 48 illustrates the operating characteristic curve (OCC) of the actuators used.

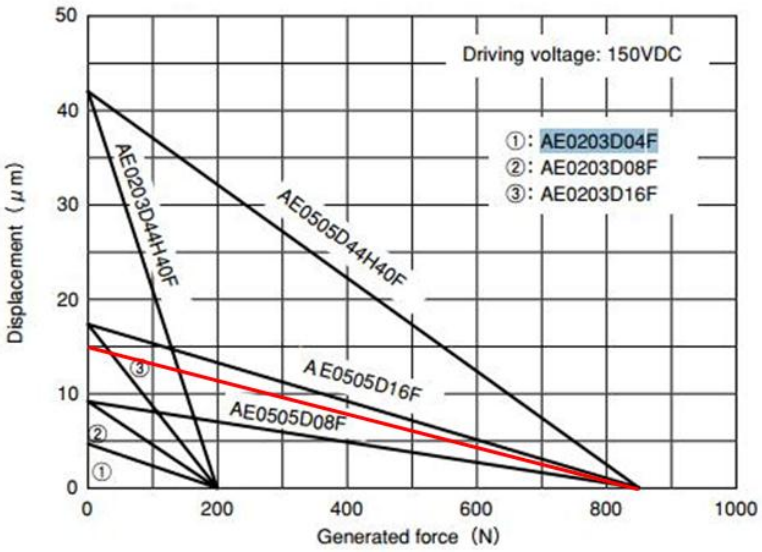

Figure 48: The OCC of the piezoelectric actuators (in red) used to adjust the prefocusing lens in X and R directions. (Note: The original curve in black has been supplied by Thorlabs™ and edited to add the characteristic curve of the specific model used in the machine (in red) based on Thorlabs™ technical support advice.)

The prefocusing lens is attached to the flexure via another PZT actuator which provides a 100 micron adjustment in the vertical (Z) direction. Figure 49 shows a CAD model of the prefocusing stage assembly.

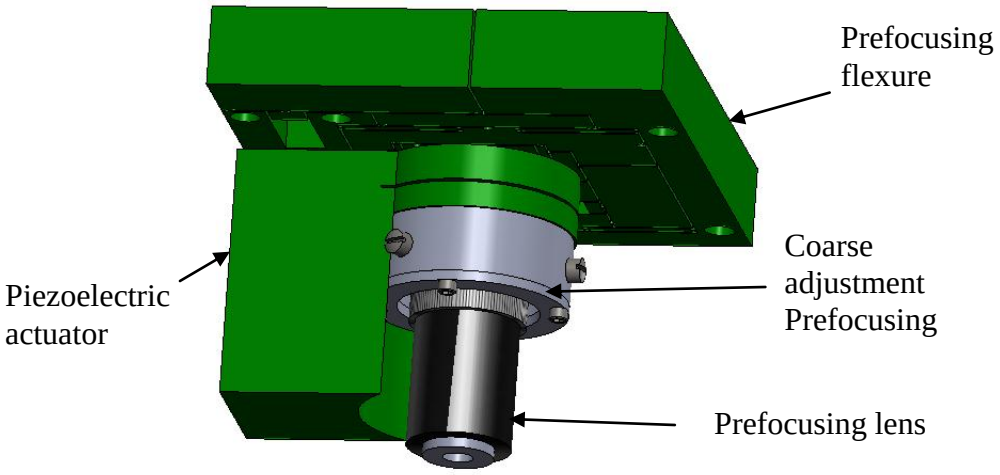

Figure 49: CAD model showing the piezoelectric actuator in the vertical (Z) direction.

3.7.6. Coarse Adjustment Prefocusing Stage

In order to provide more control on the prefocusing lens relative position with respect to the plasmonic lens, a 1-mm range coarse motion stage is used. The stage is made of Al 6061 and it was manufactured at UNC Charlotte. Figure 50 shows the relative position between the stage and the prefocusing lens.

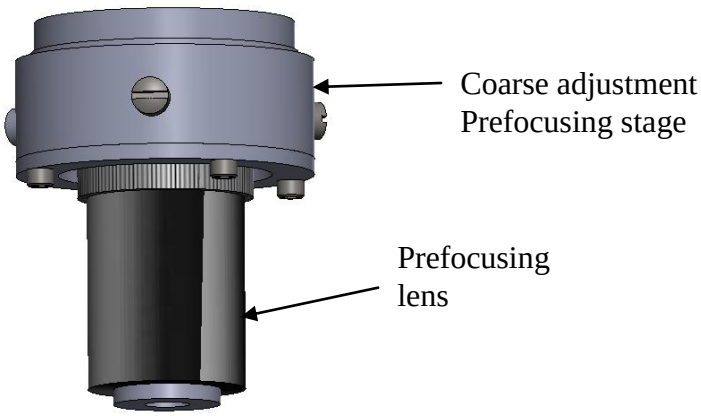

Figure 50: CAD model of coarse adjustment prefocusing stage.

The coarse adjustment stage composes a frame, a tapered disc, a slide pad, cover, set screws, and a spring preloaded plunger. Figure 51 shows CAD models of the stage assembly and elements.

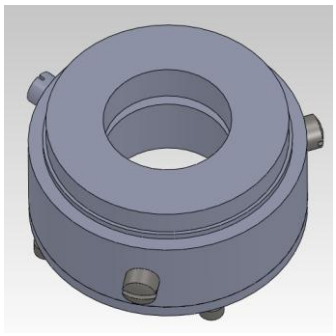

Stage assembly

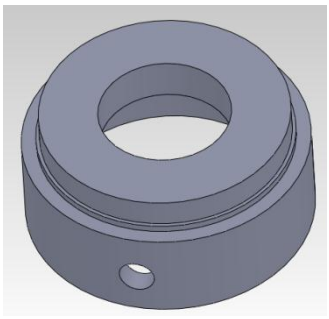

Frame

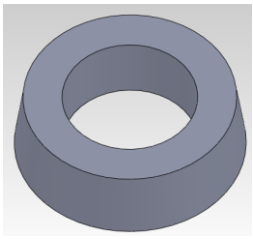

Tapered disc

Cover

Set screw

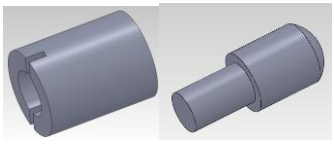

Plunger and cylinder

Figure 51: CAD models of the coarse adjustment prefocusing stage elements.

The frame has three #10-32 tapped holes located within 120˚ spacing. The prefocusing lens is attached to the stage using a fine thread which is tapped in a 14˚ included angle tapered disk as shown in Figure 52.

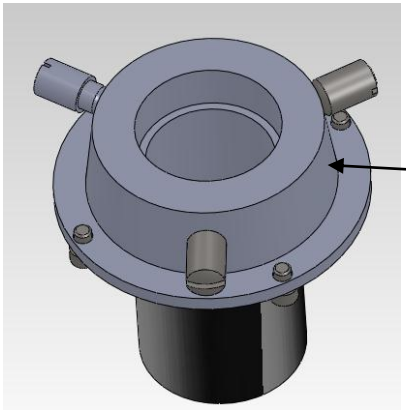

Figure 52: CAD model of the coarse adjustment prefocusing stage.

The design concept of this device is that when driving any of the two screw it pushes the disc in the axial direction of that screw against a preloaded screw, which results in planer displacement within a circle of 1 mm diameter.

3.7.7. Prefocusing Flexure Shoulders

The prefocusing flexure is attached to the main slider using two aluminum shoulders, as shown in Figure 53. Figure 54 shows CAD models of the prefocusing stage shoulders.

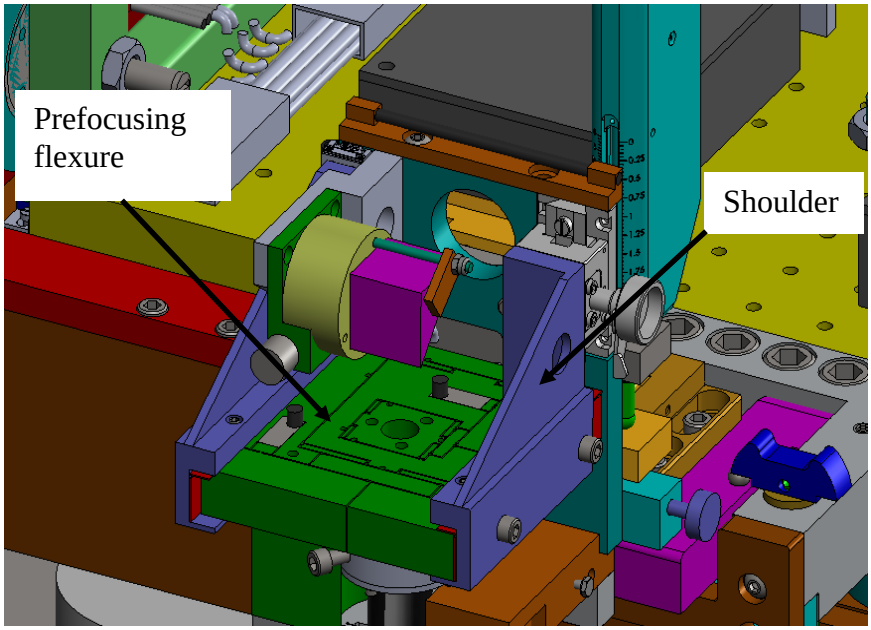

Figure 53: CAD model showing the prefocusing flexure shoulders.

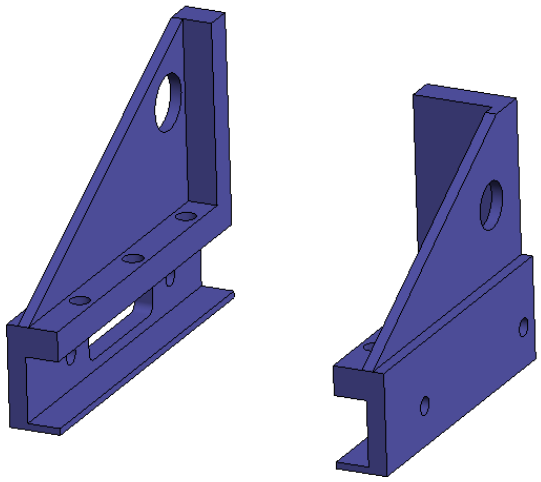

Figure 54: CAD models of prefocusing flexure shoulders.

In order to provide a vertical (Z) coarse motion to the prefocusing flexure, a 25-mm rack and pinion dovetail stage is used on the machine. The stage is made by OptoSigma™ (model number 123-4415). These devices are shown in Figure 55. Figure 56 shows the location of the rack and pinion dovetail stage on a CAD model of the writing head.

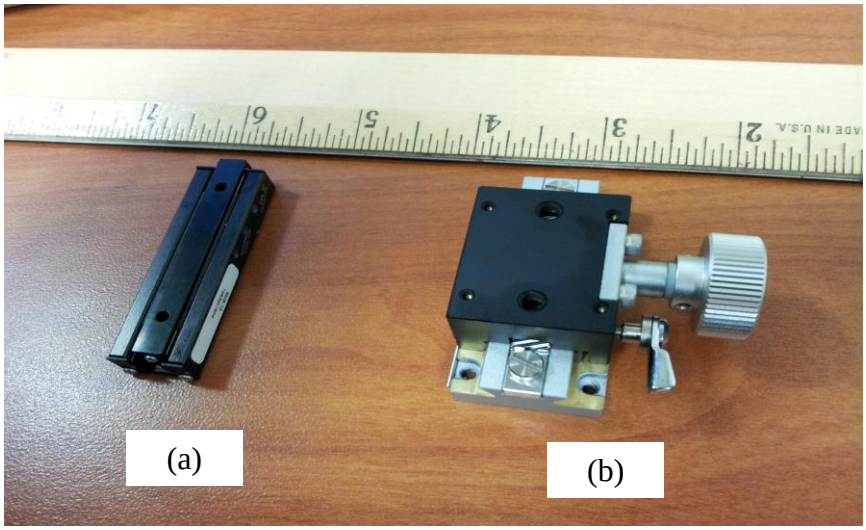

Figure 55: (a) High precision slide, (b) Rack and pinion dovetail slide [OptoSigma™, 2011].

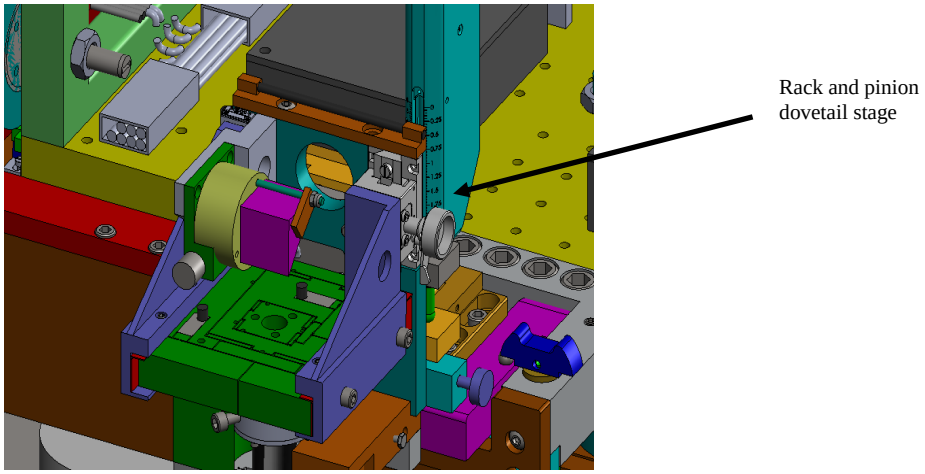

Figure 56: CAD model showing the rack and pinion dovetail stage location.

In order to move the prefocusing flexure it is necessary to introduce a high-precision slide on the other side of the writing head. The stainless steel slide chosen is made by OptoSigma™ (model number 122-2015). The location of the slide is shown in Figure 57.

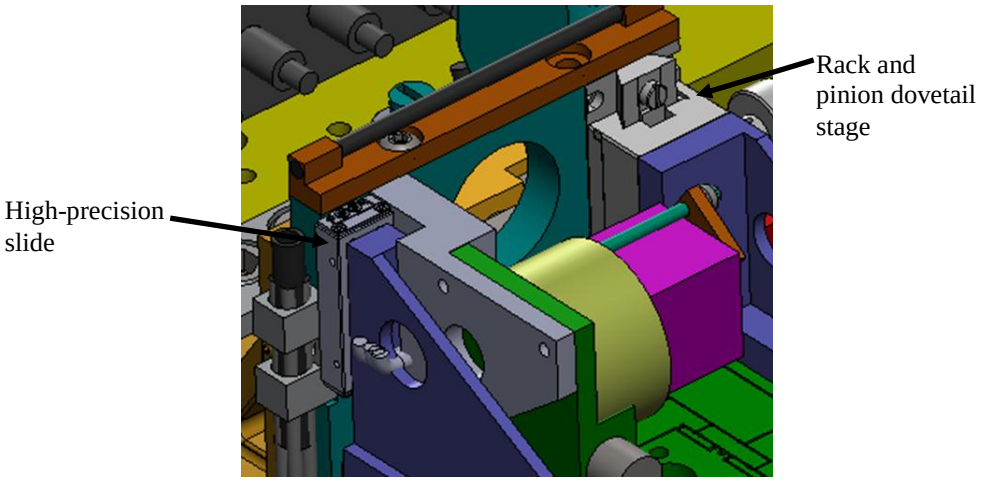

Figure 57: Location of the high-precision slide.

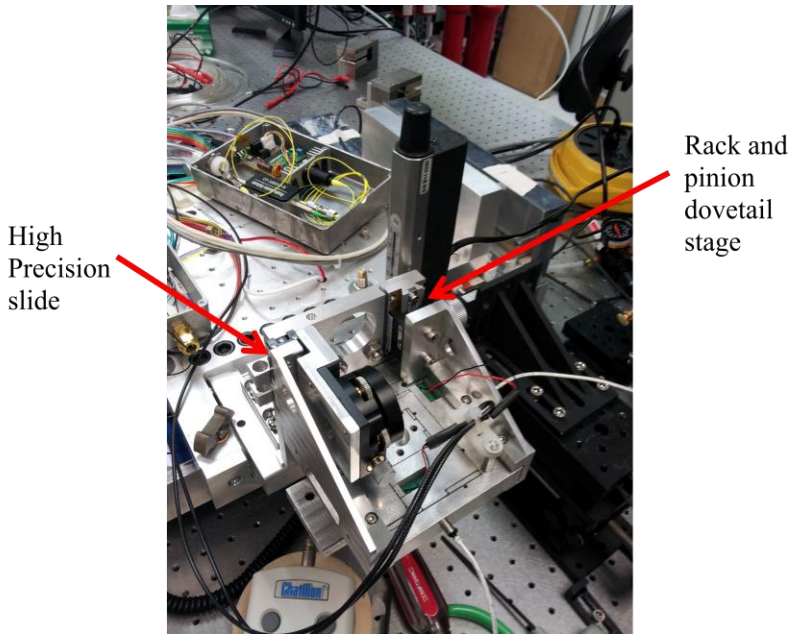

Figure 58: Installation of the rack and pinion dovetail stage and high-precision slide.

3.7.8. Suspension and Interferometer Brackets

The function of the suspension bracket is to provide a means to attach the plasmonic lens suspension to the main slider and consequently to the carriage. The diode laser interferometer bracket was introduced to the machine in order to attach the diode laser interferometer needles in place with respect to the slider. This bracket is designed by Chris Hughes at the Center for Precision Metrology (CPM) at UNC Charlotte and manufactured by Roland Hege, also at the CPM. The suspension bracket was manufactured at Suter Machine and Tool Co. Figure 59 shows the location of both brackets on the writing head.

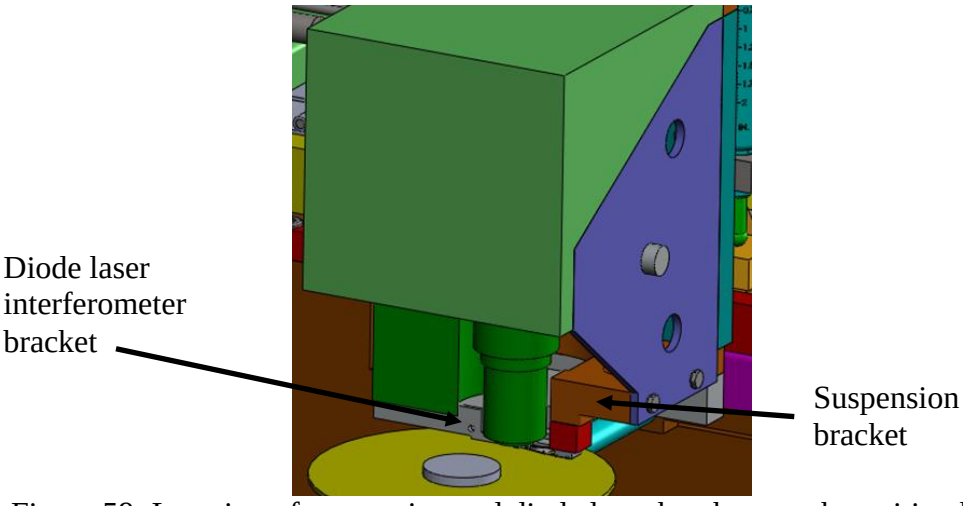

Figure 59: Location of suspension and diode laser brackets on the writing head.

Figure 60 shows a closer view on the assembly model.

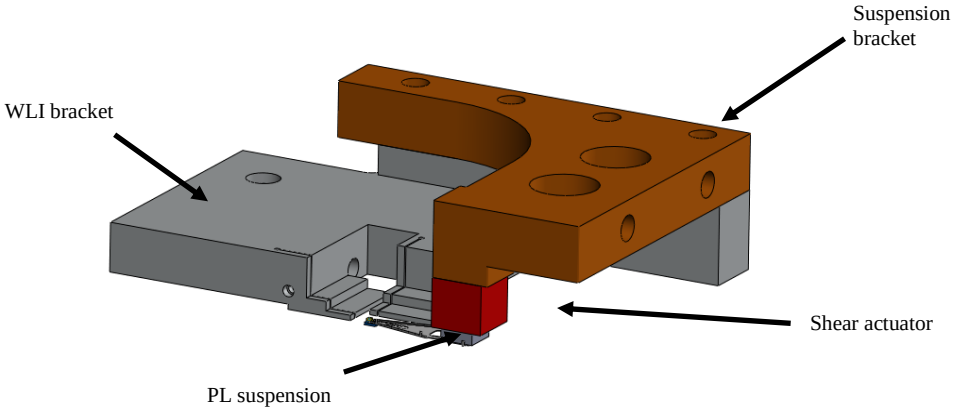

Figure 60: Model of suspension and diode laser brackets assembly.

Both brackets were assembled to the main slider using #10-32 screws. To provide accurate alignment dowel pins were used, as illustrated in Figure 61.

Dowel pins attached to the main slider Brackets attached to the main slider

Figure 61: Suspension and diode laser interferometer brackets assembly.

3.7.9 Shear Actuator

The diode laser interferometers [Hughes, 2012] were designed to measure the vibration introduced in the slider during the writing process. The vibration measurement provides an input to a closed-loop control system that generates a corrective signal which activates the shear actuator attached to the plasmonic lens suspension. The chosen shear actuator is made by Physik Instrumente™, model number 142.03 [Physik Instrumente™, 2009], which can provide 3 x 3 μm displacement. Figure 62 shows the location of the shear actuator on the writing head.

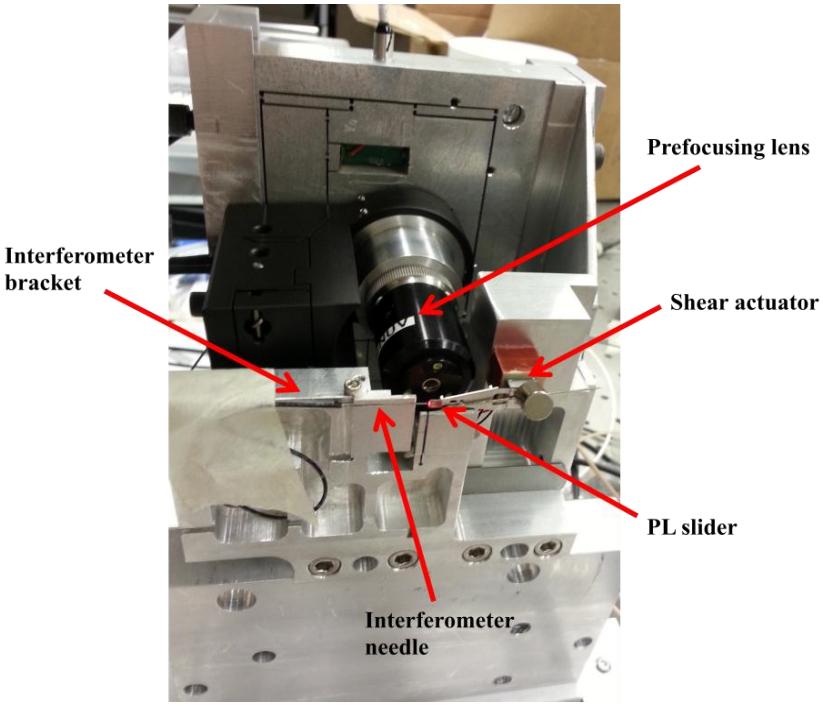

Figure 62: Location of shear actuator on the writing head.

3.8 Operational Logic Chart

This chart helps the user to better understand the machine's different configurations during all possible situations. The first two columns show the PLM usage procedures which can be summarized as follows:

1- System turned off: refers to the PLM status before starting the writing process. As we notice here the air supply to air bearings is on, and it remains on all the time to avoid damage of the bearing diamond-turned surfaces. The limit switches are on all the time, even if the machine is turned off. Also, the air supply to the high-precision spindle is on all the time.

2- System turned on.

3- Move the writing head upward using vertical motor. This step is necessary to move the plasmonic lens away from the spinning disc in order to change the plasmonic lens.

4- Rotate the writing head 90 degrees. This allows the user to easily access the plasmonic lens suspension in order to change the plasmonic lens.

5- Clamp the plasmonic lens.

6- Unclamp the previous disc, which means the high-precision spindle has to be stopped for few minutes in order to remove the disc.

7- Clamp the work disc on the disc mounting stage.

8- After changing the plasmonic lens, rotate the writing head back to the writing position.

9- Move the writing head downward using the vertical motor.

10- Use the fine adjustment device to move the plasmonic lens slider toward the spinning disc. The user should watch white light fringes on the slide air bearing surface (using the monitoring screen) until an acceptable flying height is achieved.

11- Use all coarse and fine adjustments elements to adjust the plasmonic lens and prefocusing lens in the right positions.

12- Using Halbach motors, move the carriage using the predefined speed to perform the writing process.

13- After finishing the writing process, or when the plasmonic lens slider needs to be changed, stop the writing process.

14- Move the writing head upward using the vertical motor.

15- Rotate the writing head 90 degrees in order to easily access the plasmonic lens slider.

16- Unclamp the plasmonic lens and attach the new one.

17- Unclamp the work disc if the required pattern is done.

Table 4 shows the operational logic chart of the PLM. The first row in the logic chart shows the control elements. The middle portion of the chart shows logic values as 0 (off) or 1 (on). For example, the air supply to air bearings needs to be on (1) all the time, regardless of the machine status.

Table 4: PLM's Operational Logic Chart

Element		Air bearings Air/Vaccuum Supply	Vertical Motor	Fine Adjustment device	PZT actuators on Prefocusing fixture	PZT actuators on PL lens holder	Air supply to disc mounting stage	Linear Motors	Renishaw® linear scales	Eddy Current Damper	Pressure limit switches	Electronic limit switches
Step No.	Status	Value No.										
		1	2	3	4	5	6	7	8	9	10	11
1	System turned off	1	0	0	0	0	1	0	0	0	1	1
2	System turned on	1	0	0	0	0	1	0	0	0	1	1
3	Move the writing head upward (Vertical motor on-off)	1	1	0	0	0	1	0	0	0	1	1
4	Rotate the writing head 90º	1	0	0	0	0	1	0	0	0	1	1
5	Clamp the plasmonic lens	1	0	0	0	0	1	0	0	0	1	1
6	Unclamp the previous disc from the disc mounting stage	1	0	0	0	0	1	0	0	0	1	1
7	Clamp the work disc on the disc mounting stage	1	0	0	0	0	1	0	0	0	1	1
8	Rotate the writing head back 90º	1	0	0	0	0	1	0	0	0	1	1

9	Move the writing head downward (Vertical motor on-off)	1	0	0	0	0	1	0	0	0	1	1
10	Vertical fine displacement to approach the work disc	1	0	1	0	0	1	0	0	0	1	1
11	Horizontal fine adjustment	1	0	0	1	1	1	0	0	0	1	1
12	Writing starts (Down track uniform motion)	1	0	0	0	0	1	1	1	1	1	1
13	Stop writing process (End down track motion)	1	0	0	0	0	1	0	0	0	1	1
14	Move the writing head upward (Vertical motor on-off)	1	1	0	0	0	1	0	0	0	1	1
15	Rotate the writing head 90º	1	0	0	0	0	1	0	0	0	1	1
16	Unclamp the plasmonic lens	1	0	0	0	0	1	0	0	0	1	1
17	Unclamp the work disc from the disc mounting stage	1	0	0	0	0	1	0	0	0	1	1

CHAPTER 4: MOTORS, DAMPERS, SENSORS AND ACTUATORS

4.1. Halbach Linear Array Motor

It is highly recommended that friction-free motors be used in lithography machines [Hazelton, 2007; Nieuwelaar, 2003; Hiroshi, 2004; Trumper, 1990, 1993; Williams, et al.,1993; Nguyen, 1994; Kim, 1997, 2007; Verma, et al., 2004; Holmes, 1998; Hocken, et al.,2001]. A Halbach array is a set of permanent magnets arranged in such a way that maximizes the magnetic field on one side of the array and cancels the field on the other side. The Halbach magnet array (shown in Figure 63) is made by spatially rotating patterns of magnetization [Halbach, 1980].

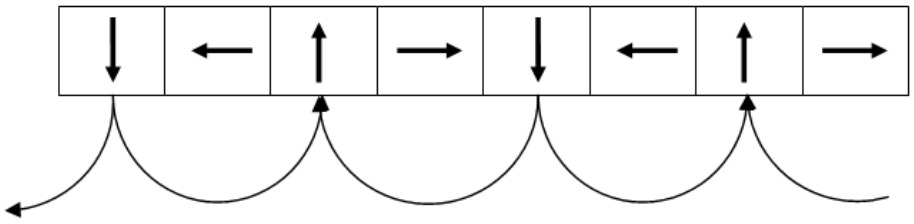

Figure 63: Halbach magnet array.

This magnet arrays configuration generates a magnetic field stronger by about 1.4 than a conventional magnetic array [Fairley, 2003]. Halbach magnet arrays used in the PLM were made of N5064 neodymium iron boron (sintered) magnets. Each magnet array consists of eight magnets. The magnets are rectangular with dimensions 40 mm x 7.44

mm x 7.44 mm each and were supplied and assembled at Dexter Co. [Dexter™, 2009] into aluminum housings. Each Halbach magnet array housing is attached to the carriage using three screws.

When using a 3-phase electromagnetic stator in combination with a Halbach magnet array a force will be generated in both horizontal (along the stator surface) and vertical (normal to the stator surface), as shown in Figure 64.

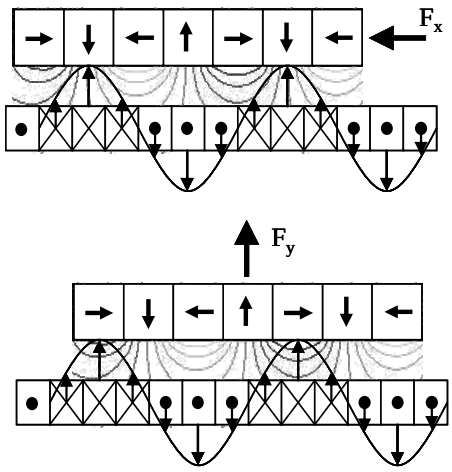

Figure 64: Illustration of Halbach array linear motor [Ozturk, 2007].

The PLM has two Halbach array linear motors, one on each side of the carriage. Figures 65-67 illustrate the Halbach magnet array assembly model.

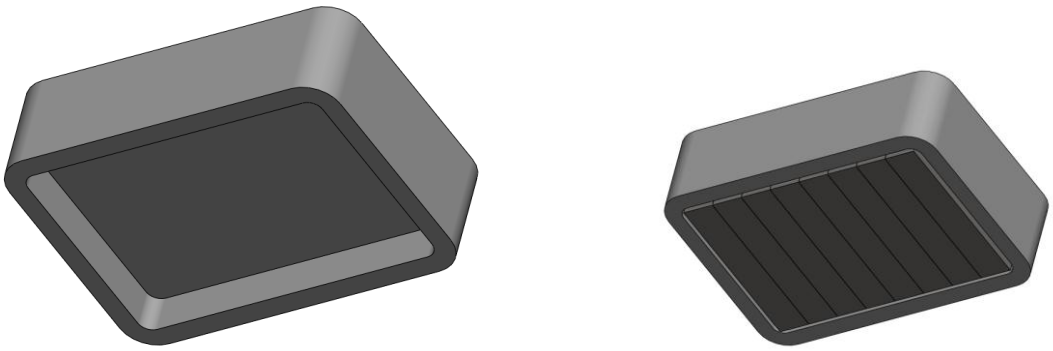

(a) (b)

Figure 65: (a) Halbach magnets array housing model, (b) Model of Halbach magnets array assembly.

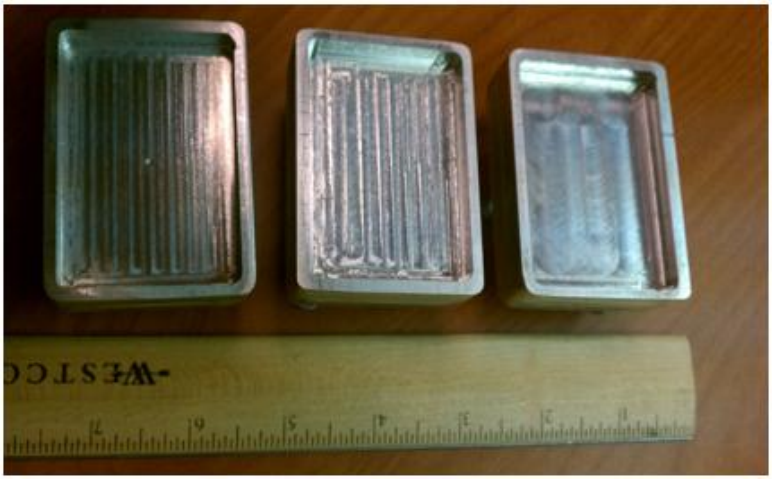

Figure 66: Halbach magnets array housing model

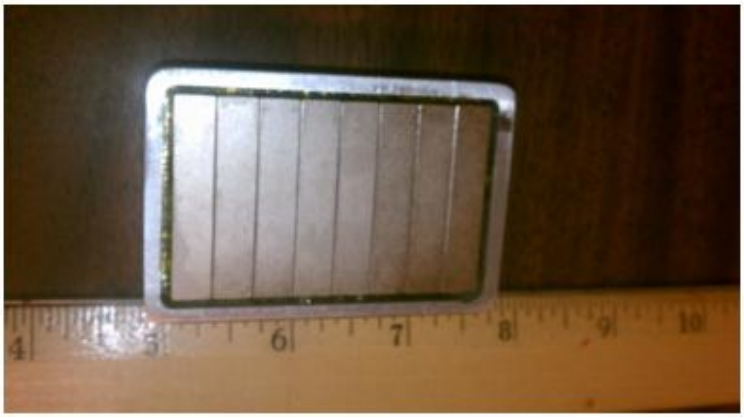

Figure 67: Magnet array assembly

The stator consists of 24 coils (8 coils per phase). The coil winding was done by Wire Winders Co. and the coils wired together at UNC Charlotte by John Brien. The carriage position is controlled by commuting the current applied on each phase separately. The stator consists of a mandrel, two end caps, and 24 coils. Figure 68 illustrates the stator model.

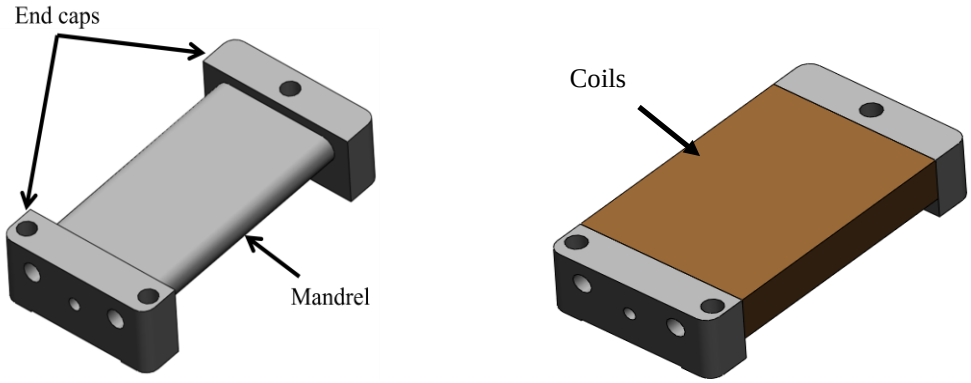

(a) (b)

Figure 68: (a) Halbach stator's frame model, (b) Halbach motor's stator model.

The mandrels were anodized to avoid any shorts due to wire scratches. The two Halbach linear motors need only two stators but it was decided to make three stators (see Figures 69 and 70) in order to avoid any trouble during the machine assembly process.

Figure 69: Stator frames.

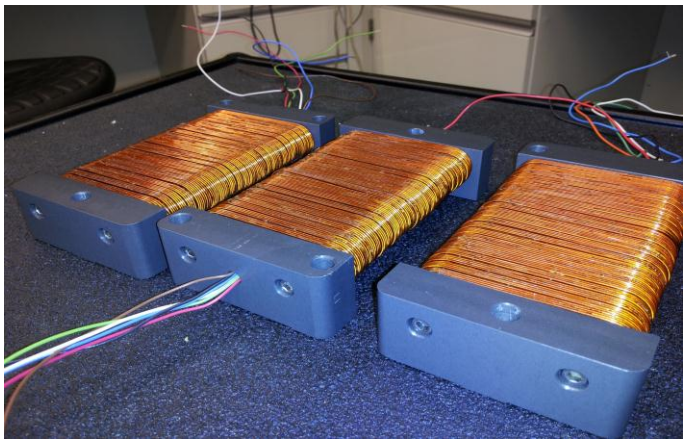

Figure 70: Halbach motor's stators.

4.2. Eddy Current Damper

The basic principle of the eddy current damper is that when a conductor moves in a stationery magnetic field, eddy currents are induced on the conductor, as shown in Figure 71 [Henry, 2000].

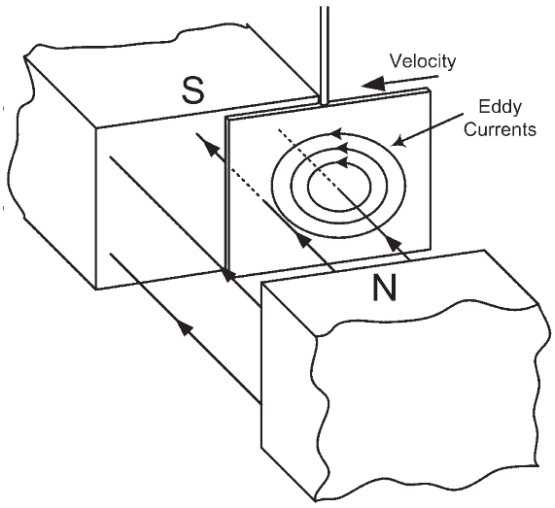

Figure 71: Generation of eddy current in a conductive material passing through a magnetic field [Henry, 2000].

The induced currents on the conductor create Lorentz forces impeding the motion [Sodano, 2004; Reitz, 1970; Davis, 1971; Schieber ,1975; Wiederick, 1987; Lee, 2002; Bae, et al., 2005].

The PLM has two eddy current dampers to provide a smooth, controllable linear motion. The dampers are both composed of a copper plate and two magnet arrays, one on each side of the plate. Each magnet array is composed of four magnets, each magnet measuring 25.4 mm x 25.4 mm x 12.7 mm. The magnet array configuration is shown in Figure 72.

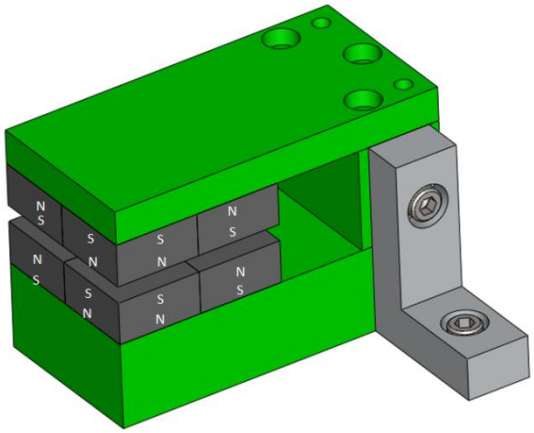

Figure 72: Magnets array polarity in eddy current damper.

This configuration concentrates the magnetic field between the magnet arrays and reduces the fringing magnetic field [Ozturk, et al., 2008]. Figure 73 shows the expected magnetic flux lines.

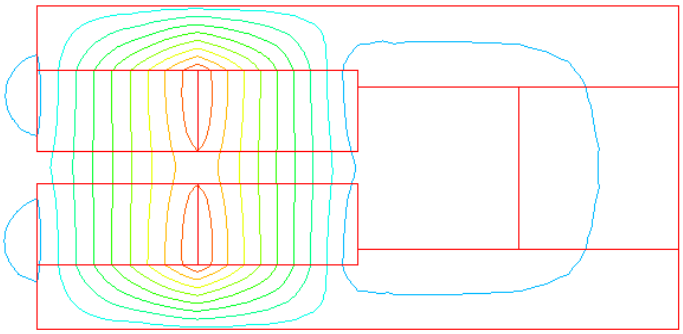

Figure 73: An example of magnetic flux lines of an eddy current damper [Ozturk, et al., 2008].

The yokes that hold the magnet array were attached to the base and the copper plates were attached to the carriage using aluminum brackets. Table 4 summarizes the eddy current parameters.

Table 5: Eddy Current Damper Parameters.

Magnet width (m)	25.4×10^{-3}
Magnet width (m)	25.4×10^{-3}
Width of the magnet array area (m)	50.8×10^{-3}
Height of the magnet array area (m)	50.8×10^{-3}
Pole projection area (m^2)	2581×10^{-6}
Thickness of the copper plate (m)	3.5×10^{-3}
Magnetic field (T)	0.95
Conductivity of copper ($1/\Omega.m$)	6.00E+07

The eddy current dampers built for the PLM were similar to those built for MAPS-II [Ozturk, et al., 2008], where the damping force can be calculated using the following formula:

$$\vec{F} = 856.6\vec{v}_0$$

The carriage average linear speed (v_0) is 5 μm/s, and at this speed each damper generates 4.28 mN damping force. Figures 74 and 75 show the location of the dampers on the PLM. The actual damping force will be measured after controlling the machine motion.

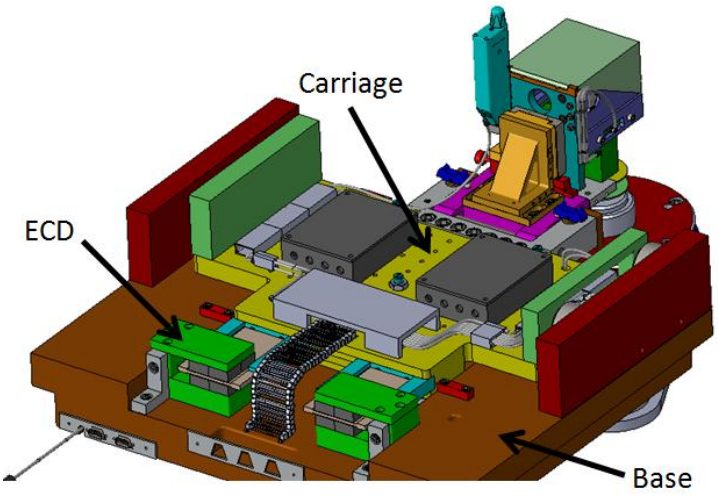

Figure 74: Illustration of the damper's locations on the PLM.

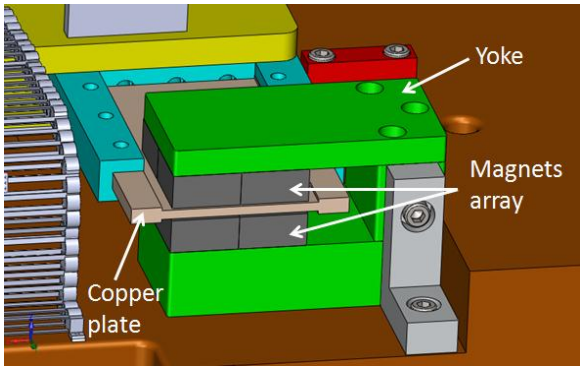

Figure 75: Illustration of a damper on the PLM model.

In order to attach the copper plates to the carriage's tail, two U-shaped brackets were designed and manufactured. Figure 76 shows a model of the copper plate and bracket assembly and Figure 77 shows a model of the copper plate assembly on the carriage.

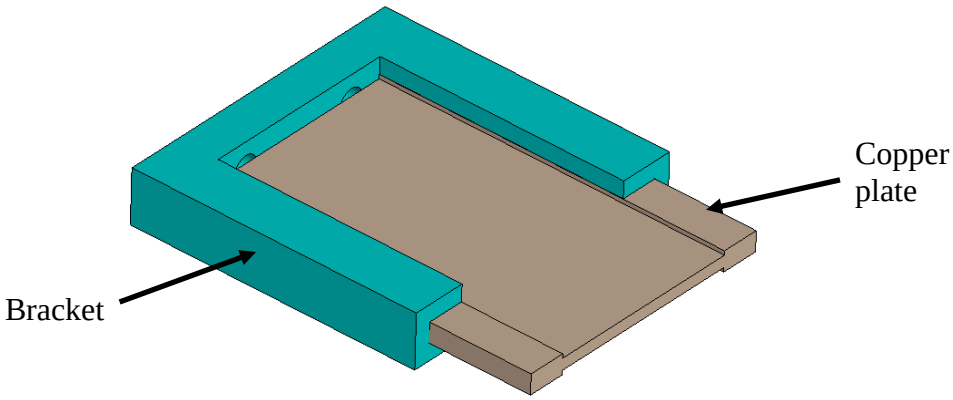

Figure 76: Copper plate and bracket assembly.

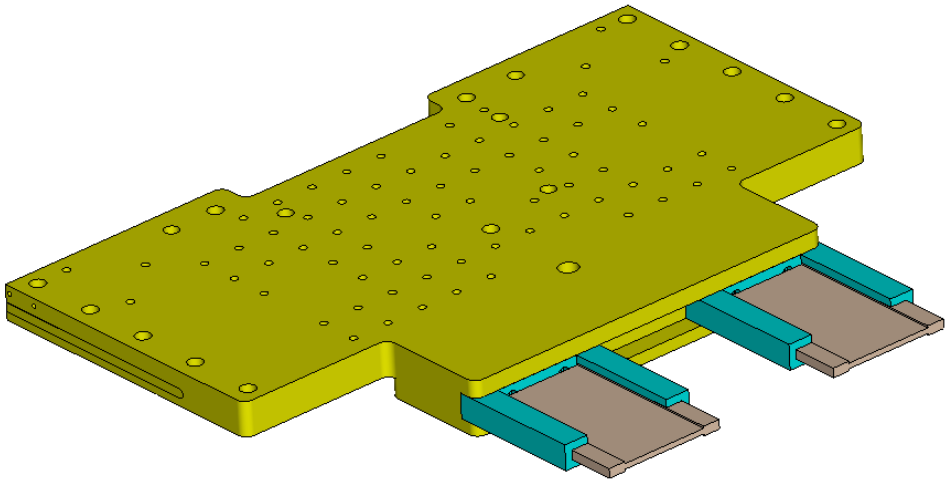

Figure 77: Illustration of a damper on the PLM model.

Figures 78 and 79 show the copper plate and bracket after manufacturing and after assembly respectively.

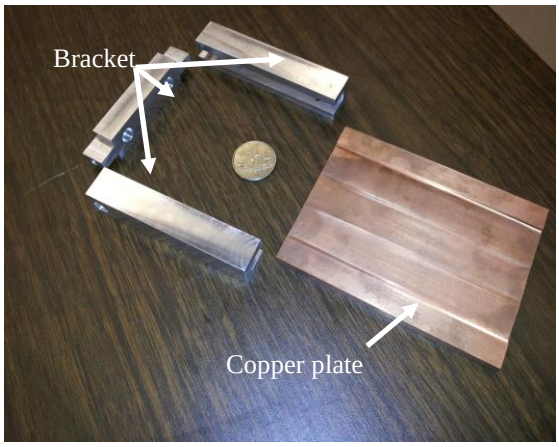

Figure 78: Bracket and copper plate before assembly.

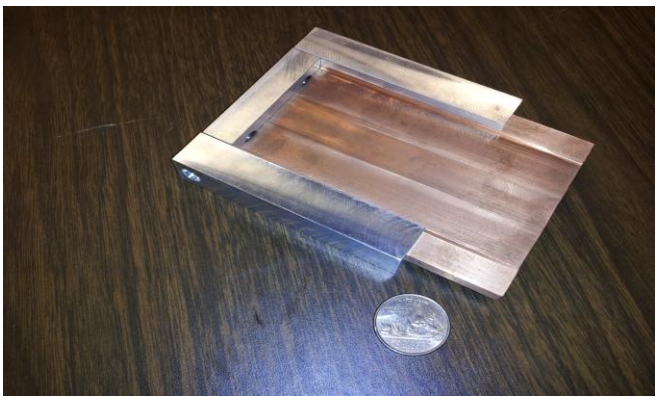

Figure 79: Bracket and copper plate assembly.

4.3. Linear Scales

The carriage linear displacement and position are determined using 5-nm resolution linear scales made by Renishaw™ on both sides of the machine (Renishaw Model RGH 25F). Also, the reading difference is used to determine the yaw while the carriage is moving. The tape scales and reference mark actuators were attached to the carriage while the read heads were attached to the base. Figure 80 illustrates the locations of these items on the carriage.

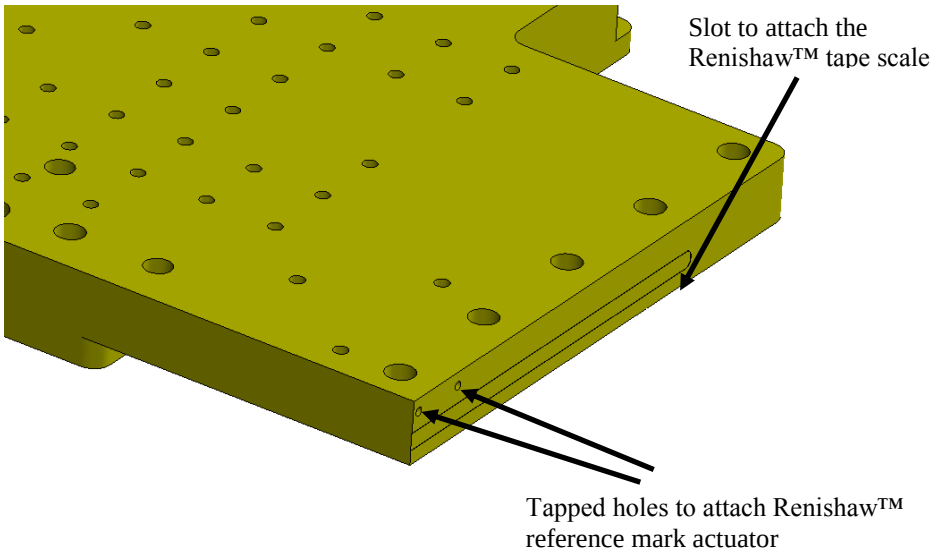

Figure 80: Illustration of the location of tape scale and reference mark actuator on one side of the carriage (note: the same configuration is on both sides of the carriage).

CHAPTER 5: DYNAMIC AND THERMAL TESTING

5.1. Testing of Air Bearings

It is necessary to check the performance of the vacuum preloaded air bearings before installing them on the machine. A testing stage was designed and manufactured at the CPM at UNC Charlotte. Figure 81 illustrates the bearing test setup.

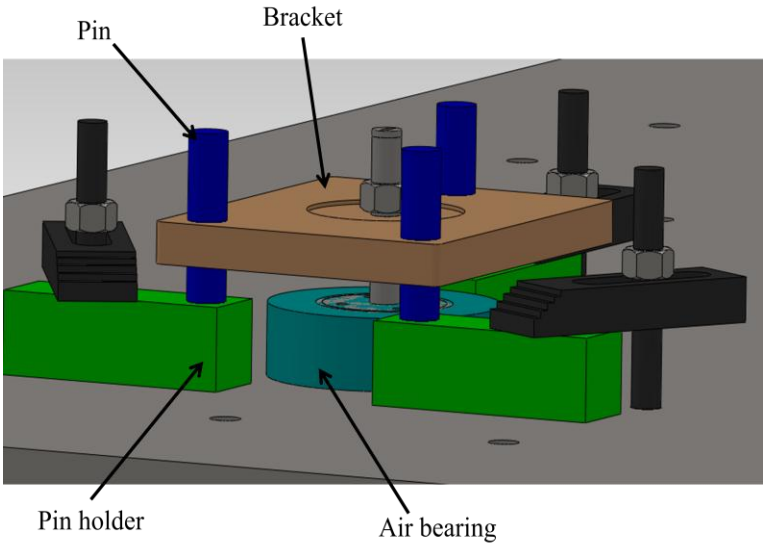

Figure 81: Illustration of the bearing test setup.

The bearing was tested at a weight range limit of 10-30 lbs. Figures 82 shows the calibration stage and Figure 83 shows the calibration setup.

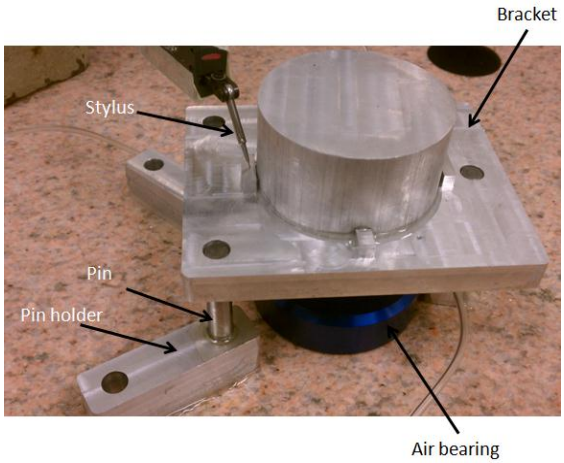

Figure 82: Air bearing calibration stage.

Figure 83: Air bearing calibration setup.

Figures 84-85 show typical calibration data. The error bar represents the 2-sigma uncertainity and is estimated based on a discussion with Dr. Robert Hocken, Director of the Center for Precision Metrology at UNC Charlotte.

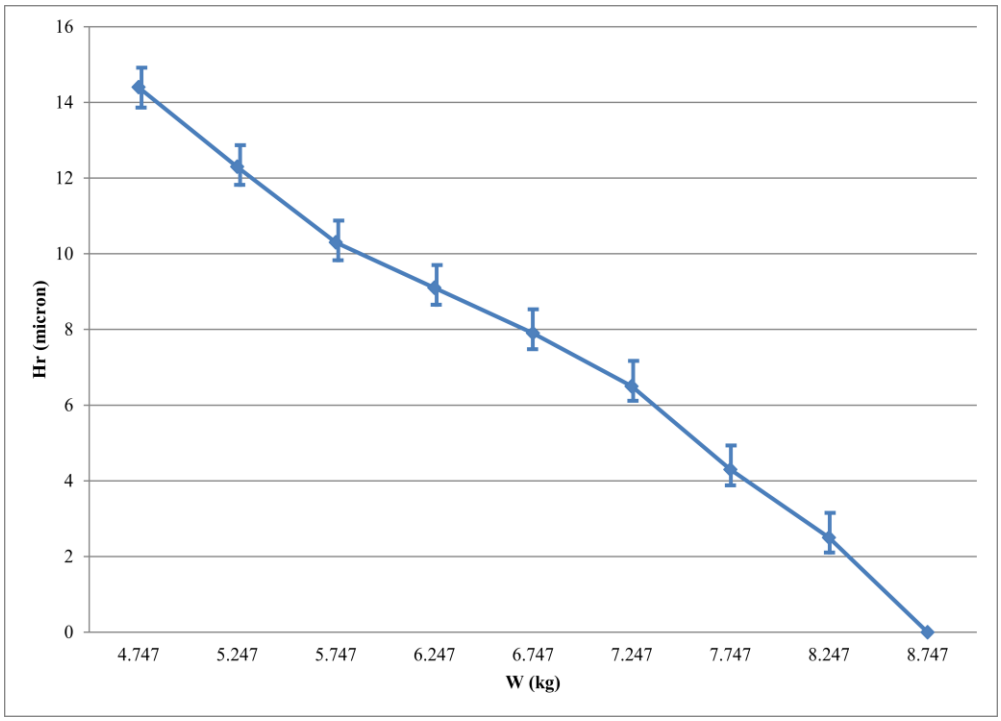

Figure 84: Effect of load change (P = 70 psi , V = 260 mmHg)

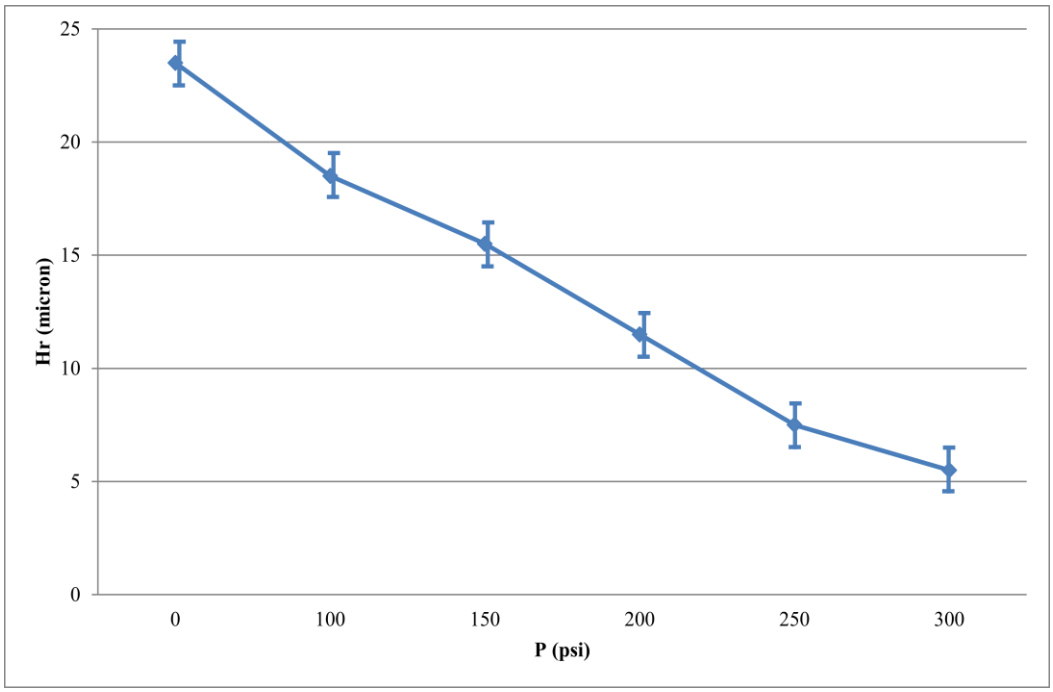

Figure 85: Effect of vacuum change (W = 6 kg , P = 60 psi)

5.2. Halbach Motor Longitudinal Force

Halbach motors generate forces in both longitudinal (parallel to the stator surface) and normal directions. In order to control the carriage motion it is important to measure the longitudinal component along the travel length. The force-position relationship is necessary to set the control values that generate the current and voltage signals for each phase on each motor. The PLM has two motors, one on each side, as shown in Figure 86.

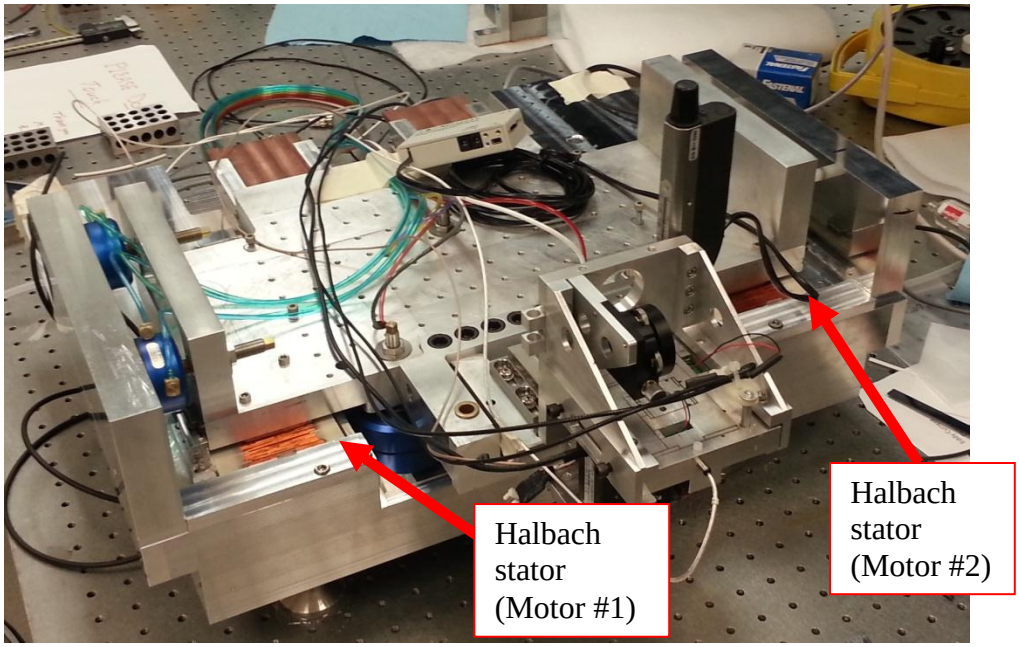

Figure 86: Locations of Halbach motors.

The force was measured for each phase and each motor separately. Figure 87 shows the measuring setup.

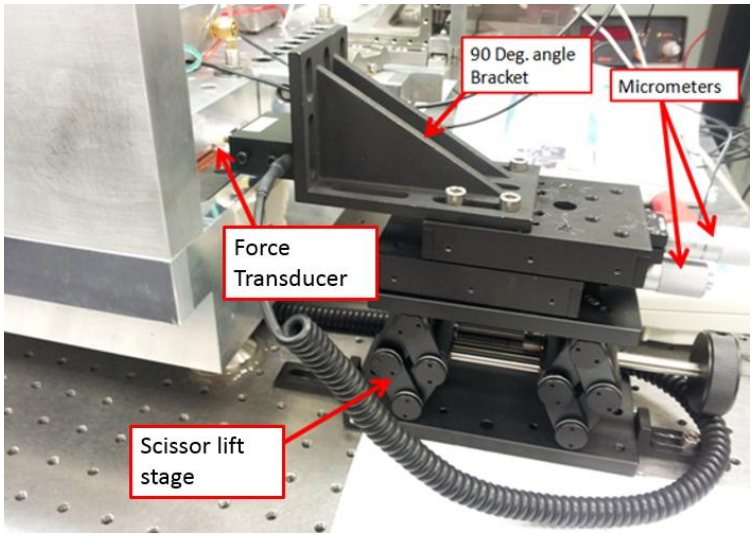

Figure 87: Force measuring setup.

Each motor is composed of three phases, namely R, S, and T. The procedure for measuring the force versus position for each phase started by applying a current of 2.7 A to the measured phase, while all other phases were disconnected. Then a set of two micrometers was used to move the carriage using steps of about 1.5 mm, starting from the home position until reaching the end of the travel length, with a total displacement of 39.00 mm. The force was measured at each position using force transducer (Figure 87) and the carriage positions were measured using the Renishaw™ 5nm scales (Section 2.2). The same procedure was applied to measure the force-position relationship for all phases. In order to measure the tension force a rubber band was used to attach the force transducer to the carriage as shown in figure 88.

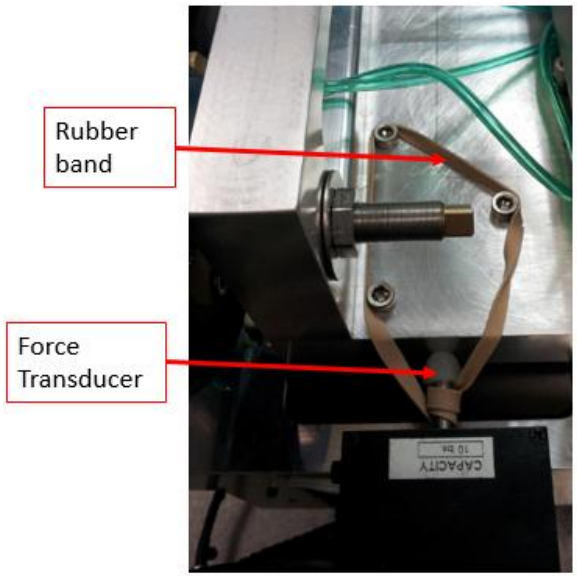

Figure 88: Preloaded contact between the force transducer and the carriage using rubber band.

Figures 89 and 90 show the measured data for both motors. The labels R, S, and T are not acronyms, and they stand for the phases 1, 2, and 3, respectively.

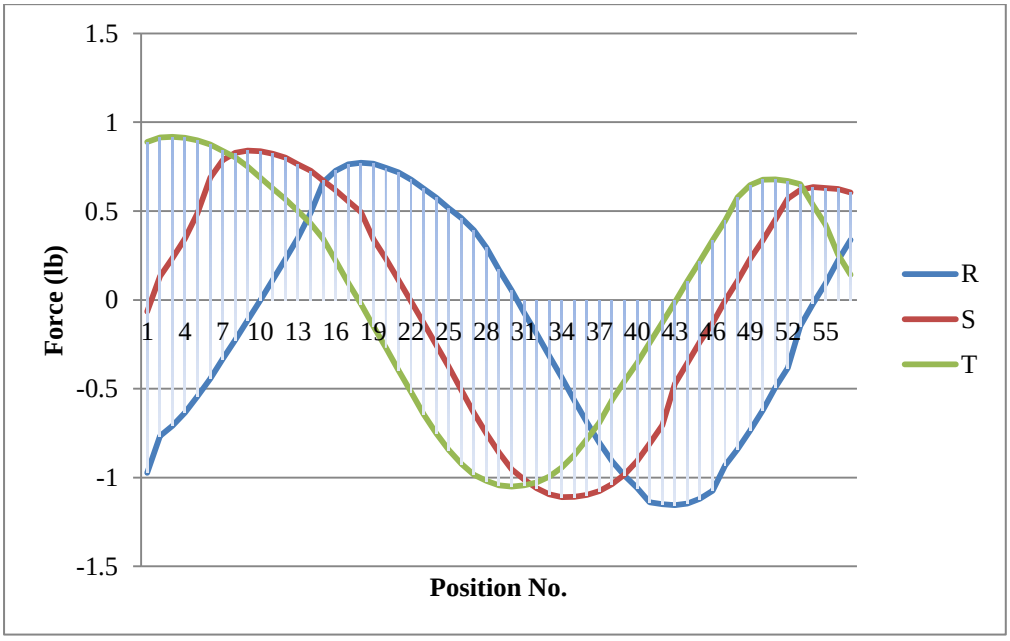

Figure 89: Force measurement data for motor #1.

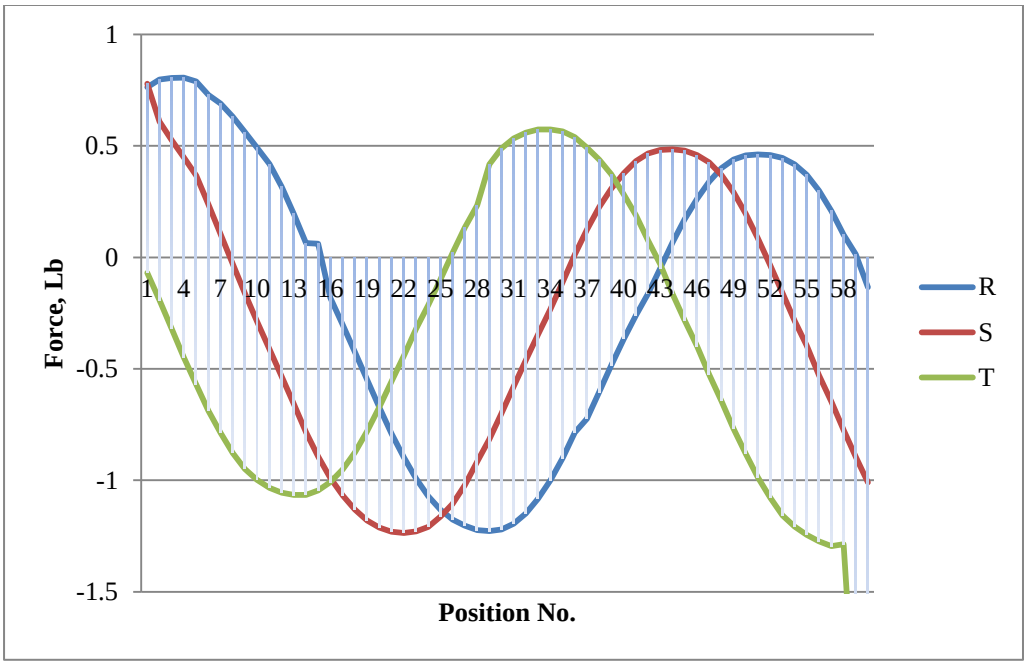

Figure 90: Force measurement data for motor #2.

It is important to mention here that the carriage position is controlled by commutating the currents applied on the three phases on each motor. Also, the measured force at different positions is affected by the perfection of the coil winding and assembly processes. The estimated 2-sigma error on these measurements is about 0.01 lbf

5.3. Halbach Motor Heat Generation

In order to measure the heat generated by the Halbach motor's stator, seven thermistors were attached to the stator surface at equal distances. Figures 91 shows the thermistors locations on the stator and Figure 92 shows the amplifier and readout interface.

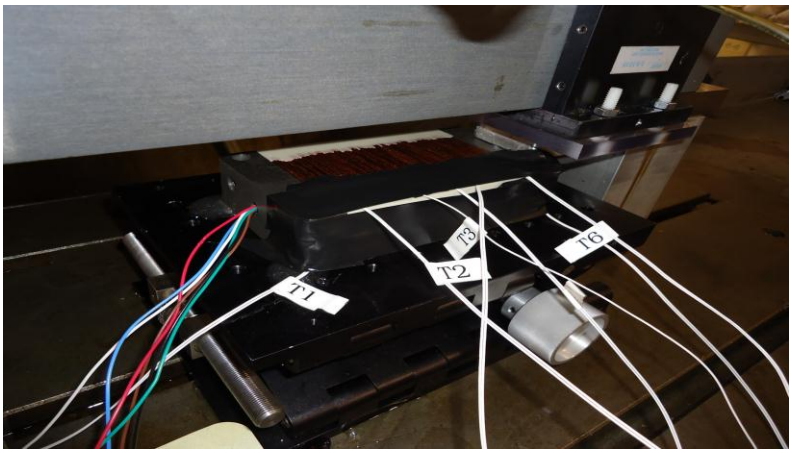

Figure 91: Thermistors locations on the stator.

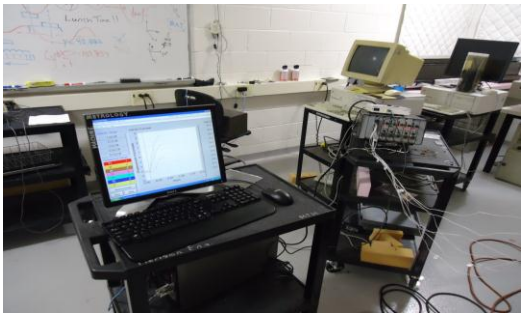

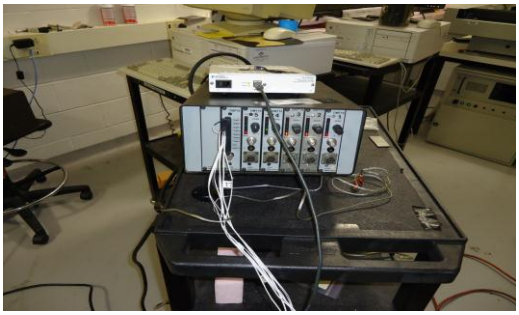

Figure 92: Amplifier and readout software.

Then the three phases were connected to 2, 2.5, and 3 A currents and the temperature recorded over a 2-hour period. The readings estimated uncertainty is +/- 0.2° C with a uniform distribution. Figures 93-98 show the measured data for this experiment.

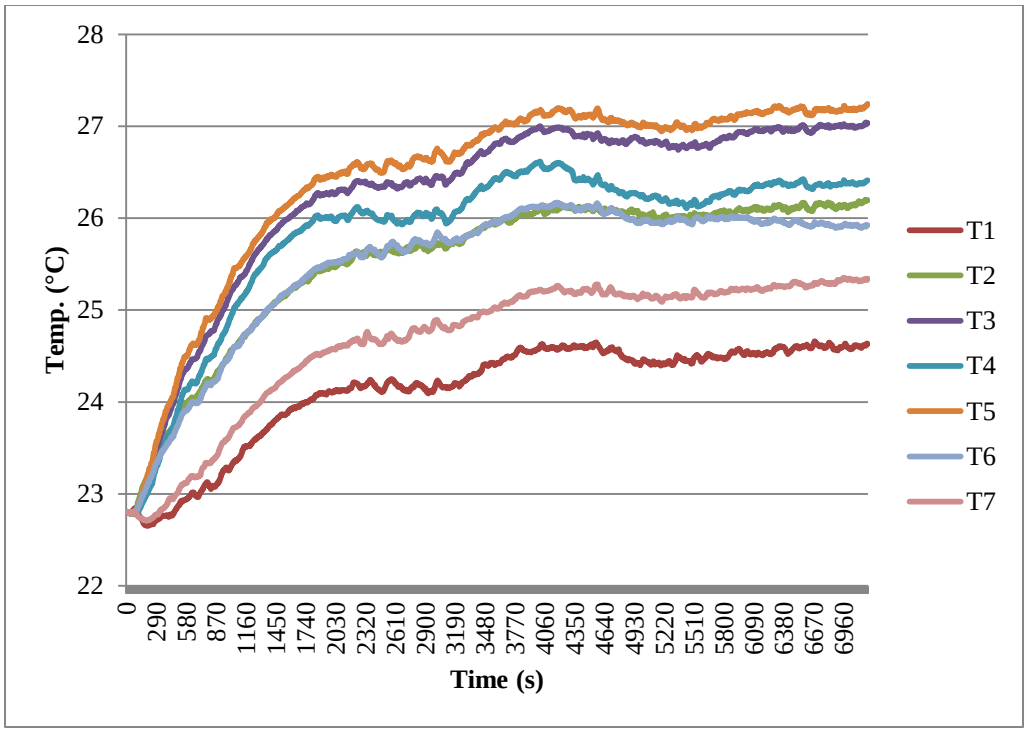

Figure 93: Temperature increase over time (Current = 2 A).

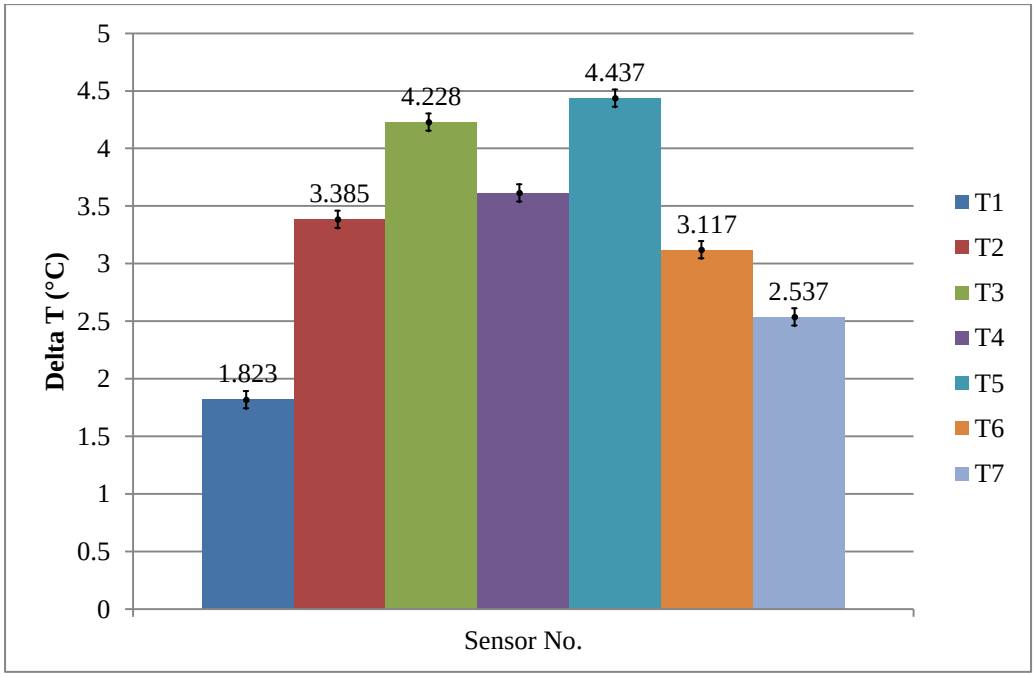

Figure 94: Relationship between thermometer location and temperature increase when passing a current of 2 A for 2 hours through the stator coils. Estimated error bar of 2 sigma is shown on the chart.

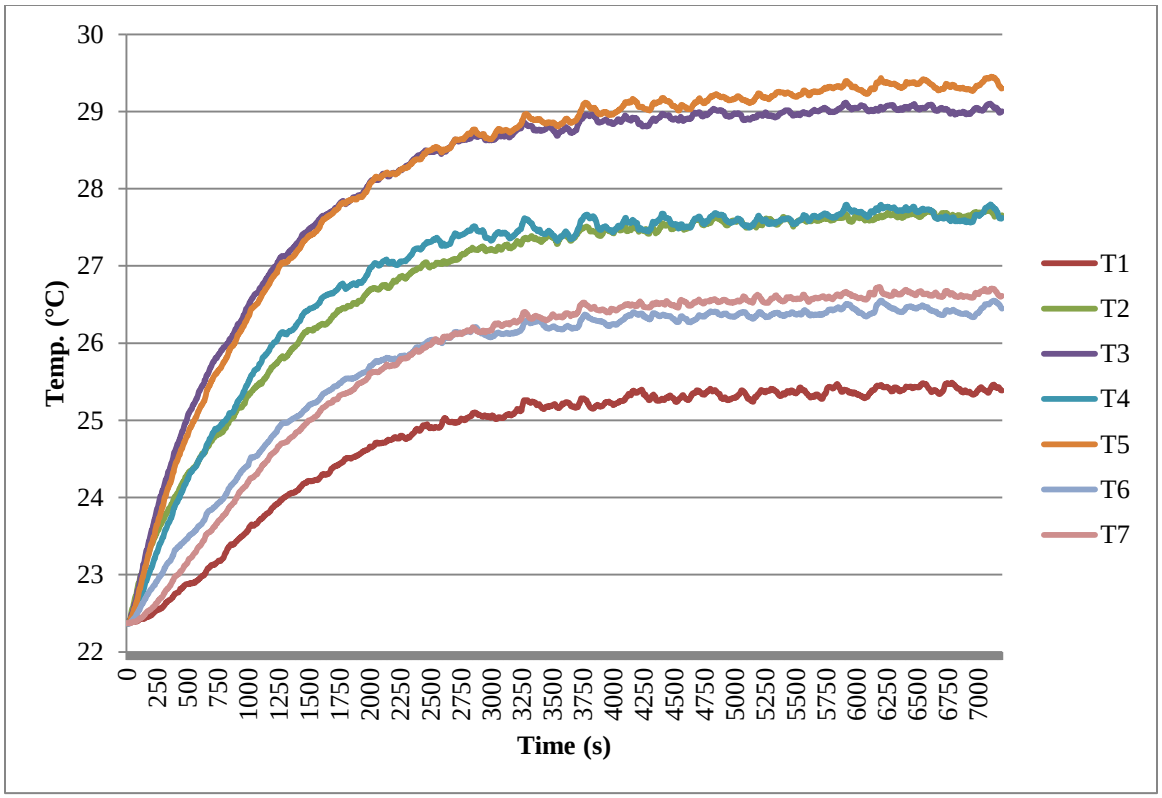

Figure 95: Temperature increase over time (Current = 2.5 A).

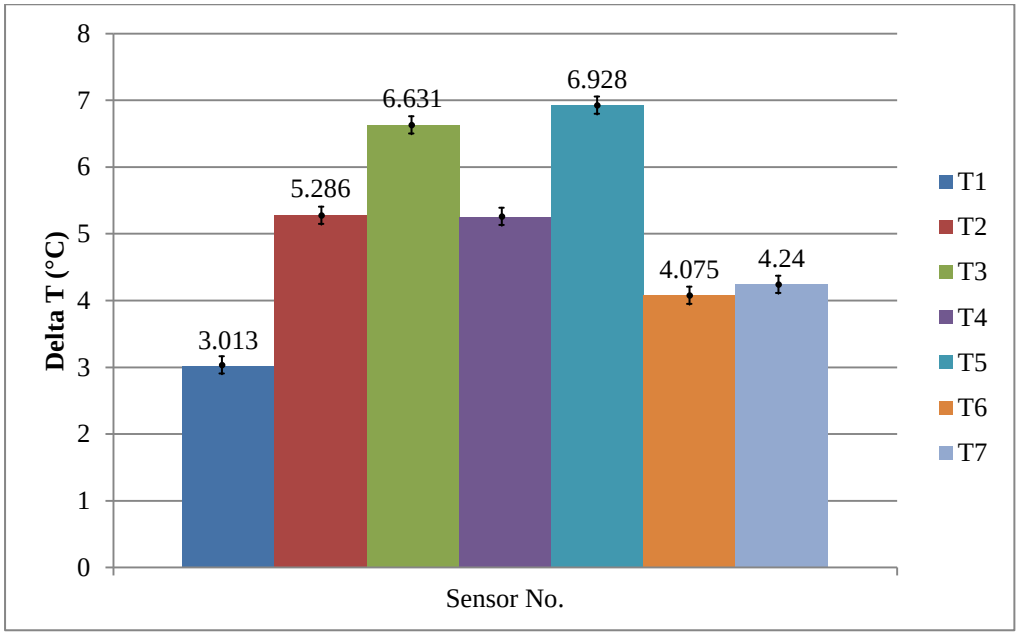

Figure 96: Relationship between thermometer location and temperature increase when passing a current of 2.5 A for 2 hours through the stator coils. Estimated error bar of 2 sigma is shown on the chart.

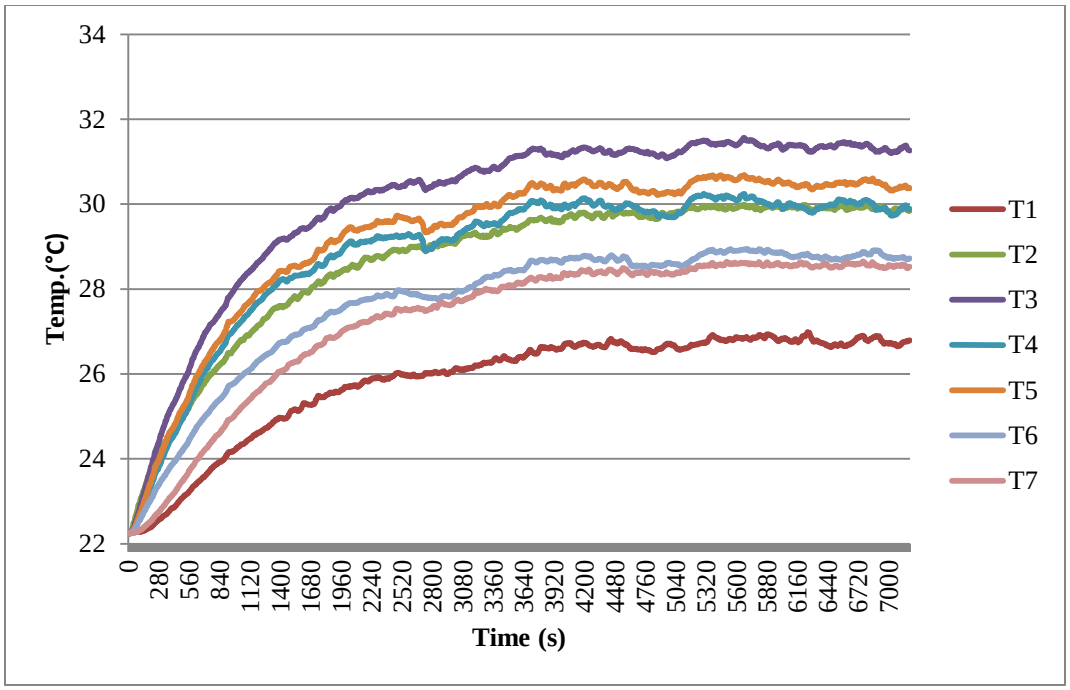

Figure 97: Temperature increase over time (Current = 3 A).

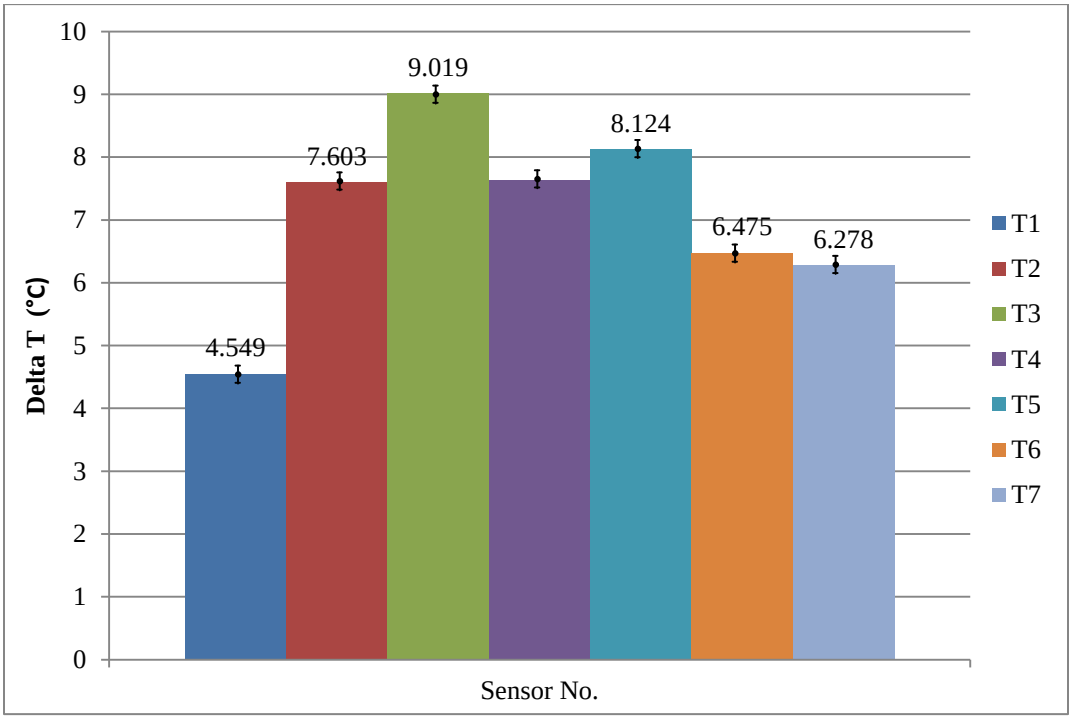

Figure 98: Relationship between thermometer location and temperature increase when passing a current of 3 A for 2 hours through the stator coils. Estimated error bar of 2 sigma is shown on the chart.

Similar motors [Fesperman, 2006] were capable of producing about 8 N at 3 A current (using 12 magnets instead of 8). The PLM's carriage motion is frictionless (using vacuum preloaded air bearings), thus the static coefficient of friction is 0.0 and the dynamic coefficient of friction - which is a function of the air shear rate and directly proportional to the velocity - is neglected at the intended velocity of 5 μm/s. It can be concluded that the estimated current needed to drive the carriage will not exceed 1.5 A, which will generate a temperature increase of less than 4 °C if connecting the three phases simultaneously at the same high current for two hours, which is not a practical case.

It is important to mention that the PLM's base will serve as a heat sink to dissipate the stator's heat. Also, some of the heat will be transferred by convection to the carriage, as shown in Figure 99. According to the PLM project partner, Dr. Adrienne Lavine (a professor at the University of California at Los Angeles), the air gap is so small where the magnets are that conduction would dominate there [SINAM, 2011].

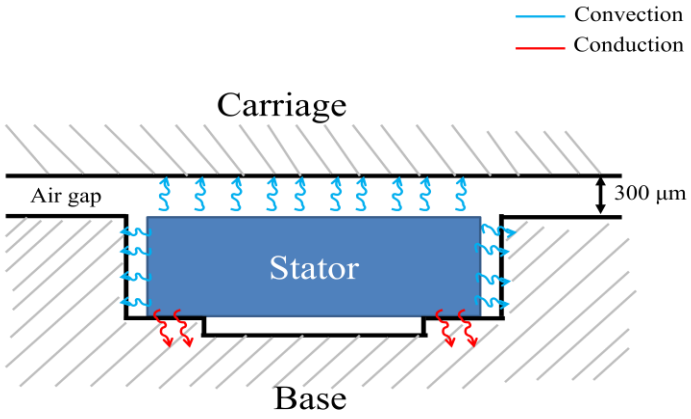

Figure 99: Heat transfer from Halbach motor stator to base and carriage.

5.4. Measuring the Fine Adjustment Range

The main slider is resting on a fine adjustment device which was manufactured at Suter Machine and Tool Company [Suter, 2009]. In order to verify the fine adjustment range a digital indicator was set in contact with the top side of the main slider as shown in Figure 100.

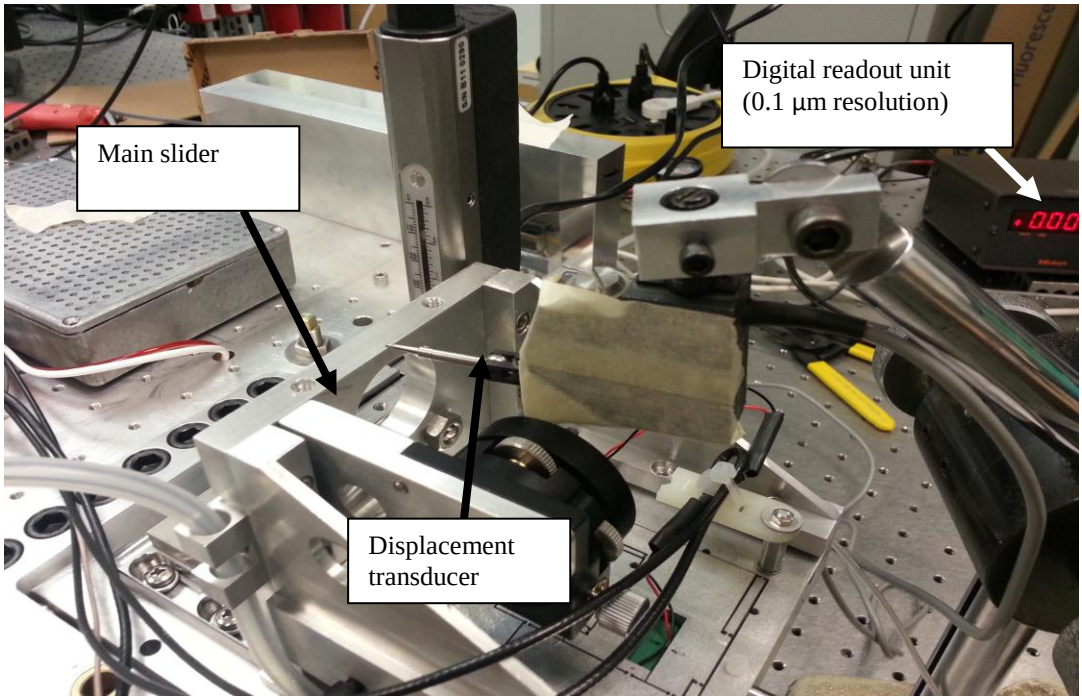

Figure 100: Measuring setup.

After performing a full range measurement it was found that the fine adjustment range was 105 μm.

CHAPTER 6: MECHANICAL ASSEMBLY AND DEBUGGING

The PLM was assembled and calibrated in the metrology lab at the Center for Precision Metrology at UNC Charlotte. The lab used is a ISO class 4 cleanroom (about 10,000 particles/m^3). The temperature inside the lab is controlled with an average of 18˚C and +/- 0.2˚C maximum variation. The PLM assembly took place in the metrology labs at the Center for Precision Metrology at University of North Carolina at Charlotte. The assembly process main phases are: base assembly, carriage assembly, and writing head assembly as shown in Figure 101.

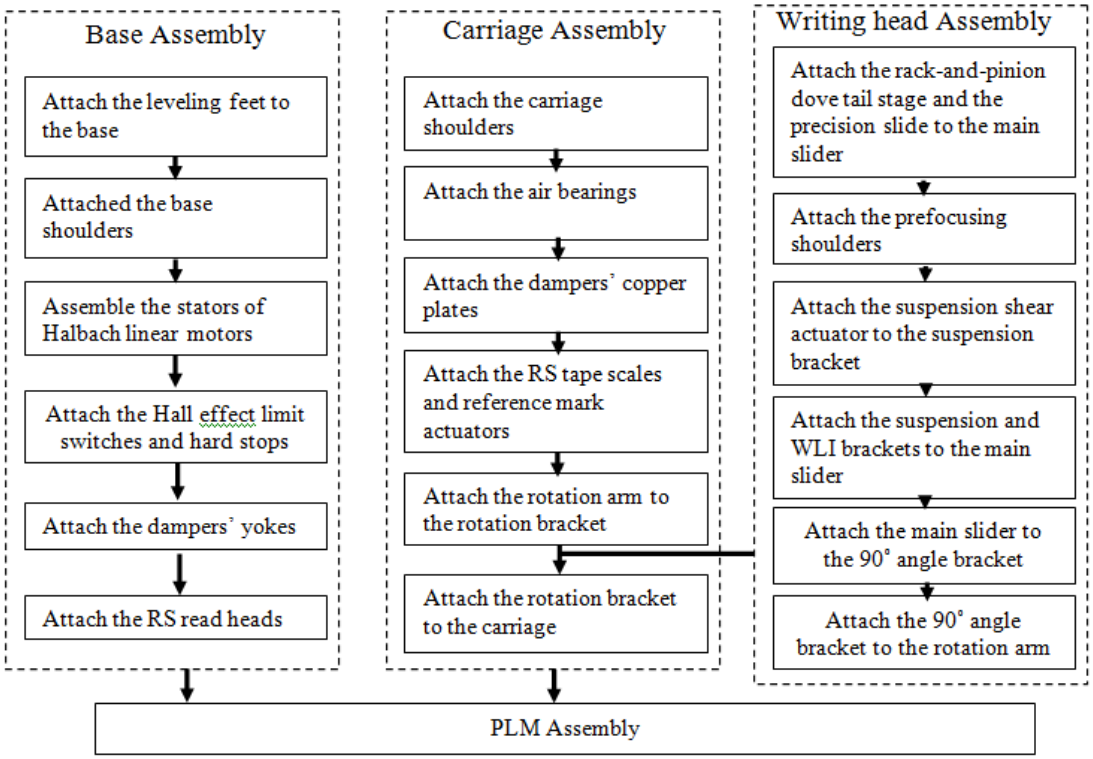

Figure 101: Assembly flowchart.

6.1. Base Assembly

Three leveling feet, having ½-20 screws, were fastened to the base bottom side. Then the Halbach motors' stators were attached to the base using #10-32 screws. Figure 103 shows the front leveling feet location on the base.

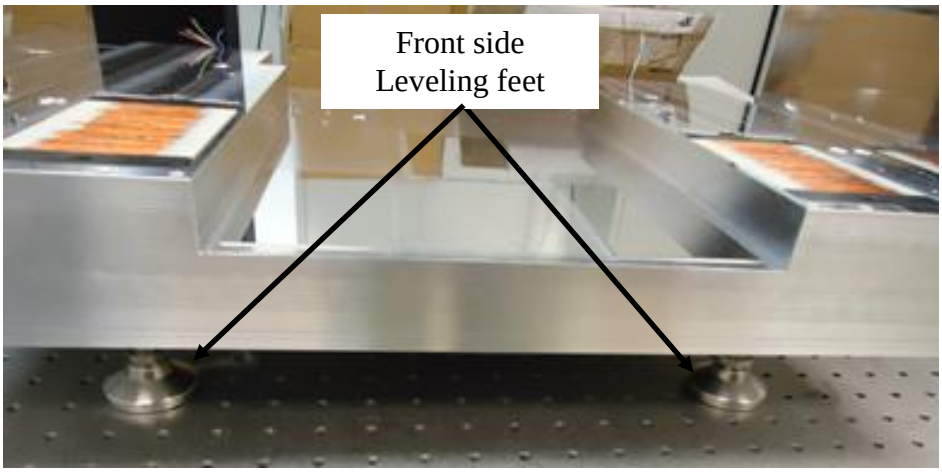

Figure 102: Halbach motor's stator assembly with base.

After assembling the leveling feet, the base shoulders were assembled to the base using 7/16-20 screws. Figure 103 shows the shoulders assembled to the base.

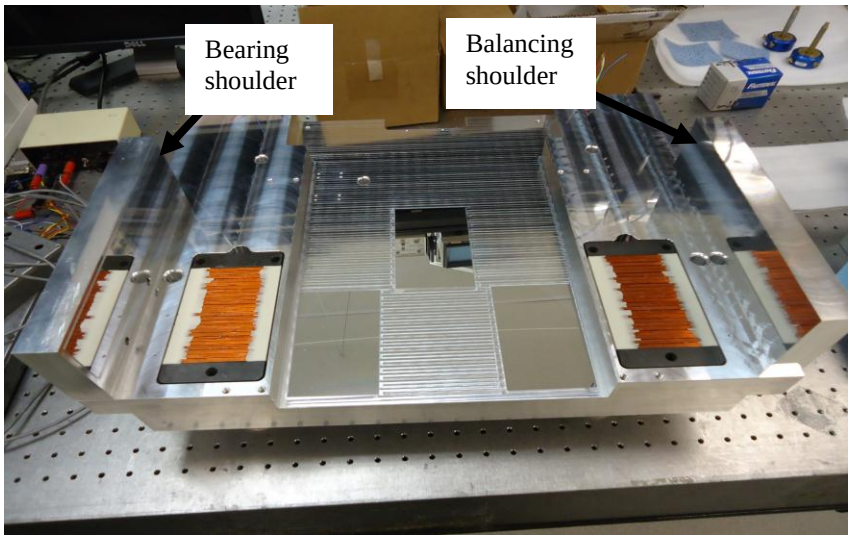

Figure 103: Base assembly.

Before proceeding with the base assembly, the base co-planarity and parallelism were measured on a coordinate measuring machine in the metrology lab at the Center for Precision Metrology at UNC Charlotte. Figure 104 shows a measurement setup of the base on a coordinate measuring machine.

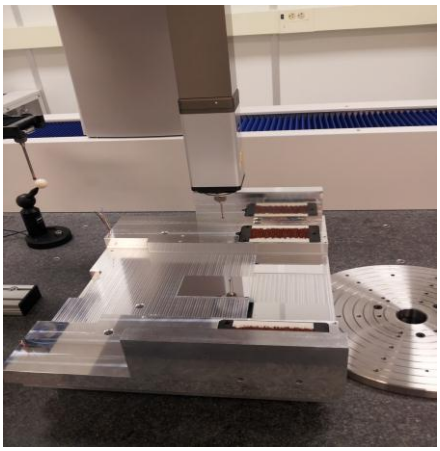

Figure 104: Base measurement.

The next step was to attach the hard stops and Hall effect limit switches to the base, as shown in Figure 105.

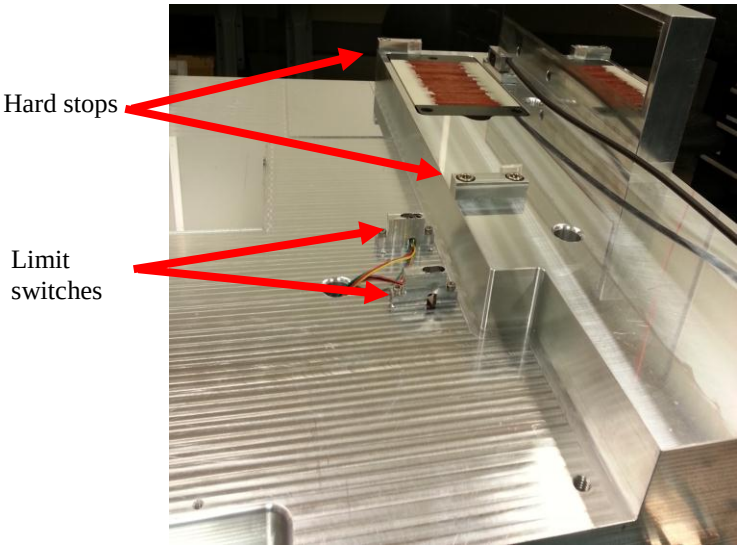

Figure 105: Hall effect limit switches and hard stops attached to the base.

6.2. Carriage Assembly

The carriage assembly process started by attaching the rotation bracket and rotation arm to the carriage as shown Figure 106.

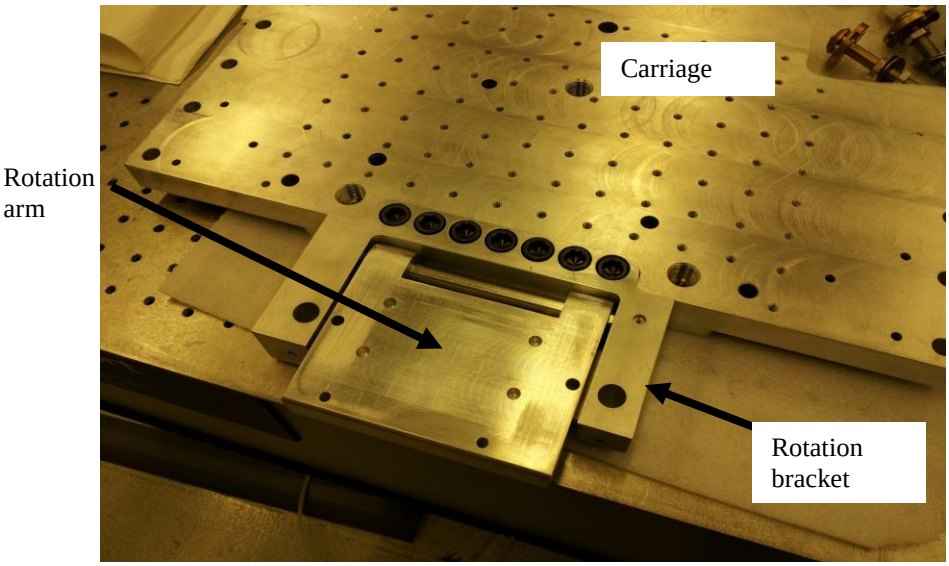

Figure 106: Carriage assembly with rotation arm.

Figure 107 illustrates the 90˚ rotation of the rotation arm.

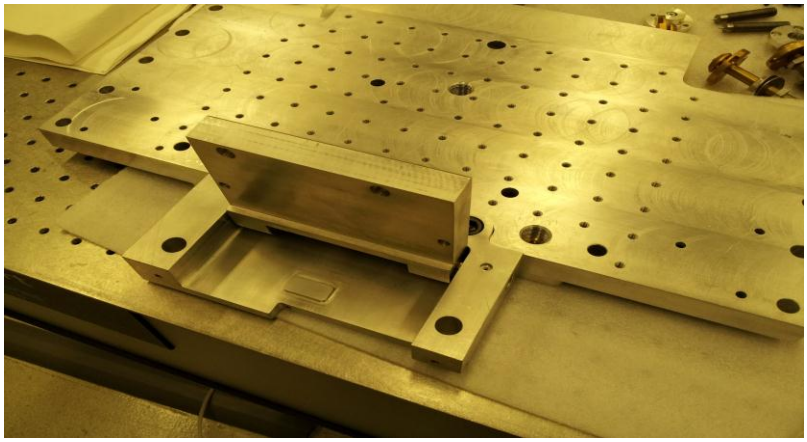

Figure 107: Rotation arm at 90° position.

Then the monitoring bracket was attached to the rotation bracket, as shown in Figure 108.

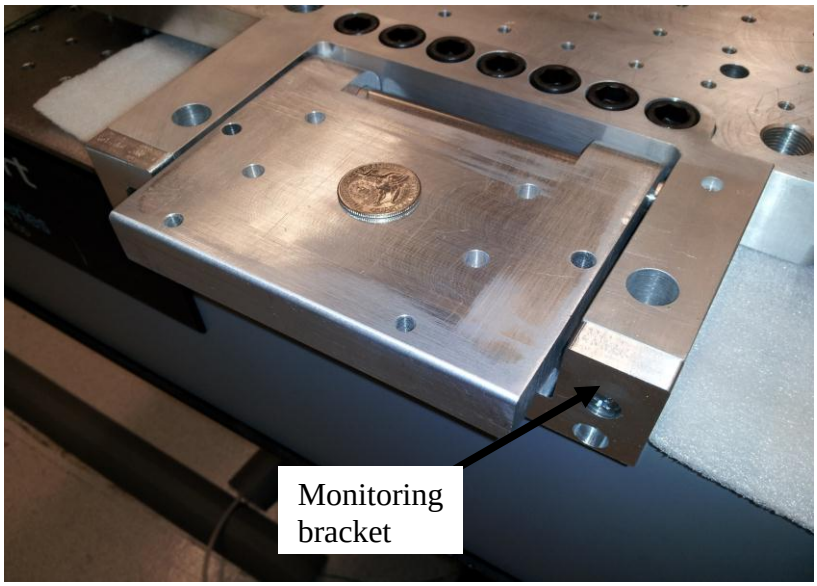

Figure 108: Monitoring bracket.

The next step was to attach the shoulders and the air bearings as shown in Figures 109 and 110.

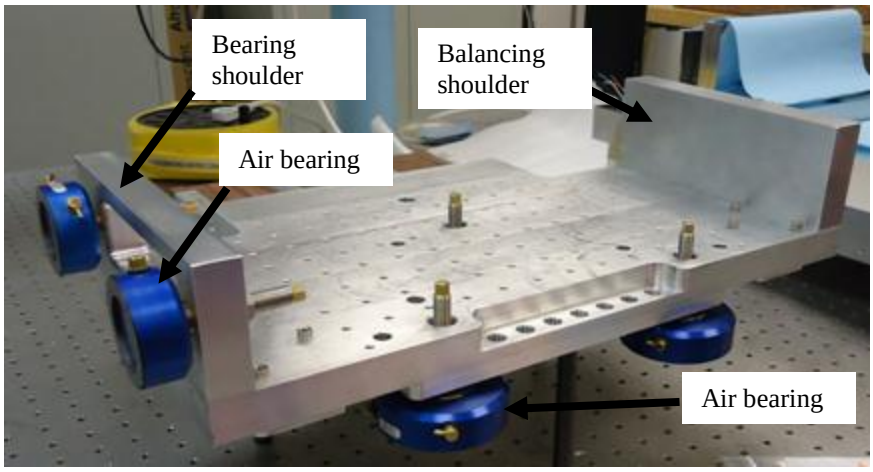

Figure 109: Shoulders and air bearing assembly.

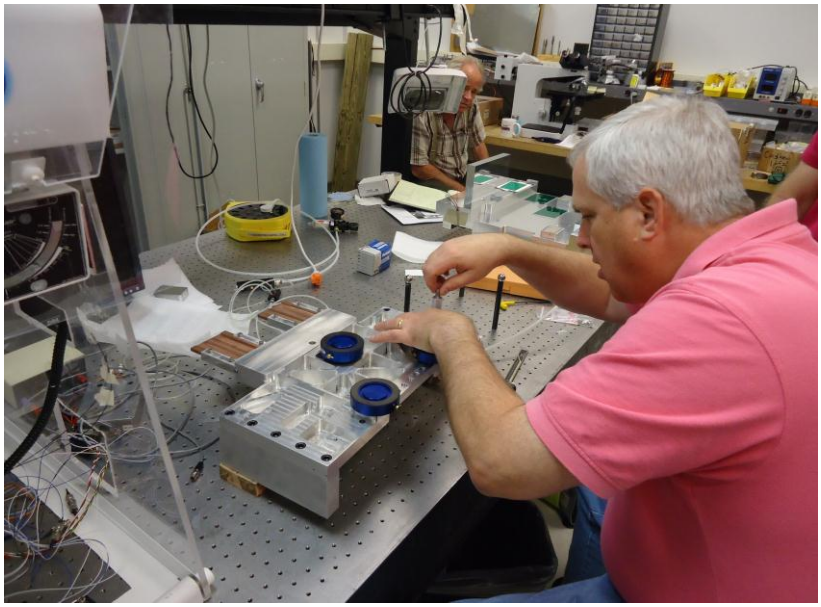

Figure 110: Greg Caskey, of the Center for Precision Metrology at UNC Charlotte, checking the level of the air bearings after assembly.

The next step was to assemble the eddy current damper's copper plates to the carriage as shown in Figures 111. Figure 112 shows one of the eddy current damper's yokes attached to the base and Figure 113 shows the eddy current damper location on the PLM.

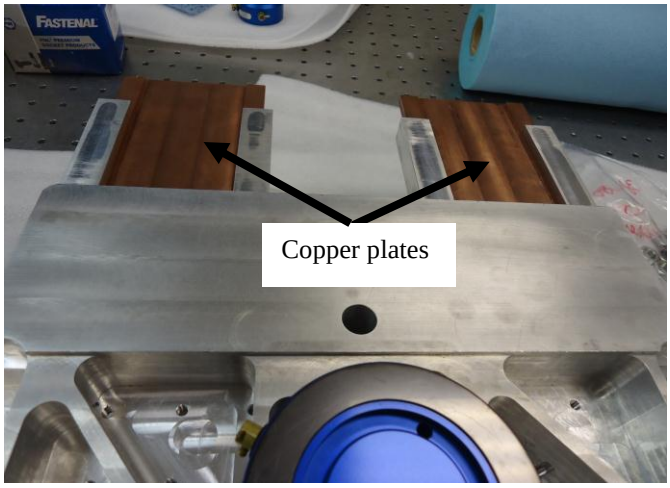

Figure 111: Illustration of the damper's copper plates assembly.

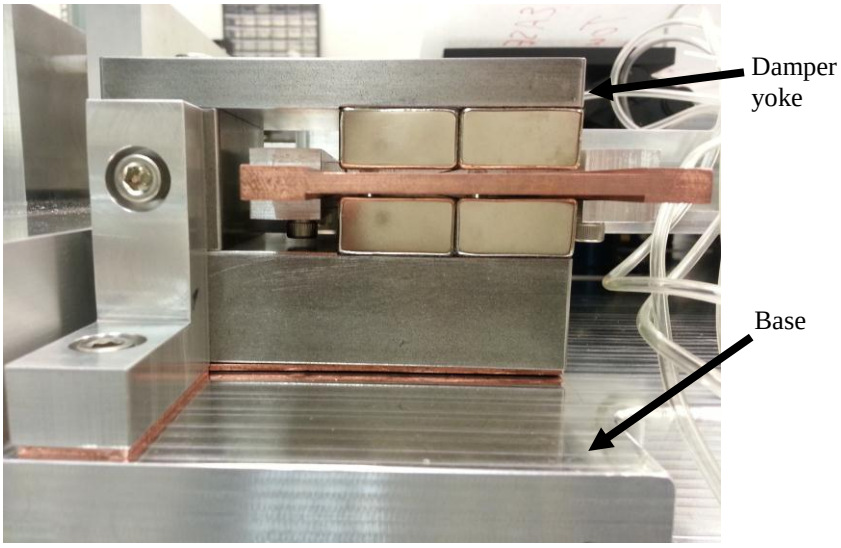

Figure 112: Eddy current damper.

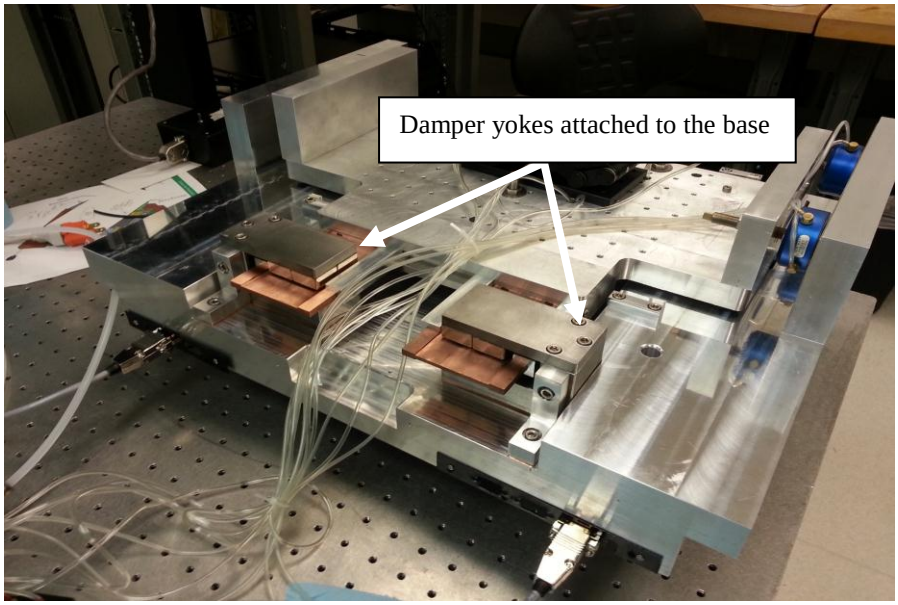

Figure 113: Eddy current damper assembly on the PLM.

The next step was to attach the magnets of the Halbach linear array motors to the carriage. The assembly is shown in Figure 114.

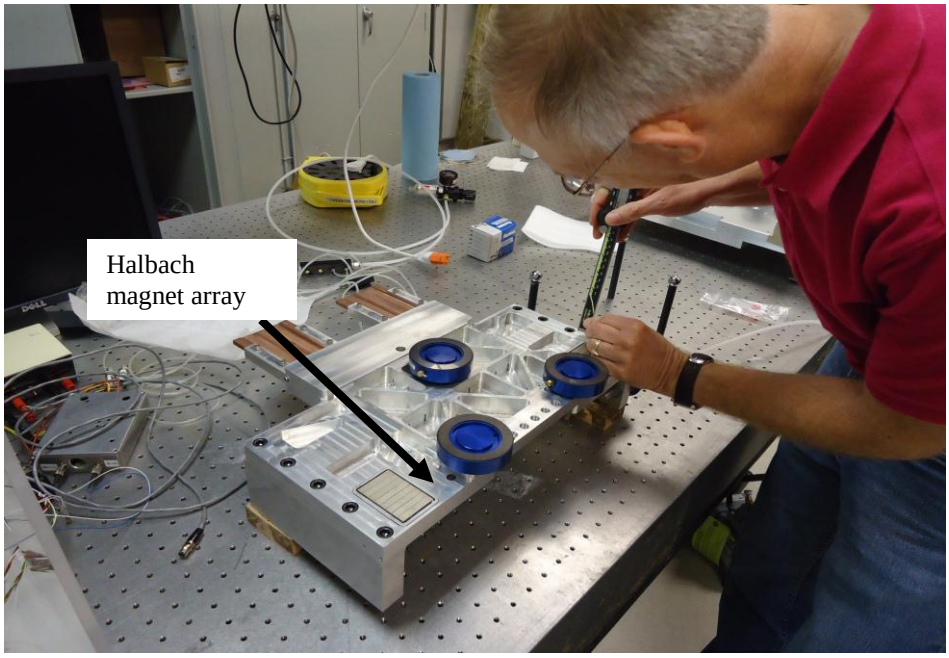

Figure 114: Dr. Jimmie Miller, of the Center for Precision Metrology at UNC Charlotte, checking the level of the Halbach magnet arrays after being assembled with the carriage.

A magnet was attached to the carriage bottom surface to activate the Hall effect limit switches when exceeding the allowable travel range limits. Figure 115 shows the limit switch activation magnet attached to the carriage.

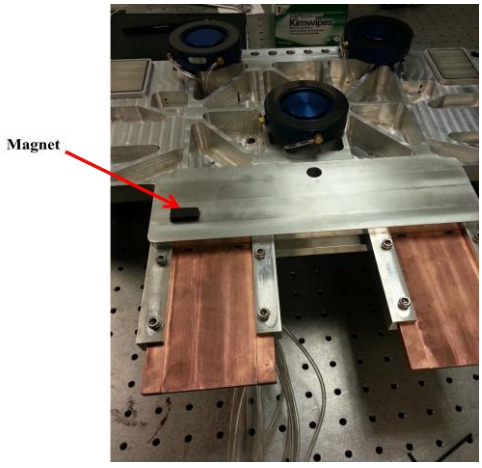

Figure 115: Magnet for Hall effect limit switch attached to the carriage.

In order to check the carriage-base compatibility it was decided to manually run the carriage on the base. In order to set the carriage magnet arrays at the right height with respect to the Halbach stators' surfaces, 303-micron shims were used on the stators and the carriage set in position with the weight supported by the Halbach motors. During this process the diamond-turned ways were covered with a thin shim for protection. The air bearing heights were adjusted until the stage barely floated and the shims were removed. The shims between stators and magnets were moved by hand to ensure that that gap is correct. Figure 116 shows the use of plastic and paper shims during the assembly process.

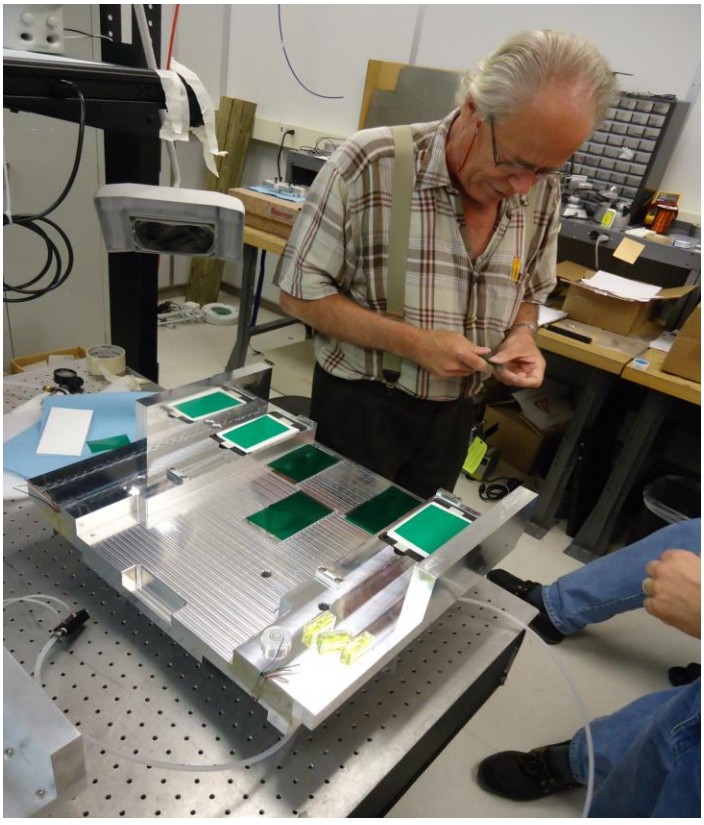

Figure 116: Dr. Robert Hocken, of the Center for Precision Metrology at UNC Charlotte, uses plastic and paper shims to set the heights of the motor magnets and to protect sensitive surfaces before carriage-base assembly.

Then, after assembling the carriage and base, the carriage was run for the first time flying on the air bearings as shown in Figure 117.

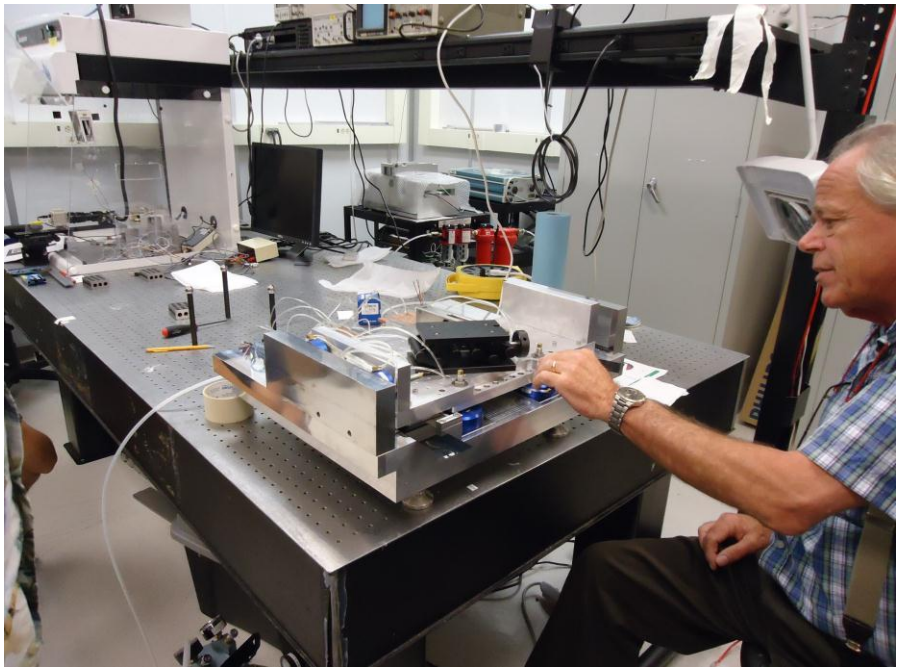

Figure 117: Dr. Robert Hocken moving the PLM carriage for the first time.

6.3. Writing Head Assembly

Firstly the linear stage, vertical motor and main slider were assembled to the 90˚ angle bracket. Then the prefocusing shoulders and the prefocusing flexure were attached to the main slider. The writing head assembly is shown in Figure 118.

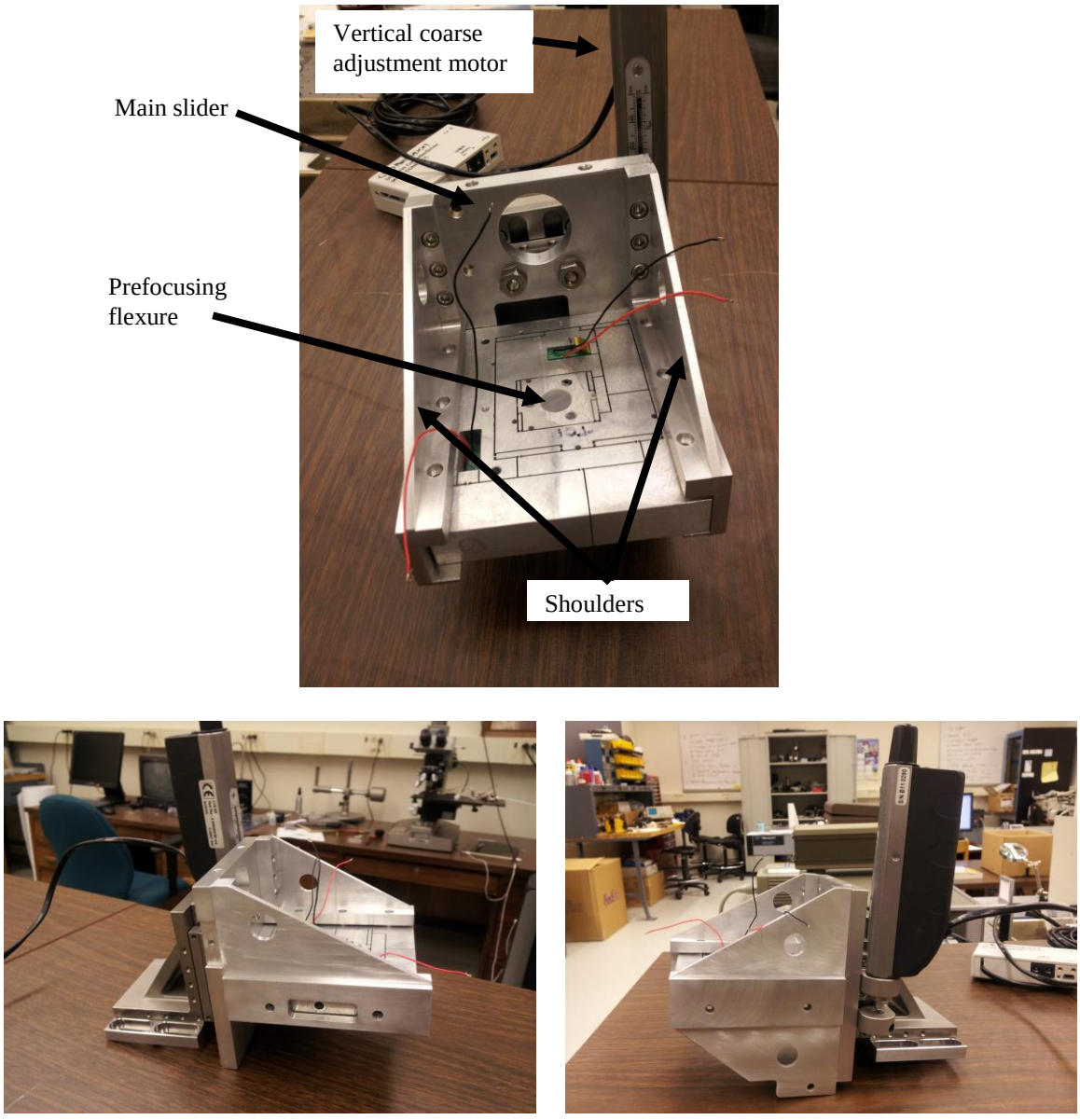

Figure 118: Illustration of the writing head assembly.

In order to assemble the prefocusing flexure, the plasmonic lens suspension bracket, and the diode laser bracket to the writing head, it was necessary to attach the writing head to the rotation arm on the PLM. This step facilitated the assembly process as the writing head assembly can easily be completed by using the 90˚ rotation arm to

rotate the whole writing head. Figure 119 shows the writing head assembly in the writing mode and Figure 120 shows the writing head in the plasmonic lens changing mode.

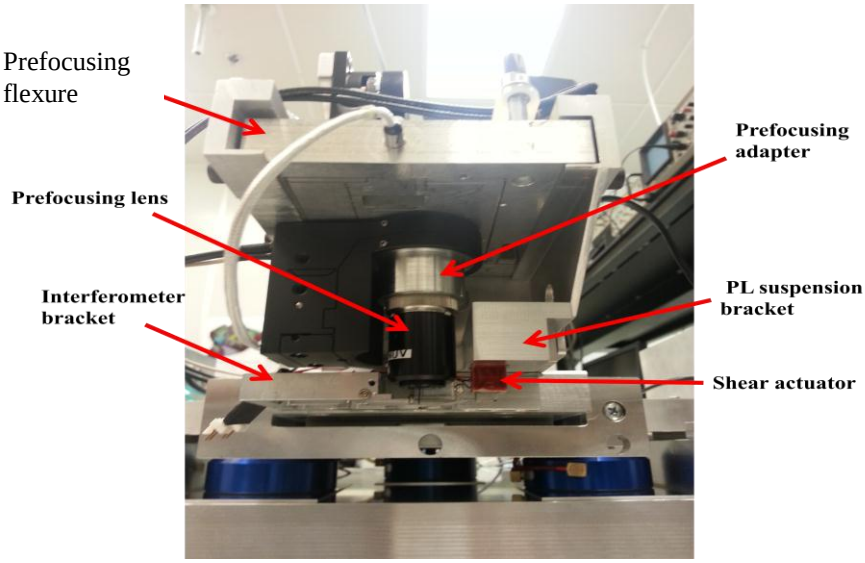

Figure 119: Writing head assembly in the writing mode.

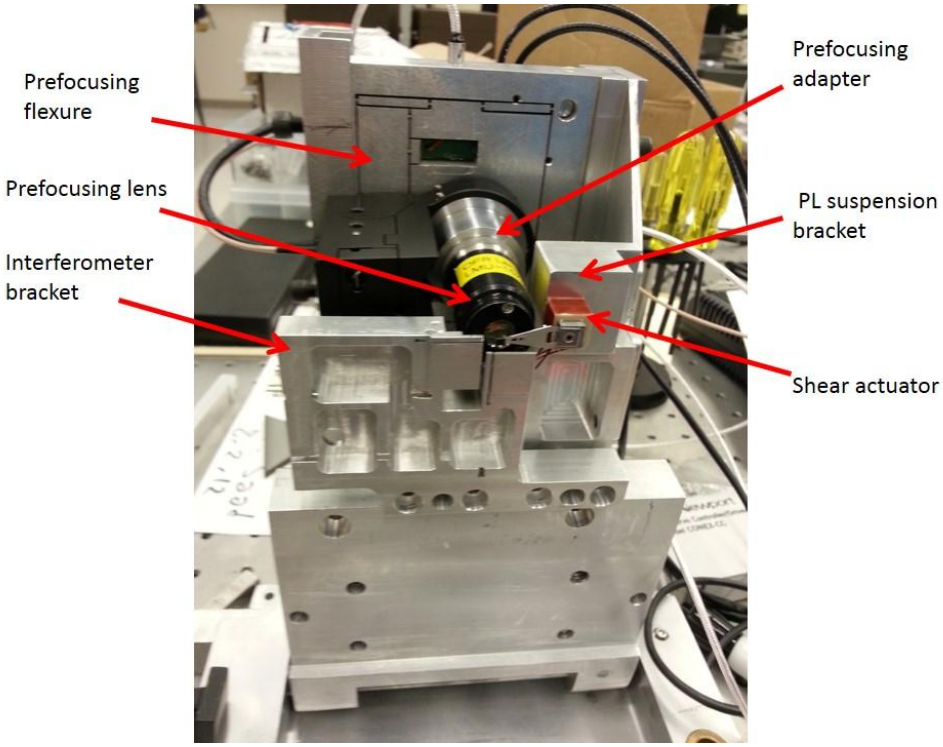

Figure 120: Writing head assembly in the plasmonic lens changing mode.

The shear actuator was attached (by Chris Hughes) to the plasmonic lens bracket using super glue before adding the bracket to the assembly.

The prefocusing lens can be adjusted in three directions, X, R, and Z, using piezoelectric actuators with a range of 50 x 50 x 100 μm, respectively. After further discussions with our project partners at University of California at Berkeley and considering the possible variations in the plasmonic lens suspension, it was recommended that coarse adjustment capability be added in the X, R, and Z directions. In order to achieve that, three more elements were added to the writing head assembly, and the main slider was adjusted to adopt these modifications. In order to provide coarse adjustment in the vertical (Z) direction, a dovetail rack and pinion stage and precise slide were added to the assembly as shown in Figure 121. More details about these two elements can be found in section 3.6.7

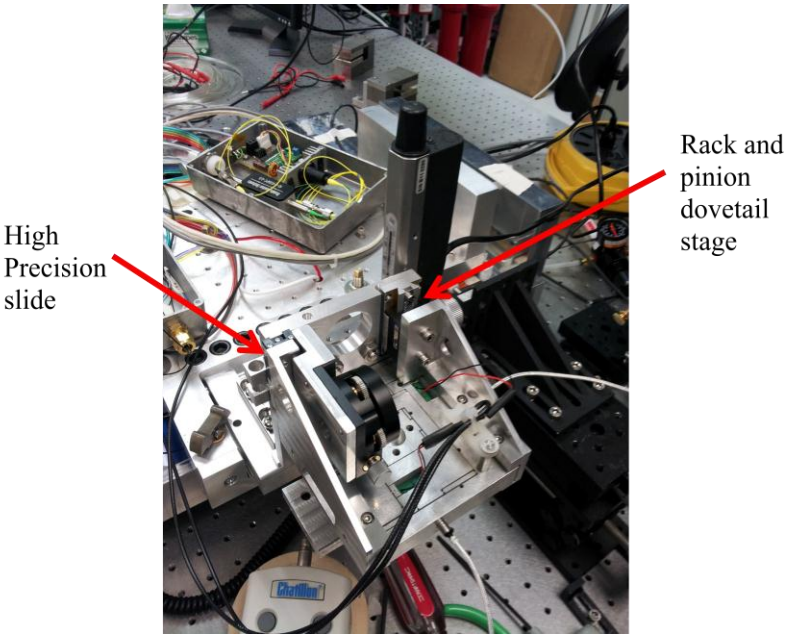

Figure 121: Installation of the rack and pinion dovetail stage and high-precision slide.

In order to provide coarse adjustment in the X and R directions, a coarse adjustment prefocusing stage was designed, manufactured, and assembled at UNC Charlotte. Figure 122 shows the stage location and assembly. Further details about the coarse adjustment prefocusing stage are found in section 3.6.6.

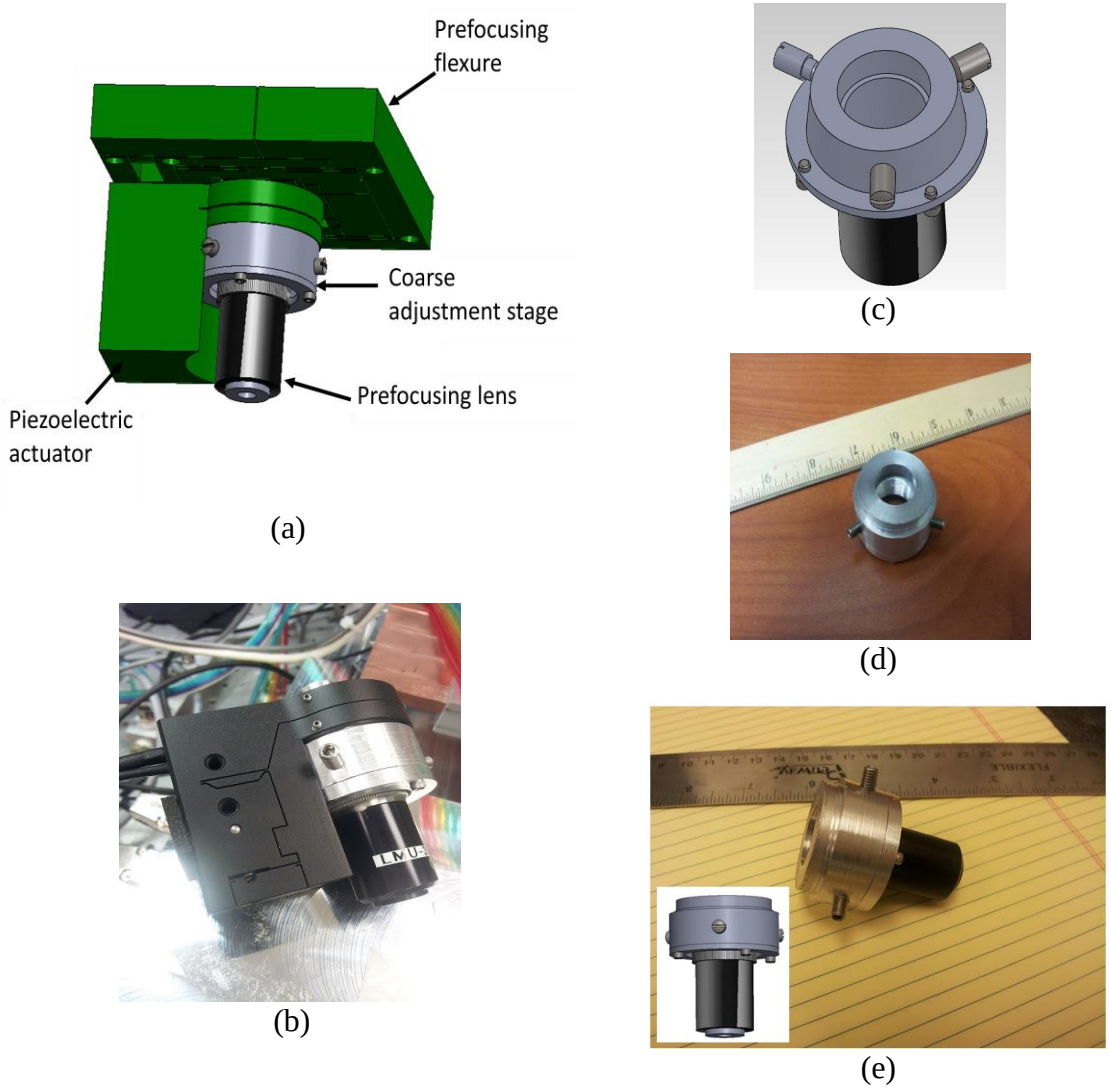

Figure 122: Coarse adjustment prefocusing stage: (a) location of the stage, (b) stage assembly with the Z-direction piezoelectric actuator, (c) CAD model showing the details inside the stage, (d) assembled stage, (e) stage assembly with the prefocusing lens.

6.4. PLM Assembly

After assembling all these parts together it is important to see the whole machine and the location of each part as shown Figures 123-125.

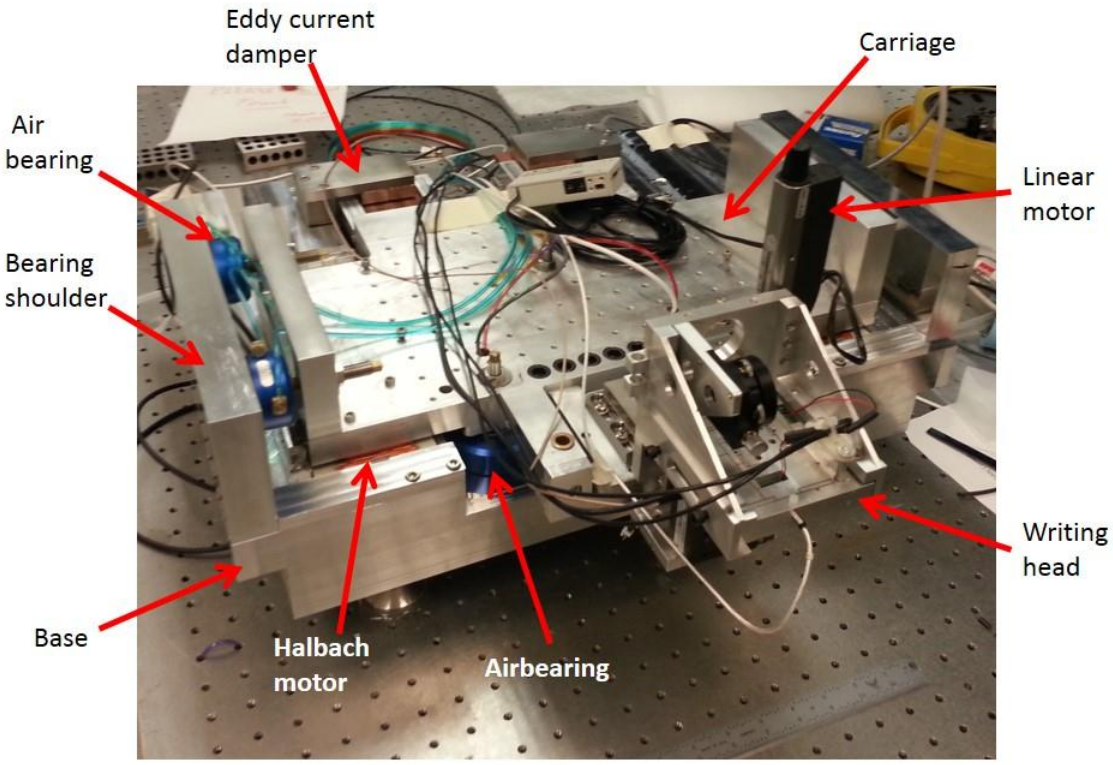

Figure 123: Plasmonic Nano-Lithography Machine (PLM)

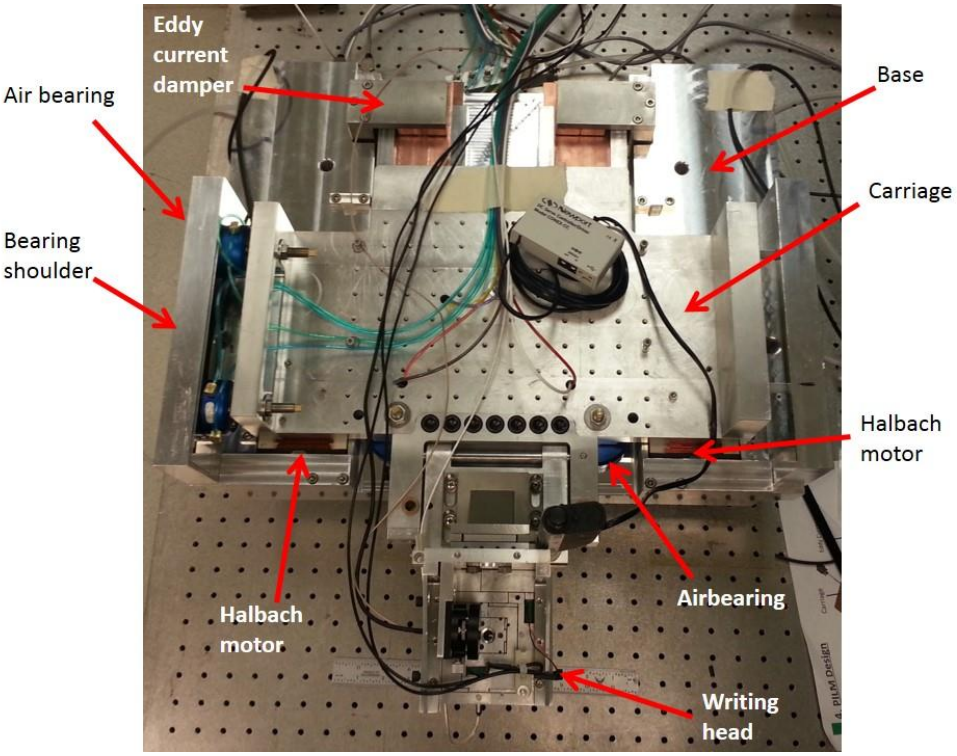

Figure 124: Plasmonic Nano-Lithography Machine (PLM)

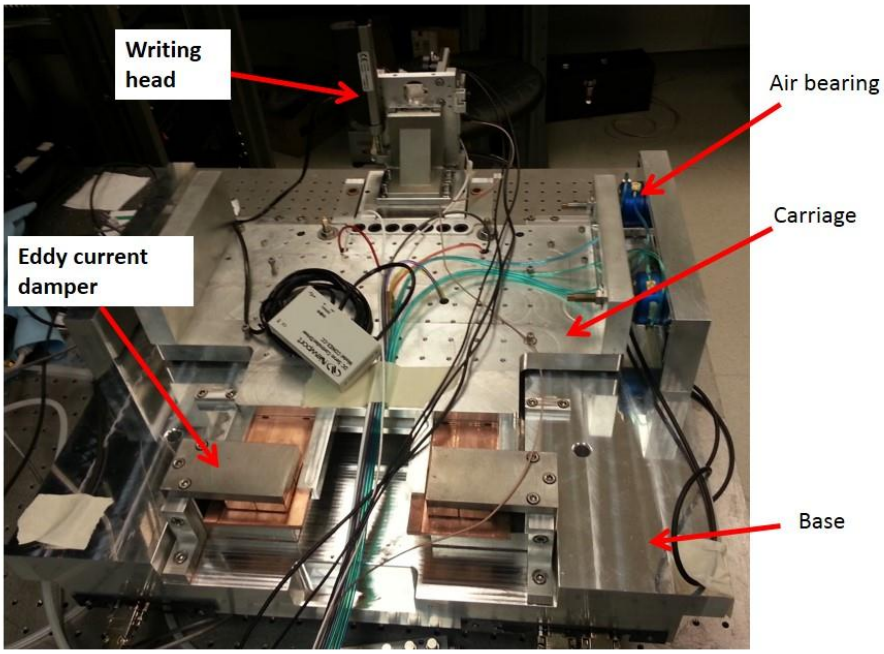

Figure 125: Plasmonic Nano-Lithography Machine (PLM)

6.4.1 Writing Head Rotation

During the plasmonic lens changing procedure the writing head is rotated 90˚ in order to easily access the plasmonic lens. Figures 126 and 127 show the PLM during the writing and the plasmonic lens changing phases respectively.

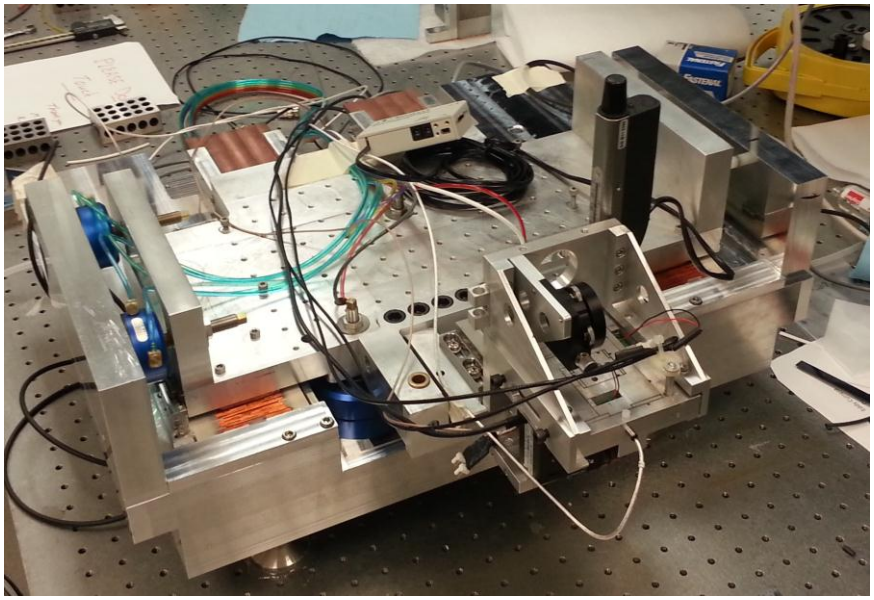

Figure 126: PLM in the writing position.

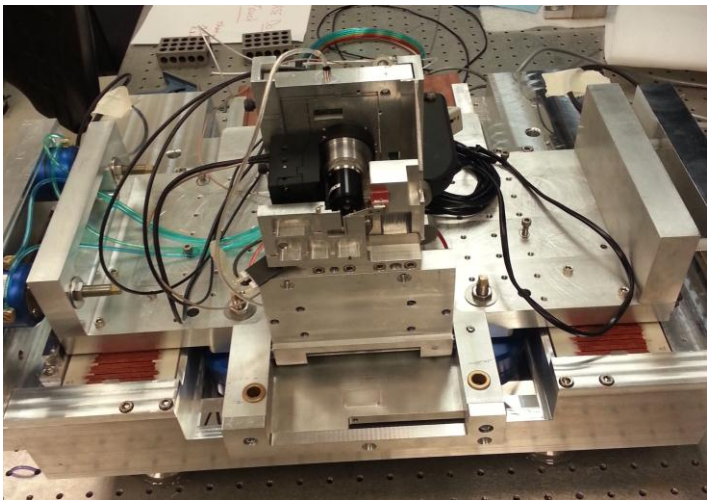

Figure 127: PLM in the plasmonic lens changing position.

Figures 128 and 129 show closer views of the plasmonic lens slider and suspension during the plasmonic lens changing process.

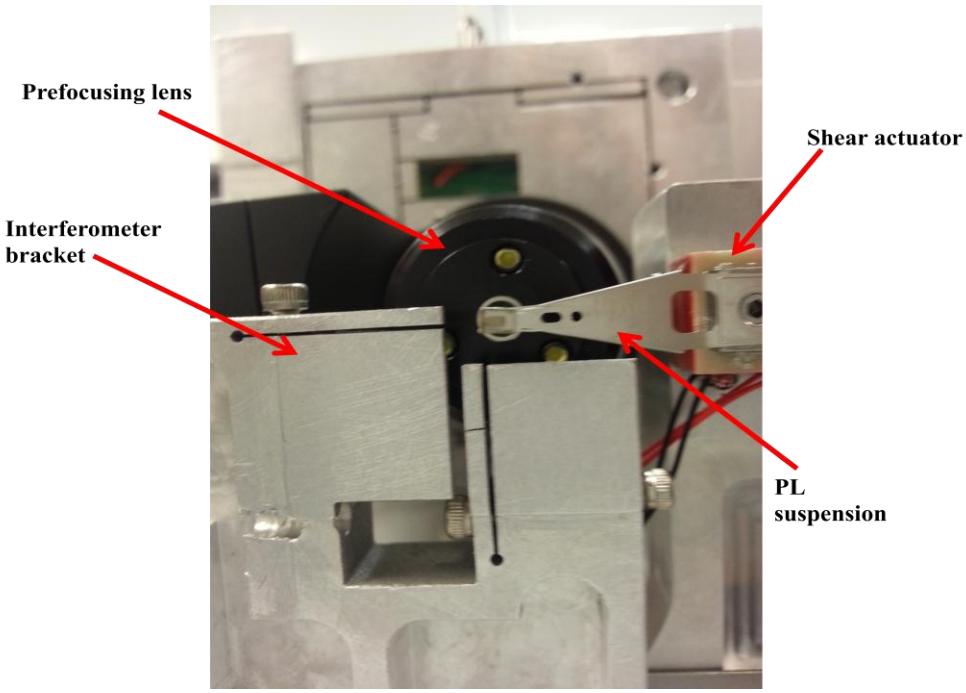

Figure 128: Plasmonic lens slider location during the plasmonic lens changing process.

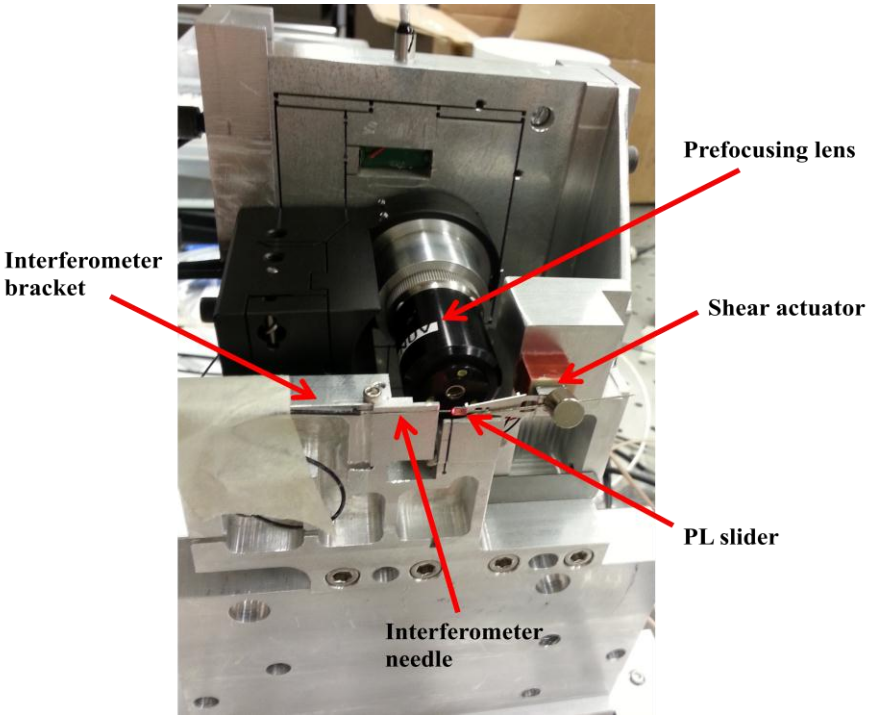

Figure 129: Plasmonic lens slider location during the plasmonic lens changing process.

The plasmonic lens suspension shown in Figure 130 is held in place by a cylindrical magnet and needle. This configuration is included only for illustrating the slider location with respect to the diode laser interferometer needle in the X and R directions. A closer view is shown in Figure 130.

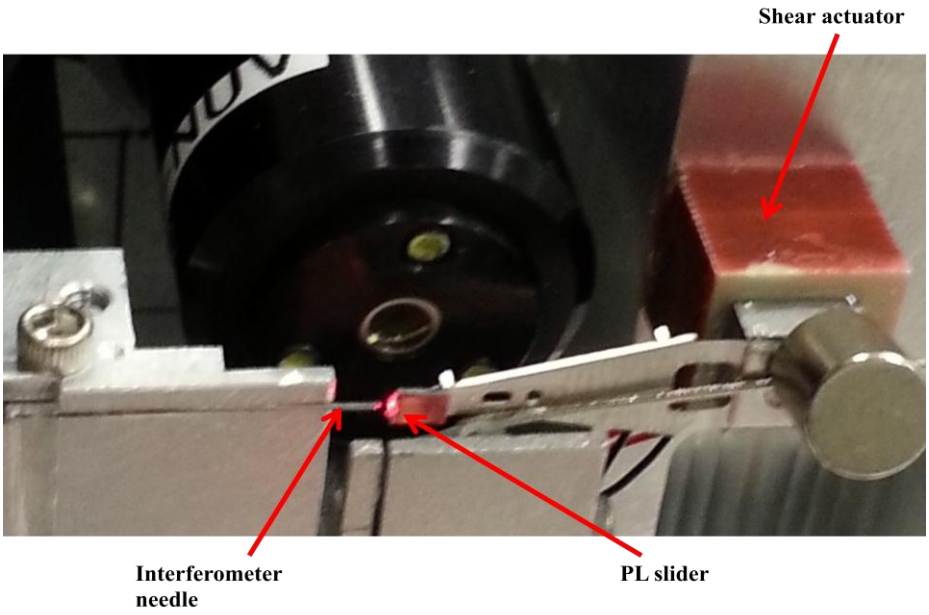

Figure 130: Plasmonic lens slider location with respect to the diode laser interferometer.

6.5. Error Analysis

When writing this thesis the PLM was not calibrated, so it is important to estimate the expected performance once it is running. The function of the PLM is to move a plasmonic lens slider precisely above a spinning disc, thus the cumulative X,Y,Z positioning error is the target of this analysis.

The positioning error, (ΔX, ΔY, ΔZ) is the distance between where the PLM control system assumes the disc is in relation to the plasmonic lens and the actual position. First of all, let's start by creating a model of the systematic geometric errors.

6.5.1. PLM Model

Based on Holmes' model [Holmes, et al., 1998, 2000], Figure 131 can represent the PLM model.

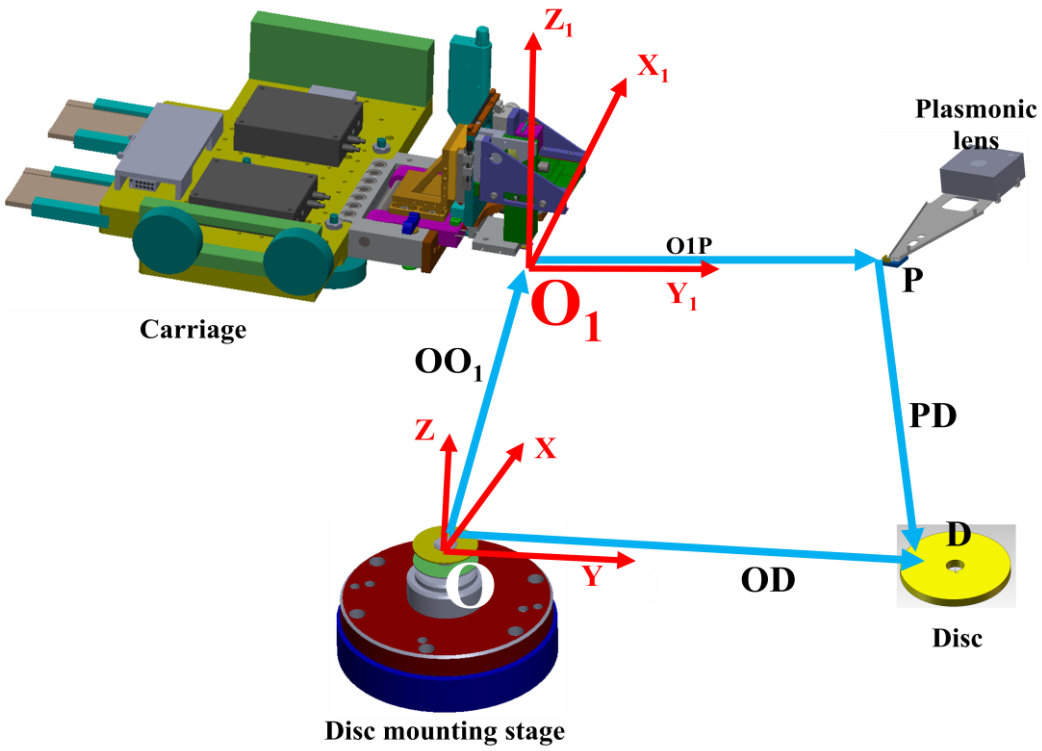

Figure 131: PLM coordinate system for error estimation (the plasmonic lens size is enlarged for illustration).

The model has two coordinate systems: the spindle coordinate system, (O), and the carriage coordinates system, (O_1). The carriage coordinate system (O_1) is located in the center of the bottom surface of the shear actuator attached to the plasmonic lens suspension bracket, as shown in Figure 132.

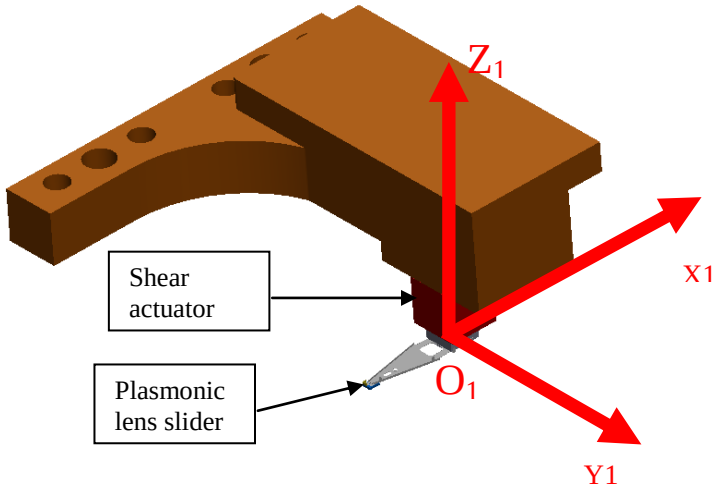

Figure 132: The carriage coordinate system.

The X_1 axis is perpendicular to the Renishaw tape scales (located on the carriage sides), the Y_1 axis is parallel to the Renishaw tape scales, and the Z_1 axis is perpendicular to both the X_1 and Y_1 axes. The positive directions of X_1, Y_1, and Z_1 are shown in the previous Figure 132. The origin of the spindle coordinate system, (O) is at the center of the spindle intersection with the top surface of the disc, as shown in Figure 133.

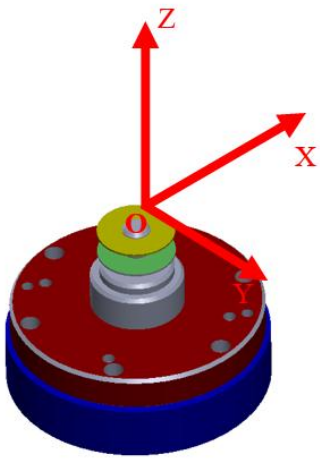

Figure 133: The spindle coordinate system.

The X, Y, and Z axes are parallel to the X_1, Y_1 , Z_1 axes, respectively.

During the writing process, the PLM Halbach motors move the carriage in the direction Y (coordinate system O – note that this direction is also called R in different sections through this thesis). Thus, the actual position of the carriage origin (O_1), in the spindle coordinate system, is defined by the vector OO_1 which extends from the origin (O) to the origin (O_1) and can be described as:

$$OO1 = \begin{bmatrix} \delta_x(Y) \\ Y + \delta_y(Y) \\ \delta_z(Y) \end{bmatrix} \tag{6.1}$$

where δ represents the systematic translation errors, as follows:

δ_x(Y): error motion in X as a function of Y position

δ_y(Y): error motion in Y as a function of Y position

δ_z(Y): error motion in Z as a function of Y position

On the other hand, rotational errors, ε, in the system cause the carriage coordinate system (O_1) to rotate with respect to the spindle coordinate system (O) as the carriage travels. This rotation can be described by the rotation matrix R_1:

$$R_1 = \begin{bmatrix} 1 & -\varepsilon_z & \varepsilon_y \\ \varepsilon_z & 1 & -\varepsilon_x \\ -\varepsilon_y & \varepsilon_x & 1 \end{bmatrix}. \tag{6.2}$$

The vectors O_1P and OD represent the location of the plasmonic lens in (O_1) and the locations of the target location on the disc in (O), respectively. O_1P extends from the origin (O_1) to the point on the plasmonic lens where the writing process is occurring and is described by

$$O_1P = \begin{bmatrix} X_{1P} \\ Y_{1P} \\ Z_{1P} \end{bmatrix} \tag{6.3}$$

OD extends from the origin (*O*) to the point on the disc where the PLM system writing process is running, and it can be described as follows:

$$OD = \begin{bmatrix} X_D \\ Y_D \\ Z_D \end{bmatrix} \tag{6.4}$$

The PLM positioning error is represented by the vector, PD, which extends from the plasmonic lens to the target location on the disc. *PD* is described by

$$PD = OP - \left[OO_1 + R_1O_1D\right] \tag{6.5}$$

The resulting position error can then be described by

$$\begin{bmatrix} \Delta X \\ \Delta Y \\ \Delta Z \end{bmatrix} = \begin{bmatrix} \delta_x(Y) - \alpha_{yx}Y - \varepsilon_z Y_P \\ \delta_y(Y) \\ \delta_z(Y) + \varepsilon_x Y_P \end{bmatrix} \tag{6.6}$$

where:

α_{yx} - Angle between Y_1 projection onto YX plane and Y

$\delta_x(Y)$ - Error motion in X as a function of Y position

$\delta_y(Y)$ - Error motion in Y as a function of Y position

$\delta_z(Y)$ - Error motion in Z as a function of Y position

ε_x - Rotation of (O_1) with respect to (O) about X_0 (Carriage Pitch)

ε_z - Rotation of (O_1) with respect to (O) about Z_0 (Carriage Yaw)

Y_P - Distance in Y between $Y_0 = 0$ and the plasmonic lens in (O)

6.5.2 Systematic Errors

6.5.2.1 Environmental Errors

The carriage motion is monitored by two 5-nm resolution scales on both sides. Figure 134 shows the location of one of the Renishaw™ scales on the PLM.

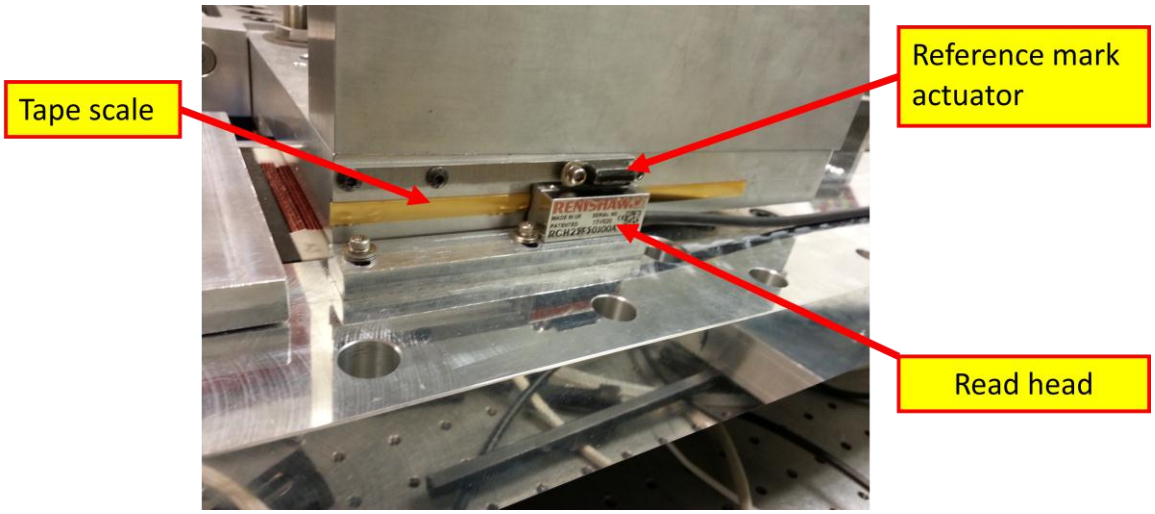

Figure 134: Location of Renishaw™ scale on the PLM.

Temperature variation can affect the uncertainty of the carriage position along the travel length. Considering (at the home position and with servo control on) the distance from the plasmonic lens slider to the read heads length is about 251 mm as shown in Figure 135, for 1°C temperature increase the carriage will expand (in the travel direction) about 5.9 µm.

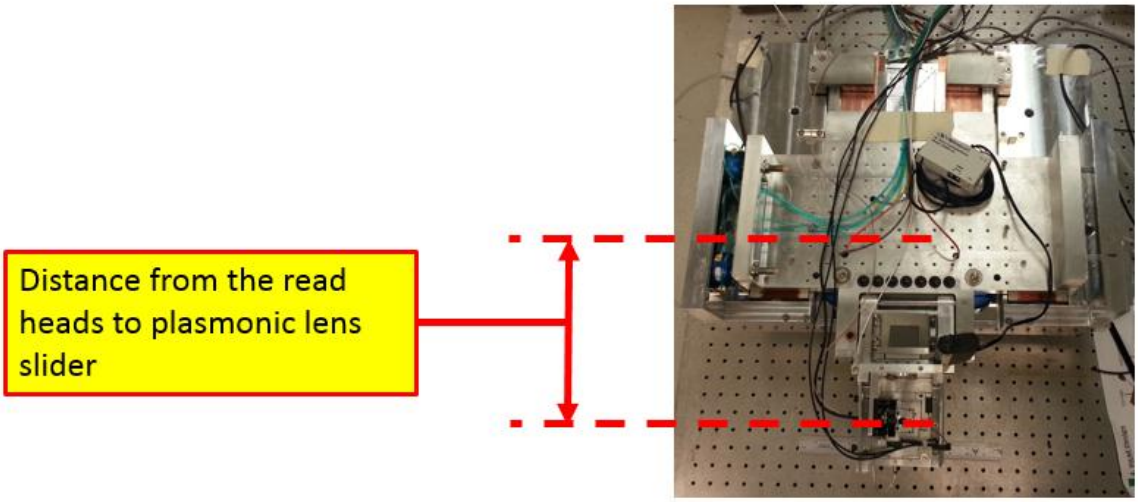

Figure 135: Distance from the read heads to the plasmonic lens slider.

This error affects the translation measurements of the carriage along the Y axis, i.e., $\delta y(Y) = 5.9\ \mu m$.

Also, the PLM is coupled with the spindle using an Al 6061 plate. This plate is designed to simplify the thermal growth so we do not get bimetal effects with the steel optical table. Figure 136 shows the distance from the spindle center to the center of front leveling feet and the distance from the read heads to the plasmonic lens slider.

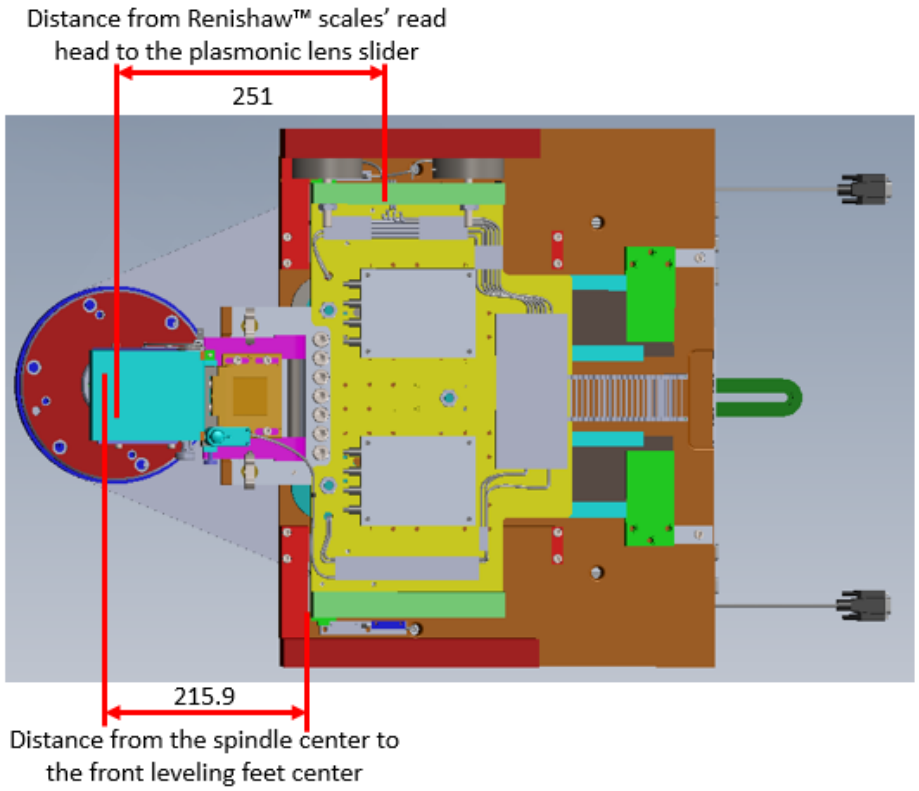

Figure 136: Illustration of the distance from the spindle center to the center of front leveling feet and the distance from the read heads to the plasmonic lens slider.

The thermal expansion error of the interferometer is neglected as the distance between the fiber optic cables and the mirrors attached to the plasmonic lens slider is about 1 mm. Also, the thermal expansion of the cap gages and piezoelectric actuators is neglected, as they are used only during the pre-writing adjustments.

6.5.2.2 Form Errors

The PLM has five air bearings, three under the carriage and two at the side. These air bearings fly over diamond-turned surfaces with flatness of about λ/4 (about 75 nm)

over the entire surface. The location of the air bearings in the X direction is shown in Figure 137.

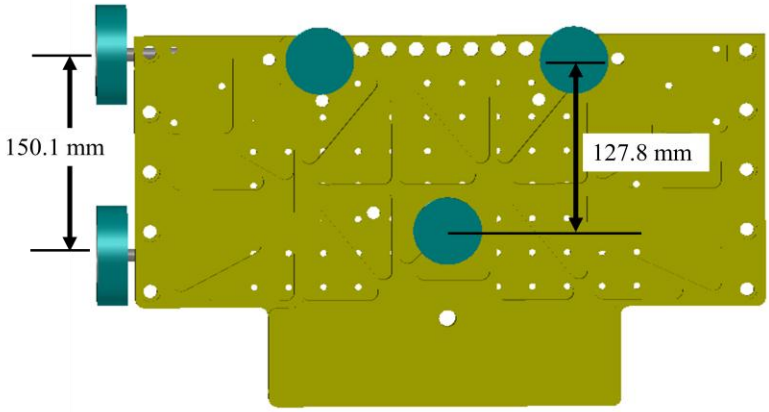

Figure 137: Air bearings location on the carriage.

Based on this configuration, the flatness error can cause pitch errors of 2.3 µrad, and yaw error of 2.0 µrad (i.e., ε_x = 2.3 µrad and ε_z = 2.0 µrad). Also, based on a travel length of 39.0 mm and the estimated angular deviation (ε_x and ε_z), the $\delta_x(Y)$ and $\delta_z(Y)$ can be estimated as 300 nm and 91 nm, respectively. It is important to mention here that Z is an insensitive direction as any deviation in this direction will be compensated by the slider.

6.5.3 Error Budget

The following table shows the PLM uncorrected error budget. Kang Ni is thermal modeling the PLM and he will perform full calibration of the machine which will be software corrected at Berkeley by the UCLA team who are building the controller. The final error results will be part of Mr. Ni's thesis.

Table 6: PLM Uncorrected Error Budget

$\delta_y(Y)$	=	5.9 μm	μm
$\delta_x(Y)$	=	300.0	nm
$\delta_z(Y)$	=	91.0	nm
ε_x	=	2.3	μrad
ε_z	=	2.0	μrad

The calibration parameters that Mr. Kang Ni will measure are [Ni, 2012]

1) Linear positioning

2) Straightness

3) Pitch

4) Yaw

In the following chapter the system integration will be discussed to show the general configuration of the PLM motions and control.

CHAPTER 7: SYSTEM INTEGRATION AND CONTROL

The PLM original control layout is designed by Kevin Chou and implemented by Yen Chi Chang from the University of California at Los Angeles (UCLA). A Labview® package has been used to monitor and control the machine. In order to clarify the main functions of the PLM system a simplified the system schematic developed by Kevin Chou is shown in Figure 138.

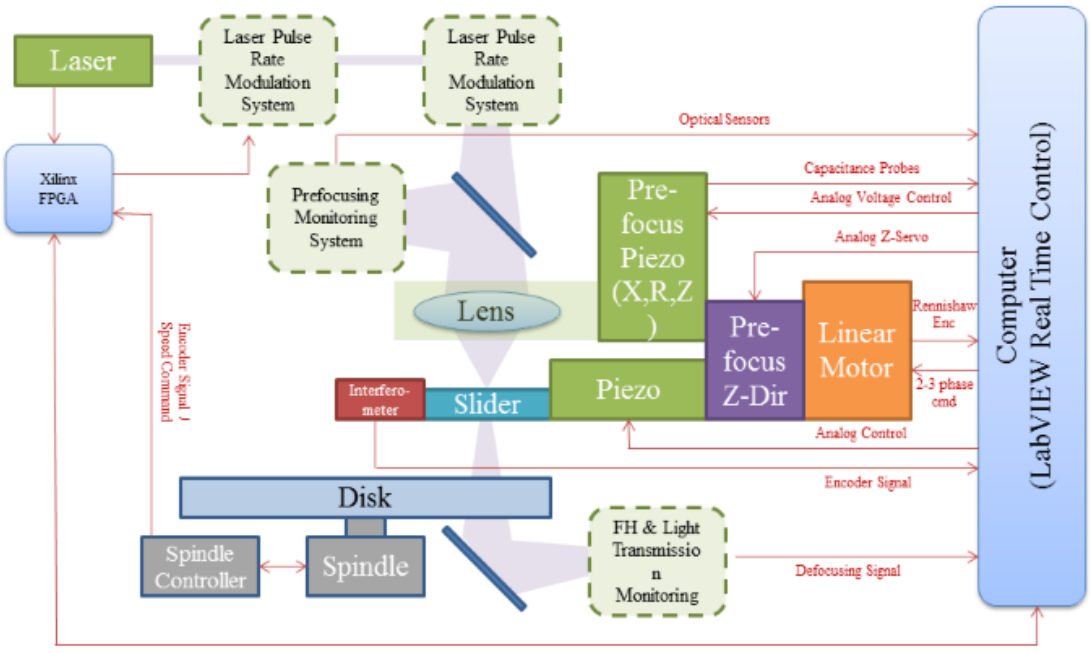

Figure 138: PLM monitor and control system schematics (simplified version based on [Chou, 2011]).

The disc typical spinning speed is 1000 RPM. This spinning motion is provided by a high-precision pneumatic spindle and monitored by an electromagnetic encoder. The

PLM provides a linear motion of the plasmonic lens slider in the radial/off-track (R) direction using Halbach motors. The plasmonic lens slider is monitored using laser diode interferometers and its position is adjustable using a two-dimensional shear actuator. The prefocusing lens is adjustable in the X, R, and Z directions using piezoelectric actuators (in addition to the coarse mechanical adjustment devices). The prefocusing is monitored using an optical sensor (developed at UC Berkeley), and the control software can determine control signals to be applied on the prefocusing piezoelectric actuators.

The plasmonic lens slider position is measured by 5-nm resolution Renishaw encoders on both sides of the carriage, and based on this measurement and the required motion parameters the control software determines the Halbach motor control signals. The laser pulse rate modulation system is necessary to adjust the UV laser pulse rate based on the spindle spinning speed monitoring signal (measured by the electromagnetic encoder) and the set lithography pattern parameters defined by the PLM user using a software package. In order to achieve an accurate pattern, the carriage off-track motion parameters must be synchronized with the disk spinning speed and the UV laser pulse rate.

CHAPTER 8: CONCLUSIONS AND FUTURE WORK

8.1 Conclusions And Future Work

The design, analysis and assembly of the Plasmonic Nanolithography Machine (PLM) were discussed in this thesis. The first chapter introduced the research problem and explained the project goals. The PLM features and specifications were discussed in the second chapter. In the third chapter a detailed description of the PLM mechanical design was introduced. Chapter 4 contains details about Halbach array linear motors, eddy current dampers, sensors and actuators.

It was important to perform dynamic and thermal tests on key components before starting the machine assembly. A summary of the tests performed is introduced in Chapter 5 followed by Chapter 6, which illustrates the PLM assembly process. In Chapter 7 the system integration is discussed showing different aspects of hardware/software interfaces.

The diode laser interferometer development is the subject of a separate thesis [Hughes, 2012]. Further, the machine control and its calibration and installation at UC Berkeley will also be the subject of a separate thesis.

During the assembly process it was clear that the accessibility of small items, such as linear scales, read heads, and reference mark actuators, was low and consumed much time to put these items in place and to tune them. It is recommended that the second generation of PLM, if there is one, have better access to all items.

The stators' coils assembly took a long time and effort from John Brien because the inlet and outlet wires for all coils were in the middle instead of having one location for each phase (for example, right, center, and left). Also, it is necessary to inform the wire winders to get the inlet and outlet wires ready to attach as it takes long time to finish this process. These changes are being made on motors being manufactured for Dr. José Yague-Fabra of the University of Zaragoza on a joint project with the Center for Precision Metrology to build a long-range atomic force microscope.

REFERENCES

Austin, M. D., Zhang, W., Ge, H., Wasserman, D., Lyon, S. A., and Chou, S. Y., 6 nm half-pitch lines and 0.04 μm2 static random access memory patterns by nanoimprint lithography, Nanotechnol. 16, 1058-61, 2005.

Bae, J. S., Kwak, M. K., and Inman, D. J., Vibration suppression of a cantilever beam using eddy current damper, J Sound and Vib. 284, 805-24, 2005.

Braun, A. E., Nanoimprint Litho Ramps for HDDs, CMOS, Semiconduct. Intl., 2008.

Broers, A. N., Harper, J. M., and Molzen, W. W., 250-A˚ linewidths with PMMA electron resist, Phys. Lett. 33, 392, 1978.

Chou, Kevin, SINAM IRG 1 video conference presentation, 2011.

Chou, S. Y., et al., Sub-10 nm imprint lithography and techniques, J. Vac. Sci. Technol. B 15, 6, 1997.

Chou, S. Y., Krauss, P. R., and Renstrom, P. J., Imprint of sub 25-nm Vias and Trenches in Polymers, App. Phys. Lett. 67, 21, 3114-16, 1995.

Chou, Stephen Y., Krauss, Peter R., and Renstrom, Preston J., Nanoimprint lithography, J. Vac. Sci. Tech. B 14(6), 1996.

Davis, L. C., and Reitz, J. R., Eddy Currents in Finite Conducting Sheets, J. Appl. Phys. 42, 11, 1971.

Dexter™ : http://www.dextermag.com/

Dummer, G.W.A., Progress in Quality Electronic Components, Proc. IRE, Washington, DC, 1952.

Early, K., Schattenburg, M. L., and Smith, H. I., Absence of resolution degradation in X-ray lithography for λ from 4.5nm to 0.83nm, Microelectronic Eng. 11, 317, 1990.

Fairley, P., 10 emerging technologies that will change the world, Technol. Rev., Cambridge, MA, 2003.

Fesperman, R. R., Multi-Scale Alignment Positioning System, Ph.D. Dissertation, UNC Charlotte, 2006.

Fesperman, Ronnie, Hocken, Robert J., et al., Multi-scale Alignment and Positioning System – MAPS, Prec. Eng. 36, 4, 517-37, 2012.

Fischer, P. B., Chou, S. Y., 10 nm electron beam lithography and sub-50 nm overlay using a modified scanning electron microscope, Appl. Phys. Lett. 62, 2989, 1993.

Gwyn, C. W., Stulen, R. H., Sweeney, D. W., and Atwood, D. T., Extreme ultraviolet lithography, J. Vac. Sci. Technol. B, 16, 3142-49, 1998.

Halbach, K., Design of permanent multipole magnets with oriented rare earth cobalt material, Nucl. Instr. & Methods 169, 1-10, 1980 (doi: 10.1016/0029-554X(80)90094-4, ISSN 0029-554X).

Hale, L. C., Principles and Techniques for Designing Precision Machines, Ph.D. Dissertation, MIT, 1999.

Hand, A., Toshiba validates imprint lithography for <32nm, Semiconduct. Intl., 2007.

Hazelton, A. J., Wafer table for immersion lithography, U.S. Patent #7,301,607, 2007.

Hiroshi, T., Electron beam lithography apparatus, U.S. Patent #6,730,916, 2004.

Hocken, R. J., Fesperman, R. R., Overcash, J. L., Ozturk, O., and Stroup, C. G., Engineering Nanotechnology: The top down approach, 8th Int. Symp. on Meas. Tech. and Intelligent Instr., Sendai, Japan, 2007.

Hocken, R. J., Trumper, D. L., and Wang, C., Dynamics and Control of the UNCC/MIT Sub-Atomic Measuring Machine, Annals of CIRP 50/1, 373-376, 2001.

Holmes, et al., The long-range scanning stage: A novel platform for scanned-probe microscopy, Prec. Eng. 24, 3, 191-209, 2000.

Holmes, Michael L., Analysis and Design of a Long Range Scanning Stage, Doctoral Dissertation, UNC Charlotte, 1998.

Hughes, Christopher V., A miniature fiber optic interferometer for measuring the motion of plasmonic writing heads, Master's Dissertation, UNC Charlotte, 2012.

Huha, Sungrnin, Keameya, Patrick, et al., EUV Actinic Defect Inspection and Defect Printability at Sub-32 nm Half-pitch, EMLC, Germany, 2009.

Kik, P. G., Maier, S. A., and Atwater, H. A., Plasmon printing – a new approach to near-field lithography, Mat. Res. Soc. Symp. Proc. 705, Y3.6, 2002.

Kilby, J. S., Miniaturized electronic circuits, U.S. Patent #3,138,743, 1964.

Kim, J. J., Jeong, Y. H., and Cho, D. W., Thermal behavior of a machine tool equipped with linear motors, Int. J of Mach. Tools & Manufact. 44, 749-758, 2004.

Kim, W. J., High-precision planar magnetic levitation, Ph.D. Dissertation, MIT, 1997.

Kim, W., Verma, S., and Shakir, H., Design and precision construction of novel magnetic-levitation-based multi-axis nanoscale positioning systems, Prec. Eng. 31, 337-350, 2007.

Lawrence Livermore National Laboratory (LLNL) Science and Technology Review, 1997 (http://www.llnl.gov/str/Sweeney.html)

Lee, K., and Park, K., Modeling eddy currents with boundary conditions by using Coulomb's law and the method of images, IEEE Trans. Magnetics 38, 2, 1333, 2002.

Lemmons, Tiffany D., Micro-fabrication of precision components, Master's Dissertation, UNC Charlotte, 2012.

Liu, Zhao-Wei, Wei, Qi-Huo, and Zhang, Xiang, Surface Plasmon Interference Nanolithography, Nano Lett. 5, 5, 957-961, 2005.

Luo, X., and Ishihara, T., Surface plasmon resonant interference nanolithography technique, Appl. Phys. Lett. 84, 4780, 2004.

Luo, Xiangang, and Ishihara, Teruya, Subwavelength photolithography based on surface-plasmon polariton resonance, Opt. Exp. 12, 14, 3055-65, 2004.

Military Handbook MIL-HDBK-5H: Metallic Materials and Elements for Aerospace Vehicle Structures (Knovel Interactive Edition), U.S. Dept. of Defense, 2003.

Newport© vibration isolation table, 2013 (www.newport.com/Vibration-Isolator-Selection-Guide/168531/1033/content.aspx)

Newport: www.newport.com

NewWay air bearings: http://web.newwayairbearings.com/bid/94248/Surprise-Vacuum-Preloaded-Air-Bearings-Provide-High-Damping

Nguyen, T. H., Automatic controls for precision magnetic suspension linear motor, M.S. Thesis, UNC Charlotte, 1994.

Ni, Kang, and Hocken, Robert J., Design and Model of a Dimensional Metrology System for Plasmonic Nano Lithography Machine, Poster, ASPE Ann. Mtg., San Diego, CA, 2012.

Nieuwelaar, V. D., Lithographic apparatus, computer program, device manufacturing method, and device manufactured thereby, U.S. Patent #6,937,318, 2003.

Noyce, R. N., Semiconductor device-and-lead structure, U.S. Patent #2,981,877, 1961.

OptoSigma: www.optosigma.com

Ozturk, O., Brien, J. F., and Hocken, R. J., Damping and Homing in a Nanoimprinting Machine, ASPE Spring Top. Mtg. Prec. Mech. Des. & Mechatron. for Sub-50nm Semiconduct. Equip., Berkeley, CA, 2008.

Ozturk, O., Multi-scale alignment and positioning system II, Ph.D. Dissertation, UNC Charlotte, 2007.

Pendry, J. B., Negative Refraction Makes a Perfect Lens, Phys. Rev. Lett. 85, 3966-69, 2000.

Physik Instrumente™: http://www.physikinstrumente.com/

Pitarke, J. M., Silkin, V. M., Chulkov, E. V., and Echenique, P. M., Theory of surface plasmons and surface-plasmon polaritons, Rep. Prog. Phys. 70, 1-87, 2007 (doi: 10.1088/0034-4885-70-1-R01).

Raether, H., Surface Plasmons on Smooth and Rough Surfaces and on Gratings, Springer, Berlin, 1988.

Rao, Zhilong, Hesselink, Lambertus, and Harris, James S., High transmission through ridge nano-apertures on vertical-cavity surface-emitting lasers, Opt. Express 15, 16, 2007.

Reitz, J. R., Forces on Moving Magnets due to the Eddy Currents, J Appl. Phys. 41, 5, 1970.

Rogers, Edward T. F., Lindberg, Jari, et al., A super-oscillatory lens optical microscope for sub-wavelength imaging, Nature Matls. 11, 2012.

Rogers, Edward T. F., Zheludev, Nikolay I., et al., Sub-wavelength focusing meta-lens, arXiv:1211.1496, 2012.

Ruben, S. D., and Tsao, T-C., Motion Control for Nanolithography, ASPE 2008 Spring Top. Mtg., Prec. Mech. Des. & Mechatron. for Sub-50nm Semiconduct. Equip., Berkeley, CA, 2008.

Ruben, S. D., Modeling, control, and real time optimization for nano-precision system, Ph.D. Dissertation, University of California at Los Angeles, 2002.

Schellekens, P., Rosielle, N., Vermeulen, H., Vermeulen, M., Wetzels, S., and Pril, W., Design for Precision: Current Status and Trends, Annals of CIRP 47, 1998.

Schieber, D., Optimal Dimensions of Rectangular Electromagnet for Braking Purposes, IEEE Trans. Magnetics 11, 3, 948, 1975.

Silverman, J. P., X-ray lithography: Status, challenges, and outlook for 0.13 µm, J. Vac. Sci. Technol. B, 15, 6, 1997.

Simon, G., Haghiri-Gosnet, A. M., Bourneix, J., Decanini, D., Chen, Y., Rousseaux, F., Launois, H., and Vidal, B., Sub-20 nm x-ray nanolithography using conventional mask technologies on monochromatized synchrotron radiation, J. Vac. Sci. & Technol. B, 15, 6, 2489-94, 1997.

SINAM RG1 weekly video conference, 2009.

SINAM RG1 weekly video conference, 2011.

Smith, S. T., and Chetwynd, D. G., Foundations of Ultraprecision Mechanism Design, CRC Press, 2003.

Sodano, Henry A., and Bae, Jae-Sung, Eddy Current Damping in Structures, The Shock and Vibr. Digest 36, 6, 469-478, 2004.

Spears, D. L., Smith, H. I., High resolution pattern replication using soft X-rays, Electron. Lett. 8, 102, 1972.

Srituravanich, Werayut, Fang, Nichoas, Sun, Cheng, Luo, Qi, and Zhang, Xiang, Plasmonic Nanolithography, Nano Letters 4(6), 1085-1088, 2004.

Srituravanich, Werayut, Pan, Liang, Wang, Yuan, Sun, Cheng, Bogy, David B., and Zhang, Xiang, Flying plasmonic lens in the near field for high-speed nanolithography, Nature Nanotech. 3, 2008.

Stuart, C., Fabrication of three-dimensional organic crossbar circuits by Nanoimprint Lithography and Nanotransfer printing, Ph.D. Dissertation, University of California at Los Angeles, 2009.

Stulen, R. H., Sweeney, D. W., Extreme Ultraviolet Lithography, IEEE J Quant. Elec. 35, 5, 1999.

Suter Machine and Tool Co.: http://www.sutermachine.com/

Taniguchi, N., On the Basic Concept of 'Nano-Technology,' Proc. Intl. Conf. Prod. Eng., Tokyo, Part II, JSPE, 1974.

Thorlabs: http://www.thorlabs.com

Trumper, D. L., Magnetic suspension techniques for precision motion control, Ph.D. Dissertation, MIT, 1990.

Trumper, D. L., Williams, M.E., and Nguyen, T. H., Magnet arrays for synchronous machines, Proc. IEEE Ind. Appl. Soc. Ann. Mtg., Toronto, Canada, 1993.

Verma, S., Kim, W., and Jie, Gu, Six-Axis Nanopositioning Device with Precision Magnetic Levitation Technology, IEEE/ASME Trans. on Mechatronics 9, 2, 2004.

Wang, Zhiming M., Nanoscale Photonics and Optoelectronics: Sci. & Tech., 2010 (doi: 10.1007/978-1-4419-7587-4-2).

Wiederick, H. D., Gauthier, N., Campbell, D. A., and Rochon, P., Magnetic braking: Simple theory and experiment, Am. J Phys. 55, 6, 500, 1987.

Williams, M. E., Trumper, D. L., and Hocken, R. J., Magnetic Bearing Stage for Photolithography, Annals of the CIRP 42/1, 607-610, 1993.

APPENDIX A: PLM PARTS TECHNICAL DRAWINGS

1. Base

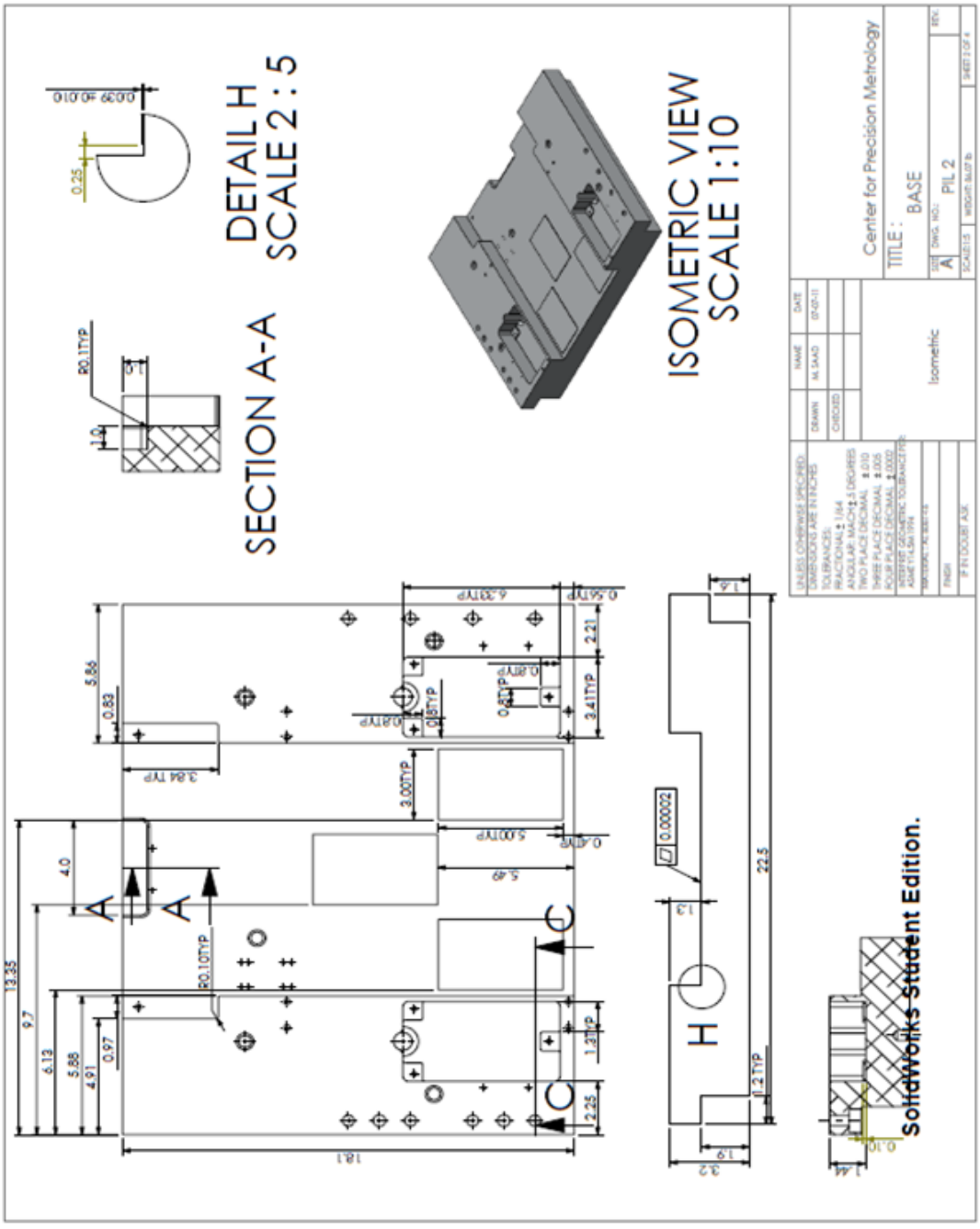

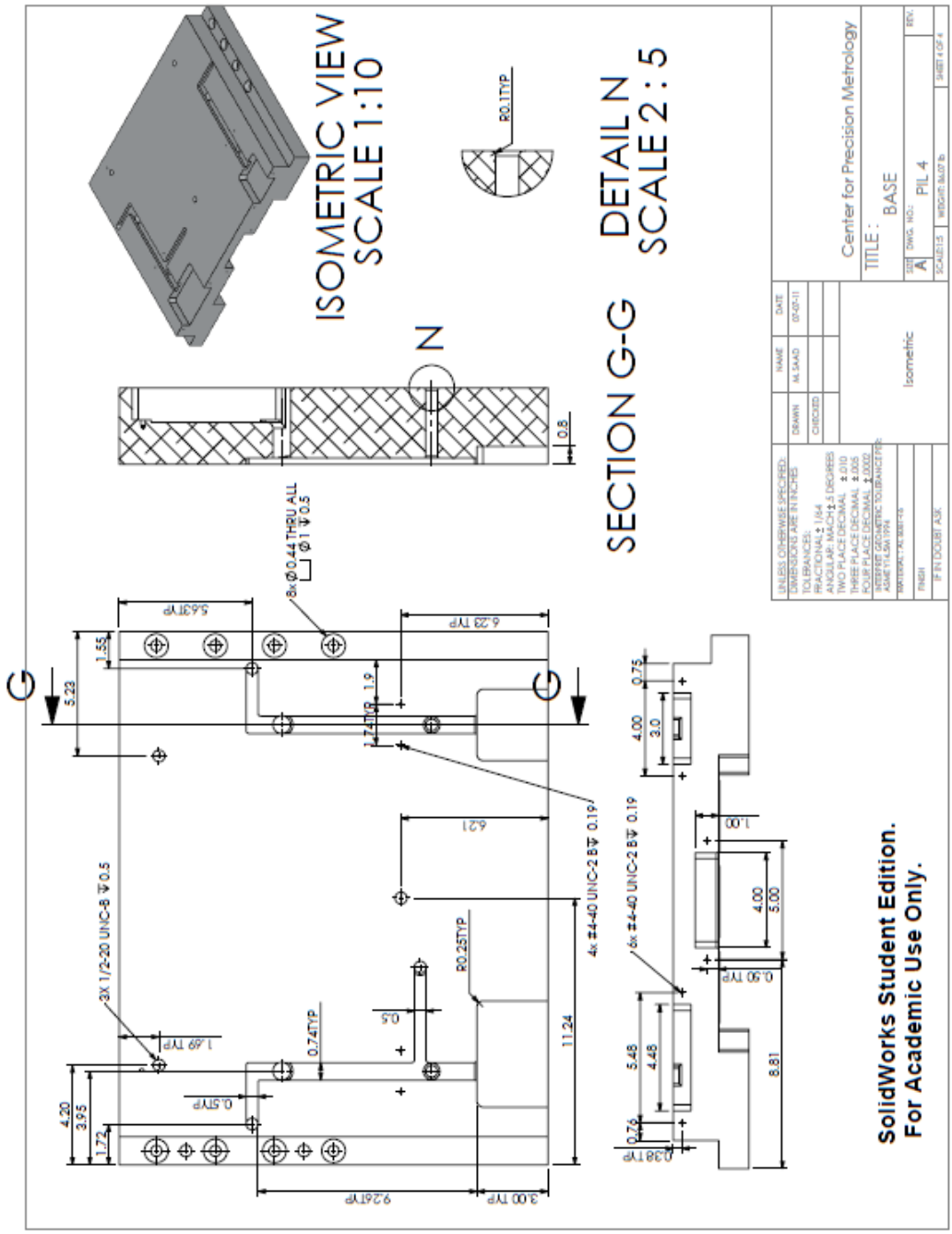
ISOMETRIC VIEW
SCALE 1:10
SECTION G-G
DETAIL N
SCALE 2 : 5
R0.17TYP
0.8
8x Ø0.44 THRU ALL
⌴ Ø1 ↧0.5
5.63TYP
6.23 TYP
1.55
5.23
1.9
1.7TYP
6.21
4x #4-40 UNC-2B↧ 0.19
3X 1/2-20 UNC-B ↧0.5
1.69 TYP
0.74TYP
0.5
R0.25TYP
0.57TYP
4.20
3.95
1.72
11.24
9.26TYP
3.00 TYP
6x #4-40 UNC-2B↧ 0.19
0.75
4.00
3.0
1.00
4.00
5.00
0.90 TYP
5.48
4.48
0.76
0.38 TYP
8.81
SolidWorks Student Edition.
For Academic Use Only.
UNLESS OTHERWISE SPECIFIED:
DIMENSIONS ARE IN INCHES
TOLERANCES:
FRACTIONAL ± 1/64
ANGULAR: MACH ± 5 DEGREES
TWO PLACE DECIMAL ± 0.10
THREE PLACE DECIMAL ± 0.005
FOUR PLACE DECIMAL ± 0.0020
INTERPRET GEOMETRIC TOLERANCING PER:
BREAK ALL SHARP EDGES
MATERIAL
FINISH
DO NOT SCALE DRAWING
DRAWN
CHECKED
NAME
DATE
M.SAAD
07-07-11
Isometric
Center for Precision Metrology
TITLE :
BASE
SIZE
A
DWG. NO.
PIL 4
REV
SCALE: 1:5
WEIGHT: 84.07 lb
SHEET 4 OF 4

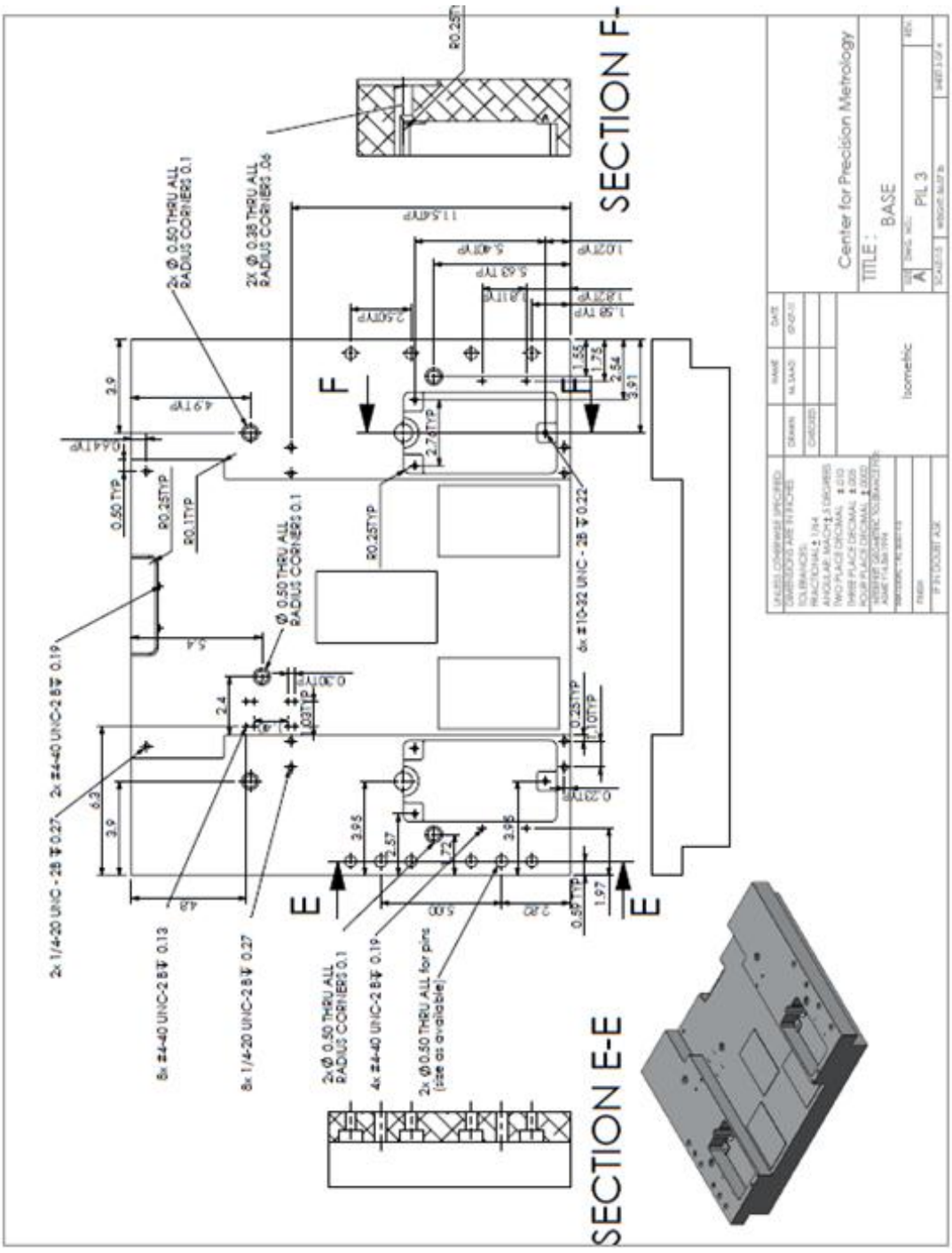
SECTION F-
SECTION E-E
Center for Precision Metrology
TITLE:
BASE
Isometric
PIL 3
A
2x Ø 0.50 THRU ALL RADIUS CORNERS 0.1
2x Ø 0.38 THRU ALL RADIUS CORNERS .06
Ø 0.50 THRU ALL RADIUS CORNERS 0.1
2x 1/4-20 UNC - 2B ▼ 0.27
2x #4-40 UNC-2B ▼ 0.19
8x #4-40 UNC-2B ▼ 0.13
8x 1/4-20 UNC-2B ▼ 0.27
2x Ø 0.50 THRU ALL RADIUS CORNERS 0.1
4x #4-40 UNC-2B ▼ 0.19
2x Ø 0.50 THRU ALL for pins (size as available)
4x #10-32 UNC - 2B ▼ 0.22

2. Carriage

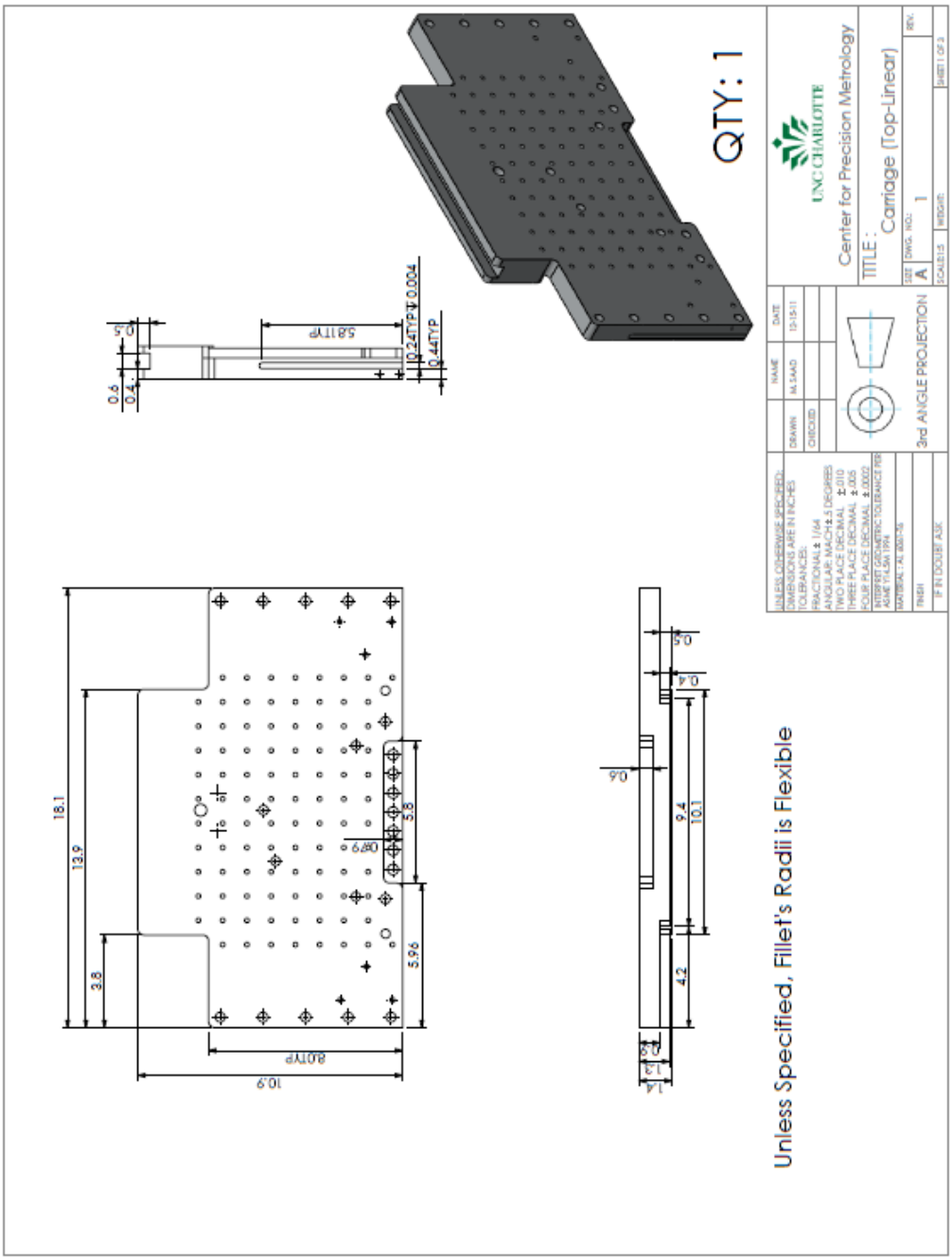
QTY: 1
UNC CHARLOTTE
Center for Precision Metrology
TITLE :
Carriage (Top-Linear)
3rd ANGLE PROJECTION
Unless Specified, Fillet's Radii is Flexible

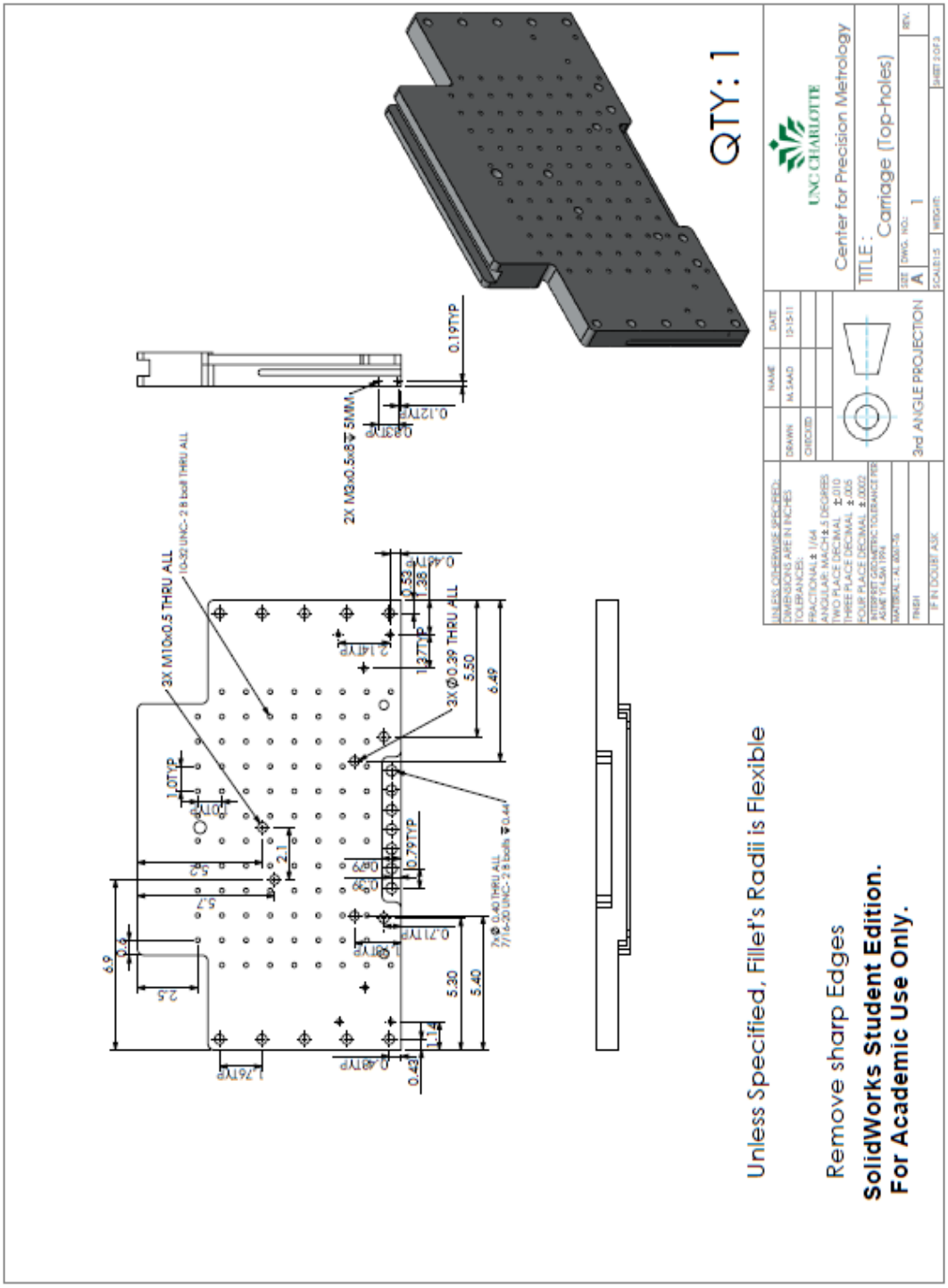
QTY: 1
UNC CHARLOTTE
Center for Precision Metrology
TITLE:
Carriage (Top-holes)
3rd ANGLE PROJECTION
Unless Specified, Fillet's Radii is Flexible
Remove sharp Edges
SolidWorks Student Edition.
For Academic Use Only.

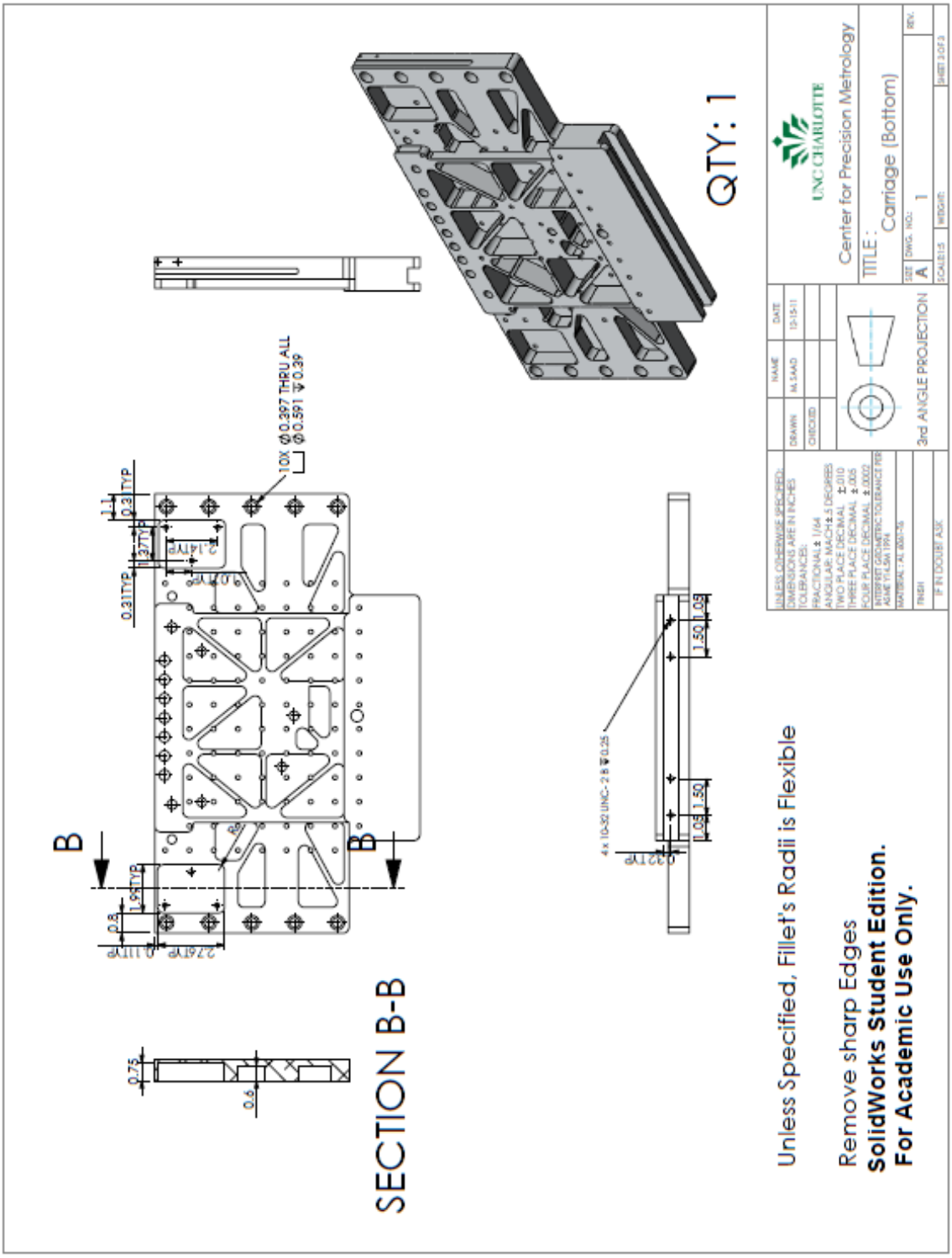
QTY: 1
UNC CHARLOTTE
Center for Precision Metrology
TITLE :
Carriage (Bottom)
3rd ANGLE PROJECTION
SECTION B-B
Unless Specified, Fillet's Radii is Flexible
Remove sharp Edges
SolidWorks Student Edition.
For Academic Use Only.

3. Base shoulder (air bearing side)

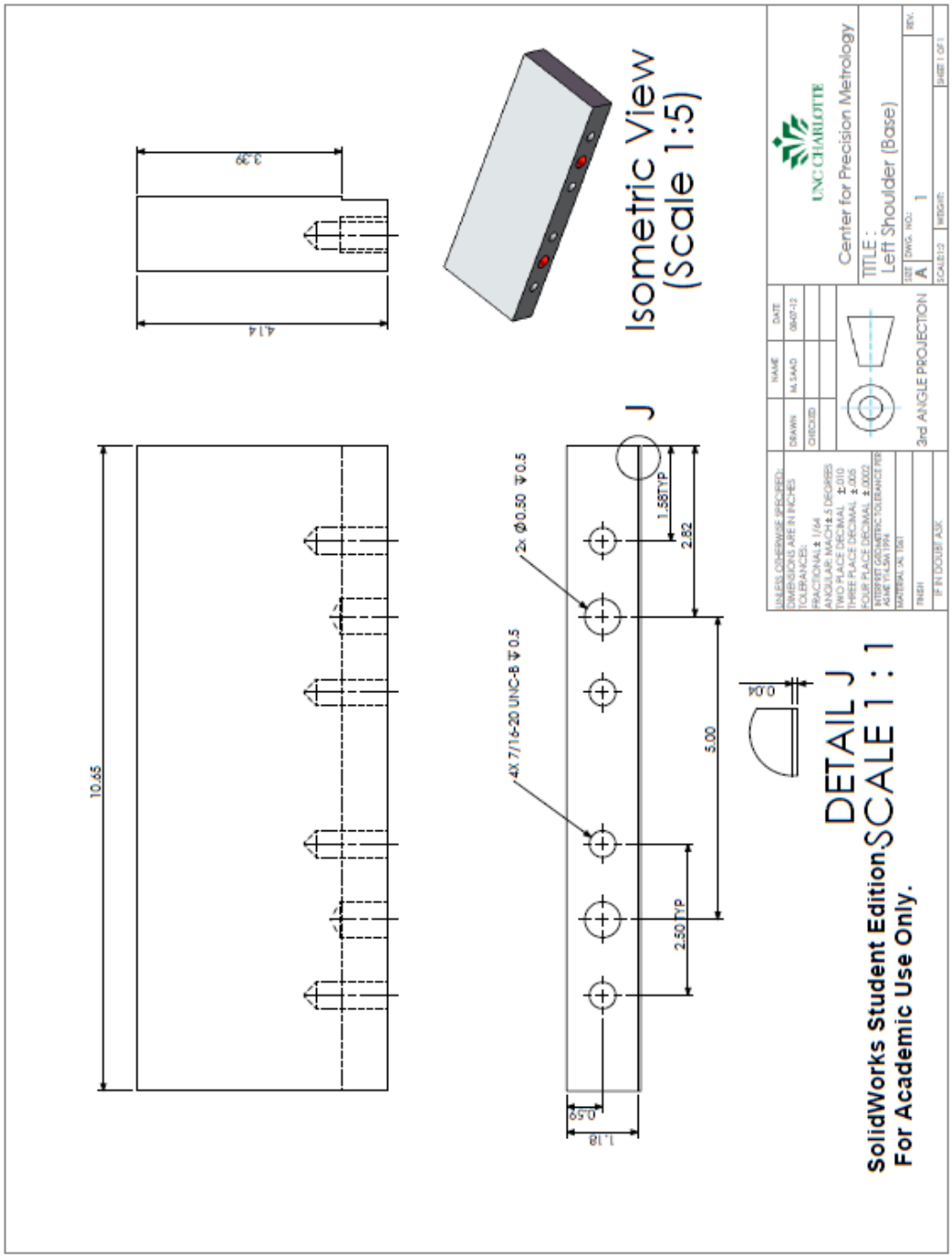

4. Base shoulder

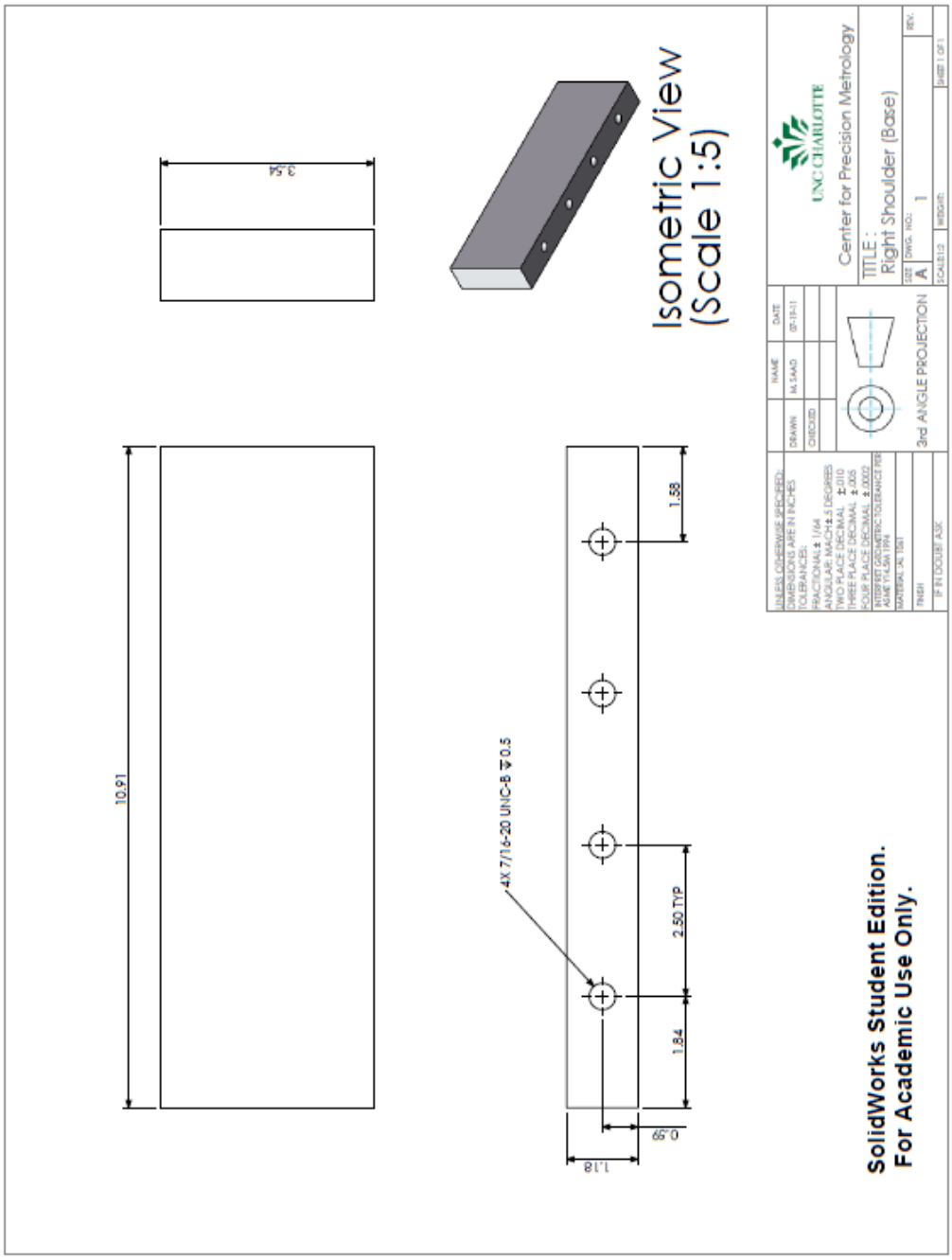

5. Carriage shoulder (air bearing side)

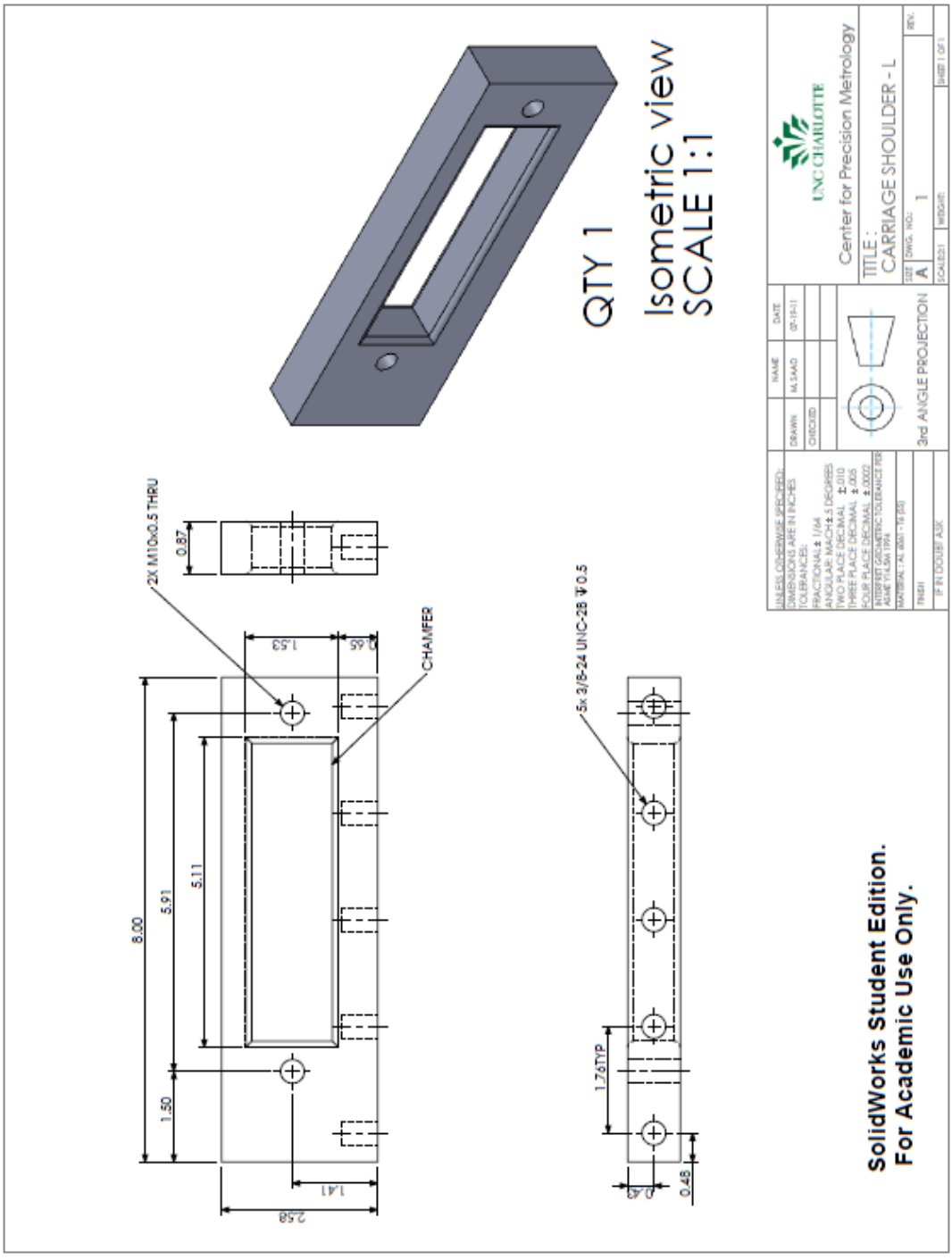

6. Carriage shoulder

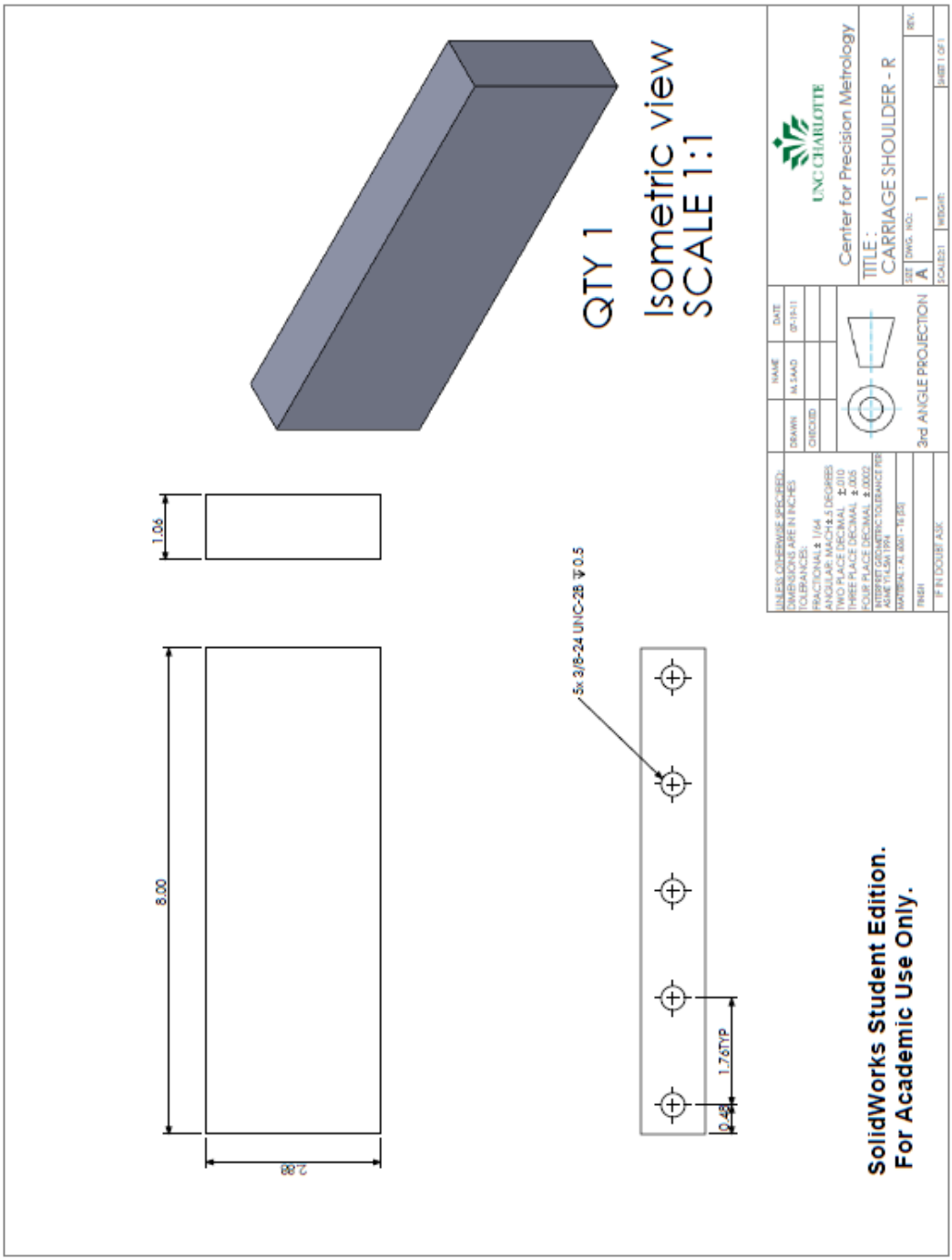

7. Main slider

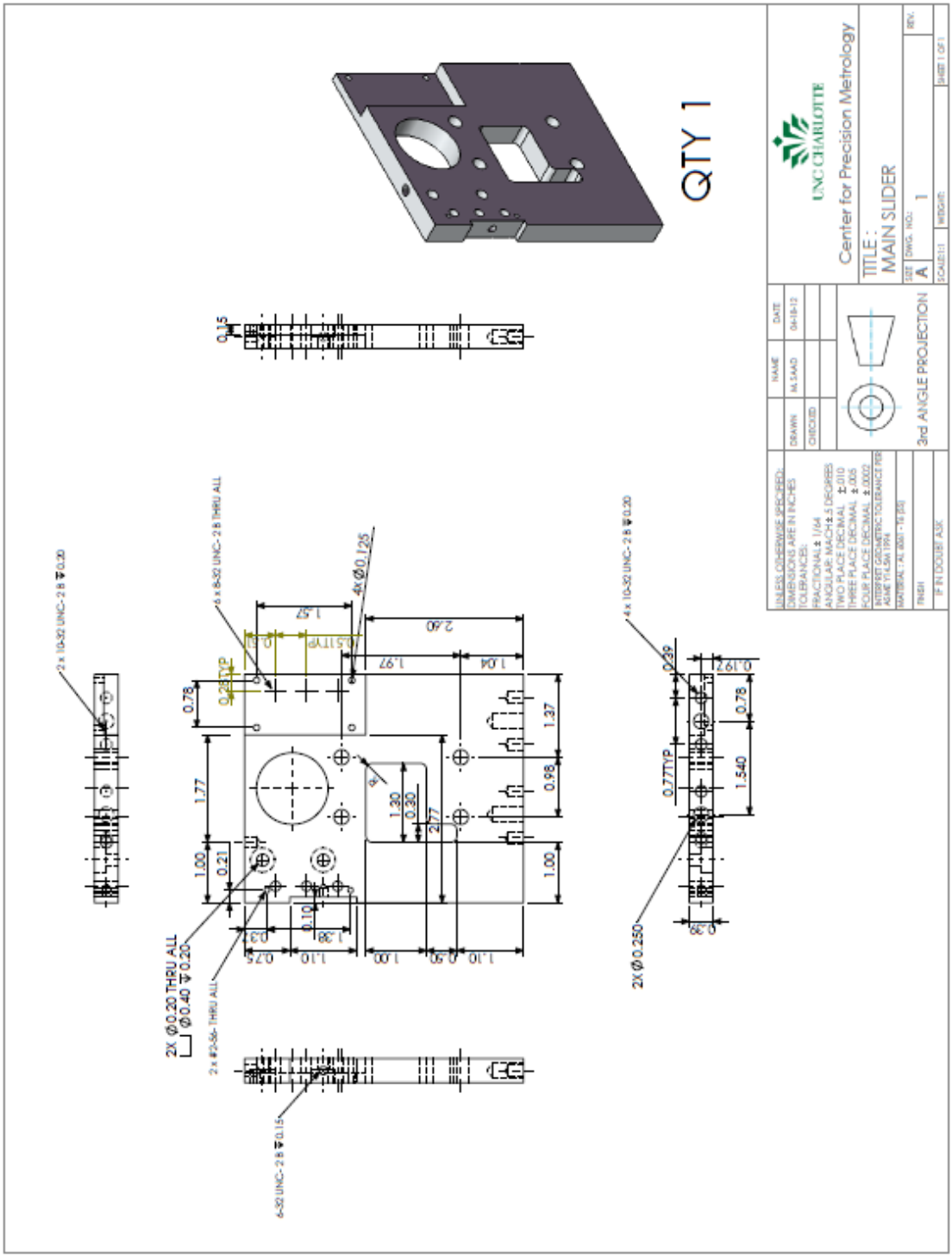

8. Prefocusing shoulder (rotation stage side)

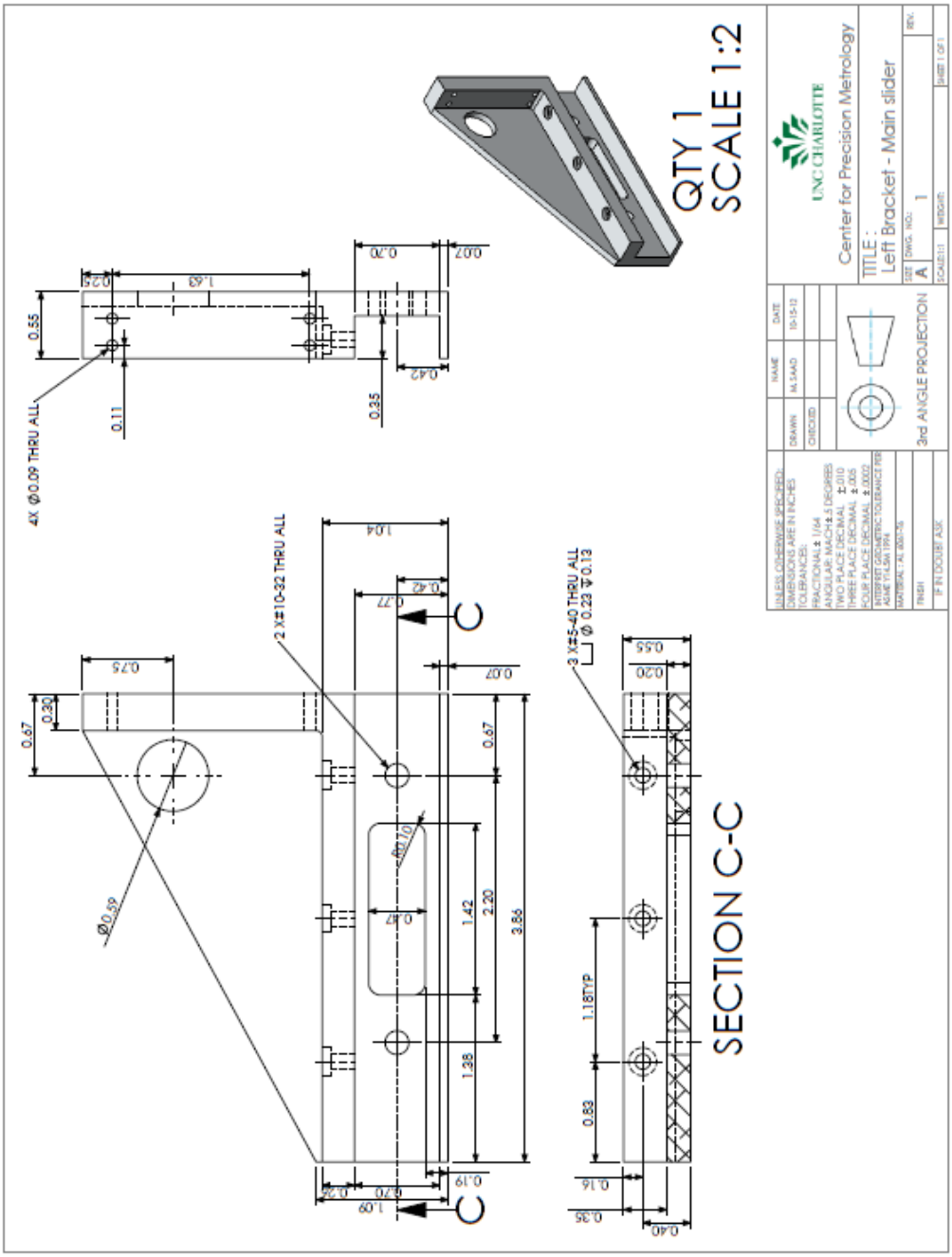

9. Prefocusing shoulder

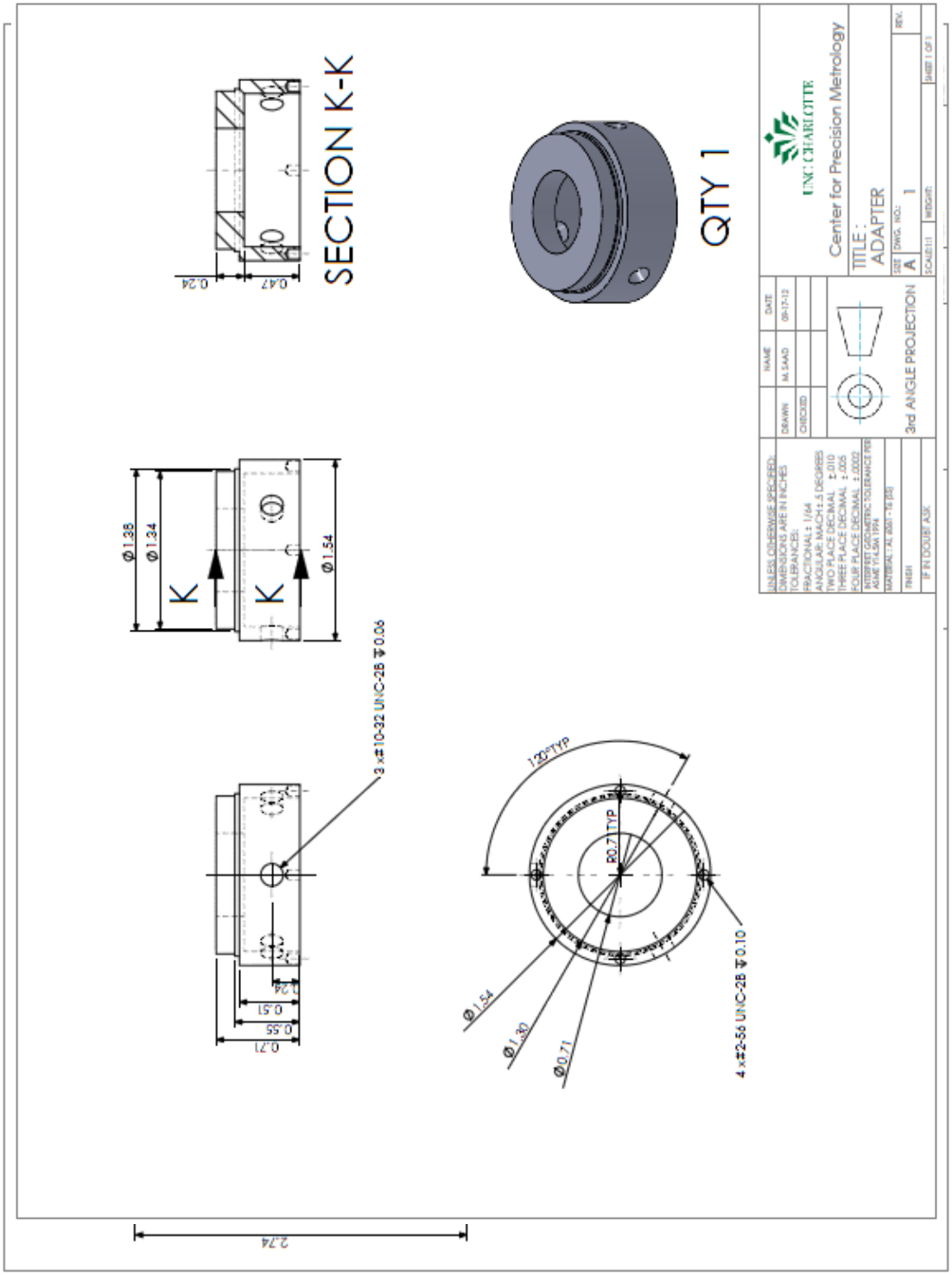

10. Frame (prefocusing lens coarse adjustment stage)

11. Disc (prefocusing lens coarse adjustment stage)

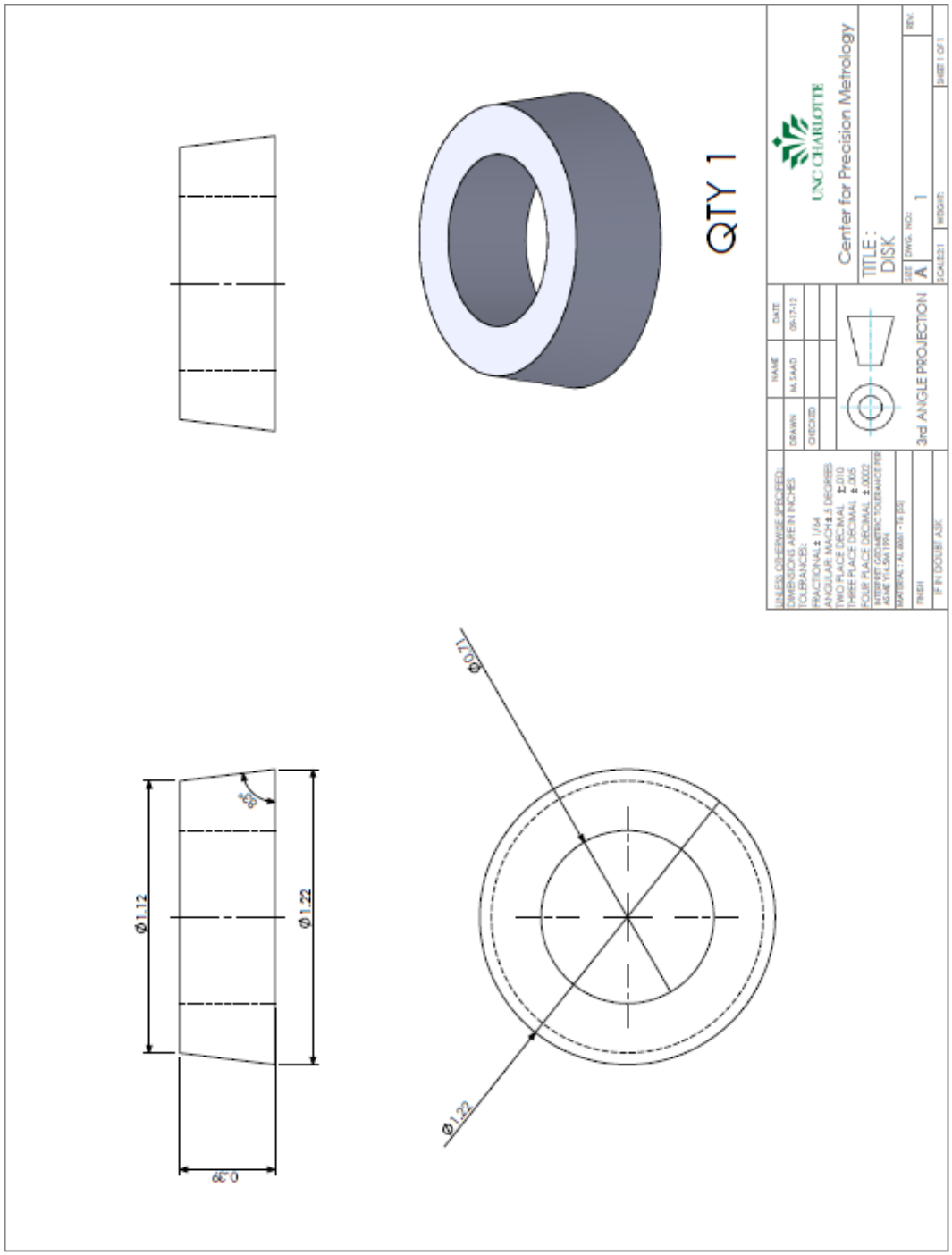

12. Cover (prefocusing lens coarse adjustment stage)

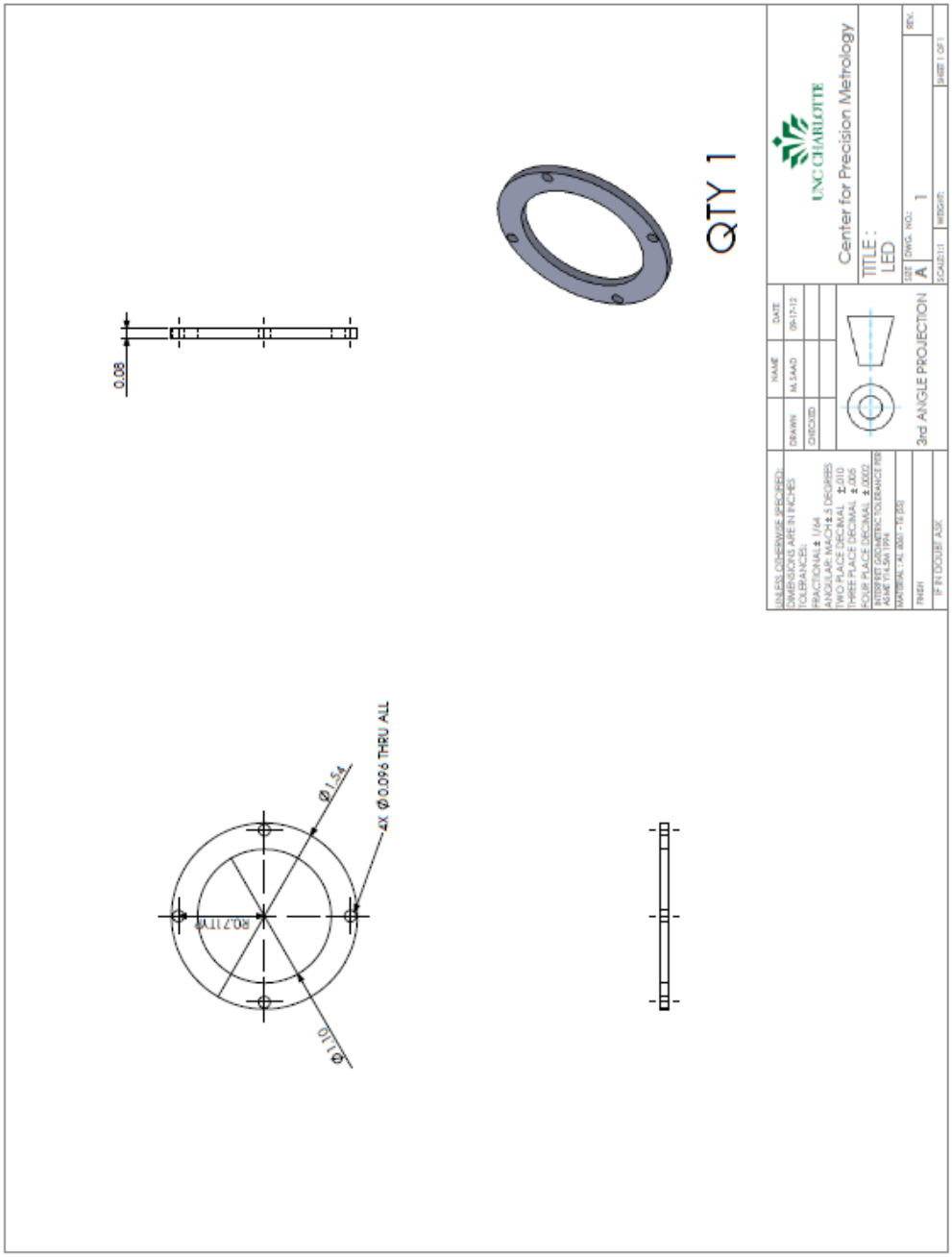

13. Motor magnet array housing

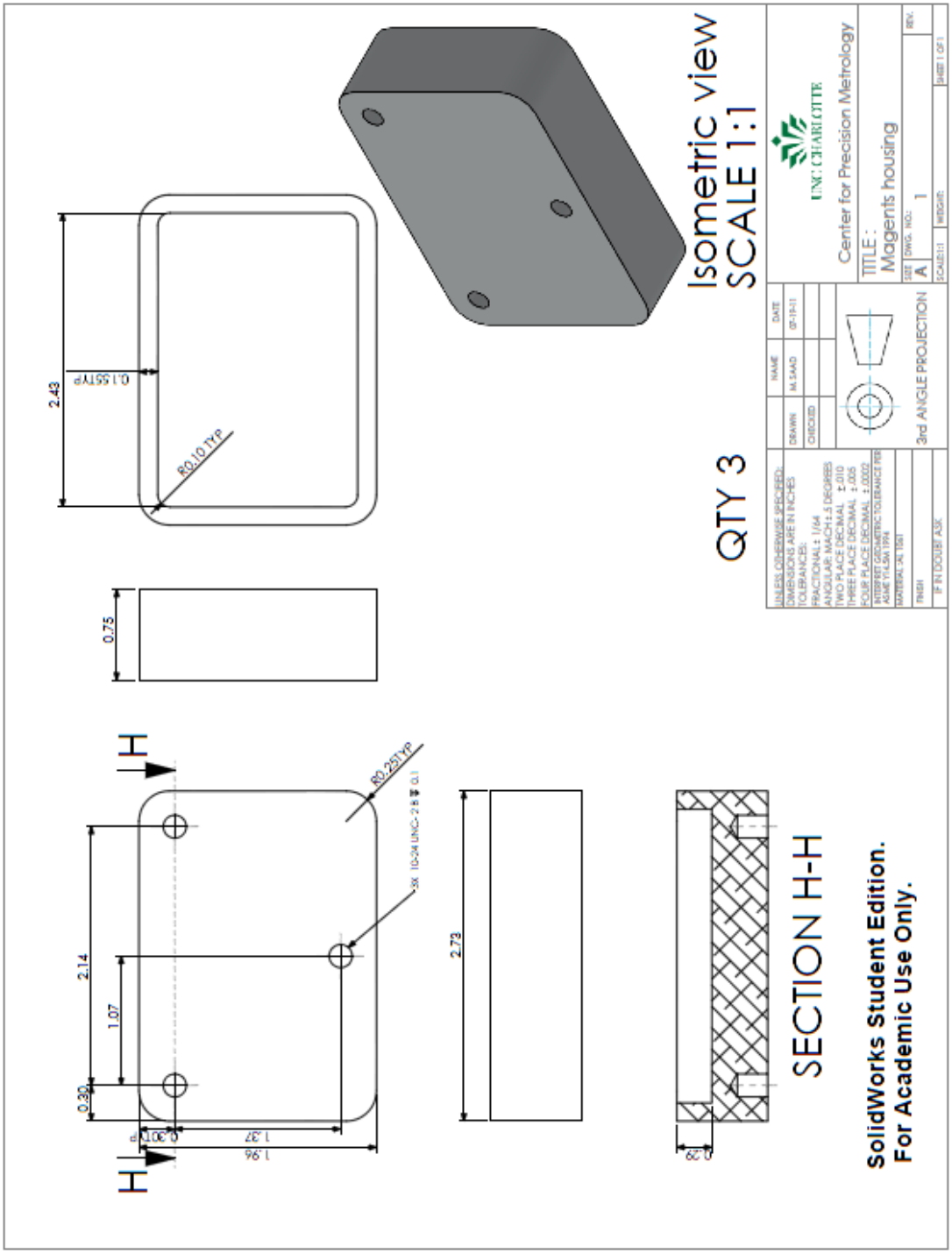

14. Stator mandrel

15. Stator end cap (cable outlet side)

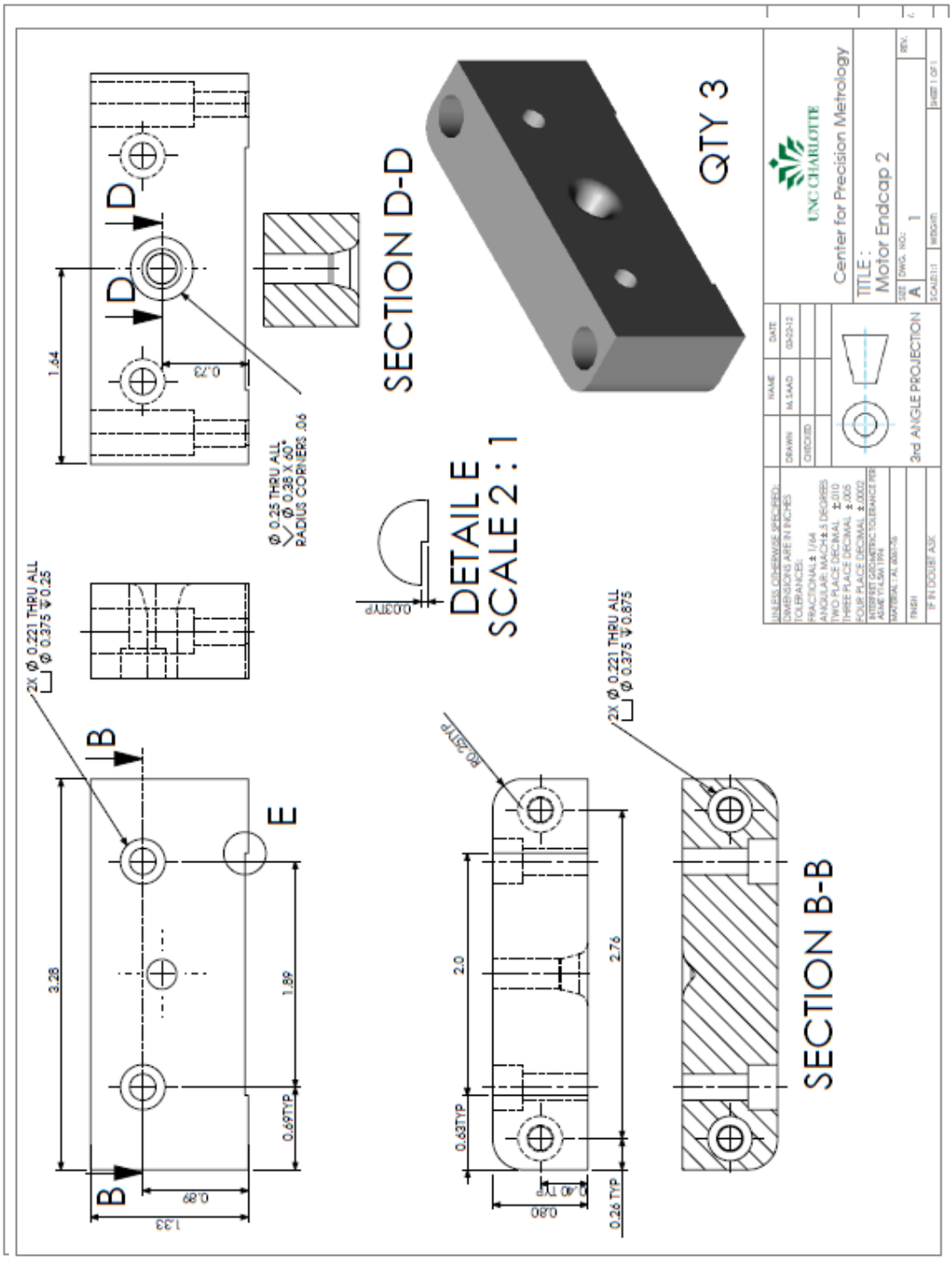

16. Stator end cap

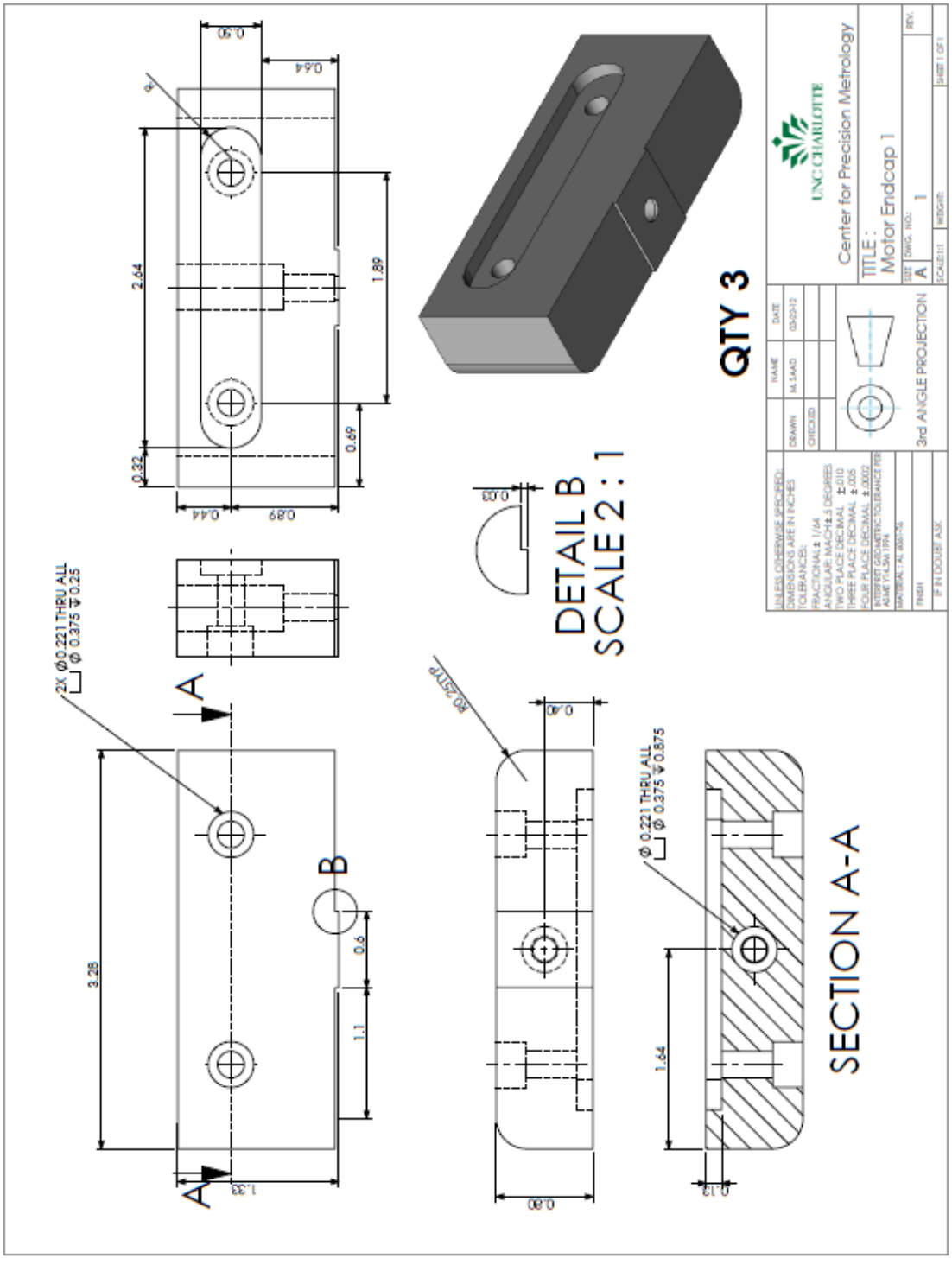

17. Suspension bracket

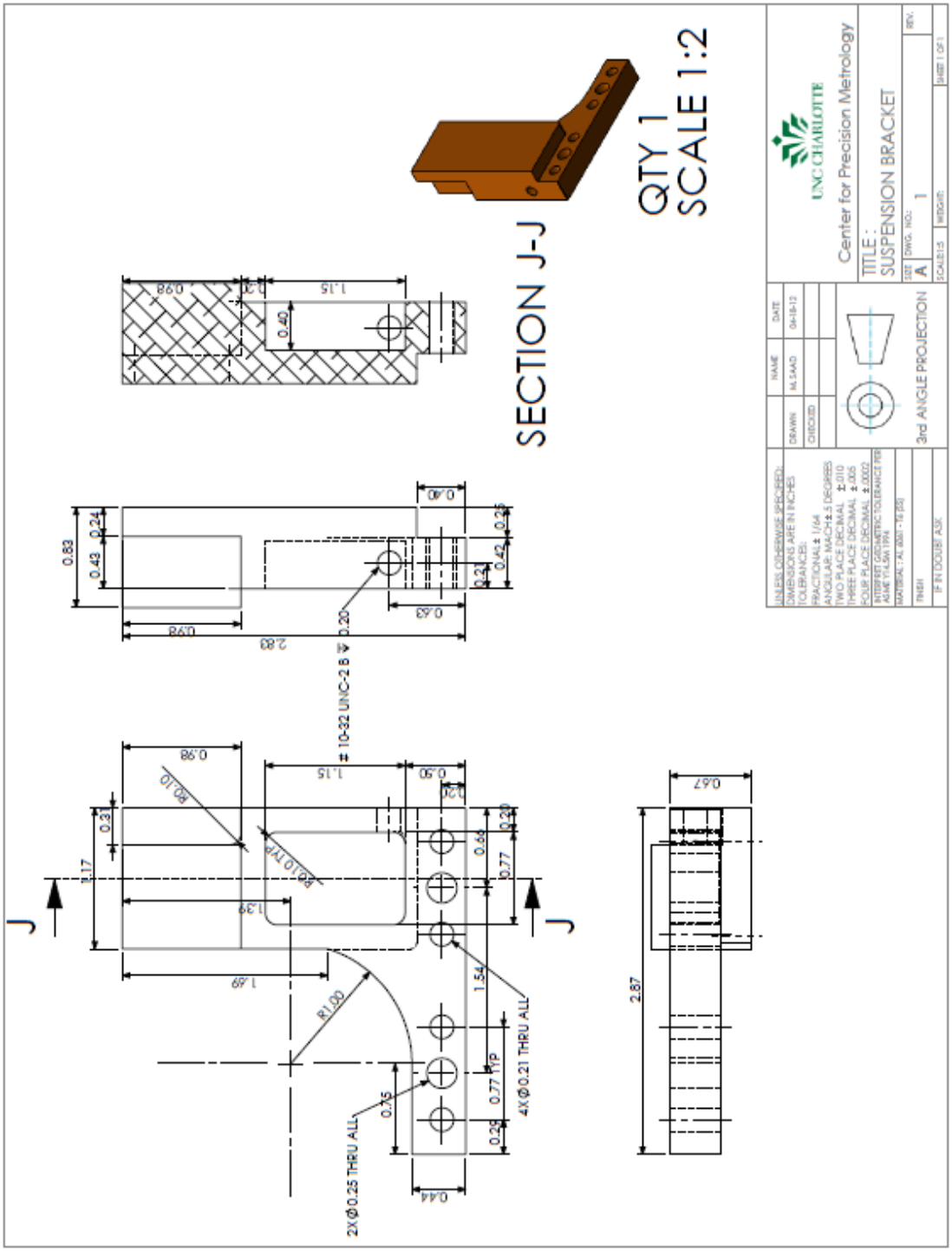

18. Rotation bracket

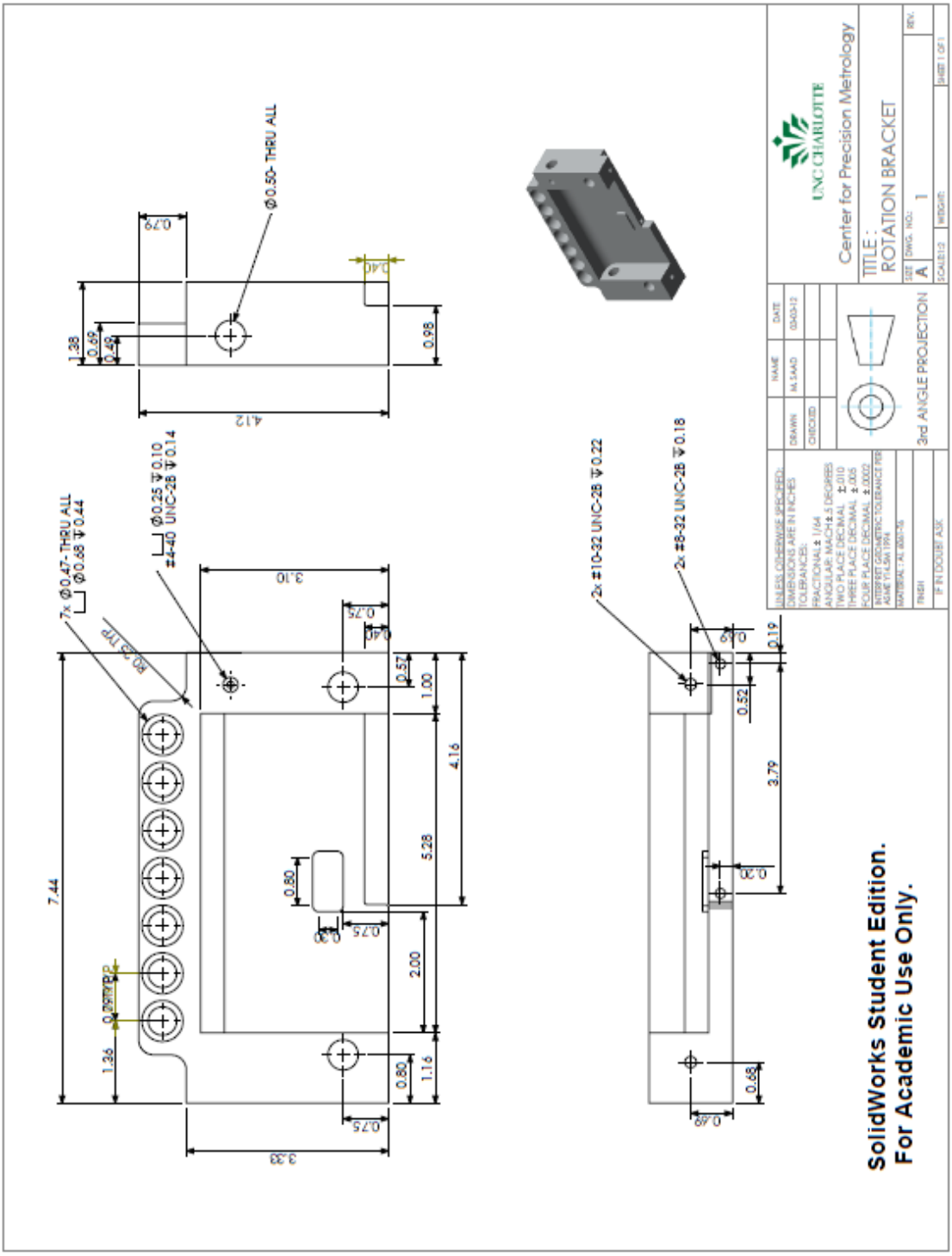

19. Rotation arm

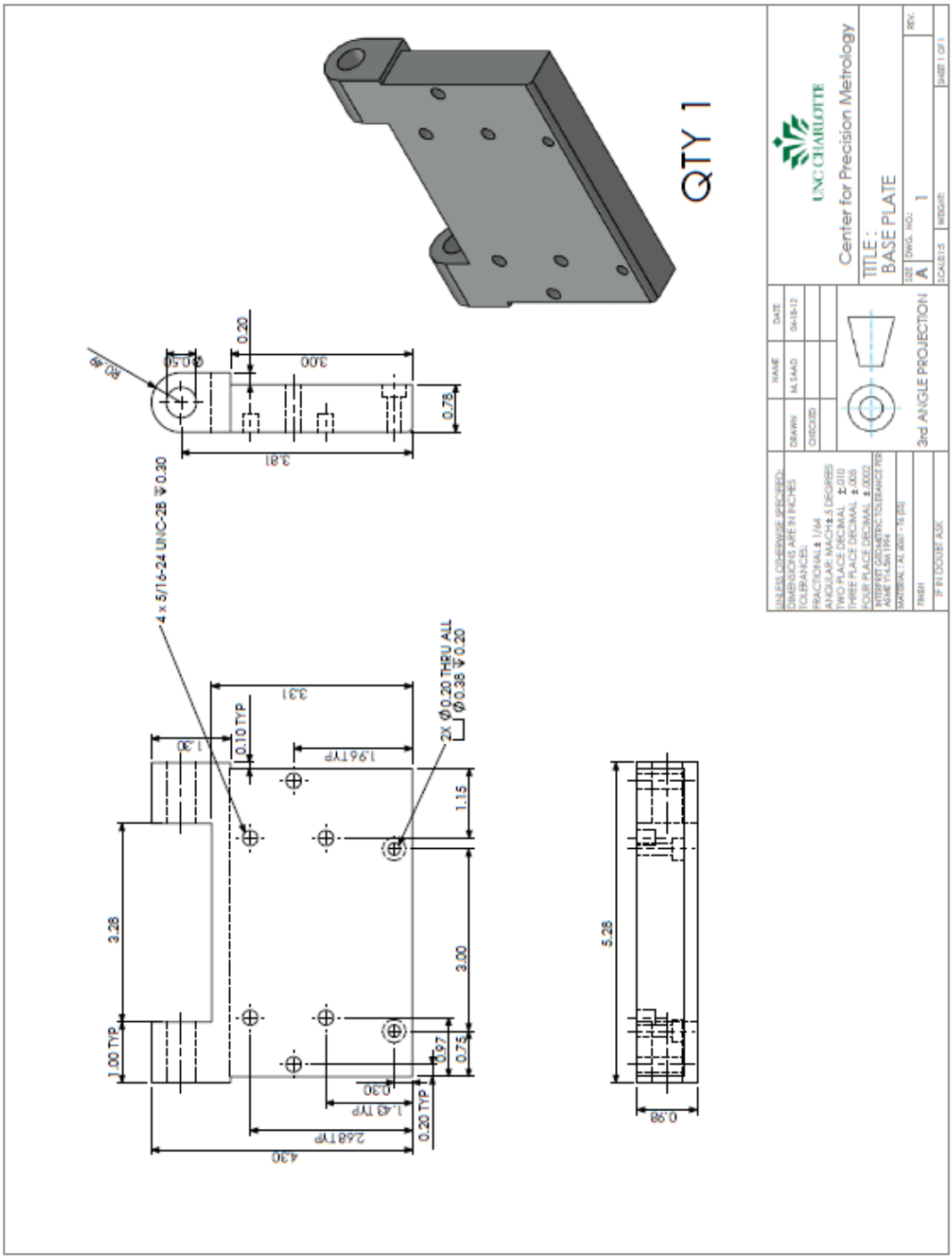

20. Rotation shoulder

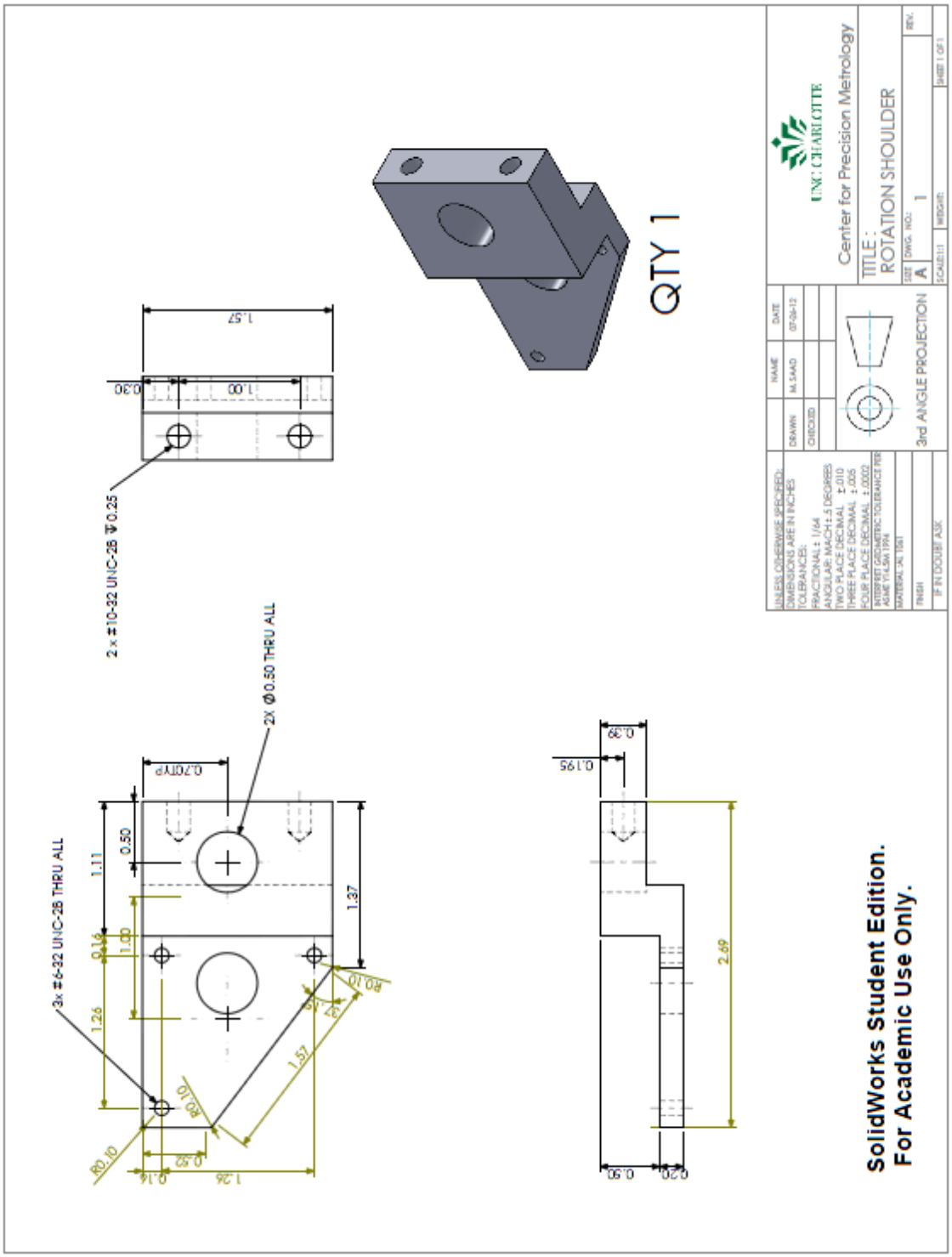

21. Prism holder (monitoring system)

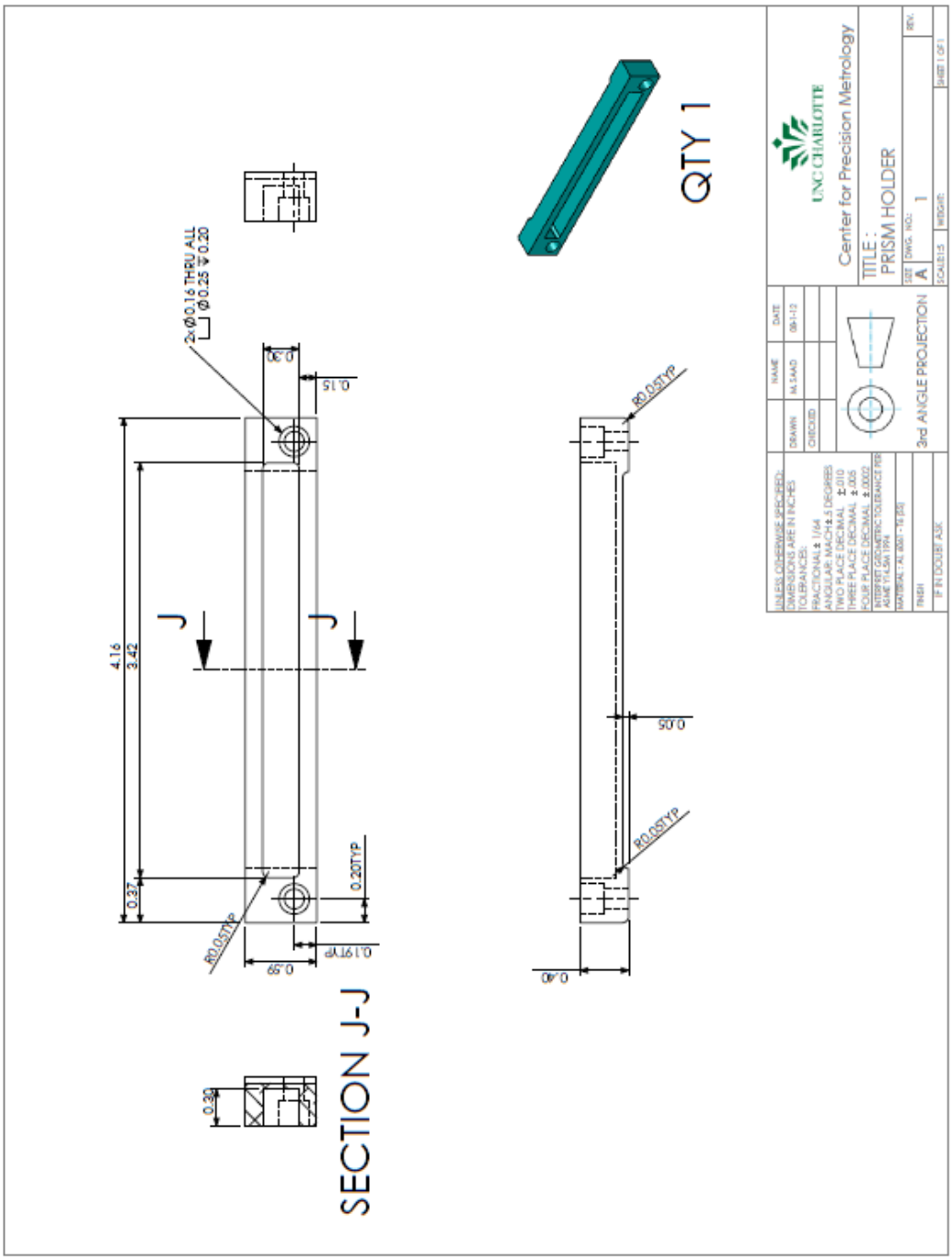

22. Bracket (monitoring system)

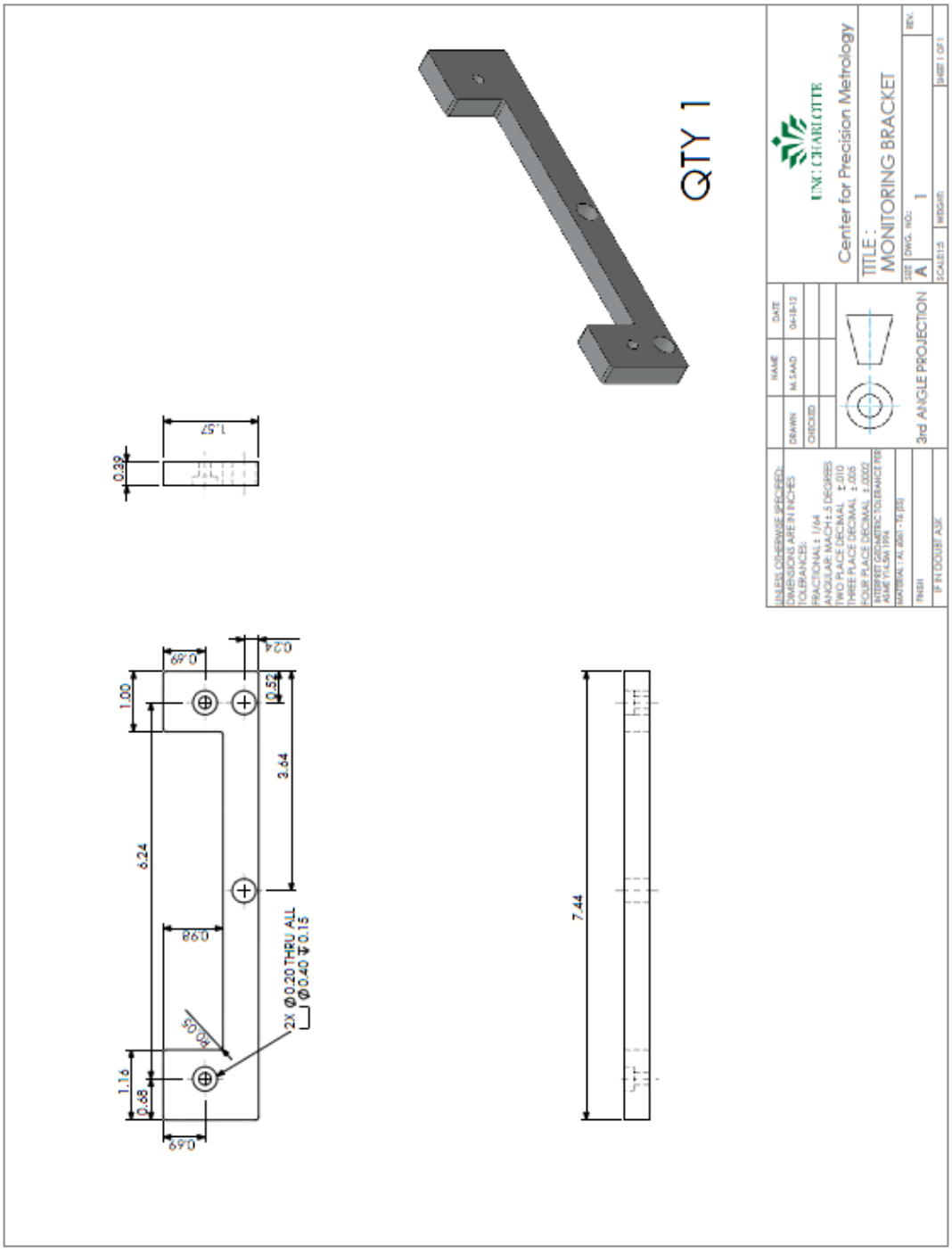

23. Index (monitoring system)

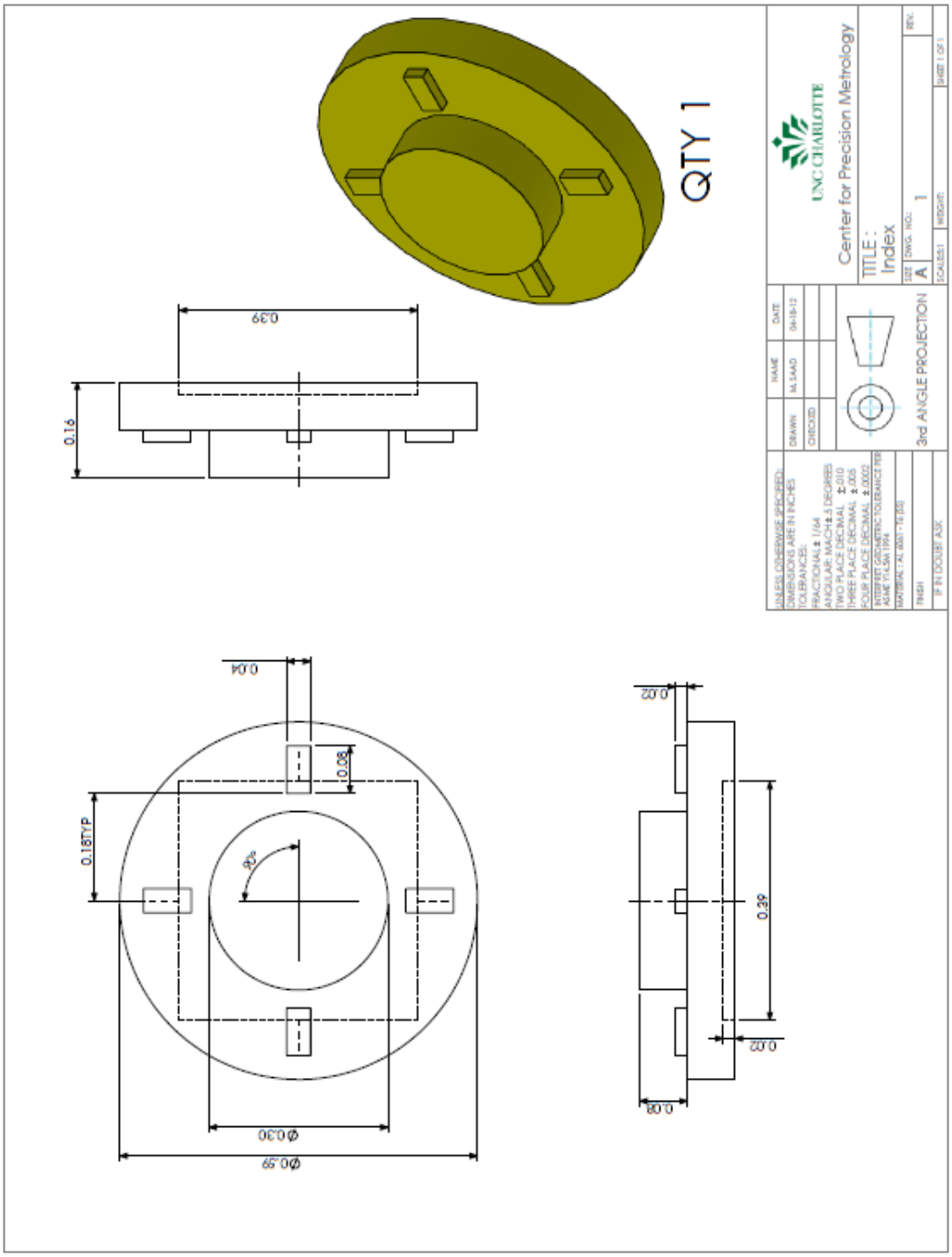

24. Index holder (monitoring system)

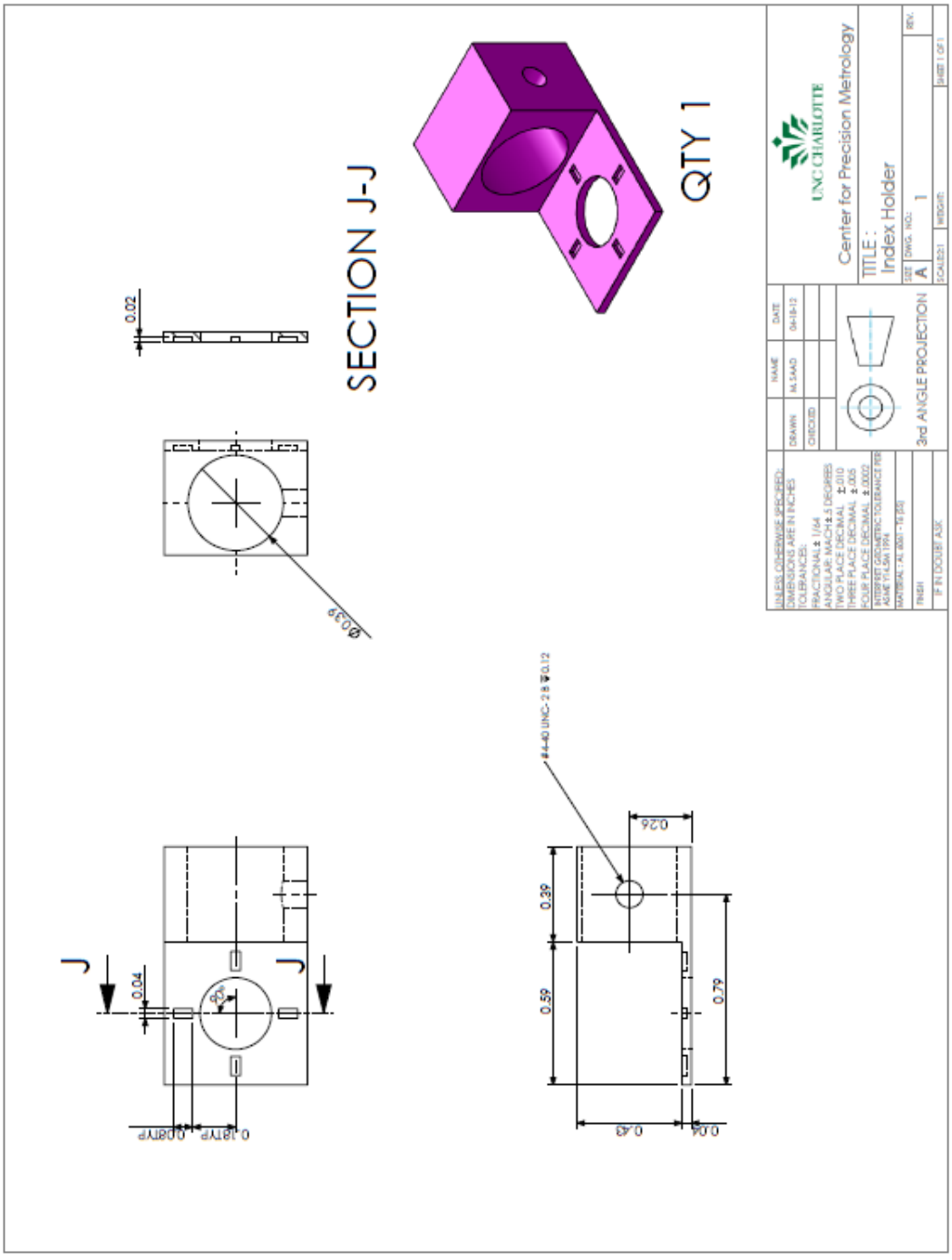

25. Base (fine adjustment device)

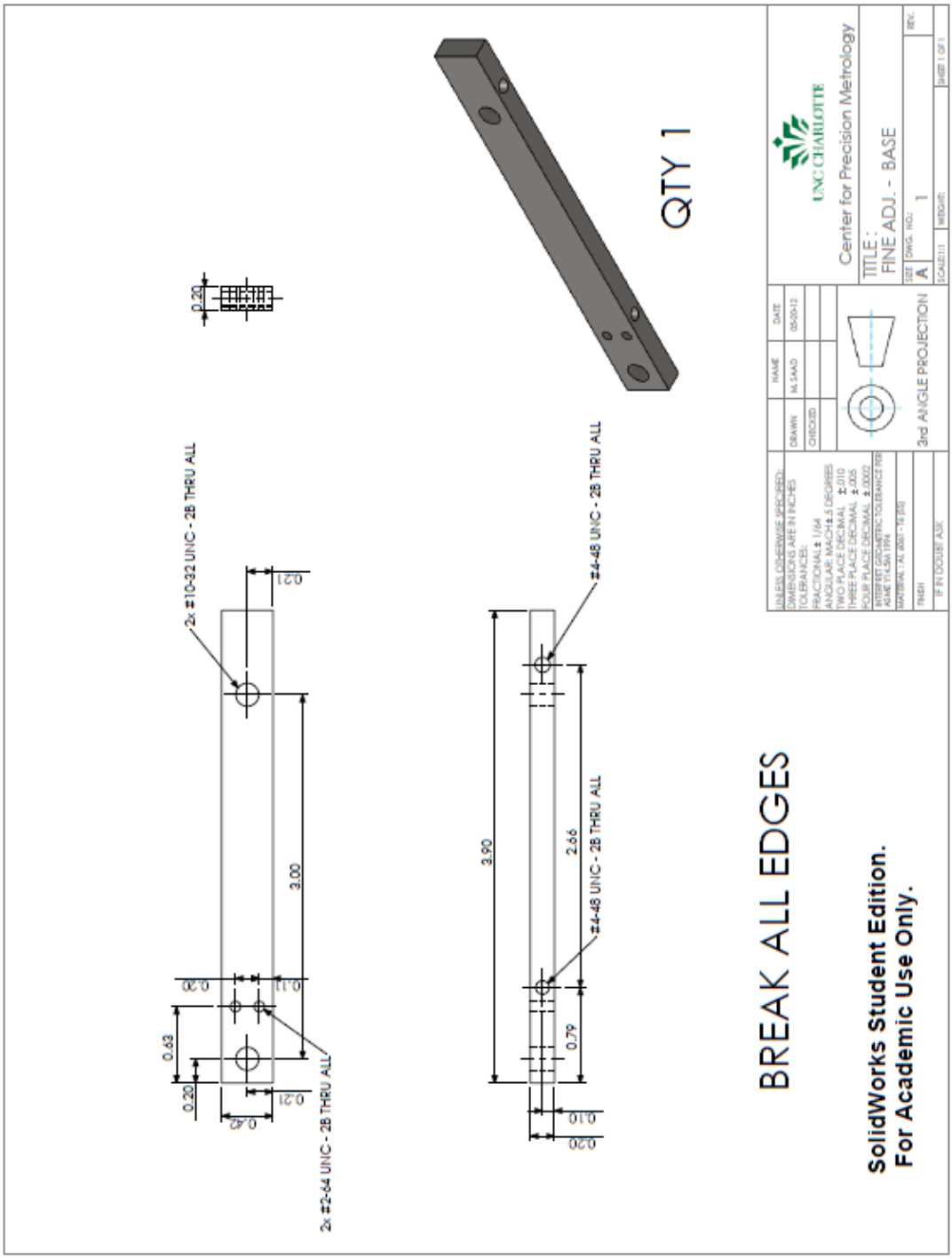
QTY 1
BREAK ALL EDGES
SolidWorks Student Edition.
For Academic Use Only.
UNC CHARLOTTE
Center for Precision Metrology
TITLE :
FINE ADJ. - BASE
3rd ANGLE PROJECTION
2x #10-32 UNC - 2B THRU ALL
2x #2-64 UNC - 2B THRU ALL
#4-48 UNC - 2B THRU ALL
#4-48 UNC - 2B THRU ALL
3.00
3.80
2.66
0.79
0.63
0.20

26. Slideway (fine adjustment device)

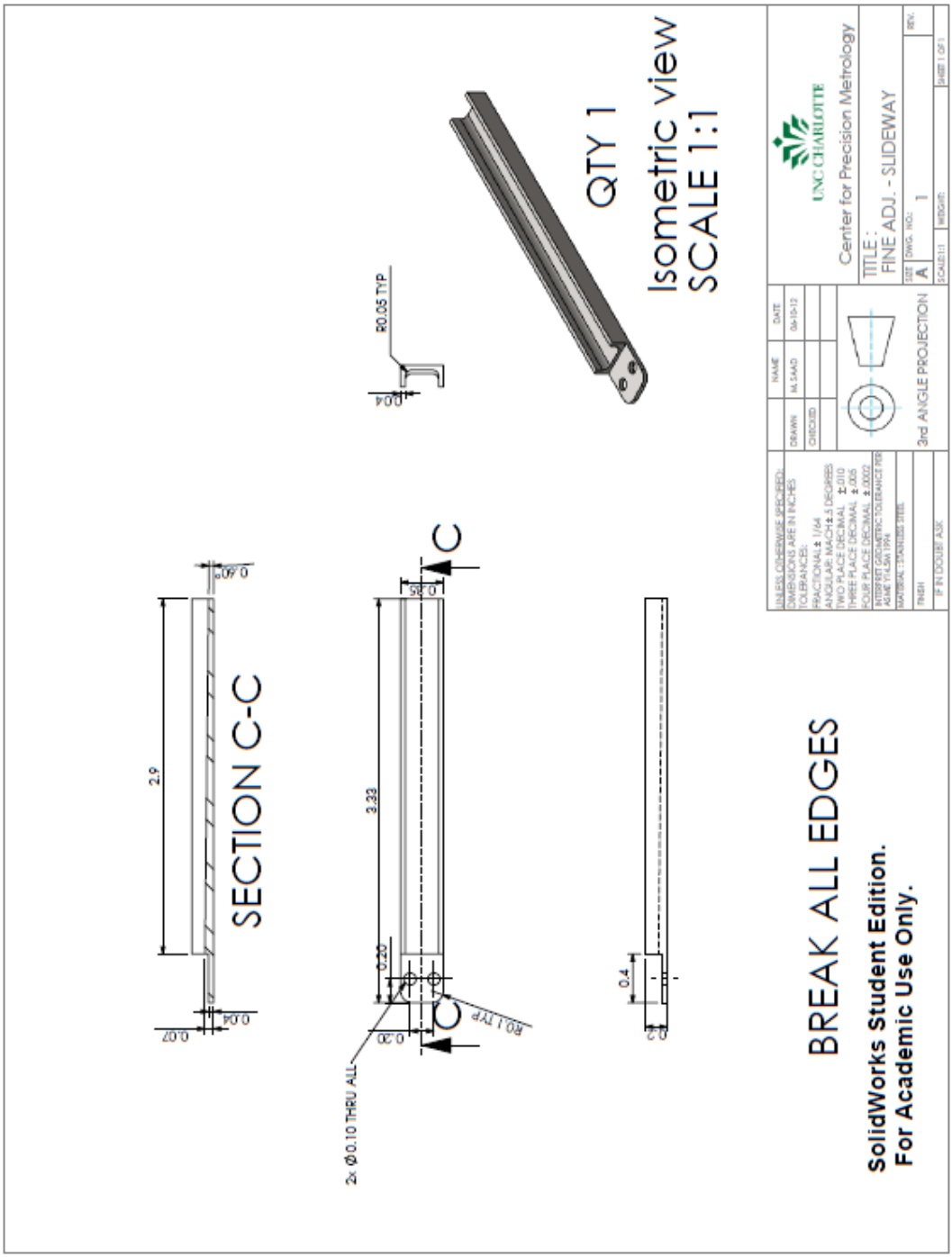

27. Slider (fine adjustment device)

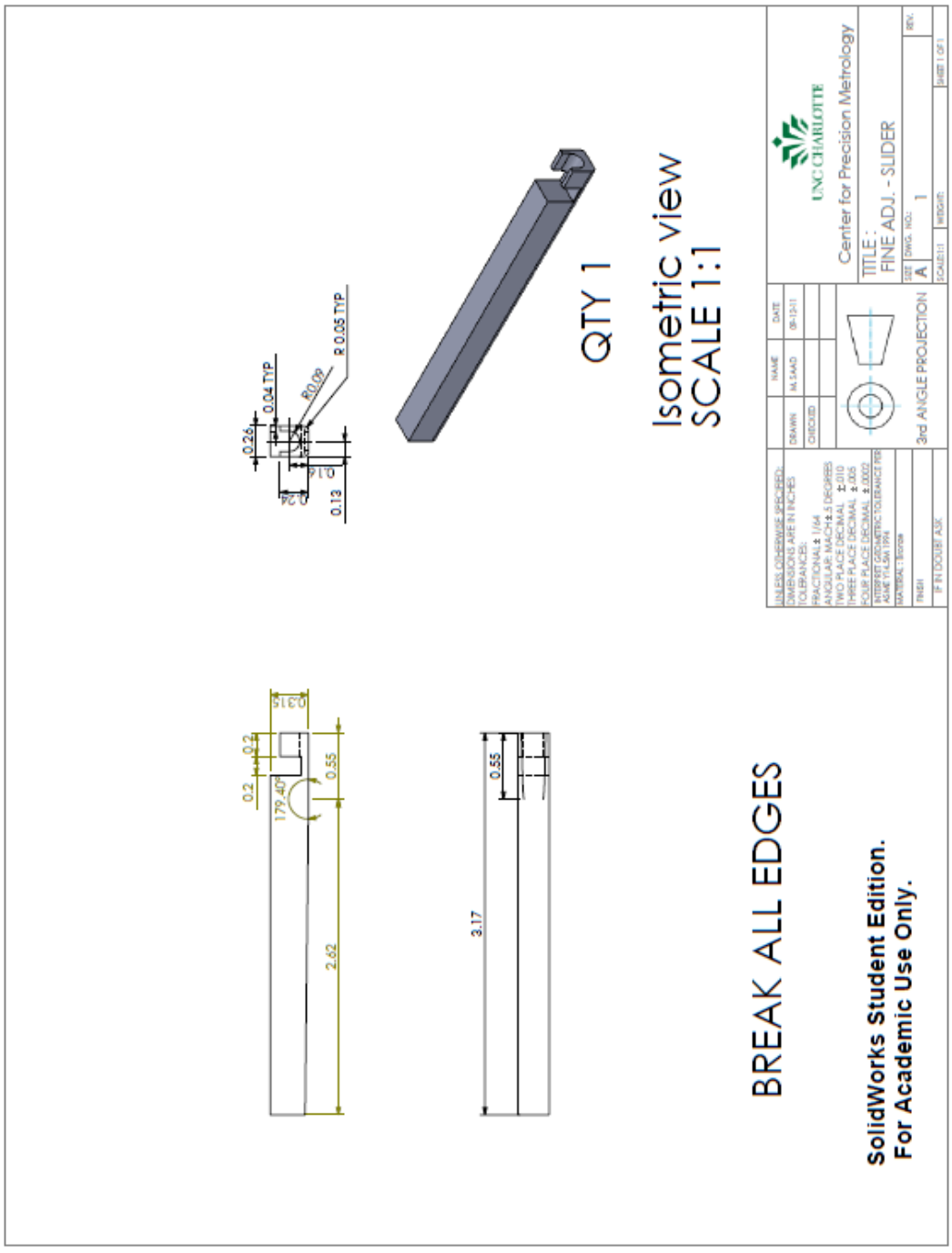

28. Cover (fine adjustment device)

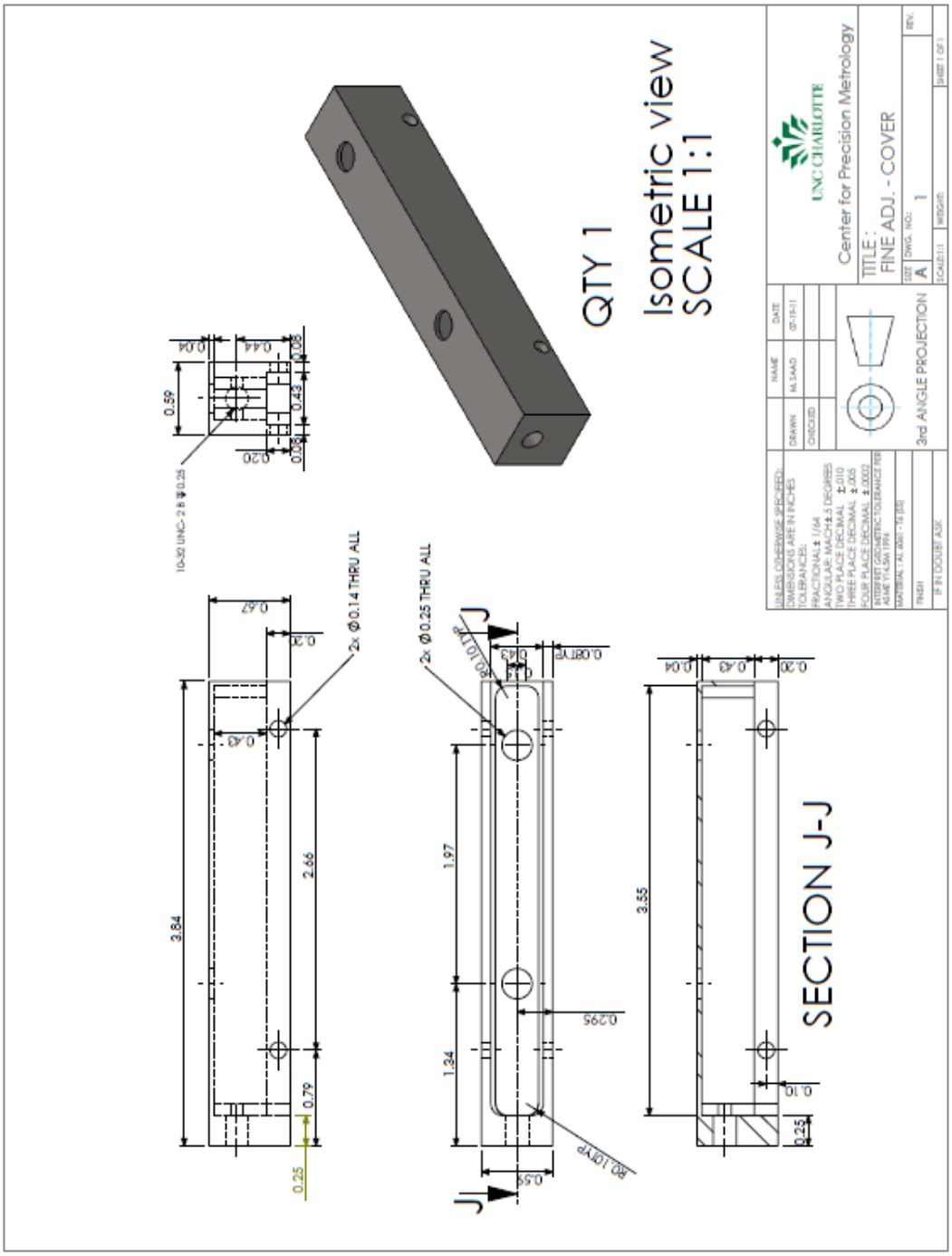

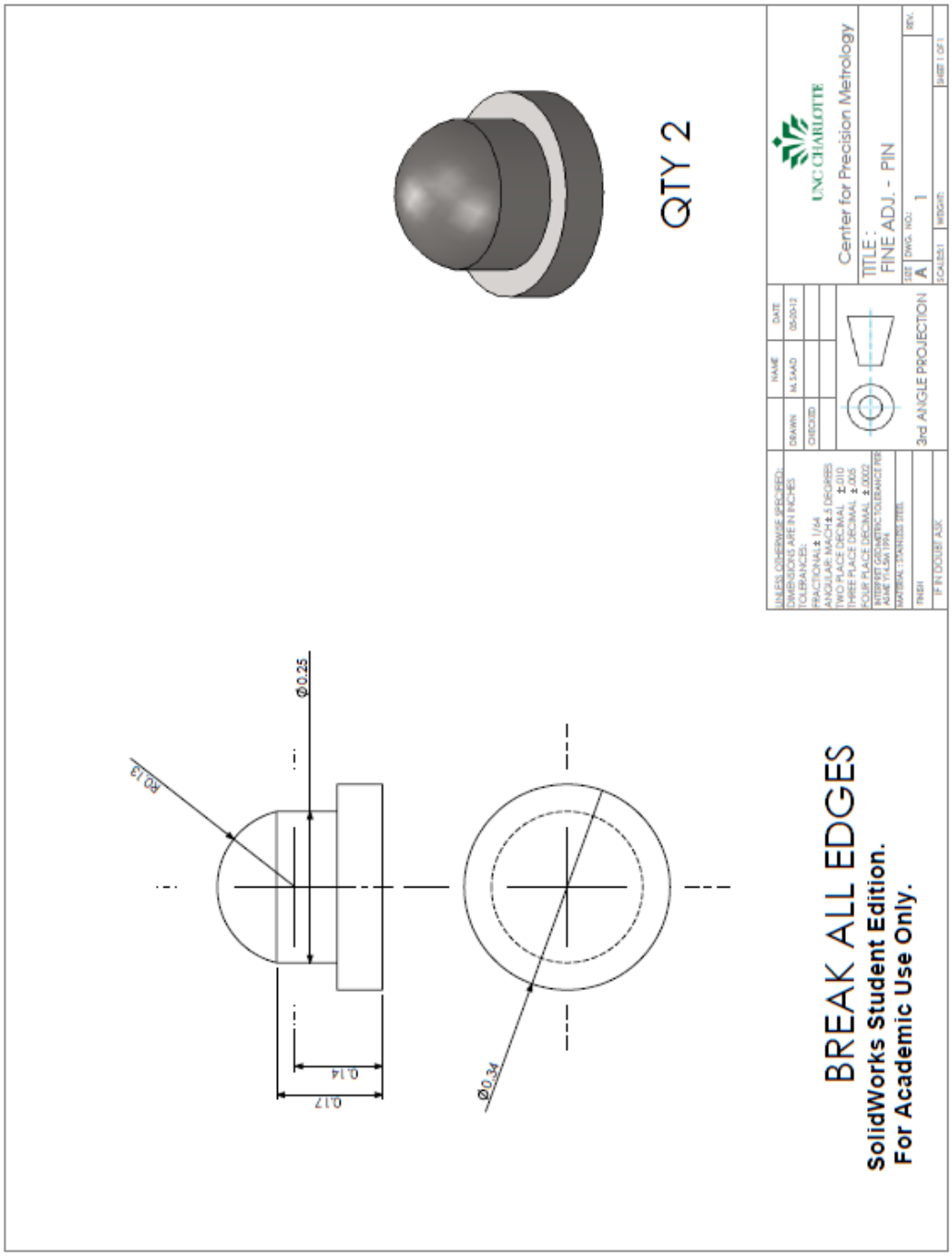
QTY 2
UNC CHARLOTTE
Center for Precision Metrology
TITLE:
FINE ADJ. - PIN
3rd ANGLE PROJECTION
BREAK ALL EDGES
SolidWorks Student Edition.
For Academic Use Only.

29. Pin (fine adjustment device)

30. Base (eddy current damper yoke)

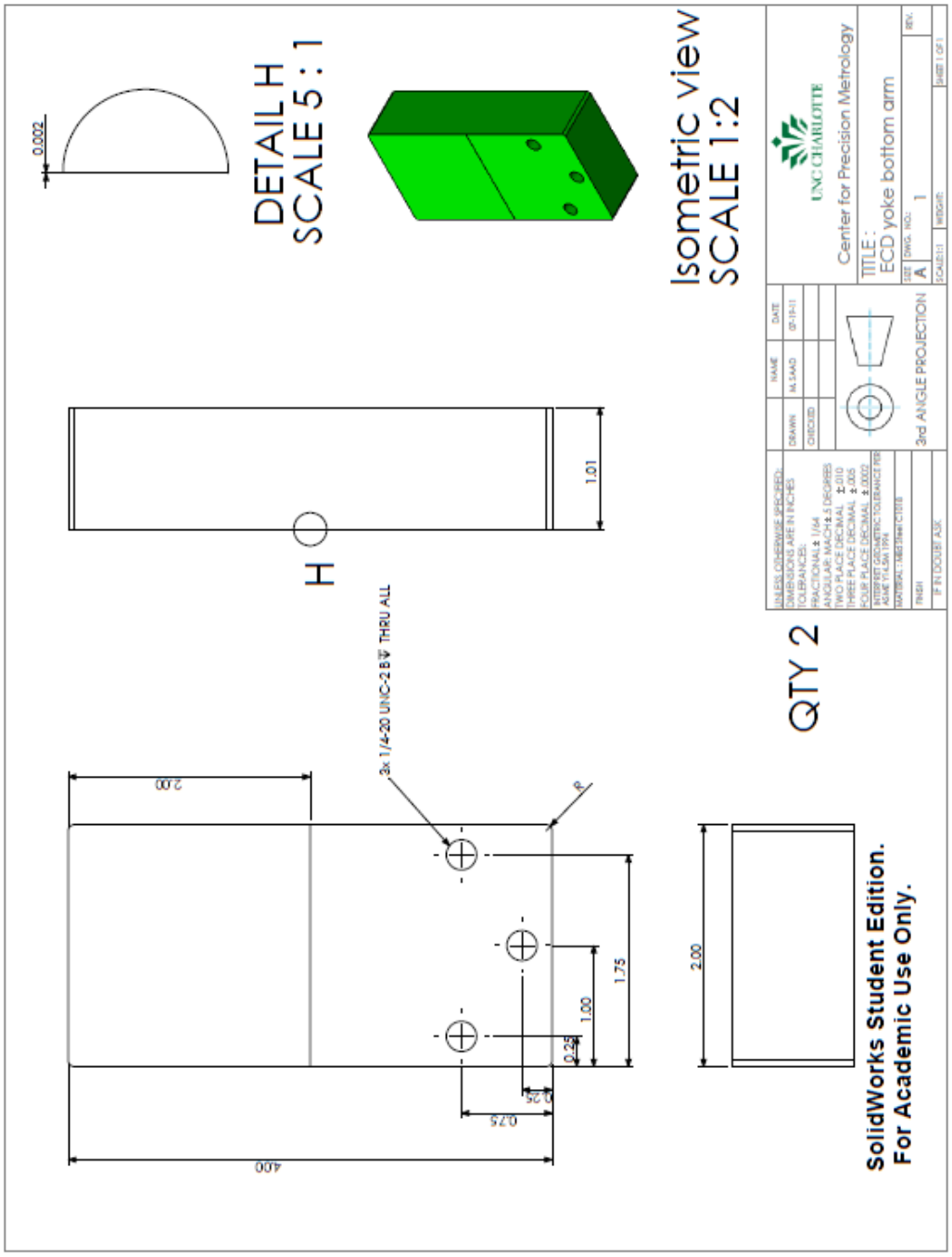

31. Plate (eddy current damper yoke)

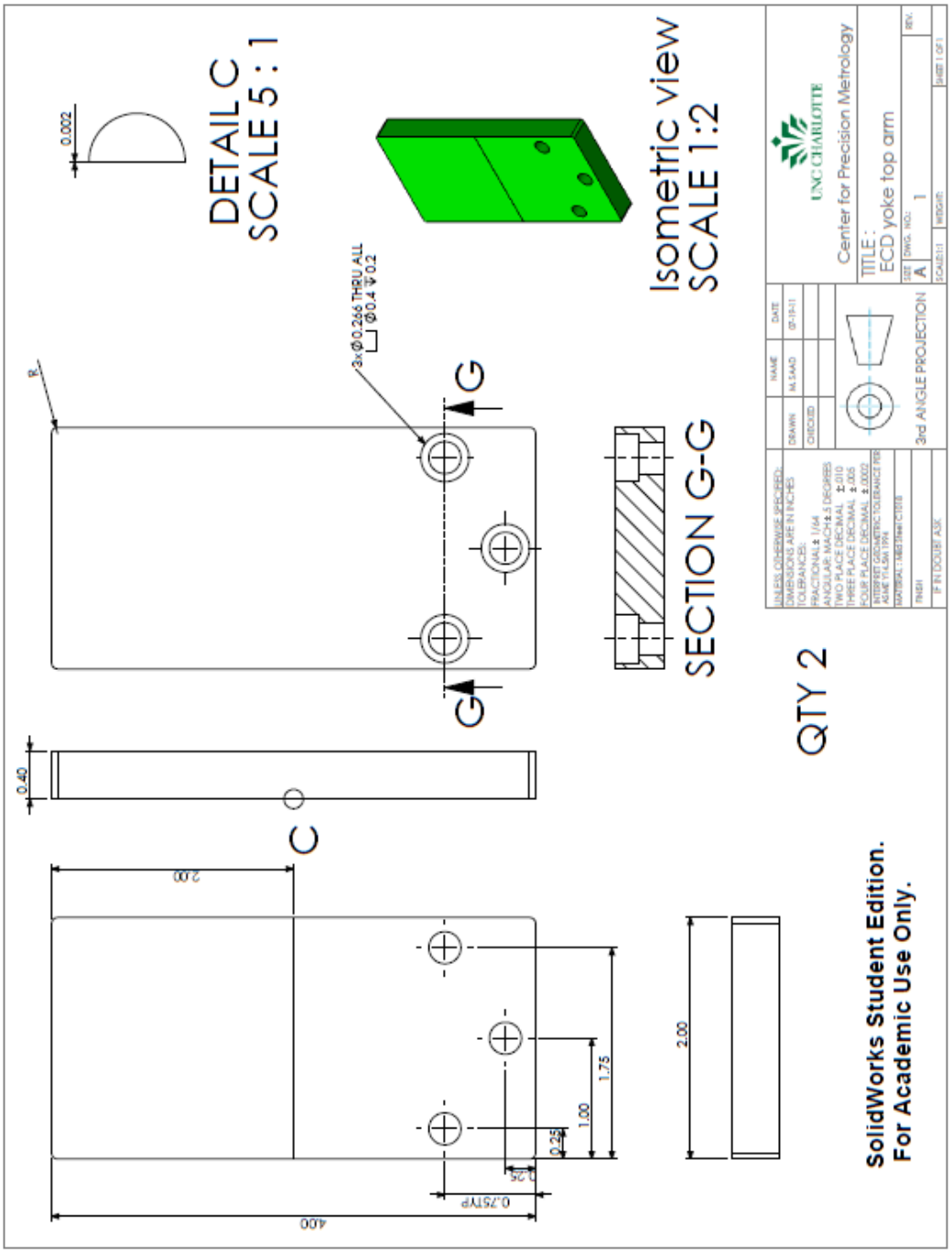

32. Spacer (eddy current damper yoke)

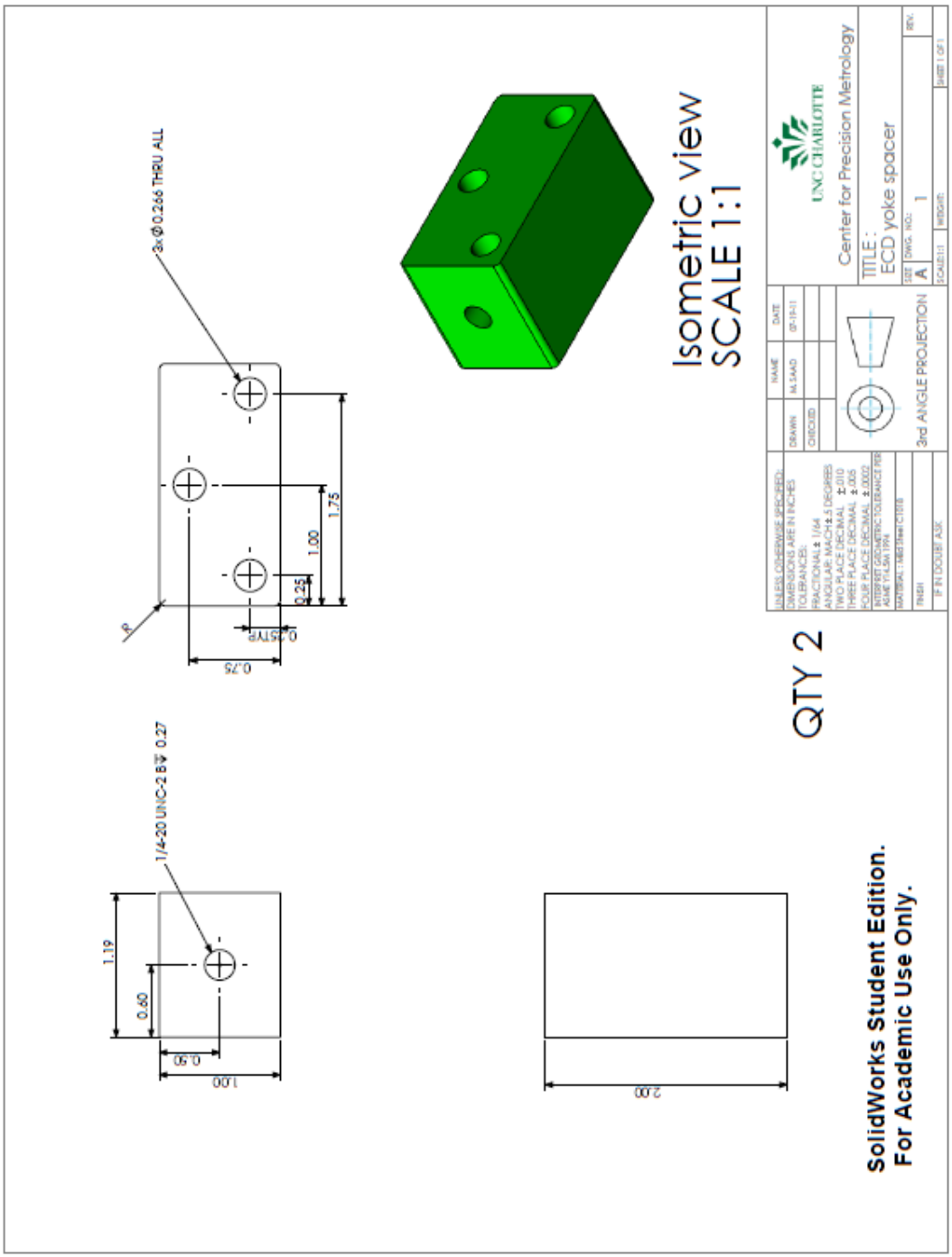

33. Shoulder (eddy current damper yoke)

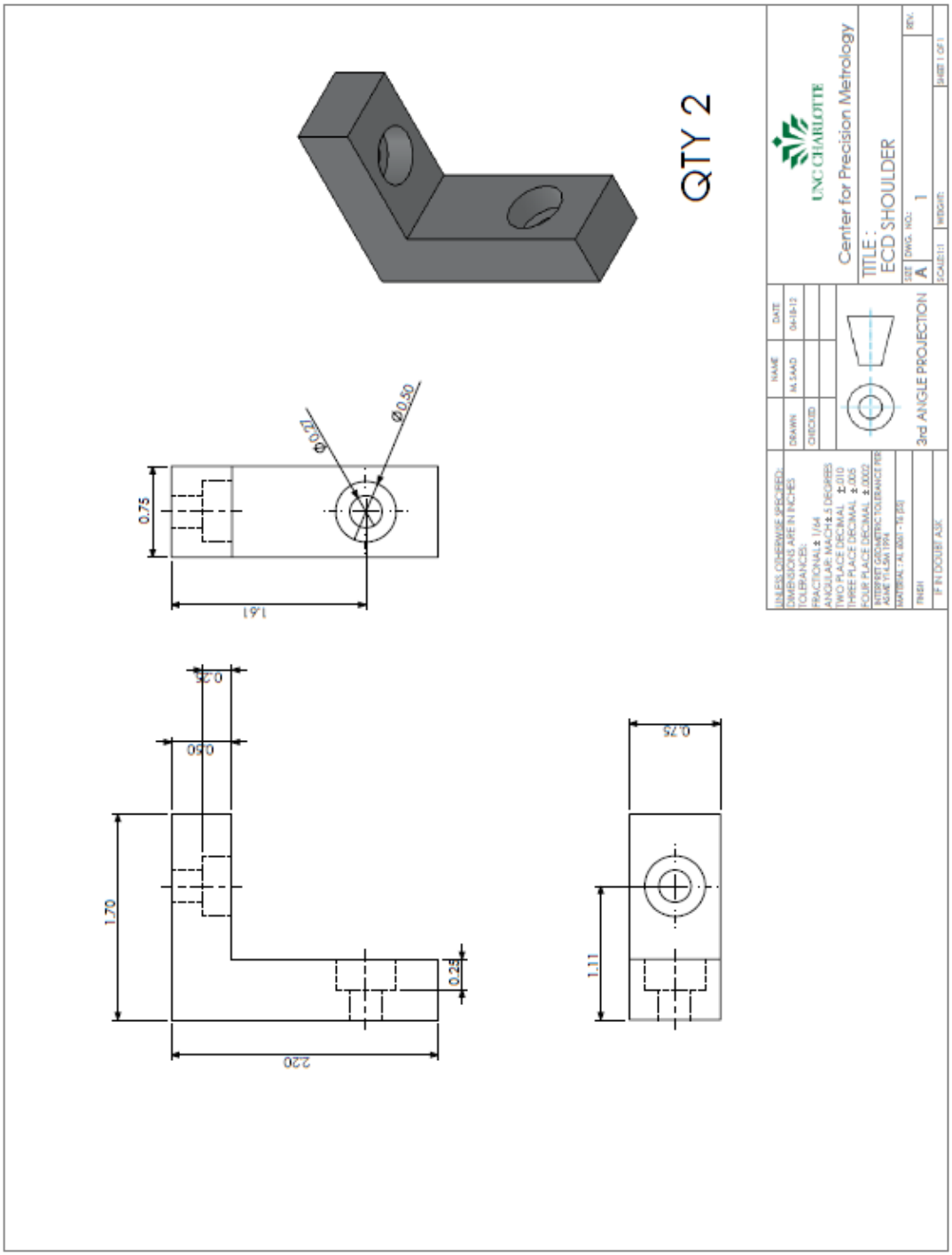

34. Copper plate holder (eddy current damper)

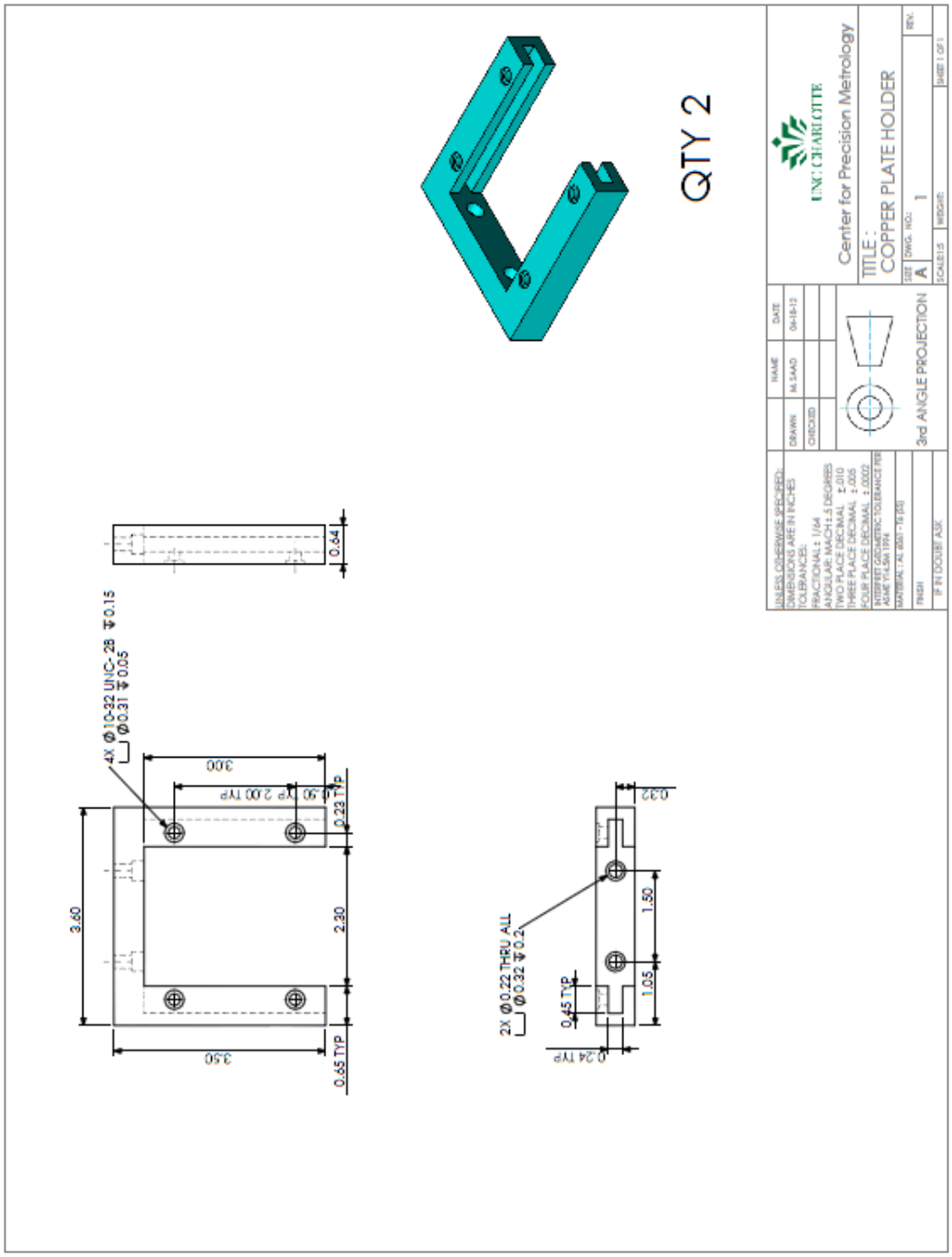

35. Copper plate (eddy current damper)

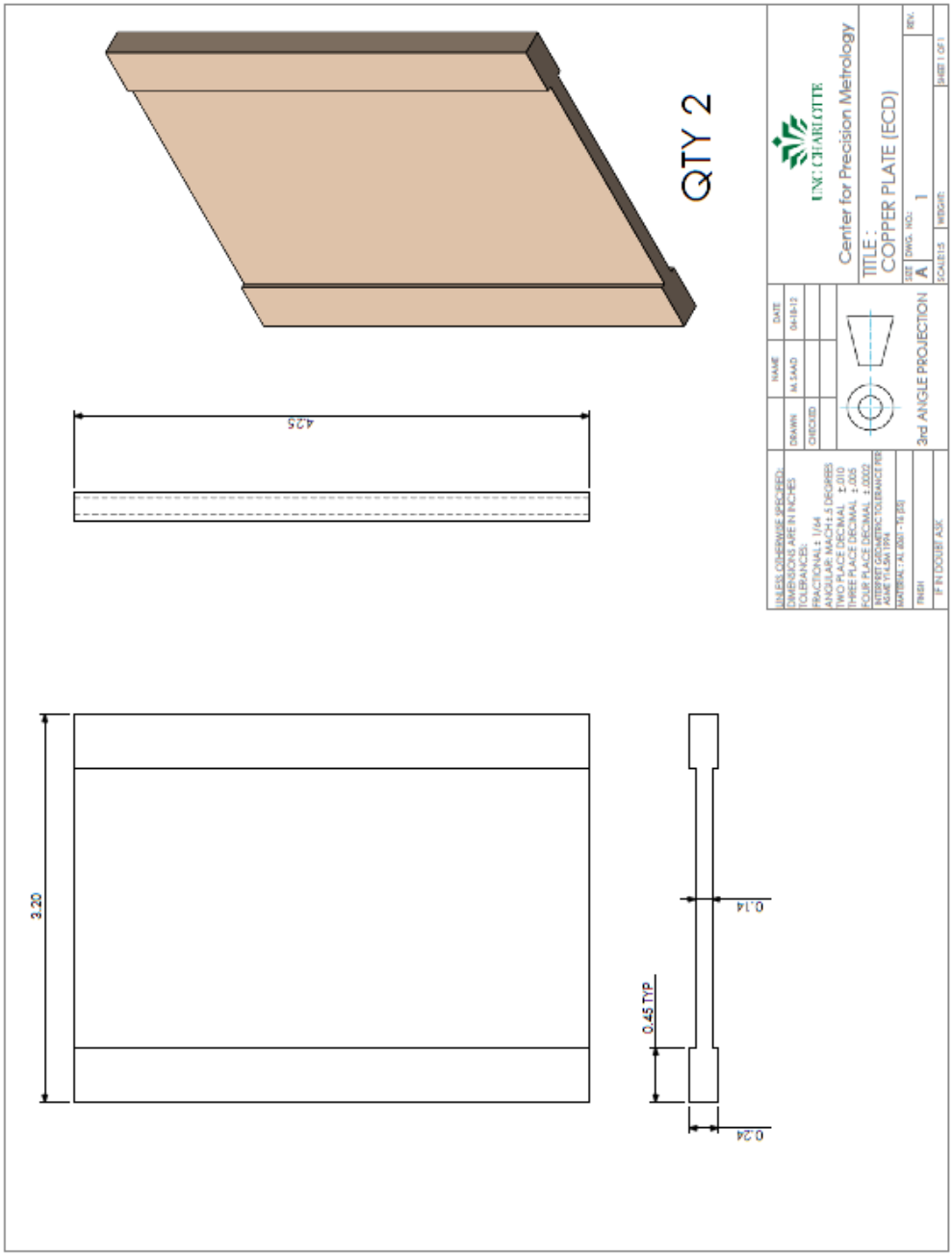

36. Limit switch base

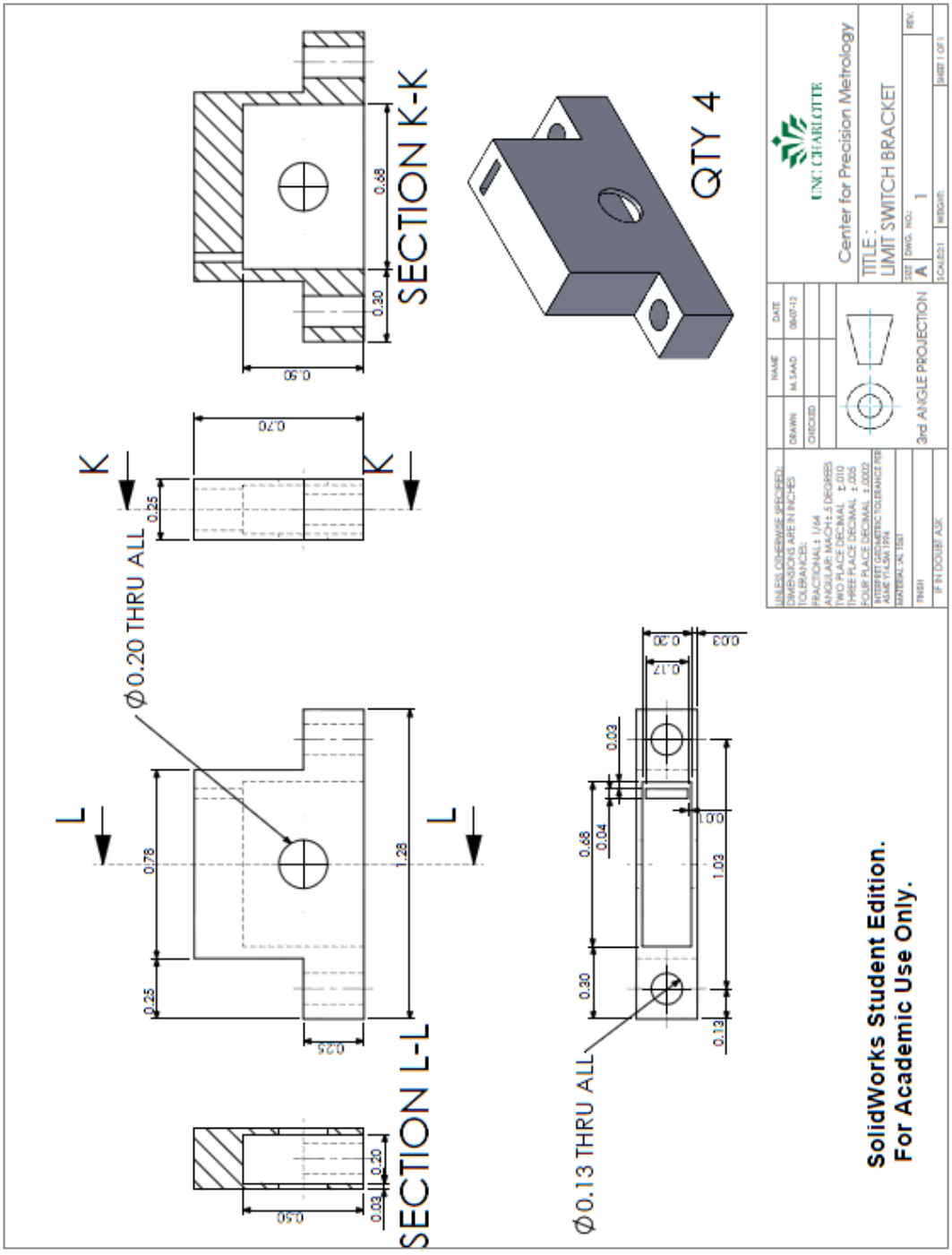

37. Hard stop

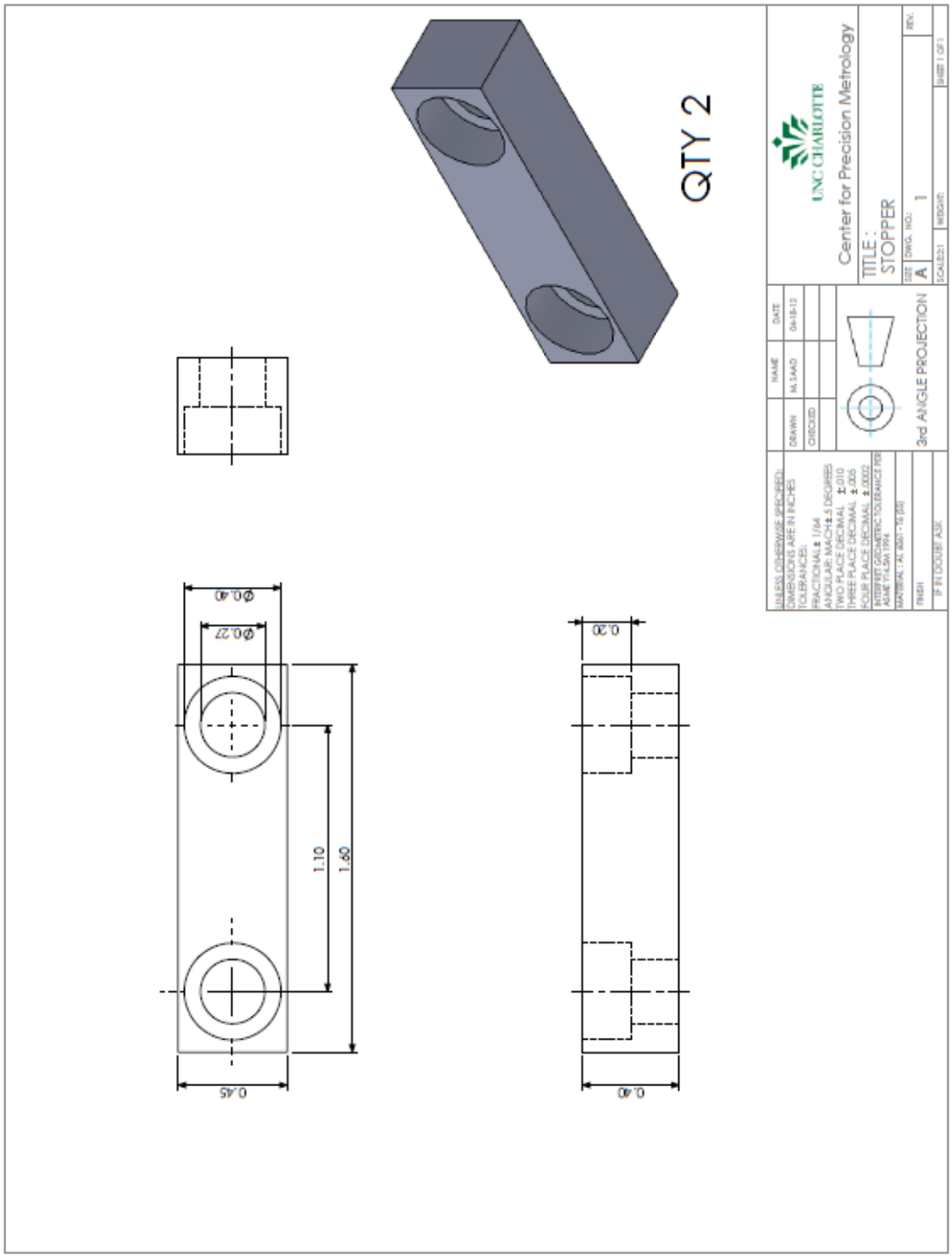
QTY 2
UNC CHARLOTTE
Center for Precision Metrology
TITLE :
STOPPER
3rd ANGLE PROJECTION
Ø0.40
Ø0.27
1.10
1.60
0.45
0.30
0.40

38. Hard stop (front - air bearing side)

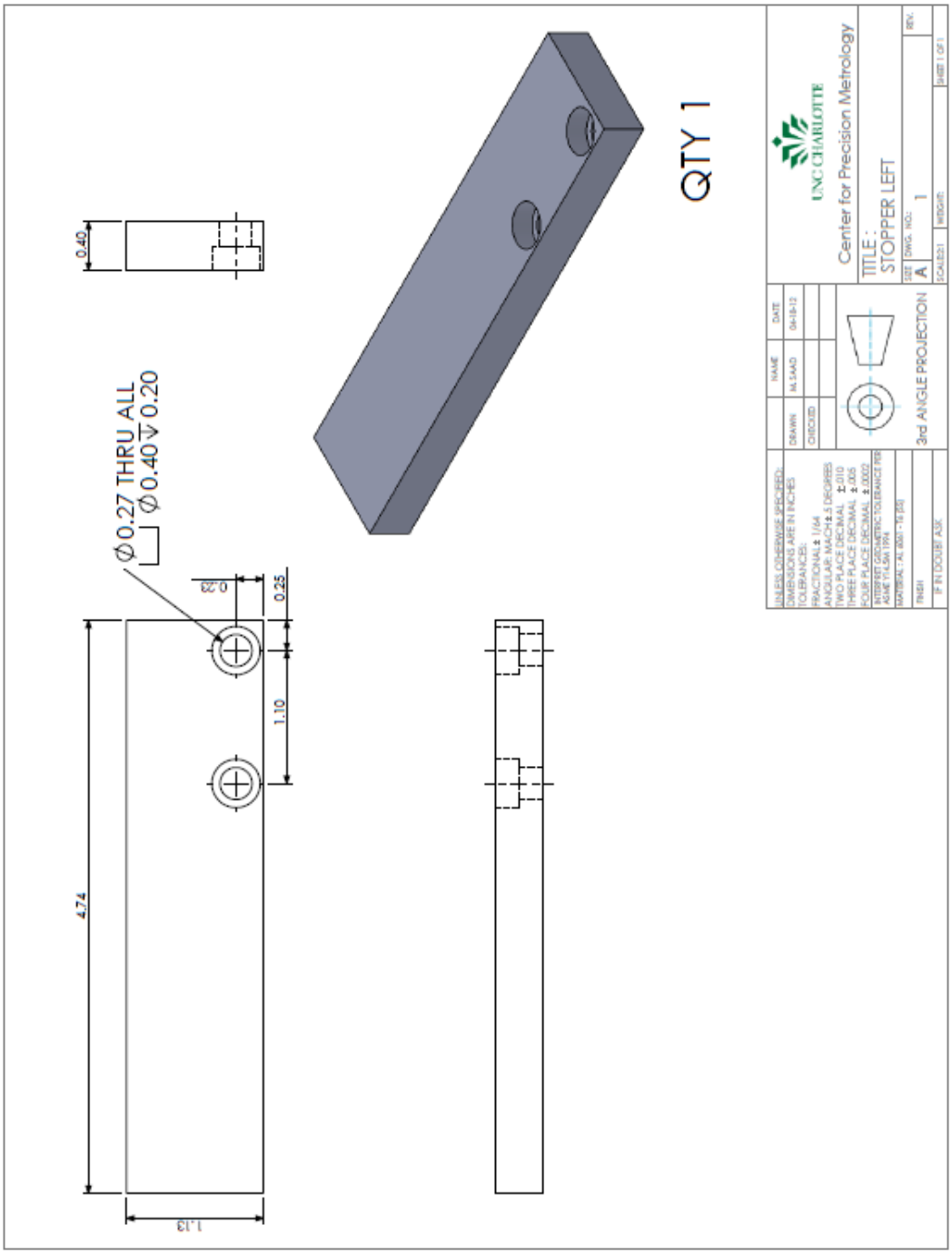

39. Hard stop (front)

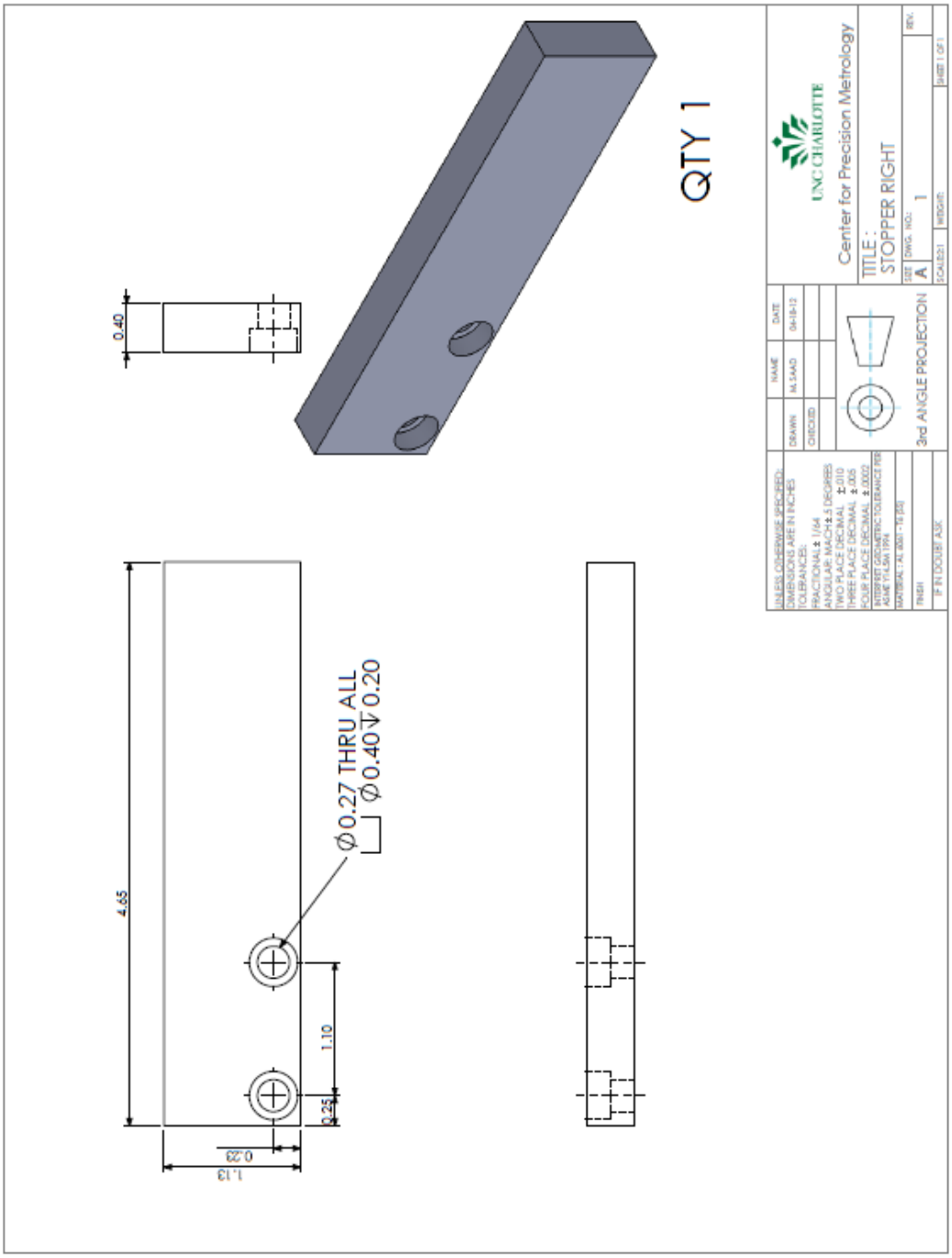

40. Locking knob

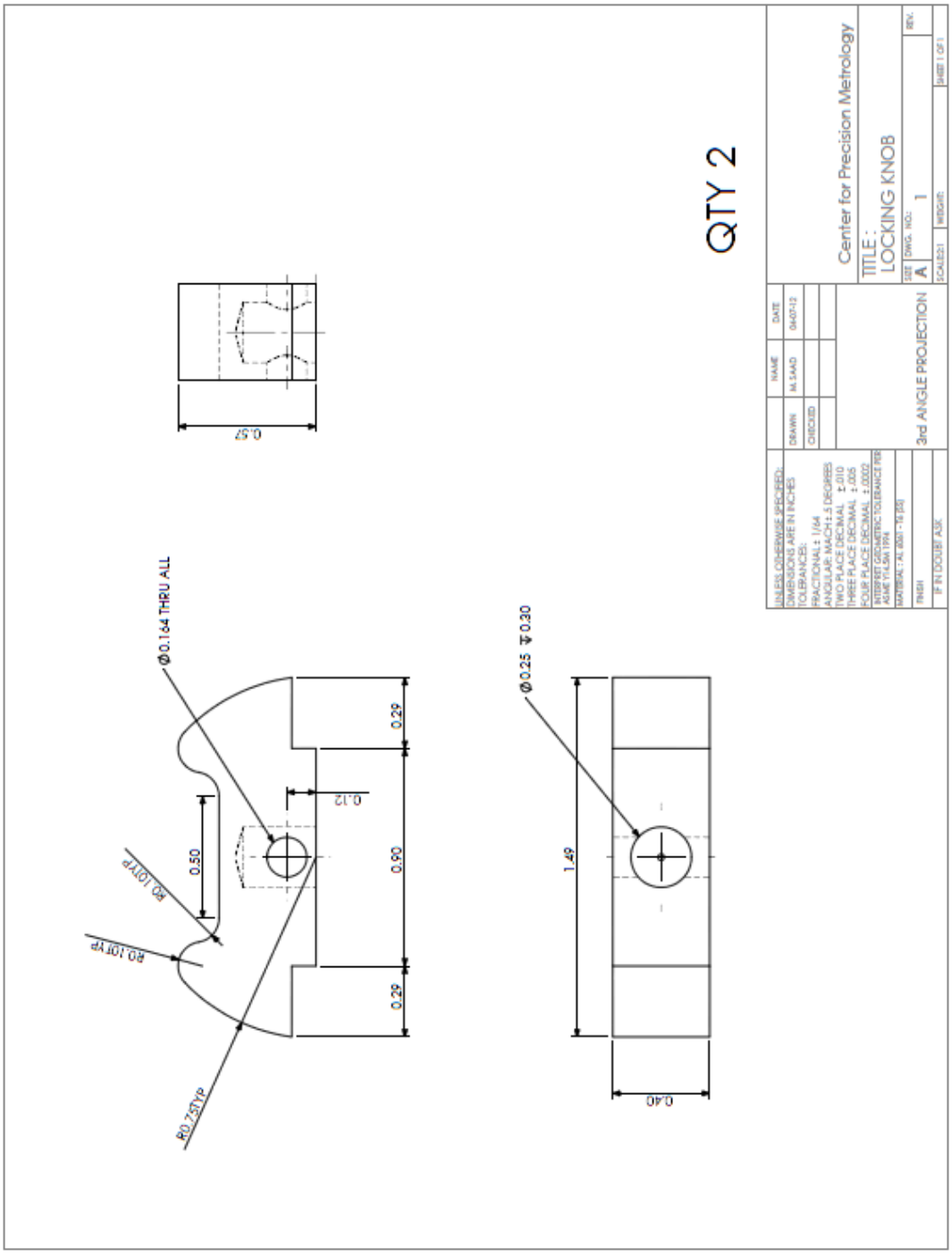

41. Thermal compensation base

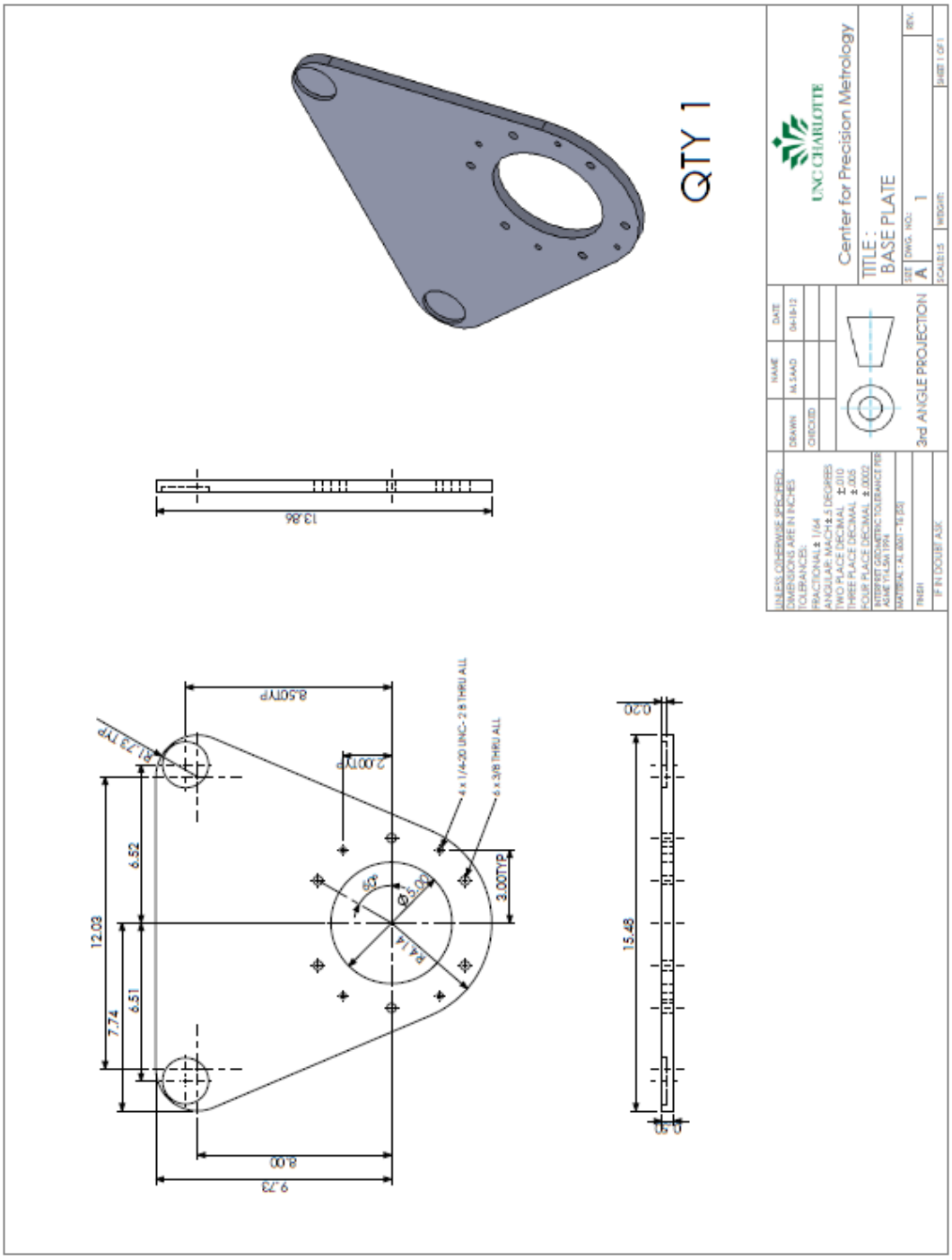

42. Spindle flange

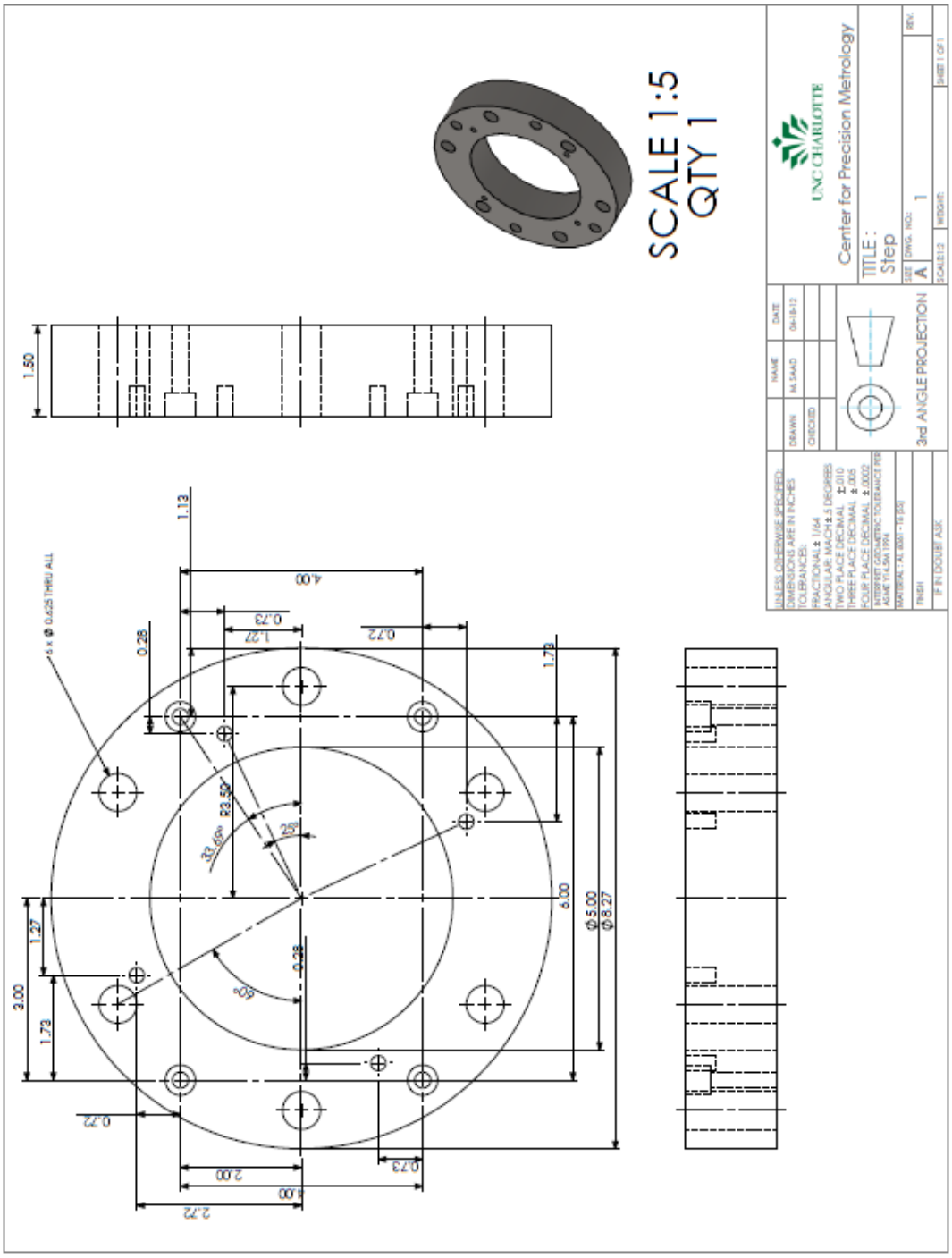

43. Renishaw read-head base (air bearing side)

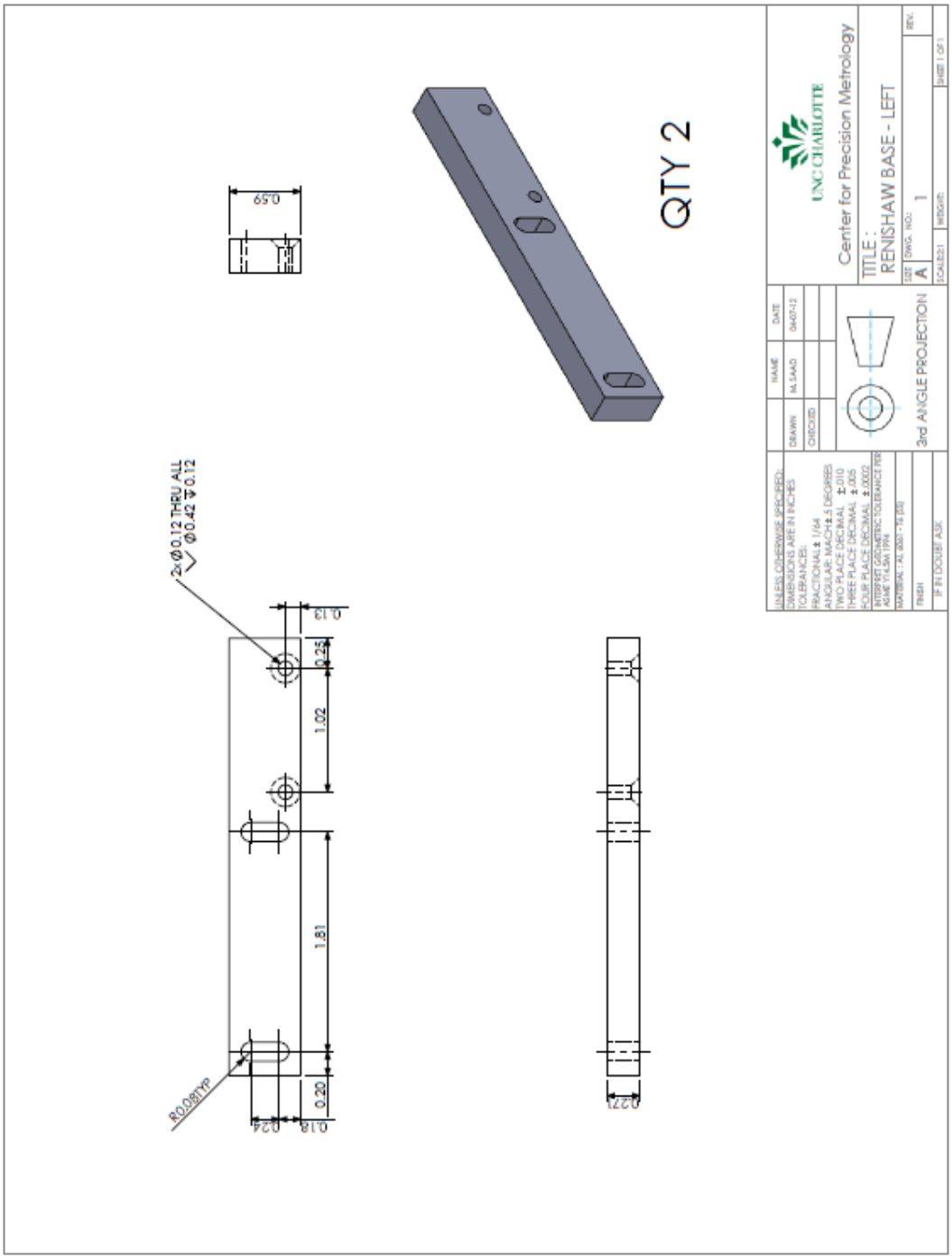

44. Renishaw read-head base

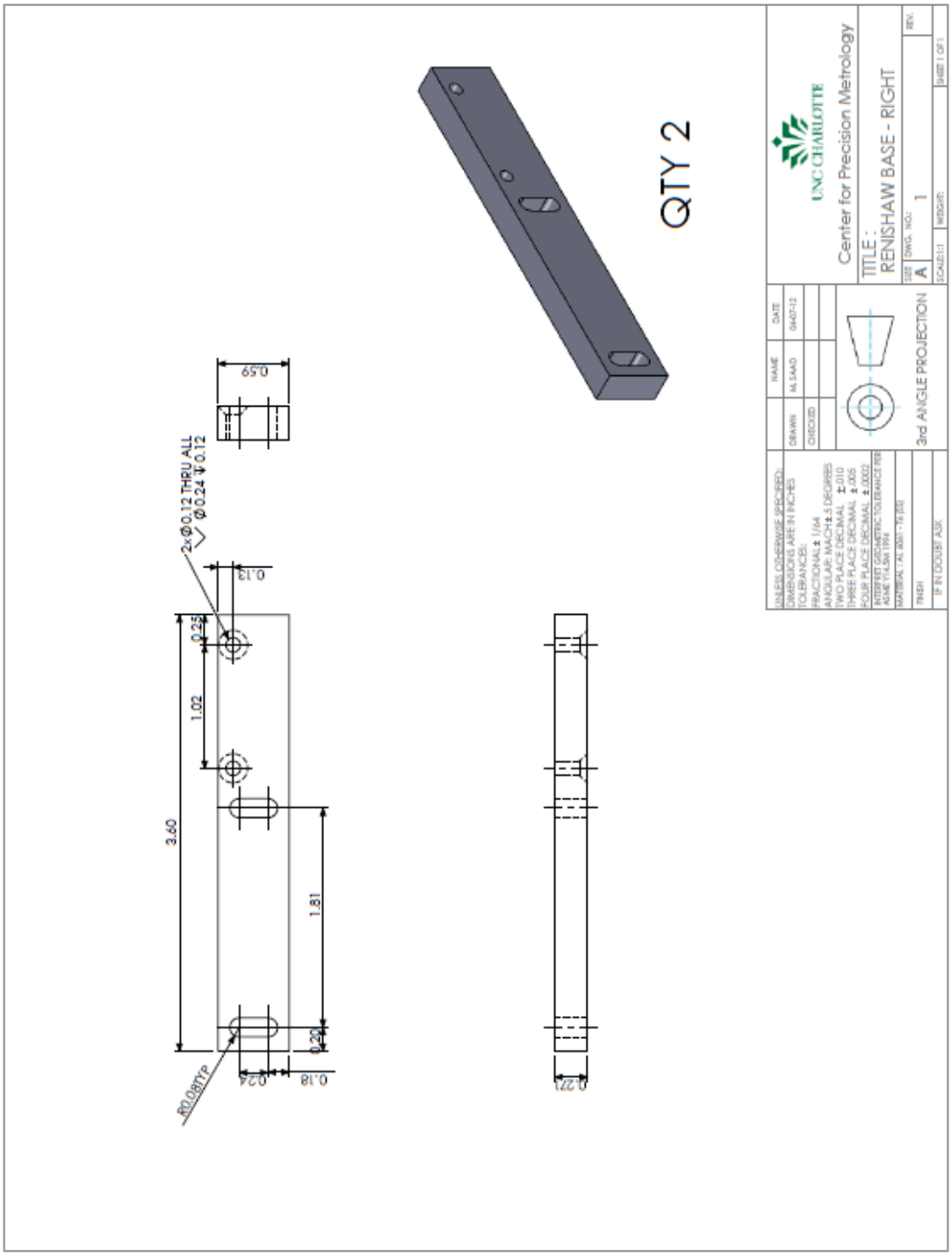

45. Base (air bearing test setup)

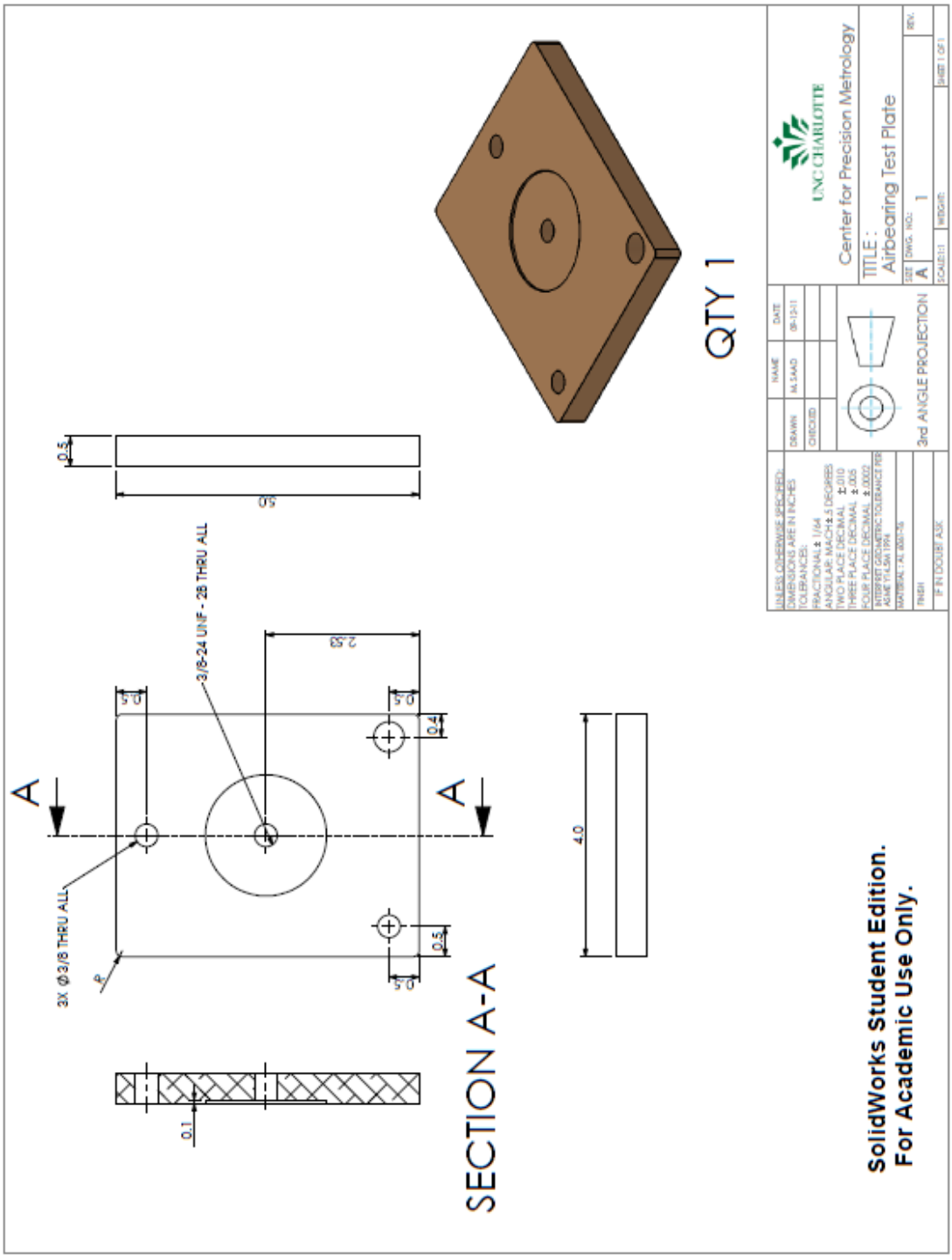

46. Spacer (air bearing test setup)

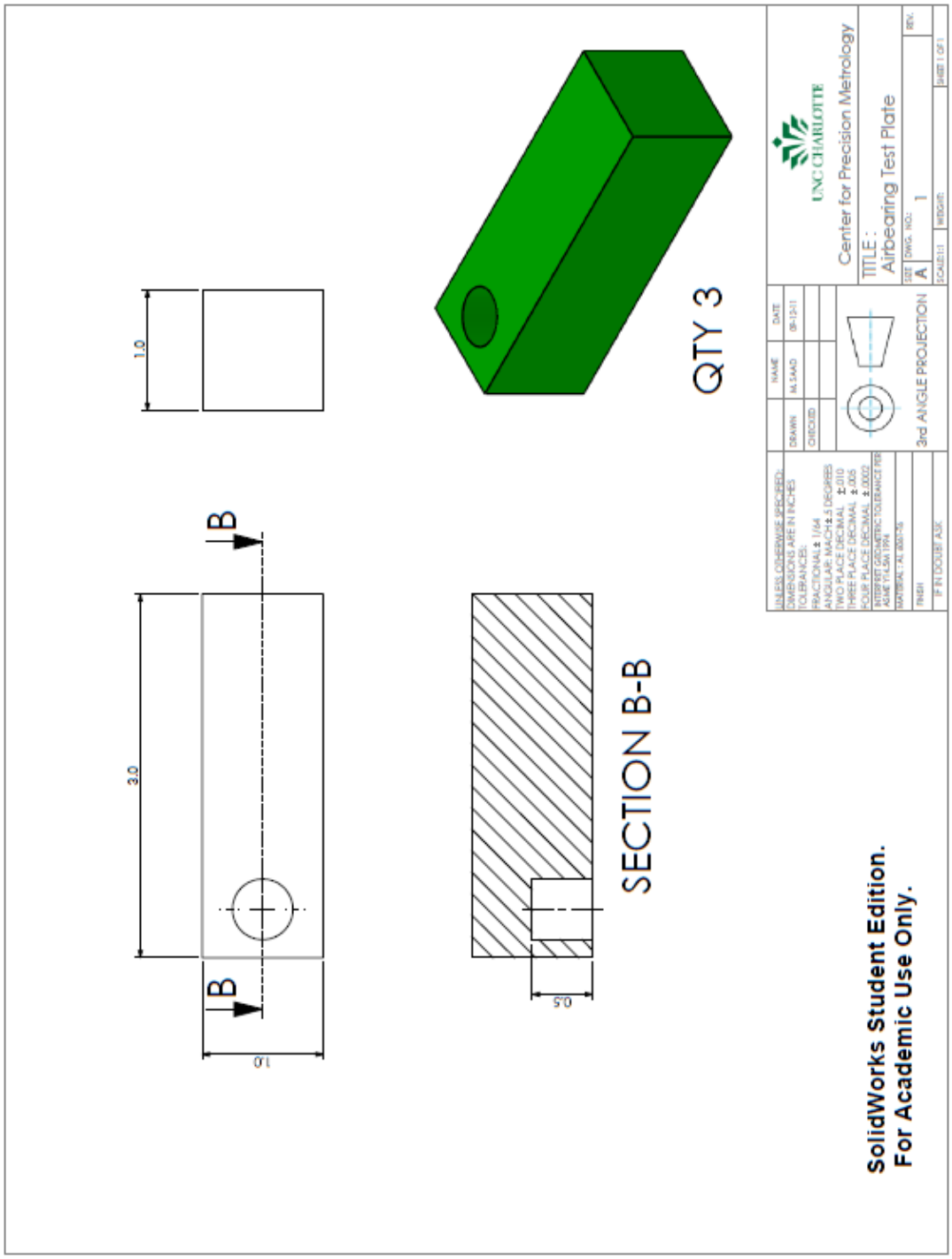

47. Wire winding template

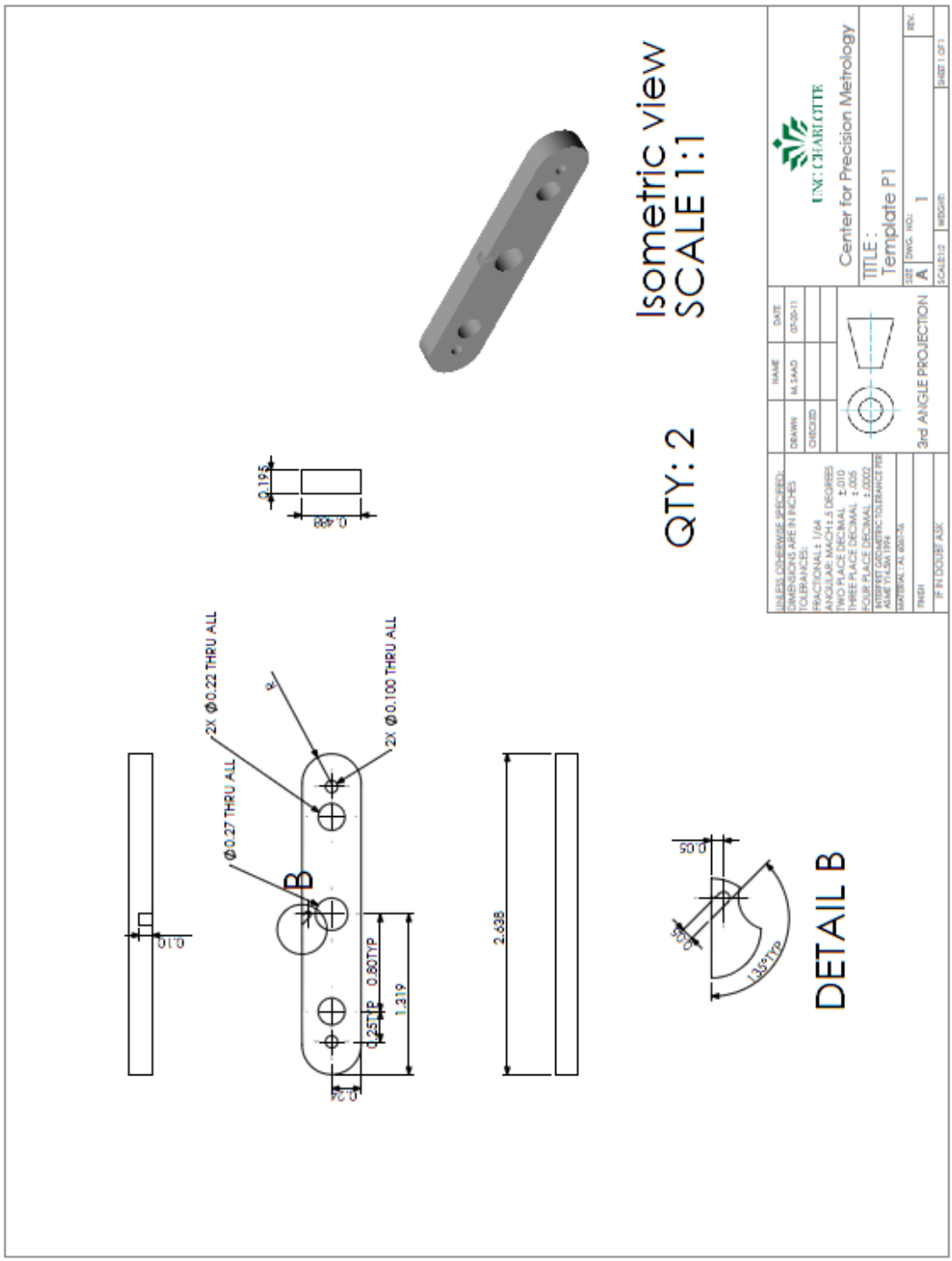

48. Wire winding shoulder (inlet)

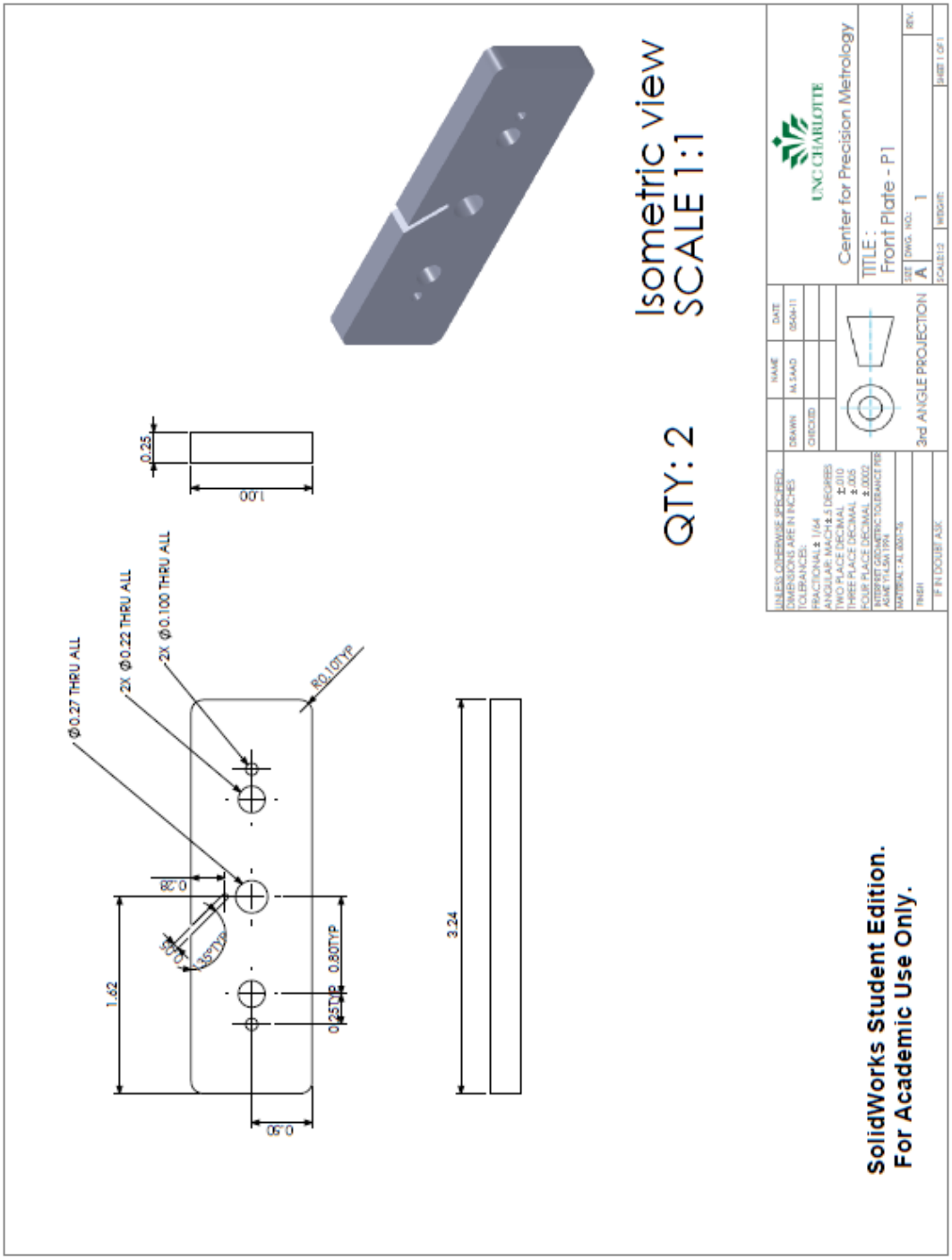

49. Wire winding shoulder (outlet)

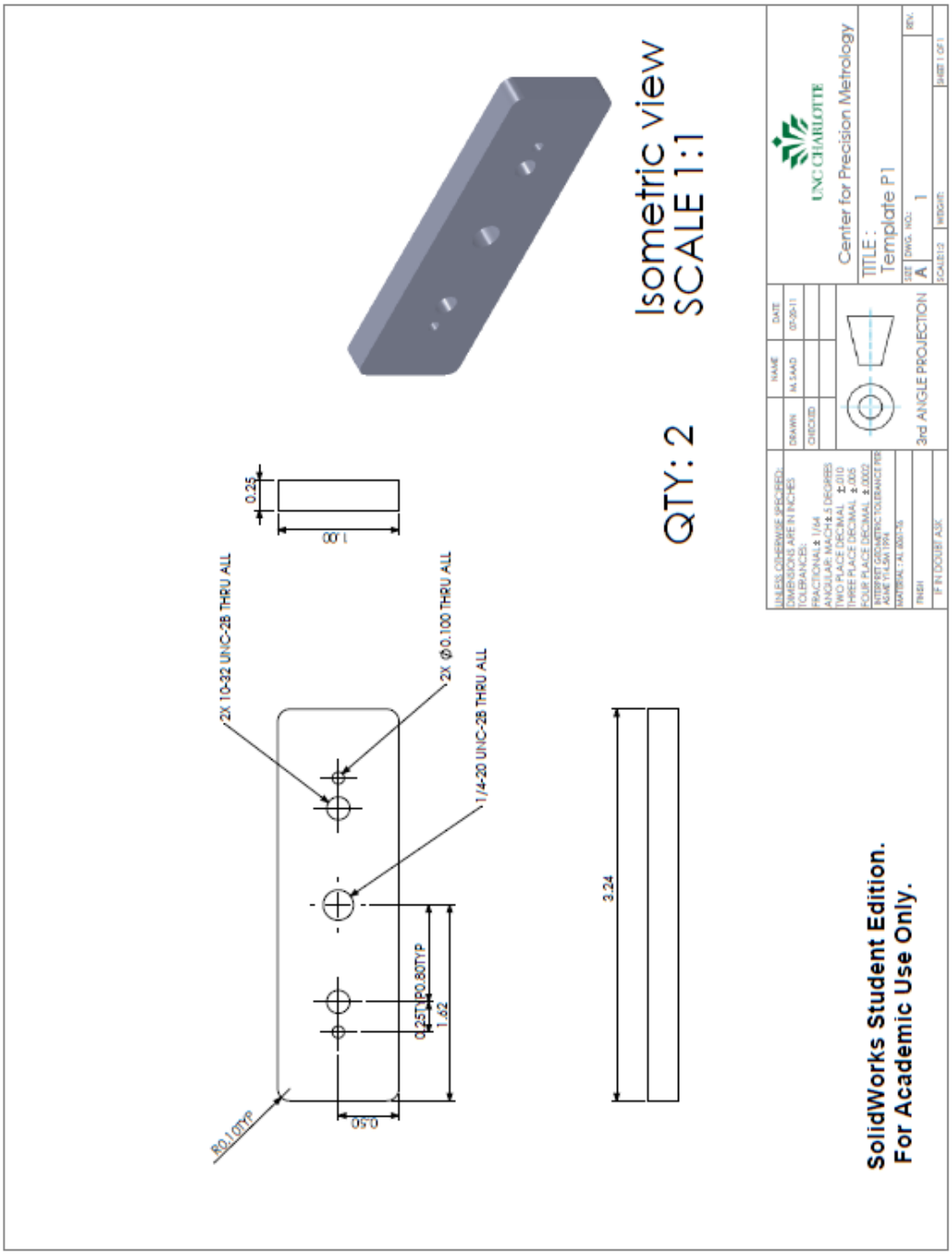

50. Wire winding spindle

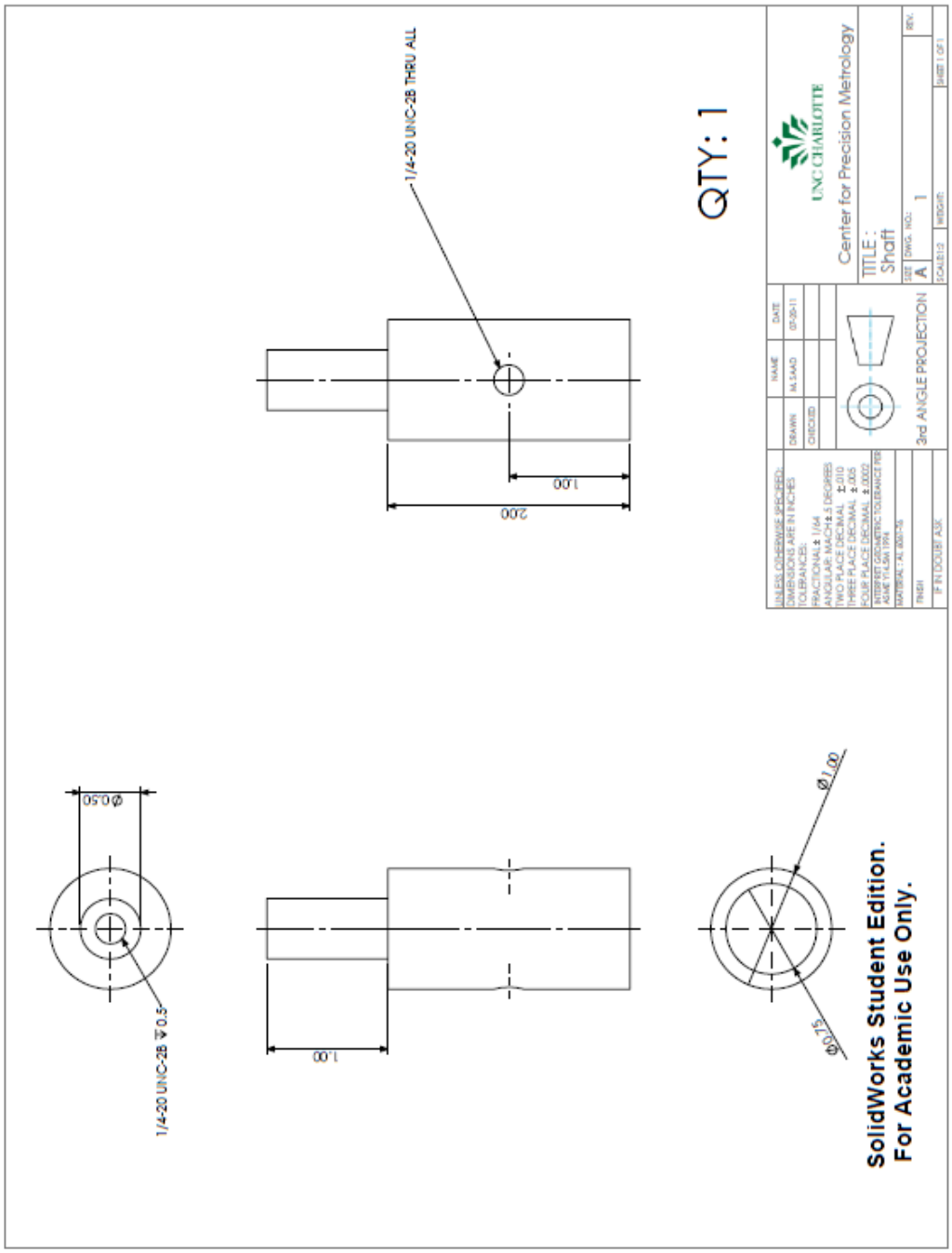

APPENDIX B: LINEAR MOTOR STATOR WIRING SCHEMATIC [Fesperman, 2006]

I = Input O = Output